Numerical simulation of deformation microstructures and folds in polar ice and ductile rocks

Dissertation der Mathematisch-Naturwissenschaftlichen Fakultät
der Eberhard Karls Universität Tübingen
zur Erlangung des Grades eines
Doktors der Naturwissenschaften
(Dr. rer. nat.)

vorgelegt von
Maria Gema Llorens Verde
aus Zaragoza (Spanien)

Tübingen
2015

Gedruckt mit Genehmigung der Mathematisch-Naturwissenschaftlichen Fakultät der
Eberhard Karls Universität Tübingen.

Tag der mündlichen Qualifikation: 24.07.2015

Dekan: Prof. Dr. Wolfgang Rosenstiel

1. Berichterstatter: Jun.-Prof. Dr. Ilka Weikusat

2. Berichterstatter: Dr. Albert Griera

3. Berichterstatter: Prof. Dr. Paul D. Bons

4. Berichterstatter: Prof. Dr. Stefan M. Schmalholz

Erklärung

Ich erkläre hiermit, dass ich die zur Promotion eingereichte Arbeit selbständig verfasst, nur die angegebenen Quellen und Hilfsmittel benutzt und wörtlich oder inhaltlich übernommene Stellen als solche gekennzeichnet habe. Ich erkläre, dass die Richtlinien zur Sicherung guter wissenschaftlicher Praxis der Universität Tübingen (Beschluss des Senats vom 25.5.2000) beachtet wurden. Ich versichere an Eides statt, dass diese Angaben wahr sind und dass ich nichts verschwiegen habe. Mir ist bekannt, dass die falsche Abgabe einer Versicherung an Eides statt mit Freiheitsstrafe bis zu drei Jahren oder mit Geldstrafe bestraft wird.
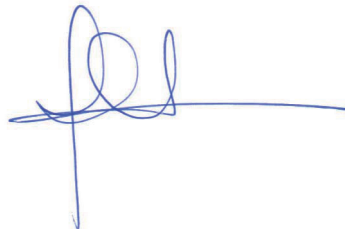
Maria Gema Llorens Verde
Tübingen, Mai 2015

Abstract

This thesis contains 8 manuscripts for peer-reviewed journals (4 published, 2 submitted, 2 to be submitted within 4 weeks) that present studies of deformation microstructures and folds in polar ice and ductile anisotropic rocks by means of numerical simulations. It is organized in four different parts that focus: (1) Viscoplastic deformation of polycrystalline polar ice in simple and pure shear coupled with dynamic recrystallisation simulating microstructure evolution and formation of folds; (2) Folding and unfolding of single and multilayers in pure and simple shear; (3) Influence of anisotropy degree and type on rotation of rigid bodies (porphyroclasts and porphyroblasts); and (4) Analysis of the effects of dynamic recrystallisation on the rheology and microstructures of partially molten rocks.

The first part (chapters 2, 3 and 4) contains three manuscripts analysing the influence of dynamic recrystallisation on deformation of pure polar ice. A full-field viscoplastic code (FFT) that fully reproduces the ice crystal's mechanical anisotropy is coupled with dynamic recrystallisation processes to perform a series of numerical simulations in pure (chapter 2) and in simple shear (chapter 3 and 4). The results show that dynamic recrystallisation (DRX) has remarkable effects on the developed ice microstructures, producing larger and more equidimensional grains and masking strain heterogeneities. DRX has only a minor effect on the formation of lattice preferred orientations (LPOs), but it has a strong influence on the relative activity of the different slip systems of ice and, therefore, on its mechanical properties. The survival probability of ice grains during recrystallisation is mostly related to the initial grain size, while crystal orientation with respect to the deformation axes plays a minor role only. The last manuscript of this part analyses how folds form in polar ice (chapter 4) as a consequence of intrinsic anisotropy when a strong LPO has developed. This mechanism can explain the development of folds in ice, without needing to invoke unrealistic viscosity contrasts between folding layers.

The second part of the thesis includes three manuscripts dedicated to the formation of folds in layered composite materials. The first of these manuscripts (chapter 5) investigates the development of folding of a single layer embedded in a softer matrix in linear and non-linear viscous media. Viscous deformation is simulated using a finite-element method (FEM) up to high strains. This study focuses on the influence of viscosity contrast, vorticity of deformation and the stress exponent on the resulting folding geometries. Folds forming in pure and simple shear do not develop distinctly different geometries, and are

thus difficult to distinguish in the field. Folds formed under non-coaxial flow are slightly more irregular with more variable axial plane orientations than in pure shear. This study demonstrates that the best tool to distinguish simple shear folds is the asymmetry of associated axial plane cleavage. Chapter (6) presents an analysis of the instantaneous stress and strain fields of the simulations studied in the previous chapter to compare the mechanical behaviour of folding rocks under pure and simple shear. Most notably, the work required to fold a competent layer is lower in simple shear than in pure shear. Chapter 7 studies the response of a folded layer that goes into the extensional field with progressive non-coaxial deformation. This contribution contains observations and evidence that help to recognise in the field whether straight layers have been folded previously. Intrafolial and cusp-like folds adjacent to straight layers are indications of previous folding if layers experienced softening during or before stretching, or if the layers were influenced by adjacent layers with different rheologies.

The third part of the thesis includes one manuscript (chapter 8) that addresses how the degree and type of anisotropy influence the rotation of rigid bodies embedded in a softer matrix (porphyroclasts and porphyroblasts) under non-coaxial flow. Viscoplastic full field numerical simulations were used to analyse systems with intrinsic anisotropies, and linear viscous FEM for the modelling of systems with composite anisotropies. The results demonstrate that a high degree of anisotropy can slow down or block the rotation of rigid objects. It thus reconciles the opposing positions in the decade-long controversy regarding the rotation of rigid objects, such as garnets, in rocks.

The final part of this thesis (chapter 9) investigates the effect of viscosity contrast, linear viscous rheology, melt fraction and wetting angle on the effective weakening of rocks with melt pockets and polar ice with air bubbles. This study is based on the coupling of a linear viscous FEM with dynamic recrystallisation, simulating the evolution in simple shear of a composite based on a foam texture. The results indicate that dynamic recrystallisation and wetting angles have a first-order impact on the deformation of the aggregate, controlling the connection of melt pockets and bulk mechanical behaviour of the rock.

Summarising, this thesis contains a number of studies that highlight how numerical simulations can give insight in structural and mechanical developments in ice and rocks, enabling better interpretation of the observed structures.

Zusammenfassung

Die vorgelegte Arbeit umfasst 8 Manuskripte für begutachtete Fachzeitschriften (4 veröffentlicht, 2 eingereicht, 2 innerhalb vier Wochen einzureichen), die numerische Simulationsstudien zu Deformationsmikrostrukturen und Falten in polarem Eis und in duktilen, anisotropen Gesteinen vorstellen. Die Arbeit ist in 4 Teile gegliedert: (1) Simulation von Mikrostrukturen und Faltenbildung in visko-plastischer Deformation gekoppelt mit Rekristallisation von polykristallinem polarem Eis in einfacher und reiner Scherung; (2) Faltung und Entfaltung von Einzel- und Mehrschichten in reiner und einfacher Scherung; (3) Einfluss des Anistropiegrades und –types auf die Rotation von starren Objekten (Porphyroklasten und -blasten); und (4) Analyse des Effekts der dynamische Rekristallisation auf die Rheologie und Mikrostruktur von partiell geschmolzenen Gesteinen.

Der erste Teil (Kapitel 2, 3 und 4) bezieht drei Manuskripte ein, die den Einfluss der dynamischen Rekristallisation auf die Deformation von reinem, polaren Eis analysieren. Ein *full-field* visko-plastischer Code (FFT), der die mechanische Anisotropie des Eiskristalls vollständig reproduziert, ist mit dynamischen Rekristallisationsprozessen gekoppelt, um eine Serie von numerischen Simulationen in reiner (Kapitel 2) und einfacher Scherung (Kapitel 3 und 4) durchzuführen. Die Ergebnisse zeigen bemerkenswerte Effekte der dynamischen Rekristallisation (*DRX*) auf die Entwicklung der Eismikrostrukturen, indem größere und equidimensionalere Körner erzeugt werden, die Bereiche von Verformungsheterogenitäten maskieren. *DRX* hat nur geringe Effekte auf die Bildung von bevorzugten Gitterorientierungen (LPOs), aber starke Effekte auf die relative Aktivität verschiedener Gleitsysteme des Eiskristalls und daher auf dessen mechanische Eigenschaften. Die Überlebenswahrscheinlichkeit der Eiskörner während der Rekristallisation hängt hauptsächlich an der ursprünglichen Korngröße, wohingegen Kristallorientierungen bezüglich der Deformationsachsen eine untergeordnete Rolle spielen. Das letzte Manuskript dieses Teils der Arbeit (Kapitel 4) untersucht Faltenbildung im polaren Eis als Konsequenz der intrinsischen Anisotropie, die sich mit starker LPO entwickelt. Dieser Mechanismus kann die Entstehung von Falten im Eis erklären ohne unrealistische Viskositätskontraste zu bemühen.

Der zweite Teil der Arbeit umfasst drei Manuskripte, die der Bildung von Falten in geschichtetem Verbundmaterial gewidmet sind. Das erste (Kapitel 5) untersucht die Entwicklung von Falten in einzelnen Schichten eingebettet in eine weiche Matrix von

linearer und nicht-linearer Viskosität. Viskose Deformation wird mit Hilfe der Methode der finiten Elemente (FEM) bis zu hohen Verformungen simuliert. Diese Studie richtet sich auf den Einfluss des Viskositätskontrastes, der Vortizität der Deformation und des Spannungsexponenten auf die resultierenden Faltengeometrien. Falten aus reiner und einfacher Scherung entwickeln keine merklich unterschiedlichen Geometrien und sind daher im Gelände nur schwer zu unterscheiden. Falten, gebildet unter nicht-koaxialem Fließen, sind leicht irregulärer mit variablerer Orientierung der Faltenachse als in reiner Scherung. Die Studie zeigt, dass das beste Hilfsmittel zur Unterscheidung von Falten einfacher Scherung die Asymmetrie der Faltenachsenschieferung ist. Kapitel 6 stellt eine Untersuchung der instantanen Spannungs- und Verformungsfelder der Simulationen des Vorkapitels vor, um das mechanische Verhalten von faltenden Gesteinen in reiner und einfacher Scherung zu vergleichen. Höchst bemerkenswert ist, dass die zur Faltung einer kompetenten Schicht aufzuwendende Arbeit in einfacher Scherung niedriger ist als in reiner Scherung. Kapitel 7 befasst sich mit der Reaktion einer gefalteten Schicht, die sich unter fortschreitender, nicht-koaxialer Deformation ins Extensionsfeld verlagert. Dieser Beitrag enthält Beobachtungen und Hinweise, die ermöglichen im Gelände zu erkennen, ob glatte Schichten vormals gefaltet waren. An glatte Schichten grenzende intrafoliale und spitze Falten sind Hinweise auf frühere Faltung, wenn die Schichten vor oder während der Streckung Erweichung erfahren haben, oder die Schichten von angrenzenden Schichten anderer Rheologie beeinflusst wurden.

Der dritte Teil der Arbeit enthält ein Manuskript (Kapitel 8), das sich mit dem Einfluss von Grad und Art der Anisotropie befasst, die diese auf die Rotation eines starren Objektes in einer weichen Matrix (Porphyroklast und -blast) unter nicht-koaxialer Deformation ausübt. Numerische, visko-plastische *full-field* Simulationen wurden zur Untersuchung von Systemen mit intrinsischer Anisotropie und linear-viskose FEM zur Modellierung von Systemen mit Kompositanisotropie verwendet. Die Ergebnisse zeigen, dass ein hoher Anisotropiegrad die Rotation von starren Objekten verlangsamen oder blockieren kann. Sie legen damit die gegenüberstehenden Positionen in einem jahrzehntelangen Disput bezüglich der Rotation von starren Objekten in Gesteinen, wie Granaten, bei.

Der letzte Teil der vorgelegten Arbeit (Kapitel 9) untersucht den Einfluss von Viskositätskontrast, linear-viskoser Rheologie, Schmelzanteil und Benetzungswinkel auf den effektiven Festigkeitsabfall von Gesteinen mit Schmelztaschen und von polarem Eis mit Luftblasen. Diese Studie basiert auf die Kopplung linear-viskoser FEM mit dynamischer Rekristallisation, durch Simulation der Entwicklung in einfacher Scherung eines Komposits mit einer *foam texture*. Die Ergebnisse weisen darauf hin, dass dynamische Rekristallisation und Benetzungswinkel einen erstrangigen Einfluss auf die Deformation des Aggregates haben, in dem sie die Verbindung der Schmelztaschen und damit die mechanischen Eigenschaften des Gesteins kontrollieren.

Zusammenfassend beinhaltet die vorgelegte Arbeit eine Vielzahl von Studien, die zeigen,

wie numerische Simulationen Einblicke in die strukturelle und mechanische Entwicklung von Gesteinen und Eis geben können, die bessere Interpretationen von beobachteten Strukturen erlauben.

x

Acknowledgements

This thesis would not have been possible without the active supervision of Ilka, Paul and Albert. Their strong support, ideas, guidance, discussions and explanations have been essential for my progress. What I have learned from them is not only scientific knowledge, but also a way to observe, think, ask fundamental questions and try to find simple solutions for complicated problems. This training is essential in science, and I think I have been very lucky having the three of them as supervisors. Therefore I am very grateful to them. I would also like to thank Daniela and Florian for the great discussions and support they have provided.

I would like to give very special thanks to my beloved husband Enrique, who convinced me 5 years ago to leave my industry job and start a new career in science. His unconditional support, help, encouragement and a lot of patience made me keep my work afloat during these years. Many thanks for being my light.

Many thanks also to my mother Maria Eulalia, brother Juan Antonio, grandmother Conchita, parents-in-law María and Antonio and sister-in-law Paula. All of them have strongly supported me and were always following the progress of this work.

I would also like to give special thanks to my friends Ana P., Ana R., Chiqui, Tania, Eduardo, Sara and Arianna, for providing the best advices and make me laugh every day.

Last by not least I would like to express my thanks to my two little daughters Julia and Inés. They have showed me what is really important in life, and I hope they will enjoy reading this thesis in the future.

Finally, many thanks to mi cat Linux, who was always around when I worked at home, jumping on the computer every 10 minutes.

Sincere thanks to all of you!

Contents

Chapter 1

Introduction

1.1 Introduction

The study of rock deformation is a fundamental topic in Natural Sciences and Engineering. Rocks can deform in different ways depending on their mechanical properties, the environment in which they are located, and the forces they are subjected to. In general, there is a transition between elastic-brittle behaviour at shallow depths of the Earth's crust and ductile viscoplastic behaviour at moderate to deep levels. An increase in depth typically implies an increase in confining pressure and temperature, which in turn reduces pressure-dependent plasticity and increases viscous and viscoplasticity of rocks (e.g. Mancktelow, 2006). Viscous deformation takes place in situations where stress depends on the strain rate at which the rock is being deformed, while plastic deformation accounts for cases in which the material flows plastically above a critical stress value, and therefore, stress is strain-rate independent (e.g. Taylor, 1934; Nicolas and Poirier, 1976). Ductile deformation (i.e. deformation without discontinuities and without loss of cohesion) is not restricted to the middle or deep crust, because it can also affect certain rocks at shallower depths. For example, evaporites, clays or marls typically undergo ductile flow close to or at the Earth's surface, resulting in structures of high economic importance such as hydrocarbon traps. Ice is another special case, since it is a mineral and monomineralic rock with a very low melting point with respect to its typical environment. This property makes ice to flow in a ductile way, similar to metamorphic rocks, but at Earth-surface conditions, in ice sheets, caps and glaciers. Ductile strain can be distributed equally within the material or can localise in certain parts of it. In the second case, strain typically appears localised in zones with continuous variations of strain across their width, without discontinuity and without loss of cohesion (e.g. Twiss and Moores, 1992; Gomez-Rivas et al., 2015). The most common structures resulting from ductile strain localisation are shear zones and ductile shear bands (e.g. Passchier and Trouw, 2005).

One of the key factors controlling strain localisation in ductile rocks is the anisotropy

of the deforming material. A material property is anisotropic when it is directionally dependent (i.e. it varies in different directions within the material). The most common types of anisotropy in geologic materials are composite and intrinsic. Composite anisotropy (e.g. Treagus, 1997) can arise from the aggregation of two or more phases. In this case, each individual phase could present isotropic or anisotropic behaviour in isolation. But the mix of two or more phases with contrasting rheologies normally results in a material that has different properties in different directions. A typical example of composite anisotropy is a rock formed by the stacking of layers with different compositions. Another type of anisotropy is the so-called intrinsic anisotropy (Griera et al., 2011; 2013), which arises when a lattice-preferred orientation (LPO) and/or a shape-preferred orientation (SPO) develops. LPOs can form from viscoplastic flow with or without recrystallisation, viscous flow or anisotropic crystal growth (e.g. Mainprice and Nicolas, 1989). Crystals in the viscoplastic field typically deform by glide of dislocations along slip planes. According to the von Mises criterion (e.g. Lister et al. 1978), five independent slip systems are required to describe plastic deformation by dislocation glide of a crystal in continuity with its neighbours. If other deformation mechanisms are involved, fewer slip systems need to be invoked for the system to work (e.g. Mainprice and Nicolas, 1989). These processes include lattice rotation, diffusional creep, dissolution-precipitation creep and fracturing. In most mineral systems, one slip system is dominant over the others, thus requiring a lower critical resolved shear stress (CRSS) in order to be activated. Aggregates of such minerals, such as polar ice, typically have high intrinsic bulk anisotropies when they are deformed. Apart from that, viscous flow of heterogeneous rocks containing non-equidimensional minerals can also result in the development of macroscopic intrinsic anisotropies, because they develop SPOs (e.g. Takeda and Griera, 2006). This phenomenon takes place when minerals with high aspect ratios rotate in the viscous medium acquiring a stable orientation according to the imposed flow field. Planar minerals, such as mica, typically favour the development of SPOs, and hence anisotropies, in polymineralic rocks. The presence of other anisotropic minerals, such as amphibole, pyroxene, olivine or feldspar, may also enhance the development of SPOs. The formation of intrinsic anisotropies as a consequence of LPOs and/or SPOs with progressive deformation typically results in the development of a foliation or cleavage, which is the most common macroscopic penetrative fabric in metamorphic rocks (e.g. Hobbs et al., 1976). The macroscopic degree of anisotropy is defined by the ratio between viscosity under normal stress and viscosity under shear stress ($m = \eta_N / \eta_S$; Treagus, 2003). A fundamental problem for investigations on monomineralic anisotropic rocks, such as ice, is the absence of indicators of the flow field such as foliations, despite their intrinsically anisotropic behaviour (Fig. 1.1a.b).

Understanding and predicting the deformation of anisotropic rocks is not straightforward, especially because their behaviour under an applied stress is very complex. This is mainly due to: (1) the variety of deformation mechanisms and agents operating in these

systems and the interactions between them, (2) the range of deformation conditions (pressure, temperature, confining pressure, kinematic of deformation, etc.), which in fact change the balance between deformation processes, and (3) the variety of resulting anisotropies and microstructures, which in turn alter the mechanical properties of the deforming rock. The vast majority of the existing literature on rock deformation focuses on the study of isotropic rocks and addresses processes in isolation. However, there is still a large number of open questions regarding how anisotropic rocks deform, and how different deformation mechanisms operate and interact, and what the range of resulting microstructures is. Understanding them is a fundamental scientific problem nowadays. This thesis focuses on the analysis of the deformational behaviour of polar ice and ductile anisotropic (metamorphic) rocks through numerical simulations, and provides frameworks to better understand and unravel the deformation histories from the resulting microstructures, as well as link their development to the mechanical behaviour of the rock. These microstructures include grain and subgrain boundaries (Fig. 1.1a,b), folds (Fig. 1.1c,d), rigid objects (porphyroblasts and porphyroclasts; Fig. 1.1e,f) and pockets of molten rock within a framework of solid minerals (Fig. 1.1g,h). A series of fundamental problems associated with the development of deformation microstructures are studied. The main objectives are to:

- Understand and systematically analyse how dynamic recrystallisation affects the microstructural and mechanical evolution of polar ice during deformation.

- Compare how polar ice deforms in pure and simple shear boundary conditions.

- Understand how deformation of polar ice can result in the formation of strain localisation structures such as kink bands, which can then be used as kinematic indicators.

- Address the issue of whether non-coaxial deformation produces asymmetric fold shapes in multi-layered composite rocks, and compare fold geometries developed in pure and simple shear boundary conditions.

- Answer the question of whether it is possible to recognise if straight rock layers have been previously folded, and what the parameters involved in this process are.

- Systematically analyse the influence of the degree and type of anisotropy (intrinsic and composite) on the rotational behaviour of rigid objects (porphyroblasts and porphyroclasts) embedded in layered or foliated rocks.

- Study the influence of viscosity contrast, wetting angle, melt fraction and strain rate on the kinematic and mechanical behaviour of partially molten rocks.

To investigate these questions, series of numerical simulations were performed with the modelling platform ELLE (www.elle.ws; Bons et al., 2008). This PhD thesis is organised

in eight chapters, each of them corresponding to a manuscript either published in a scientific journal, in review for publication or in an advanced state of preparation for submission. The chapters are grouped in four categories, depending on the studied material, the processes involved, the type of anisotropy (composite or intrinsic) and the resulting microstructures. The first part studies the deformation of polar ice under pure and simple shear boundary conditions, by simulating full-field viscoplastic deformation coupled with dynamic recrystallisation. Three manuscripts (chapters 2, 3 and 4) analyse systems that develop intrinsic anisotropies with progressive deformation, comparing pure and simple shear boundary conditions. They focus on the microstructures, the development of LPOs, the activity of crystal slip systems, the mechanical evolution of the deforming medium and the influence of dynamic recrystallisation. Additionally, a chapter addressing the mechanisms controlling the development of folds in polar ice, using the same modelling approach, is included. These results are very useful to understand and predict flow of polar ice under different conditions in ice sheets, which in turn affect the spreading of signals used to unravel and predict the effects of climate changes. The second part is composed of three manuscripts (chapters 5, 6 and 7) analysing the development of folds in linear and non-linear viscous composite materials, typically layered rocks. Chapter 5 provides a comparison of fold development in single layers deformed in pure and simple shear boundary conditions, and presents a series of tools for structural analysis using folds in the field. Chapter 6 analyses the mechanical behaviour of folding rocks in pure and simple shear, by quantifying instantaneous stress and strain from the numerical models. Chapter 7 addresses the key issue of whether it is possible to know if a straight layer has been previously folded. The third part includes a comprehensive manuscript (chapter 8) discussing how the degree and type of anisotropy affect the rotation rates of rigid objects (porphyroblasts and porphyroclasts) embedded in ductile rocks. A review of the existing literature on rigid object rotation is first presented, followed by a set of complex simulations of the rotation of growing and non-growing objects in materials with different degrees and types of anisotropies (from intrinsic to composite). These simulations use the techniques described in the two previous parts: full-field viscoplastic deformation (part 1) and linear viscous deformation (part 2). The resulting microstructures are analysed, in addition to the rotational behaviour of such objects and their implication for structural analysis. The last part of the thesis includes a manuscript summarising a numerical study of the deformation of partially molten rocks (chapter 9) which investigates the influence of the wetting angle, melt fraction, linear viscous rheology and viscosity contrast on the bulk mechanical behaviour of these rocks.

The present chapter (1) introduces these studies, grouped into the four categories. Finally, a summary of the techniques and workflows used in the thesis is presented.
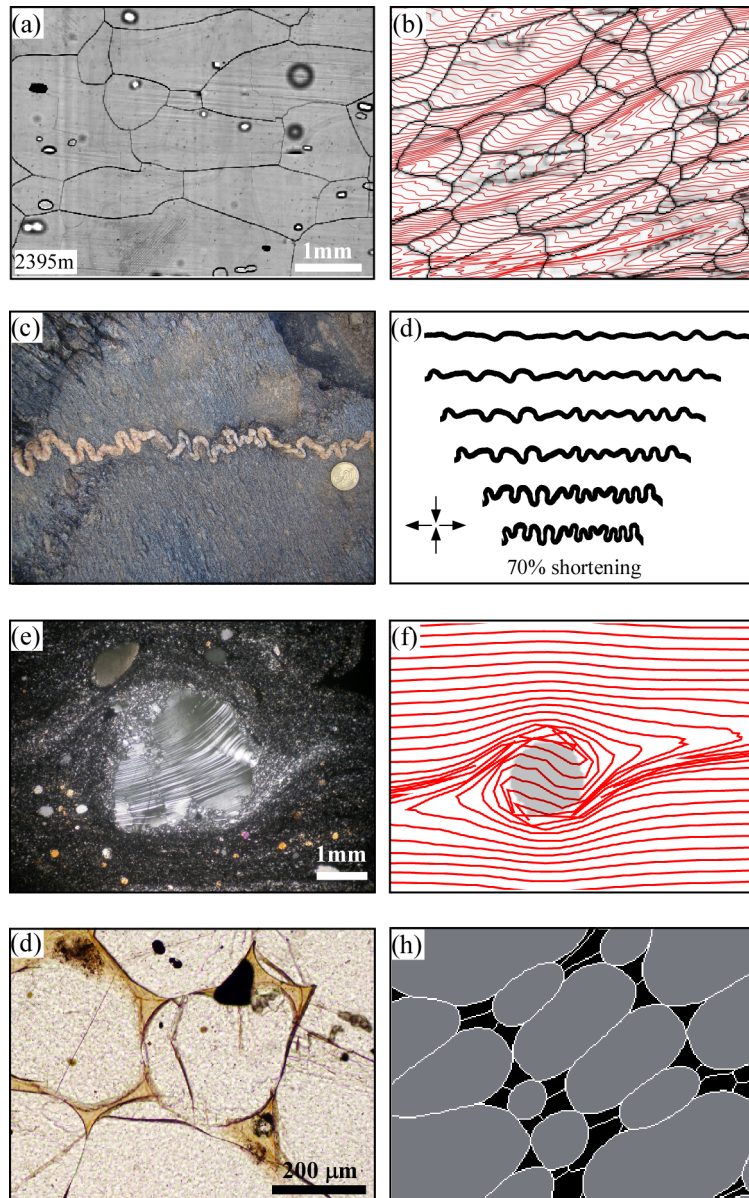
Figure 1.1: Examples of deformation microstructures and numerical simulations studied in this PhD thesis. (a) Microphotograph of polar ice microstructures from the EPICA-DML core in Antarctica (photo courtesy of Ilka Weikusat). Thick lines represent grain boundaries and thin lines subgrain boundaries (Thermal etching grooves). Air hydrates appear as bright (intact) and dark spots (decomposed). It is not possible to estimate the real amount of deformation from these types of microstructures, due to the absence of strain markers. (b) Numerical simulation of pure ice deformation under simple-shear boundary conditions with dynamic recrystallisation processes (chapter 3). A passive marker grid displayed in red is used in these simulations to show the finite strain field, which is masked by recrystallisation. (c) Example of a folded quartz vein embedded in a metapelite-metapsammite rock from Puig Culip (Cap de Creus, E Pyrenees). (d) Numerical simulation of a folded layer under pure shear boundary conditions up to 70% of shortening, presented in chapter 5. (e) Microphotograph of a mantled plagioclase porphyroclast (δ-clast) from a mylonitic zone in the Ivrea-Vervano area (Italian Alps) (photo courtesy of Albert Griera). The geometry of the inclusion trail reveals the rotation direction of the porphyroclast relative to its surrounding matrix. (f) Numerical simulation of a porphyroclast embedded in a matrix with an intrinsic anisotropy which was originally parallel to the shear plane. This simulation is presented in chapter 8. Red lines show the orientation of a passive marker grid. (d) Example of a partially molten rock (basalt) from Hawaii, from Holness (2010). Rounded and smoothly curved olivine grains (yellowish) are surrounded by melt (brown glass). (e) Numerical simulation of a two-phase (solid-melt) composite material under simple shear conditions coupled with grain boundary migration (chapter 9).

1.2 Part 1 – Deformation and microstructures of polar ice

The mechanical behaviour of polar ice masses has a direct impact on the environment, as well as on human society, because they play a fundamental role in controlling sea level changes and the evolution of climate on a global scale (e.g. Kennicutt et al. 2014). Quantification of Antarctic ice sheet mass changes has demonstrated an acceleration of mass loss during the last decade, profoundly in its western part, less dramatic in its eastern part (Turner et al., 2014). This has a direct influence on the climate systems of the whole planet, since the global sea level could potentially increase by 64 metres if the Antarctic ice sheet losses about 26.5 million cubic kilometres of mass, which would be drained into the oceans (Lemke et al., 2007). Therefore, understanding how and why ice sheets lose mass is currently a scientific priority. Besides sliding over the bedrock studied intensely to understand the subglacial systems, internal deformation supplies the large ice masses towards the coast. There are many factors controlling the deformation of ice sheets, glaciers and caps. They determine the relationship between the magnitudes and orientations of stresses and the flow rates of an ice body. The bulk behaviour of large ice masses is the result of the behaviour of the aggregate of individual ice grains. Therefore, understanding ice deformation at the micro- and mesoscale is essential in order to develop large-scale ice sheet flow models and to interpret climatic signals acquired from ice cores (e.g. Faria et al., 2010). Ice sheets are valuable paleoclimate records, since it is possible to reconstruct the past climate evolution by studying the composition of air bubbles, dust and impurities stored in ice masses. However, polar ice sheets are strongly affected by deformation and recrystallisation processes, which can significantly alter their microstructures and can indeed produce spreading and mixing of climate signals of different origins (e.g. Faria et al., 2010).

Ice research is not only useful for unravelling past climate changes, and predicting future ones. Ice is also considered an ideal rock analogue (Wilson, 1981; 1983), because it deforms in a way that is very similar way to some metamorphic rocks, following a non-linear power-law flow law, called "Glen's law" (Glen, 1958). In this constitutive equation strain rate ($\dot{\varepsilon}$) is proportional to the deviatoric stress (σ) to the power of a stress exponent (n). Ice is assumed to deform by dislocation creep (Schulson and Duval 2009), similar to other anisotropic minerals such as quartz or olivine. Ice is a very useful material to be used as a metamorphic rock analogue for performing deformation experiments because it is very close to its melting point. Therefore, deformation mechanisms such as dynamic recrystallisation can be studied in the laboratory without requiring deformation devices able to achieve very high pressures and temperatures.

There are many types of ice crystal structures, but only hexagonal ice (*Ih*) is present on Earth. This type of ice exhibits viscoplastic and highly anisotropic behaviour when it

is subjected to low differential stress. The reason for this anisotropy is that deformation is mainly accommodated along the basal crystal plane, instead of prismatic and pyramidal planes. The critical resolved shear stress (CRSS) required to activate slip of dislocations along the basal plane of ice is about 60 to 100 times lower than that necessary to produce glide along prismatic and pyramidal ones (e.g. Duval et al., 1983; Montagnat et al., 2014; Wilson and Zhang, 1996). Strain is therefore mostly accommodated by slip along the basal plane, with relatively minor contributions of the other slip systems (Ashby and Duval 1985). The orientation of a crystal in polycrystalline ice is determined by its crystallographic axes, where the c-axis is perpendicular to the basal plane. When c-axes are randomly distributed, ice is considered to behave isotropically. On the contrary, when a lattice preferred orientation (LPO) develops in polycrystalline ice, the material is considered anisotropic (e.g. Faria et al., 2014b). During flow, ice quickly develops LPOs by lattice rotation, almost perpendicular to the shear plane in simple shear, and parallel to the shortening direction in pure shear boundary conditions. Such LPOs indeed lead to the development of intrinsic anisotropies. The bulk behaviour of large ice masses is thus strongly influenced by the viscoplastic anisotropy of its grains and the orientation of their lattices (Van der Veen and Whillans, 1990; Mangeney et al., 1997).

Apart from viscoplastic deformation, the mechanical behaviour and microstructures of ice is also strongly affected by other processes, such as recrystallisation and recovery. Ice has a very high homologous temperature and low strain rates under natural conditions (Jacka and Li, 1994; Kipfstuhl et al., 2006), with dynamic recrystallisation being particularly important. Depending on the strain rate and temperature, ice is affected by different types of recrystallisation, which can operate simultaneously (Faria et al., 2014a): (1) normal (i.e. static) grain growth (NGG), driven by grain-boundary surface energy, (2) rotational recrystallisation or polygonisation (RRX), where the lattices within grains rotate creating tilt walls and developing subgrains, and (3) strain-induced migrational recrystallisation ($SIBM$), driven by energy stored due dislocations in the lattice. All these processes modify the shape and size of grains, and it is generally assumed that they hardly affect the evolution of LPOs. Classic interpretations of grain sizes and c-axis orientation distributions in polar ice cores are based on the "three-stage model" (De la Chapelle et al., 1998), where recrystallisation processes in ice sheets are divided according to depth: normal grain growth would only affect the upper hundreds of meters (Gow, 1969), followed by rotational recrystallisation at intermediate depths (Alley et al., 1995), and strain-induced migrational recrystallisation only affecting the bottom part of ice sheets (Duval et al., 1983). However, several authors (Kipfstuhl et al., 2006; Weikusat et al., 2009; Faria et al., 2014c) have pointed out that the grain-size evolution in polar ice can indeed be interpreted in terms of strain and temperature, in a way that these processes are not restricted to certain depths but can take place at all levels depending on the deformation conditions.

In polar ice sheets, ice deforms in pure shear boundary conditions near the ice divide,

with compression and extension in the vertical horizontal directions, respectively. Simple shear deformation affects the ice away from the divide and close to the bedrock (Cuffey and Paterson, 2010). It is therefore crucial for understanding bulk polar ice behaviour to study its fabrics and microstructural evolution in response to stress and time under different types of deformation (i.e. under different strain rates and vorticities). In chapters 2 and 3 a series of numerical simulations of pure ice deformation under pure and simple shear deformation conditions are presented, respectively. These simulations are performed using a crystal plasticity code that reproduces deformation by dislocation glide, coupled with *DRX*, including *GBM* and recovery processes at different strain rates.

Studies of the NEEM ice core (North Greenland) have confirmed the fatal effect of large-scale folding on the palaeoclimate record, but have also shown how this can be compensated if folding is seriously considered (NEEM 2013). To understand the folding mechanisms in ice sheets, occurring from macro- to micro-scales, recent observations have focused on disturbances visible as centimetre scale folds. They appear at about 1700 m as smooth waves and evolve into overturned z-folds with increasing depth. At these depth conditions ice is anisotropic (intrinsic anisotropic), since LPOs have been developed (Montagnat et al. 2014). It is not necessary to assume different rheologies between layers (i.e. composite anisotropy) to initiate these disturbances as suggested as prerequisite before and shown to be an important mechanism in Part 2 (chapter 4). A complementary analysis of lattice orientation distributions for corresponding ice core samples shows that grains with c-axes deviating from the homogeneous-LPO matrix are distributed in stripes parallel to the axial planes of the folded layers revealed by visual stratigraphy (Svensson et al., 2005). These observations suggest that intrinsic anisotropy produces localised kink bands, causing a passive rotation of the crystal orientation. Chapter 4 presents a study of folding of polar ice with observations from the aforementioned core, together with numerical simulations of viscoplastic ice deformation coupled with dynamic recrystallisation. This study aims to reproduce the development of localised shear bands in media with intrinsic anisotropies, and capture the main controls on folding of polar ice.

1.3 Part 2 – Folding and unfolding of single and multilayers

Deformation structures are typically used by geologists to understand how rocks deform and to quantify it. These structures typically include fractures, folds, veins, foliations and hard inclusions, among many others. Folds are widely used in structural analysis, since they are classical indicators of shortening direction and amount, kinematics of deformation and rock properties (Treagus, 1982; Hudleston, 1986; Ramsay and Huber, 1987; Hudleston and Lan, 1993). Folds tend to form in rocks containing relatively competent layers embedded in a softer matrix, when such layers are subjected to shortening (Biot, 1961; Ramberg, 1961; Chapple, 1968; Fletcher, 1974; 1977; Smith, 1975; 1977). Therefore, these types of rocks can be normally regarded as systems with a composite anisotropy. The viscosity or competence contrast between folding layers and their surrounding matrix has a strong influence on the resulting fold geometries, as it determines the initial wavelength and amplification rate of the developing folds (Biot, 1961; Ghosh, 1966; Sherwin and Chapple, 1968; Fletcher, 1974; 1977; Johnson and Fletcher, 1994). However, the viscosity contrast is not the only factor controlling folding. Strain-dependent rheology (Lan and Hudleston, 1991; Schmalholz et al., 2005) and mechanical anisotropy (Toimil and Griera, 2007) also play a fundamental role to determine when and how folds form. Folds located within ductile shear zones tend to present a strong asymmetry that has been widely used as a shear sense indicator. (e.g. Ramsay and Huber, 1983; Passchier and Williams, 1996; Carreras et al., 2005; Alsop and Holdsworth, 2006). The formation of such asymmetric folds has historically been explained by a mechanism in which pre-existing folds are passively sheared (e.g. Ghosh, 1966; Hudleston and Lan, 1993). However, it is important to note that non-coaxial deformation does not necessarily produce asymmetric fold shapes (Ghosh, 1966), and therefore caution must be taken when unravelling deformation kinematics using fold geometries. Several studies concluded that the only reliable indicator of folding under non-coaxial flow is the asymmetry of axial planar cleavage (Manz and Wickman, 1978), since fold geometries themselves do not sigificantly differ between pure and simple shear. Another key observation is that asymmetric folds can also develop in coaxial boundary conditions if layers are initially oblique to the maximum shortening direction (Treagus, 1973; Viola and Manktelow, 2005). Therefore, unravelling kinematic using fold geometries is not straightforward. In fact, no studies systematically addressed this key issue before the publication of two of the manuscripts presented in this PhD thesis (Llorens et al., 2013a; 2013b; 2014).

Although highly non-coaxial flow (i.e. simple shear) is very common in the Earth's crust, only few studies analysed fold development in general shear conditions, or in situations where layers were oblique to the maximum shortening direction (Treagus, 1973; Viola and Mancktelow, 2005). Moreover, most of the existing knowledge of fold mechanics, derived

from theoretical and field studies (Biot, 1961; Treagus, 1982; Fletcher, 1977; Ramsay and Huber, 1987; Schmalholz and Podldchikov, 2000), experiments (Manz and Wickham, 1978; Abassi and Mancktelow, 1992; Bons and Urai, 1996; Tikoff and Peterson, 1998) and numerical simulations (Parrish et al., 1976; Huddleston and Stephansson, 1973; Anthony and Wickham, 1978; Hudleston and Lan 1994; Zhang et al., 1996, 2000; Mancktelow, 1999; Viola and Mancktelow, 2005; Frehner and Schmalholz, 2006; Schmalholz, 2008; Hobbs et al., 2008; Kocher et al., 2008) is based on the analysis of single- or multilayer folding in pure shear, where layers are parallel to the maximum shortening direction. This PhD thesis addresses the key issue of distinguishing folds formed in pure and simple shear boundary conditions, focusing on linear and non-linear deformation of single layers up to high strain. Chapter 5 presents a manuscript published in Journal of Structural Geology (Llorens et al., 2013a), addressing this fundamental problem using finite-element numerical simulations up to high strain. This study analyses the influence of viscosity contrast, initial layer orientation and stress exponent on the resulting fold patterns. A comparison between pure and simple shear fold development allow us to capture the differences between these two kinematic end-member conditions, and to find at which range of non-coaxiality a fold may have formed. Chapter 6 presents a short manuscript analysing the mechanics of folding of the models presented in chapter 5. This study is published as a chapter in the book Mathematics of Planet Earth (Llorens et al., 2014), and analyses stress and strain distributions in the folding layers, as well as the energy (work) required to form folds in a range of conditions.

Apart from the kinematic issue, another key problem when doing structural analysis with folds is the fact that straight layers found in the field could have been previously folded. This can happen depending on the orientation of the layer with respect to the deformation field. For example, a layer may have first been folded and then stretched again if it underwent two or more deformation events with the principal stresses oriented in different directions. In such a case the layer would have been first shortened and later extended (Hudleston and Lan, 1993). In other situations, a layer can be first folded and subsequently unfolded during the same tectonic phase if it rotates from the compressional into the extensional field during progressive deformation in non-coaxial flow (Ramsay, 1980; Passchier, 1988). This is a typical case in ductile shear zones, where the flow field tends to be close to simple shear. Despite the common occurrence of such situations, there are almost no studies addressing the issue of how to recognise whether a straight layer has been previously folded. Before the study published in chapter 6 of this thesis (Llorens et al., 2013b), only Means (1999) considered this problem.

Geologists assume that when a layer is subjected to extension it can either thin or break into lenses or blocks. The second case leads to the formation of boudinage, which is typically seen as the most common structure formed in extension (Lloyd et al., 1982; Ghosh and Sengupta, 1999). However, if a folded layer is extended, such folds would,

in the absence of fracturing, first unfold. The viscosity ratio between the layer and its matrix plays a fundamental role in determining how the layer unfolds. If, for example, the layer keeps its original viscosity contrast while it is being unfolded, we can expect it to be completely straight after it has suffered the same amount of stretching during unfolding as shortening during folding. However, the viscosity ratio between the layer and matrix can be modified during progressive deformation if there are changes in strain rate, metamorphic conditions (pressure and temperature), or strain-dependent rheology (Hobbs et al., 1990; Talbot, 1999). In these cases, unfolding can strongly vary depending on whether the rock hardens or softens during progressive deformation. Much more complex situations can arise if the rock is multi-layered. In these cases, layers with different viscosities and mechanical properties can influence each other, thus preventing unfolding or enhancing it (Ez, 2000; Carreras et al., 2005). Chapter 7 of this thesis presents the first published systematic study of unfolding. This manuscript was published in Geology (Llorens et al., 2013b), and presents a series of viscous single-layer and multi-layers deformed first in simple shear boundary conditions, first in compression, and then in extension. The study focuses on the influence of rheology changes during deformation, and also presents examples of unfolding influenced by interactions between layers.

1.4 Part 3 – Rotation of rigid objects (porphyroblasts and porphyroclasts) embedded in rocks with intrinsic and composite anisotropies

Rigid objects (porphyroblasts and porphyroclasts) embedded in a softer matrix are normally used as indicators of sense of shear, kinematic vorticity number, finite strain, and deformation history (Hobbs et al., 1976; Ramsay and Huber, 1987; Passchier and Trouw, 2005). *Porphyroclasts* are non-growing objects inherited from the host rock material, harder than their surrounding matrix, whose shape and orientation are modified by deformation (Passchier and Simpson, 1986). They are of primary interest for structural analysis, since they are often surrounded by wings of material (the "mantle") that appears recrystallised from the porphyroclast, developing monoclinic symmetries in non-coaxial flow (Passchier and Simpson, 1986; Bjørnerud, 1989; Hanmer and Passchier, 1991). These geometries include sigma and delta clasts, and are widely used as shear-sense indicators. When metamorphic minerals are affected by changes in pressure and temperature, they can overgrow their matrix. If the object is relatively harder than its matrix, it can be called a *porhpyroblast*. Porphyroblasts are useful tools that are widely used to link deformation and metamorphism (e.g. Johnson, 1999), since they can develop sigmoidal or spiral inclusion patterns while they grow, sometimes displaying the relationship between internal and external foliation (Wilson, 1971; Bell et al., 1992; Passchier et al., 1992). The interpre-

tation of these structures under non-coaxial flow has been a topic of a heated debate for two decades. Some authors consider that rigid objects embedded in a softer matrix do rotate with progressive deformation (e.g. Rosenfeld, 1970; Schoneveld, 1977). Their rotational behaviour can be described with the analytical solution of Einstein (1906), if the stiff object is embedded in a linear viscous medium. However, other authors proposed alternative models in which hard object do not rotate, and their inclusion patterns are explained by near orthogonal foliations produced by successive deformation phases (e.g. Bell et al., 1992). These two models would predict an opposite sense of shear for a given case, among different number of deformation phases (Johnson, 1999). This debate has resulted in a large number of published studies, supporting both theories (e.g. Passchier et al., 1992; Bell et al., 1992) and review publications (Johnson, 1999; Jiang and Williams, 2004; Fay et al., 2008; Johnson, 2009). The assumption that rigid objects do rotate significantly is based on field, experimental and numerical observations. However, it has been proposed that the rotation rate can be strongly reduced, inhibited or even reversed depending on different factors. These include, for example, strain localisation in the matrix (Griera et al., 2011), mechanical interaction between neighbouring inclusions (Jessell et al., 2009), confined shear flow (Marques and Coelho, 2001) or incoherent matrix-inclusion interfaces (Ildefonse and Mancktelow, 1993). Although metamorphic rocks are generally heterogeneous and anisotropic, most of the existing experiments and numerical simulations tended to address the rotation problem assuming a linear homogeneous isotropic medium. This is a strong limitation, because metamorphic rocks tend to develop foliations and commonly contain localisation structures (e.g. shear bands), which can strongly affect deformation partitioning and, therefore, rigid body rotation rates. Chapter 8 of this thesis contains an extensive review of numerical studies addressing rigid body rotation, and presents three series of new numerical simulations to understand the influence of the degree and type of anisotropy on rigid object rotation. The three series include: (1) growing and non-growing objects embedded in an intrinsically anisotropic matrix characterised by a LPO, (2) growing objects embedded in a matrix with a composite anisotropy, with the objects larger than the layer widths, and (3) non-growing objects embedded within either hard or soft layers within a multi-layered medium (i.e. with composite anisotropy). Models of series (1) are simulated using the full-field viscoplastic code (FFT), while series (2) and (3) are modelled using linear viscous finite element models (BASIL). The influence of the degree and type of anisotropy on the rotation rate is systematically explored in each case, as well as the impact of simultaneous strain localisation and object rotation.

1.5 Part 4 – Deformation microstructures and mechanical behaviour of partially molten rocks

The previous chapters address the deformation of anisotropic rocks composed of solid phases. However, rocks at certain pressure-temperature conditions can also contain a fraction of melt, which strongly influences their mechanical behaviour. The principal effect of partial melting in the lithosphere is weakening, which can strongly influence exhumation of ultra-high pressure rocks during continental subduction (e.g. Whitney et al., 2009) and in syn- to late-orogenic ductile flow of the lower crust in mature collision zones (e.g. Teyssier and Whitney, 2002). The bulk strength of a rock is the integral of the strengths of the different mineral phases it contains. Addition of melt induces bulk weakening, due to the fact that the molten material has a significant lower strength than that of solid mineral phases. This weakening effect is also observable in cases in which there is a second phase with a relatively low viscosity, such as for example air bubbles in polar or glacier ice.

One of the main parameters controlling the effective weakening of partially molten rocks is the connectivity of the molten phase. Rocks normally present weaker bulk behaviour in cases where melt pockets are connected than in situations where they appear isolated (Bons and Cox, 1994). The bulk viscosity of a partially molten rock depends on: (1) the viscosity of the mineral and melt phases, (2) the wetting angle of melt (ω) and (3) the melt fraction. The wetting angle is proportional to the ratio between the surface energies for the solid and the melt regions, being the equilibrium angle between two solid-liquid boundaries and a solid-solid boundary. Air bubbles in ice have wetting angles close to $\omega=180°$ (Azuma et al., 2012; Faria et al., 2014c), while partially molten rocks, like silicate and Fe-Ni melt in olivine rocks, have lower wetting angles ($\omega= 30°$ to 60°-130°, respectively). The deformation behaviour and resulting microstructures of two phase aggregates of solid minerals and melt are controlled by the competition between deformation and dynamic recrystallisation. Viscous deformation will tend to modify the shape of melt pockets and their distribution, thus changing the bulk rheology of the aggregate. The higher the strain rate, the more pockets will deform. On the contrary, dynamic recrystallisation by grain boundary migration (*GBM*) will constantly modify the shape of solid grains and melt pockets, trying to reach the minimum energy (i.e. equilibrium) state (e.g. Groebner and Kohlstedt, 2006; Walte et al., 2011). The competition between these two processes defines two regimes under which the aggregate can evolve: (1) the deformation-dominated regime, which would occur at high strain rates and in rocks with large grain sizes, and (2) the recrystallisation-dominated regime, which would be associated with low strain rates and small grain sizes (Groebner and Kohlstedt, 2006). Laboratory deformation experiments of partially-molten rocks are usually performed at strain rates several orders of magnitude higher that natural ones. Therefore, the balance of processes operating at such high strain rates is different from that at natural strain rates. This limitation is typically avoided by

doing a dynamic scaling of the rock's grain size and the strain rate at which it is deformed, in order to have comparable results. However, numerical simulations are a powerful tool to study deformation of partially molten rocks, since the scaling limitation can be overcome and a large number of simulations with varying parameters can be analysed. Numerical simulations allow exploring the balance between dynamic recrystallisation, grain size and strain rate, and allow studying the geometric and mechanic evolution of the system.

Chapter 9 of this thesis presents a series of simple-shear deformation simulations of two-phase linear viscous composites, coupled with grain boundary migration. These models are used investigate the microstructural and mechanical evolution of partially molten rock aggregates and ice-air bubble composites. Different scenarios are explored, addressing the influence of: (1) strain rate, (2) second-phase wetting angle, (3) viscosity contrast between the phases and (4) second-phase fraction. Variable strain rates are simulated by altering the ratio between viscous deformation and dynamic recrystallisation (*GBM*). This approach allows investigating the microstructural and mechanical evolution of the aggregate in the two aforementioned domains (i.e. recrystallisation- and deformation-dominated systems). One main outcome is that the strong strain weakening observed in experiments on partial melts may not occur in nature at much lower strain rates, where dynamic recrystallisation can maintain equilibrium melt distributions.

1.6   The ELLE numerical simulation platform

ELLE is an open-source modelling platform used to simulate the development of microstructures during tectonic and/or metamorphic processes (Jessell et al. 2001; Bons et al. 2008; Piazolo et al. 2010). ELLE has been used to simulate a variety of microstructural processes, including dynamic recrystallisation (Piazolo et al., 2002; Montagnat et al., 2014), grain growth (Jessell et al., 2001; Jessell et al., 2003; Roessiger et al., 2011), strain localisation (Jessell et al., 2005; Griera et al., 2011), and deformation of two-phase materials (Jessell et al., 2009). ELLE is particularly designed to model the interaction of multiple processes that act on a microstructure simultaneously. It is therefore ideally suited for the investigations that are presented in this thesis, which mostly deal with the interaction of deformation and recrystallisation. Each process is normally simulated in ELLE as an individual (i.e. isolated) module, and the evolution of systems undergoing different processes simultaneously is modelled by combining individual processes in a loop. Each loop represents one time step, which can be adjusted depending on what is being simulated. Elements in ELLE are defined with a 2D geometry microstructure of contiguous set of polygons, termed *flynns*, which are connected by boundary nodes, termed *bnodes*. One bnode can be connected to either two or three neighbour bnodes. ELLE allows including a superimposed regular grid of unconnected nodes (*unodes*), which are used for representing points within the material. Unodes are useful for simulating processes within

polygons, or processes that require regular grids, such as full-field viscoplastic deformation (FFT). Unodes are also useful to track the instantaneous and finite deformation fields by inserting a passive marker grid. Properties in ELLE can be assigned to flynns (where each flynn has an homogeneous rheology), bnodes or unodes. The system is normally simulated as a 2D dimensionless square cell with periodic horizontal and vertical boundaries. In this way, the cell can be infinitely repeated in all directions. The wrapping boundaries allow maintaining the unit cell square in simple shear simulations, because the model region falling outside the bounding box can be repositioned into the square cell after every step of deformation, bringing back all the elements (Jessell et al., 2009). However, the model bounding box in pure shear changes during deformation, since these boundary conditions do not allow repositioning elements. In this thesis, different ELLE processes have been combined in order to reproduce natural processes during ice and rock deformation:

- *Viscoplastic deformation using a full-field numerical approach (FFT).* Chapters 2, 3, 4 and 8 use a combination of a full-field viscoplastic deformation code (FFT) coupled with ELLE modules used to simulate processes like dynamic recrystallisation and recovery. This approach has been successfully used to simulate dynamic recrystallisation of polycrystalline pure ice during simple and pure shear viscoplastic deformation. FFT uses a fast Fourier algorithm to provide a solution of the micromechanical problem by finding a stress and strain rate field that minimises the average local work-rate (Lebensohn, 2001). The FFT approach provides geometrically necessary dislocations estimation and deformation induced lattice rotation from the stress and velocity fields. From these calculated parameters, the ELLE processes, grain boundary migration and recovery, are simulated. The method is explained in detail in chapter 2.2.

- *Linear and non-linear viscosity deformation simulations of composite materials, using a finite element (FEM) method.* Viscous deformation of composite materials (chapters 5, 6, 7, 8 and 9) is simulated with the BASIL FEM module (Housemann et al., 2008). This code models deformation of a 2D sheet in plane-strain based. It computes viscous strain rates and the associated stress fields for linear and non-linear rheologies. The method is explained in detail in chapter 5.2.

- *Dynamic recrystallisation.* Dynamic recrystallisation (DRX) is simulated in this thesis including two processes: (1) grain boundary migration (GBM) and (2) recovery. GBM is simulated using a front-tracking approach (Becker et al., 2008), which is driven by reduction of grain boundary energy (grain boundary curvature) and internal strain energy (dislocation density). This process reduces the stored strain energy by moving the high-angle grain boundary (HAGB) and sweeping high dislocation density areas. Recovery is another effective process to reduce the intra-granular stored energy

simulating processes like annihilation and rearrangement of dislocations, reducing the intra-granular misorientation (Borthwick et al., 2013). Both processes are used in the simulations presented in chapters 2, 3 and 4. They are explained in Chapter 2.2. Grain boundary migration is also used to simulate deformation of partially molten rocks coupled with viscous deformation (chapter 9), although in this case strain energy associated with dislocation density is not considered. Instead, this *GBM* code is only based on a minimisation of Gibbs' free energy grain boundary movement (Becker et al., 2008; Roessiger et al., 2014).

The ELLE code is the product of an informal consortium of developers. This thesis used code developed by others, but also new code or code modified by the author. Apart from code development, the author also carried out extensive debugging and testing of the various modules used for this thesis. Appendix 1 provides the main blocks of source code used for this thesis and a brief summary of the main development contributions by the author.

1.7   Conclusions

This thesis presents a number of applications of numerical modelling to the deformation of ice and rocks on the micro- to meso-scale. Particular attention is given to the interaction of processes that determine the evolving structure and mechanical properties. In addition, the simulations were carried out to high strains, more than usually achieved in numerical simulations or physical experiments. The outcomes of the individual studies are listed above and are too diverse to be summarised here. However, a main outcome is that the numerical simulations show that interaction of processes is a primary factor in the deforming materials and that these simulations are a crucial tool to link experiments and observations on naturally deformed rocks and ice and an important step forward in the interpretation of natural structures, from microstructures in polar ice sheets to folds in rocks.

1.8   References

- Abassi, M.R., Mancktelow, N.S., 1992. Single layer buckle folding in non-linear materials - I. Experimental study of fold development from an isolated initial perturbation. Journal of Structural Geology 14, 85-104.

- Alley, R.B., Gow, A.J., Meese, D.A., 1995. Mapping c-axis fabrics to study physical processes in ice. Journal of Glaciology 41 (137), 197-203.

- Alsop, G.I., Holdsworth, R.E., 2006. Sheath folds as discriminators of bulk strain type. Journal of Structural Geology 28, 1588-1606.

- Anthony, J.M., Wickham, J.S., 1978. Finite-element simulation of asymmetric folding. Tectonophysics 47, 1-14.

- Ashby, M.F. and Duval, P., 1985. The creep of polycrystalline ice. Cold Regions Science and Technology 11(3), 285-300.

- Azuma, N., Miyakoshi, T., Yokoyama, S. and Takata, M., 2012. Impeding effect of air bubbles on normal grain growth of ice. Journal of Structural Geology, 42, 184-193.

- Becker, J.K., Bons, P.D. and Jessell, M.W., 2008. A new front-tracking method to model anisotropic grain and phase boundary motion in rocks. Computers and Geosciences, 34, 201-212

- Bell, T.H., Johnson, S.E., Davis, B., Forde, A., Hayward, N. and Wilkins, C., 1992. Porphyroblast inclusion-trail orientation data: eppure non son girate!. Journal of Metamorphic Geology 10, 295-307.

- Biot, M.A., 1961. Theory of folding of stratified viscoelastic media and its implication in tectonics and orogenesis. Geological Society of America Bulletin 72, 1595–1632.

- Bjørnerud, M., 1989. Toward a unified conceptual framework for shear-sense indicators. Journal of Structural Geology 11, 1045-1049.

- Bons, P.D. and Cox, S.J.D., 1994. Analogue experiments and numerical modelling on the relation between microgeometry and flow properties of polyphase materials. Materials Science and Engineering A175, 237-245.

- Bons, P.D. and Urai, J.L., 1996. An apparatus to experimentally model the dynamics of ductile shear zones. Tectonophysics 256, 145–164.

- Bons, P.D., Koehn, D. and Jesell, M.W., 2008. Microdynamics simulation: Berlin, Springer, 406 pp.

- Borthwick V.E., Piazolo S., Evans L., Griera A. and Bons P.D., 2013. What happens to deformed rocks after deformation? A refined model for recovery based on numerical simulations. Geological Society London, Special Publications 394, 215 – 534.

- Carreras, J., Druguet, E. and Griera, A., 2005. Shear zone-related folds. Journal of Structural Geology 27, 1229–1251.

- Chapple, W.M., 1968. A mathematical theory of finite amplitude rock-folding. Geological Society of America Bulletin 79, 47–68.

- Cuffey, K.M., and Paterson, W.S.B., 2010. The physics of glaciers. Academic Press.

- De la Chapelle, S., Castelnau, O., Lipenkov, V. and Duval, P., 1998. Dynamic recrystallization and texture development in ice as revealed by the study of deep ice cores in Antarctica and Greenland. Journal of Geophysical Research 103, 5091-5105.

- Duval P., Ashby M. and Anderman I., 1983. Rate controlling processes in the creep of polycrystalline ice. The Journal of Physical Chemistry 87(21), 4066-4074.

- Einstein, A., 1906. Eine neue Bestimmung der Moleküldimensionen. Annalen der Physik 19, 289–306.

- Ez, V., 2000. When shearing is a cause of folding: Earth-Science Reviews 51, 155–172.

- Faria, S.H., Freitag, J. and Kipfstuhl, S., 2010. Polar ice structure and the integrity of ice-core paleoclimate records. Quaternary Science Reviews 29, 338-351.

- Faria H.G., Weikusat I. and Azuma N., 2014a. The microstructure of polar ice. Part I: Highlights from ice core research. Journal of structural geology 61, 21–49.

- Faria H.G., Weikusat I. and Azuma N., 2014b. The microstructure of polar ice. Part II: State of the art. Journal of structural geology 61, 21 – 49.

- Faria, S.H., Kipfstuhl, S. and Lambrecht, A., 2014c. The EPICA-DML Deep Ice Core. Springer, Heidelberg

- Fay, C., Bell, T.H. and Hobbs, B.E., 2008. Porphyroblast rotation versus nonrotation: Conflict resolution!. Geology 36, 307-310.

- Fletcher, R.C., 1974. Wavelength selection in the folding of a single layer with power-law rheology. American Journal of Science 274, 1029–1043.

- Fletcher, R.C., 1977. Folding of a single viscous layer: Exact infinitesimal-amplitude solution. Tectonophysics 39, 593-606.

- Frehner, M. and Schmalholz, S.M., 2006. Numerical simulations of parasitic folding in multilayers. Journal of Structural Geology 28, 1647-1657.

- Ghosh, S.K., 1966. Experimental tests of buckling folds in relation to strain ellipsoid in simple shear deformations. Tectonophysics 3, 169-185.

- Ghosh, S.K. and Sengupta, S., 1999. Boudinage and composite boudinage in superposed deformations and syntectonic migmatization: Journal of Structural Geology 21, 97-100.

- Glen, J.W., 1958. The flow law of ice: A discussion of the assumptions made in glacier theory, their experimental foundations and consequences. IASH Publ, 47, 171-183.

- Griera, A., Bons, P.D., Jessell, M.W., Lebensohn, R.A., Evans, L. and Gomez-Rivas, E., 2011. Strain localization and porphyroclast rotation. Geology 39, 275-278.

- Griera, A., Llorens, M.-G., Gomez-Rivas, E., Bons, P. D., Jessell, M. W., Evans, L. A. and Lebensohn, R., 2013. Numerical modelling of porphyroclast and porphyroblast rotation in anisotropic rocks. Tectonophysics 587, 4–29.

- Groebner, N. and Kohlstedt, D.L., 2006. Deformation-induced metal melt networks in silicates: implications for core–mantle interactions in planetary bodies. Earth and Planetary Science Letters, 245, 571–580.

- Gomez-Rivas, E., Griera, A. and Llorens, M.-G., 2015. Fracturing of ductile anisotropic multilayers: influence of material strength. Solid Earth, in press.

- Gow, A.J., 1969. On the rates of growth of grains and crystals in south polar firn. Journal of Glaciology 8 (53), 241-252

- Hanmer, S. and Passchier, C.W., 1991. Shear-sense indicators: a review. Geological Survey of Canada paper 90, 1-72.

- Hobbs, B.E., Means, W.D. and Williams, P.F., 1976. An Outline of Structural Geology. Wiley , New York, 571 pp.

- Hobbs, B.E., Muhlhaus, H.B. and Ord, A., 1990, Instability, softening and localization of deformation (in Deformation mechanisms, rheology and tectonics): Geological Society Special Publications 54, 143-165.

- Hobbs, B., Regenauer-Lieb, K. and Ord, A., 2008. Folding with thermal-mechanical feedback. Journal of Structural Geology 30, 1572-1592.

- Holness, M., 2010. Decoding dihedral angles in melt-bearing and solidified rocks. In: (Ed.) M.A. Forster, and John D. Fitz Gerald, The Science of Microstructure - Part I, Journal of the Virtual Explorer 35, 2. doi:10.3809/jvirtex.2011.00265

- Houseman, G., Barr, T. and Evans, L., 2008. Basil: stress and deformation in a viscous material. In: Bons, P.D., Koehn, D., Jessell, M.W. (Eds.), Microdynamics Simulation. Lecture Notes in Earth Sciences 106. Springer, Berlin, pp. 405.

- Hudleston, P.J. and Stephansson, O., 1973. Layer shortening and fold shape development in the buckling of single layers. Tectonophysics 17, 299–321.

- Hudleston, P.J., 1986. Extracting information from folds in rocks. Journal of Geological Education 34, 237–245.

- Hudleston, P.J. and Lan, L., 1993. Information from fold shapes. Journal of Structural Geology 15, 253-264.

- Hudleston, P.J. and Lan, L., 1994. Rheological controls on the shapes of single-layer folds. Journal of Structural Geology 16, 1007-1021.

- Ildefonse, B. and Mancktelow, N.S., 1993. Deformation around rigid particle: influence of slip at the particle/matrix interface. Tectonophysics 221, 345–359.

- Jacka, T.H. and Li, J., 1994. The steady-state crystal size of deforming ice. Annals of Glaciology 20, 13-28.

- Jessell, M., Bons, P.D., Evans, L., Barr, T. and Stüwe, K. 2001. Elle: the numerical simulation of metamorphic and deformation microstructures. Computers And Geosciences 27, 17-30.

- Jessell, M.W., Kostenko, O. and Jamtveit, B,. 2003. The preservation potential of microstructures during static grain growth. Journal of Metamorphic Geology 21(5), 481–491.

- Jessell, M.W., Siebert, E., Bons, P.D., Evans, L. and Piazolo, S., 2005. A new type of numerical experiment on the spatial and temporal patterns of localization of deformation in a material with a coupling of grain size and rheology. Earth and Planetary Science Letters 239(3), 309-326.

- Jessell, M.W., Bons, P.D., Griera, A., Evans, L.A. and Wilson, C.J.L, 2009. A tale of two viscosities. Journal of Structural Geology, 31, 719-736.

- Jiang, D. and Williams, P.F., 2004. Reference frame, angular momentum, and porphyroblast rotation. Journal of Structural Geology 26, 221-2224.

- Johnson, S.E., 1999. Porphyroblast microstructures: A review of current and future trends. American Mineralogist 84, 1711-1726.

- Johnson, A.M. and Fletcher, R.C., 1994. Folding of Viscous Layers, Columbia University Press, New York.

- Johnson, S.E., 2009. Porphyroblast rotation and strain localization: Debate settled!. Geology 37, 663-666.

- Kennicutt, I.I., Chown, S.L., Cassano, J.J., Liggett, D., Massom, R., Lloyd, S. and Peck, L.S., 2014. Six priorities for Antarctic science. Nature 512(7512), 23-25.

- Kipfstuhl, S., Hamann, I., Lambrecht, A., Freitag, J., Faria, S.H., Grigoriev, D. and Azuma, N., 2006. Microstructure mapping: a new method for imaging deformation-induced microstructural features of ice on the grain scale. Journal of Glaciology 52 (178), 398-406.

- Kocher, T., Mancktelow, N.S., Schmalholz, S.M., 2008. Numerical modelling of the effect of matrix anisotropy orientation on single layer fold development. Journal of Structural Geology 30, 1013-1023.

- Lan, L. and Hudleston, P.J., 1991. Finite-element models of buckle folds in non-linear materials. Tectonophysics 199, 1-12.

- Lebensohn R.A., 2001. N-site modelling of a 3D viscoplastic polycrystal using fast Fourier transform. Acta Materialia, 49(14), 2723–2737.

- Lemke, P., Ren, J., Alley, R. B., Allison, I., Carrasco, J., Flato, G., Fujii, Y.,Kaser, G., Mote, P., Thomas, R. H. and Zhang, T., 2007. Observations: changesin snow, ice and frozen ground. In: Solomon, S., Qin, D., Manning, M.,Chen, Z., Marquis, M., Averyt, K. B., Tignor, M., Miller, H. L. (Eds.), ClimateChange 2007: The Physical Science Basis. Contribution of WorkingGroup I to the Fourth Assessment Report of the Intergovernmental Panel onClimate Change (IPCC). Cambridge University Press, Cambridge.

- Lister, G.S., Paterson, M.S. and Hobbs, B.E., 1978. The simulation of fabric development in plastic deformation and its application to quartzite: the model. Tectonophysics 45, 107-158.

- Llorens, M.-G., Bons, P.D., Griera, A., Gomez-Rivas, E. and Evans, L. A., 2013a. Single layer folding in simple shear: Journal of Structural Geology 50, 209-220.

- Llorens, M.-G., Bons, P.D., Griera, A. and Gomez-Rivas, E., 2013b. When do folds unfold during progressive shear?: Geology 41, 563-566.

- Llorens, M. G., Bons, P.D., Griera, A. and Gomez-Rivas, E., 2014. Mechanics of Fold Development in Pure-and Simple Shear. In Mathematics of Planet Earth (pp. 763-766). Springer Berlin Heidelberg.

- Lloyd, G.E., Ferguson, C.C., and Reading, K., 1982. A stress transfer model for the development of extension fracture boudinage: Journal of Structural Geology 4, 355-372.

- Mainprice, D. and Nicolas, A., 1989. Development of shape and lattice preferred orientations: application to the seismic anisotropy of the lower crust. Journal of Structural Geology, 11(1), 175-189.

- Mancktelow, N.S., 1999. Finite-element modelling of single-layer folding in elastoviscous materials; the effect of initial perturbation geometry. Journal of Structural Geology 21, 161-177.

- Mancktelow, N.S., 2006. How ductile are ductile shear zones?. Geology 34, 345-348.

- Mangeney, A., Califano, F. and Hutter, K., 1997. A numerical study of anisotropic, low Reynolds number, free surface flow of ice sheet modeling. Journal of Geophysical Research 102 (B10), 22,749-22,764.

- Manz, R. and Wickham, J., 1978. Experimental analysis of folding in simple shear. Tectonophysics 44, 79–90.

- Marques, F.O. and Coelho, S., 2001. Rotation of rigid elliptical cylinders in viscous simple shear flow: analogue experiments. Journal of Structural Geology 23, 609–617.

- Means, W.D., 1999, Reversed structures and bounce structures: are they recognizable? Are they real?: Journal of Structural Geology 21, 917-921.

- Montagnat M., Castelnau O., Bons P.D., Faria S.H., Gagliardini O., Gillet-Chaulet F., Grennerat F., Griera A., Lebensohn R.A., Moulinec H., Roessiger J. and Suquet P., 2014. Multiscale modeling of ice deformation behavior. Journal of Structural Geology, 61, 78 – 108.

- Nicolas, A. and Poirier, J.P., 1976. Crystalline plasticity and solid state flow in metamorphic rocks (pp. 444). London: Wiley.

- Parrish, D.K., Krivz, A. L. and Carter, N. L., 1976. Finite-element folds of similar geometry. Tectonophysics 32, 183-207.

- Passchier, C.W., 1988. Analysis of deformation paths in shear zones: Geologische Rundschau 77, 309-318.

- Passchier, C.W. and Simpson, C., 1986. Porphyroclast systems as kinematic indicators. Journal of Structural Geology 8, 831-843.

- Passchier, C.W., Trouw, R.A.J., Zwart, H.J. and Vissers, R.L.M., 1992. Porphyroblast rotation: eppur si muove?. Journal of Metamorphic Geology 10, 283-294.

- Passchier, C.W. and Williams, P.R., 1996. Conflicting shear sense indicators in shear zones; the problem of non-ideal sections. Journal of Structural Geology 18, 1281–1284.

- Passchier, C.W. and Trouw, R.A.J., 2005. Microtectonics (2nd enlarged edition). Springer Verlag, Berlin.

- Piazolo, S. Bons, P.D., Jessell, M.W., Evans, L. and Passchier, C.W., 2002. Dominance of microstructural processes and their effect on microstructural development: insights from numerical modelling of dynamic recrystallization. Geological Society of London Special Publications 200, 149-170.

- Piazolo, S., Jessell, M.W., Bons, P.D., Evans, L. and Becker, J.K., 2010. Numerical simulations of microstructures using the Elle platform: A modern research and teaching tool. Journal of the Geological Society of India 75, 110-127.

- Ramberg, H., 1961. Contact strain and folding instability of a multilayered body under compression. Geologische Rundshau 51, 405-439.

- Ramsay, J.G., 1980, Shear zone geometry: a review: Journal of Structural Geology 2, 83-99.

- Ramsay, J.G. and Huber, M.I., 1983. The Techniques of Modern Structural Geology, vol I: Strain Analysis. Academic Press, London.

- Ramsay, J.G. and Huber, M.I., 1987. The Techniques of Modern Structural Geology. In: Folds and Fractures, vol. II. Academic Press, London.

- Roessiger, J., Bons, P.D., Grieram A., Jessell, M.W., Evansm L., Montagnat, M., Kipfstuhl, S., Faria, S.H. and Weikusat, I., 2011. Competition between grain growth and grain size reduction in polar ice. Journal of Glaciology 57(205), 942-948.

- Roessiger, J., Bons P.D., and Faria S.H., 2014. Influence of bubbles on grain growth in ice. Journal of Structural Geology 61, 123-132.

- Rosenfeld, J.L., 1970. Rotated garnets in metamorphic rocks. Special Paper of the Geological Society of America, 129.

- Schulson, E.M. and Duval, P., 2009. Creep and fracture of ice (pp. 432). Cambridge: Cambridge University Press.

- Schmalholz, S.M., 2008. 3D numerical modelling of forward and reverse folding of a viscous single-layer: Implications for the formation of fold and fold patterns. Tectonophysics 446, 31-41.

- Schmalholz, S.M. and Podladchikov, Y.Y., 2000. Finite amplitude folding: transition from exponential to layer length controlled growth. Earth and Planetary Science Letters 181, 619-633.

- Schmalholz, S.M., Podladchikov, Y. and Jamtveit, B., 2005. Structural softening of the lithosphere. Terra Nova 17, 66 – 72.

- Schoneveld, C., 1977. A study of some typical inclusion patterns in strongly paracrystalline rotated garnets. Tectonophysics 39, 453-471.

- Sherwin, J.-A. and Chapple,W.M., 1968. Wavelengths of single layer folds: a comparison between theory and observation. American Journal of Science 266, 167-179.

- Smith, R.B., 1975. Unified theory of the onset of folding, boudinage, and mullion structure. Geological Society of America Bulletin 86, 1601–1609.

- Smith, R.B., 1977. Formation of folds, boudinage, and mullions in non-Newtonian materials. Geological Society of America Bulletin 88, 312–320.

- Svensson, A., Nielsen, S.W., Kipfstuhl, S., Johnsen, S.J., Steffensen, J.P., Bigler, M., Ruth, U. and Röthlisberger, R., 2005. Visual stratigraphy of North Greenland Ice Core Project (NorthGRIP) ice core during the last glacial period. Journal of Geophysical Research, D110.

- Talbot, C.J., 1999, Can field data constrain rock viscosities?: Journal of Structural Geology 21, 949–957.

- Takeda Y.T. and Griera A., 2006. Rheological and kinematical responses to flow of two-phase rocks. Tectonophysics 427, 95-113.

- Taylor, G.I., 1934. The mechanism of plastic deformation of crystals. Part I. Theoretical. Proceedings of the Royal Society of London. Series A, Containing Papers of a Mathematical and Physical Character, 362-387.

- Teyssier, C. and Whitney, D., 2002. Gneiss domes and orogeny. Geology 30, 1139-1142.

- Tikoff, B. and Peterson, K., 1998. Physical experiments of transpressional folding. Journal of Structural Geology 20, 661-672.

- Toimil, N.C. and Griera, A., 2007. Influence of viscosity contrast and anisotropy on strain accommodation in competent layers. Journal of Structural Geology 29, 787-801.

- Treagus, S.H., 1973. Buckling stability of a single-layer system, oblique to the principal compression. Tectonophysics 19, 271-289.

- Treagus, S.H., 1982. A new isogon – cleavage classification and its application to natural and model fold studies. Geological Journal 17, 49–64.

- Treagus, S.H., 1997. Deformation partitioning in folds: implications for fold geometry and cleavage patterns, in: Evolution of Geological Structures in Micro- to Macro-Scales, edited by: Sengupta, S., Chapman and Hall, London, 341–372.

- Treagus, S.H., 2003. Viscous anisotropy of two-phase composites, and applications to rocks and structures. Tectonophysics 372, 121-133.

- Turner, J., Barrand, N.E., Bracegirdle, T.J., Convey, P., Hodgson, D. A., Jarvis, M. and Klepikov, A., 2014. Antarctic climate change and the environment: an update. Polar Record, 50(03), 237-259.

- Twiss, R.J. and Moores, E.M., 1992. Structural Geology, W.H. Freeman, New York.

- Van der Veen, C.J. and Whillans, I.M., 1990. Flow law for glacier ice: comparison of numerical predictions and field measurements. Journal of Glaciology 36, 324-339.

- Viola, G. and Mancktelow, N.S., 2005. From XY tracking to buckling: axial plane cleavage fanning and folding during progressive deformation, Journal of Structural Geology 27, 409–417.

- Walte, N.P., Rubie, D.C., Bons, P.D. and Frost, D.J., 2011. Deformation of a crystalline aggregate with a small percentage of high dihedral-angle liquid: Implications for core-mantle differentiation during planetary formation. Earth and Planetary Science Letters 305, 124-134.

- Weikusat I., Kipfstuhl S., Faria S.H., Azuma N. and Miyamoto A., 2009. Subgrain boundaries and related microstructural features in EDML (Antarctica) deep ice core. Journal of Glaciology, 55(191), 461-472.

- Whitney, D., Teyssier, C. and Rey, P.F., 2009. The consequences of crustal melting in continental subduction. Lithosphere 1, 323-327.

- Wilson, C.J. and Zhang, Y., 1996. Development of microstructure in the high-temperature deformation of ice. Annals of Glaciology 23, 293-302.

- Wilson, M. R., 1971. On syntectonic porphyroblast growth. Tectonophysics 11, 239-260.

- Wilson, C.J.L., 1981. Experimental folding and fabric development in multi-layered ice. Tectonophysics 78, 139-159.

- Wilson, C.J.L., 1983. Foliation and strain development in ice mica models. Tectonophysics 92, 93-122

- Zhang, Y., Hobbs, B.E., Ord, A. and Mühlhaus, H.B., 1996. Computer simulation of sigle-layer buckling. Journal of Structural Geology 18, 643-655.

- Zhang, Y., Mancktelow, N.S., Hobbs, B.E., Ord, A. and Mühlhaus, H.B., 2000. Numerical modelling of single-layer folding: Clarification of an issue regarding the possible effects of computer codes and the influence of initial irregularities. Journal of Structural Geology 22, 1511-1522.

Contributions

Chapter 2. **Llorens, M-.G.**, Griera, A., Bons, P.D., Lebensohn, R. Roessiger, J. and Weikusat, I. Dynamic recrystallisation of ice aggregates during co-axial viscoplastic deformation: a numerical approach. Submitted to the *Journal of Glaciology.*

Scientific ideas: 50% - Data generation: 90% - Analysis and Interpretation: 80% - Paper writing: 70%

Chapter 3. **Llorens, M-.G.**, Griera, A., Bons, P.D., Lebensohn, R. and Weikusat, I. Full-field predictions of pure ice dynamic recrystallisation under simple shear conditions. Manuscript in advance preparation to be submitted to *Earth and Planetary Science Letters.*

Scientific ideas: 50% - Data generation: 90% - Analysis and Interpretation: 80% - Paper writing: 70%

Chapter 4. Jansen, D., **Llorens, M-.G.**, Westhoff, J., Steinbach, F., Bons, P.D., Kipfstuhl, S., Griera, A. and Weikusat I. Small-scale disturbances in the stratigraphy of the NEEM ice core: observations and numerical simulations. Manuscript in advance preparation to be submitted to *The Cryosphere.*

Scientific ideas: 40% - Data generation: 30% - Analysis and Interpretation: 30% - Paper writing: 20%

Chapter 5. **Llorens, M-.G.**, Bons, P.D., Griera, A., Gomez-Rivas, E. and Evans, L.A. 2013. Single layer folding in simple shear. *Journal of Structural Geology* 50, 209-220.

Scientific ideas: 50% - Data generation: 90% - Analysis and Interpretation: 80% - Paper writing: 70%

Chapter 6. **Llorens, M-.G.**, Bons, P.D., Griera, A. and Gomez-Rivas, E. 2014. Mechanics of fold development in pure and simple shear. In: Pardo-Igúzquiza, E., Guardiola-Albert, C., Heredia, J., Moreno-Merino, L., Durán, J.J. and Vargas-Guzmán, J.A. (Eds). *Mathematics of Planet Earth.* Lecture Notes in Earth System Sciences, pp. 763-766. Springer.

Scientific ideas: 60% - Data generation: 90% - Analysis and Interpretation: 80% - Paper writing: 70%

Chapter 7. **Llorens, M-.G.**, Bons, P.D., Griera, A. and Gomez-Rivas, E. 2013. When do folds unfold during progressive shear?. *Geology* 41, 563-566.

Scientific ideas: 50% - Data generation: 90% - Analysis and Interpretation: 80% - Paper writing: 70%

Chapter 8. Griera, A., **Llorens, M-.G.**, Gomez-Rivas, E., Bons, P.D., Jessell, M.W., Evans, L.A. and Lebensohn, R. 2013. Numerical modelling of porphyroclast and porphyroblast rotation in anisotropic rocks. *Tectonophysics* 587, 4-29.

Scientific ideas: 15% - Data generation: 50% - Analysis and Interpretation: 35% - Paper writing: 35%

Chapter 9. Ganzhorn, A.C., **Llorens, M-.G.**, Gomez-Rivas, E., Roessiger, J., Labrousse, L., Walte, N.P. and Bons, P.D. The effect of dynamic recrystallization on the rheology and microstructures of partially molten rocks. Submitted to *Earth and Planetary Science Letters.*
Scientific ideas: 20% - Data generation: 80% - Analysis and Interpretation: 50% - Paper writing: 40%

Chapter 2

Dynamic recrystallisation of ice aggregates during co-axial viscoplastic deformation: a numerical approach

Maria-Gema Llorens[a,b], Albert Griera[c], Paul D. Bons[a], Jens Roessiger[a], Ricardo Lebensohn[d]and Ilka Weikusat[a,b]

[a]Departament of Geosciences, Eberhard Karls University Tübingen, Germany
[b]Alfred Wegener Institute for Polar and Marine Research, Bremerhaven, Germany
[c]Departament de Geologia, Universitat Autònoma de Barcelona, Cerdanyola del V., Spain
[d]Material Science and Technology Division, Los Alamos National Laboratory, USA

Abstract

Results of numerical simulations of co-axial deformation of pure ice up to high strain, combining full-field modelling with recrystallisation, are presented. Grain size and LPO analysis and comparisons between simulations at different strain rates show how recrystallisation has a major effect on the microstructure, developing larger and equidimensional grains, but a relatively minor effect on the development of a preferred orientation of c-axes. Although c-axis distributions do not vary much, recrystallisation appears to have a distinct effect on the relative activities of slip systems, activating the pyramidal slip system and affecting the distribution of a-axes. The simulations reveal that the survival probability of individual grains is strongly related to the initial grain size, but only weakly dependent on hard or soft orientations with respect to the flow field. Dynamic recrystallisation reduces the initial hardening that is followed by a steady state, which is characteristic for pure-shear deformation.

Keywords

2.1 Introduction

Ice is a common mineral on the Earth's surface. Thick ice sheets cover Greenland and Antarctica. How much ice is stored in these ice sheets depends on its mechanical properties, as the weight of the ice masses causes a steady flow of ice towards the surrounding oceans. The mechanical properties of ice, therefore, directly impact on human society through its role in controlling sea level (Kennicutt et al., 2014). At natural strain rates of $< 10^{-6}$ s^{-1} (e.g. Budd and Jacka, 1989), ice is a ductile material, assumed to deform dominantly by dislocation creep (e.g. Schulson and Duval, 2009), similar to other rock-forming minerals, such as quartz and olivine at much higher absolute, but similar homologues temperatures. In contrast to these minerals, ice on Earth only occurs very close to its melting temperature.

Ice on Earth is exclusively Ih, with a hexagonal structure. The strong viscoplastic anisotropy of single ice crystals constitutes the first complexity in describing and modelling the behaviour of the flow of ice (Duval and Castelnau, 1995). The critical resolved shear stress (CRSS) to activate dislocation slip on the basal plane is about 60 to 100 times lower than on prismatic and pyramidal planes (Duval et al., 1983; Montagnat et al., 2013; Wilson and Zhang, 1996). Strain is therefore mostly achieved by slip on the basal plane, with relatively minor contributions of the other slip planes (Ashby and Duval, 1985).

The bulk behaviour of large ice masses results from the behaviour of the ensemble

of individual ice grains. This behaviour is thus strongly influenced by the viscoplastic anisotropy of these grains and the orientation of their lattices, usually expressed in the orientation of their c-axis. During flow, ice quickly develops a lattice preferred orientation (LPO) by lattice rotation (Azuma and Higashi, 1985; Alley, 1988, 1992; Jacka and Li, 2000). The ice microstructure is further evolving through time by recrystallisation that is driven by grain-boundary (GB) surface energy and by strain energy. The mechanical properties of ice masses are therefore not constant, but the result of complex, time-dependent coupling between deformation and microstructural evolution. Understanding this coupling is of paramount importance for studies on the flow behaviour of polar ice sheets.

2.1.1 Flow of polar ice sheets

Experiments on ice show it has a strongly strain-dependent behaviour (Jacka, 1984; Azuma, 1994; Treverrow et al., 2012; Budd et al., 2013). Initial, transient or primary creep is dominated by dislocation glide on the basal plane and is associated with an increase in strength (Montagnat et al., 2006). Secondary creep is reached at a few % of strain, when recrystallisation sets in and the maximum strength is reached and the material begins to soften again (Glen, 1955). A lattice preferred orientation develops during tertiary creep where a steady state may be reached after ca. 10% of strain (Budd and Jacka, 1989, Treverrow et al., 2012). Although secondary creep is highly transient, it is the stage on which the commonly used flow law is based. "Glen's law" (Glen, 1958) describes the relation between deviatoric stress (σ) and strain rate ($\dot{\varepsilon}$) with a power law with a stress exponent, n:

$$\dot{\varepsilon} = A_{(T,\mu s)}\sigma_n \tag{2.1}$$

This law is based on the maximum strength that is reached during secondary creep. In most studies, it is assumed that $n = 3$, although values ranging from 1 to 5 have also been reported, based e.g. on experiments (Goldsby and Kohlstedt, 2001) and observations on ice sheets (Cuffey and Kavanaugh, 2011; Gillet-Chaulet et al., 2012). The pre-exponential factor depends on temperature (T), but also on the microstructure (μ_s), in particular the LPO. The effect of LPO is usually incorporated by using a LPO-dependent scalar "enhancement factor" (see Faria et al., 2014b). This enhancement factor changes the absolute strain rate at a given stress, but not the sensitivity of strain rate to a change in stress, defined by n.

2.1.2 Microstructures of deforming ice

Laboratory experiments and deep drill cores through glaciers and ice sheets are the most important sources of information on ice microstructures (e.g. Wilson et al., 2013; Faria

et al., 2014a, 2014b; Piazolo et al., 2012, Weikusat et al., 2009). The three dominant processes that affect the shape and size of grains are sub-grain formation or polygonisation, and grain boundary migration driven by strain energy and by grain boundary surface energy (Urai et al., 1986). All three processes operate concurrently, albeit in different proportions, mainly depending on strain rate and temperature (Faria et al., 2014b). Grain boundary surface energy-driven grain growth in isolation ("normal grain growth"; *NGG*) leads to an increase in grain size by reduction of grain boundary surface area (Azuma et al., 2012). Polygonisation, in geology also termed "rotational recrystallisation" (*RRX*) (Urai et al., 1986), is a recovery process whereby the lattices in regions within grains rotate relative to each other by the formation of tilt walls. Progressive rotation causes tilt walls to become true grain boundaries, which causes a reduction of the grain size. A dynamic balance between grain growth and polygonisation is invoked by some authors (Mathiesen et al, 2004; Durand et al., 2008; Roessiger et al., 2011, 2012; Azuma et al., 2012). The third process, also called "strain-induced migrational recrystallisation" (*SIBM*) (Urai et al., 1986; Drury and Urai, 1990; Tullis et al., 1990; Stipp and Tullis, 2003) is driven by the energy stored within the lattice in the presence of dislocations. Variations in stored energy (or strain energy) cause grain boundaries to bulge into regions with highest stored energy, leading to the formation of irregular or lobate grain boundaries.

Based on grain-size profiles, it is proposed that the three recrystallisation processes dominate at different depths (De la Chapelle et al., 1998): *NGG* in the upper few hundreds of meters, followed by *RRX* and finally *SIMRX* in the lowest few hundreds of meters in ice sheets, where a sudden increase in grain size is observed in drill cores. However, several authors (Kipfstuhl et al., 2006, 2009; Faria et al., 2014c; Weikusat et al., 2009) have challenged the tri-partite model for ice sheets and showed that all three processes operate at all levels, albeit in different proportions, decoupling the recrystallisation phenomenon from simple depth considerations and describing grain size evolution by strain and temperature conditions (Faria et al., 2014c).

Dislocation creep is assumed to be largely insensitive to grain size and shape (Poirier, 1985; Schulson and Duval, 2008). However, recrystallisation is expected to strongly influence flow properties of ice, if it influences the LPO (Duval and Castelnau, 1995; Duval et al., 2000; Kocks et al., 2000). For example, if crystals with certain orientations are more prone than others to be consumed by migrational recrystallisation owing to their higher dislocation density, migrational recrystallisation would directly influence the LPO, and hence the strength. The study of the interaction between deformation and recrystallisation is thus clearly relevant to improve our understanding and quantification of the flow of ice, from a small volume to that of polar ice sheets.

2.1.3 Numerical modelling of microstructural evolution in ice

Much insight in the mechanical and microstructural behaviour of ice has been gained from experiments (Azuma and Higashi, 1985; Wilson, 1986; Budd and Jacka, 1989; Jacka and Li, 2000; Treverrow et al., 2012; Piazolo et al., 2012). However, one major limitation of experiments is that deformation rates are inevitably higher than those typical in nature by several orders of magnitude, especially in case of slowly flowing polar ice sheets ($\dot{\varepsilon} \approx 10^{-10}$ – 10^{-13} s^{-1}, Montagnat and Duval, 2004; Budd and Jacka 1989). Numerical modelling provides a solution to this, as it is limited by computational power and the sophistication of the algorithms, but not by scale, stress or strain rate.

Theoretical and computational studies have been performed for many years in order to understand the deformation and microstructural evolution (Sachs, 1928, Taylor, 1938). Crystal plasticity based finite element (FE) implementations have been used in the past to model plastic deformation of polycrystalline materials (Becker, 1991; Mika and Dawson, 1998; Raabe et al., 2001; Delannay et al., 2003; Diard et al., 2005). However, the large number of degrees of freedom needed in FE calculations, which restricts the size of the simulated microstructure, and the use of averaged properties are important limitations. To overcome these and to be able to predict the micromechanical behaviour, a full-field formulation based on fast Fourier transforms (FFT) (Moulinec and Suquet, 1994) is used to simulate plastic deformation in heterogeneous materials, such as composites (Moulinec and Suquet, 1998; Michel et al., 2000 and Idiart et al., 2006) or polycrystals (Lebensohn, 2001; Lebensohn et al., 2004, 2005 and 2008). Polycrystal full-field models differ from mean-field models (Sachs 1928, Taylor 1938, Lebensohn and Tomé, 1993) in that the latter explicitly or implicitly assume homogeneous deformation at single crystal level.

Previous full field simulations applied to ice were mostly limited to low finite strain (less than 4% of shortening, (Montagnat et al., 2011) with the exception of a brief example of high-strain FFT modelling in Montagnat et al. (2013). Most studies dealing with FFT-modelling of ice only considered viscoplastic deformation and only few included recrystallisation (Durand, 2004; Montagnat et al., 2013). Considering that ice is near to its melting point at natural conditions, a numerical study on ice recrystallisation processes coetaneous with deformation up to high strain, subject of this paper, is long overdue.

In this contribution we present models combining FFT-based simulations to determine local plastic deformation with recrystallisation up to high strain. The model will be illustrated with pure-shear, plane-strain deformation of pure, polycrystalline Ih ice. We will show how recrystallisation has a major effect on the microstructure, but, perhaps counter-intuitively, only a minor effect on LPO development. Although LPO's do not vary much, recrystallisation appears to have a distinct effect on the relative activities of slip systems.

2.2 Methods

In this study we numerically model the microstructural evolution of an aggregate of pure ice grains during deformation and recrystallisation in 2D pure shear. The approach is based on the coupling between modelling deformation of the viscoplastic polycrystal with a full-field theory formulation (numerically implemented in the FFT code by Lebensohn (2001) and Lebensohn et al. (2008)) and the microstructural modelling platform ELLE (Jessell et al., 2001a; Bons et al., 2008) designed to simulate the recrystallisation processes. The FFT approach provides the stress and velocity fields, from which deformation induced lattice rotation and an estimate of geometrically necessary dislocation densities are calculated. These data, as well as a map of the grain boundary network are used to simulate intra-crystalline recovery and grain boundary migration driven by the reduction of surface energy and stored strain energy generated by dislocations.

The data structure of the models consists of two basic layers (Fig. 2.1a-b): (1) a contiguous set of polygons (termed *flynns*) that are themselves defined by boundary nodes (*bnodes*) and connected by straight boundary segments, and (2) a set of unconnected nodes (*unodes*) that provide a higher resolution of physical properties within grains. The correspondence between both codes is done using the *unodes* layer that allows a direct mapping between the regular computational grid required by the FFT code and the material information required by ELLE.

In the next sections we briefly provide the basics of the governing and constitutive equations and numerical implementation of both approaches.

2.2.1 Viscoplastic deformation – FFT

The FFT-based formulation provides an exact solution of the mechanical problem by finding a strain-rate field and a stress field, associated with a kinematically admissible velocity field, which minimizes the average local work rate under the compatibility and equilibrium constraints (see Lebensohn, 2001 and Lebensohn et al., 2008 for a detailed description of the method, and Montagnat et al. 2013 for its application to ice). The method is based on the fact that the local mechanical response of a periodic heterogeneous medium can be calculated as a convolution integral between the Green function of a linear reference homogeneous medium and the actual heterogeneity field. The use of the FFT algorithm reduces the convolution integrals in Cartesian space to simple products in Fourier space and allows getting the mechanical fields by transforming that product back to real space. As the heterogeneity field depends on the unknown mechanical fields, an iterative scheme based on augmented Lagrangian is used to determine stress and strain-rate fields that fulfil the compatibility and equilibrium constraints (Michel et al., 2001). In general, the FFT approach has a better numerical performance than simulations based on the Finite Element Method (Prakash and Lebensohn, 2009; Roters et al., 2011), but it is
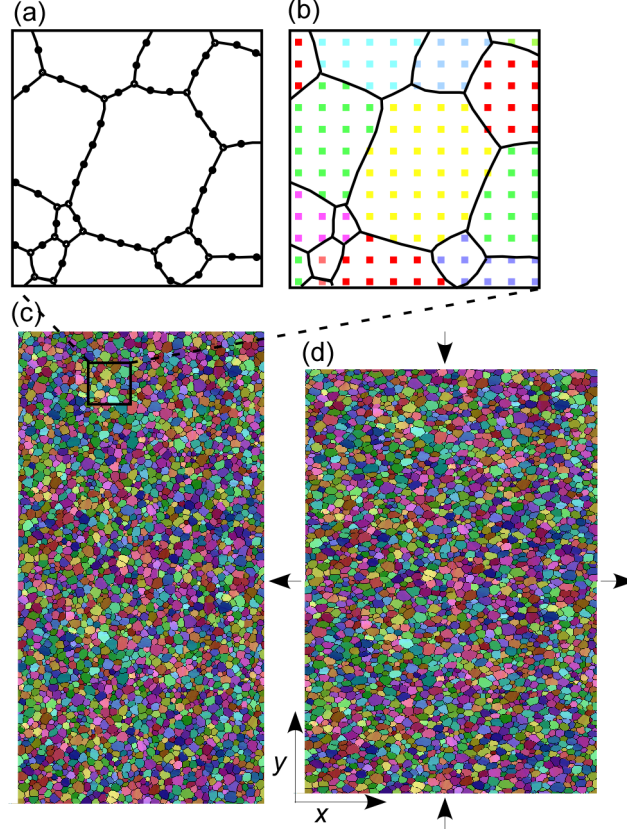
Figure 2.1: Basic data structure and set up of the simulations. The ELLE data structure has two different layers: (a) boundary nodes (double or triple nodes) that define polygons (grains), and (b) a regular mesh of unconnected nodes to store dislocation density and lattice orientations used for the FFT calculation. The initially 2x1 model with 3260 grains (c) is deformed in pure shear with 2% vertical shortening every step (d).

restricted to periodic boundary conditions and requires discretisation into a regular grid.

The constitutive behaviour of the polycrystal aggregate is defined using a non-linear viscous rate-dependent crystal plasticity approach where deformation on the crystal scale is assumed to be accommodated by dislocation glide only. The constitutive equation between the strain rate and the deviatoric stress $\sigma'(\mathbf{x})$ is defined using a non-linear viscous response given by,

$$\dot{\varepsilon}_{ij}(\mathbf{x}) = \sum_{s=1}^{N_s} m_{ij}^s(\mathbf{x})\dot{\gamma}^s(\mathbf{x}) = \dot{\gamma}_0 \sum_{s=1}^{N_s} m_{ij}^s(\mathbf{x}) \left| \frac{m^s(\mathbf{x}) : \sigma'(x)}{\tau^s(\mathbf{x})} \right|^n \operatorname{sgn}(m^s(\mathbf{x}) : \sigma'(\mathbf{x})) \qquad (2.2)$$

where the sum runs over all N_s slip systems, m^s is the symmetric Schmid tensor defined by the dyadic product of the vector normal to the glide plane and the Burgers vector of slip system s, and $(\dot{\gamma}^s)$ and τ^s are, respectively, the shear-strain rate and the critical resolved shear stress of slip system s, $\dot{\gamma}_0$ is a reference strain rate and n the stress exponent (inverse of the strain-rate sensitivity). The critical resolved shear stress associated with each material point can potentially change according to a hardening or softening law (e.g.

Lebensohn et al., 2008). This was not considered in this study, where all critical resolved shear stresses are kept constant during simulations.

After each time increment Δt, the microstructure is updated using an explicit scheme. The new position of a point $\mathbf{x}$ of the Fourier grid is determined using the velocity fluctuation term $\tilde{v}_i(\mathbf{x})$ arising from the heterogeneity field as

$$X_i(\mathbf{x}) = x_i^0 + (\dot{E}_{ij}x_j^0 + \tilde{v}_i(\mathbf{x})) \times \Delta t \tag{2.3}$$

where $(\dot{E}_{ij})$ is the macroscopic strain rate. The rotation-rate of the crystal lattice $\dot{\omega}_{ij}^p(\mathbf{x})$ is given by,

$$-\dot{\omega}_{ij}^p(\mathbf{x}) = \sum_{s=1}^{N_s} \alpha_{ij}^s(\mathbf{x})\dot{\gamma}^s(\mathbf{x}) \tag{2.4}$$

where $\alpha_{ij}^s(\mathbf{x})$ is the antisymmetric Schmid tensor.

An estimate of the dislocation-density field can be found using the strain gradient plasticity theory (e.g., Fleck and Hutchinson, 1997; Wen et al., 2005, Gudmundson, 2004), based on Ashby's concept of geometrically necessary dislocations (GND; Ashby, 1970). Following this approach, GND are dislocations required to maintain strain compatibility across the material. The presence of GND (ρ) produces a strain energy storage associated with lattice distortion that, according to Ashby (1970), is related to the absolute value of the effective plastic strain gradient (e.g. Brinckmann et al., 2006; Estrin and Kim, 2007)

$$\rho = \frac{\eta^p}{b} \tag{2.5}$$

where b is the magnitude of the Burgers vector and η^p is the effective plastic strain gradient derived by Gao et al. (1999) as

$$\eta^p = \sqrt{\frac{1}{4}\eta_{ijk}^p \eta_{ijk}^p} \tag{2.6}$$

and

$$\eta_{ijk}^p = \varepsilon_{ik,j} + \varepsilon_{jk,i} + \varepsilon_{ij,k} \tag{2.7}$$

where $\varepsilon_{ik,j}$ indicates the partial derivatives of the plastic strain tensor with respect to the reference coordinates. Although other, higher order approaches to calculate the dislocation densities resulting from the activity of each slip systems are possible (see e.g. Ma et al., 2006; Roters et al., 2010), or the Nye's dislocation density tensor can be used (e.g., Nye, 1953; Ashby, 1970; Kröner, 1962), we simplify our approach by assuming a constant Burgers vector for all systems and, therefore, dislocations arising from basal and non-basal slip systems are not differentiated.

2.2.2   Recrystallisation – ELLE

The numerical platform ELLE was used in this study to simulate the recrystallisation processes. The modular programming of ELLE provides a highly versatile data transfer and allows coupling between various processes that affect a microstructure (Jessell et al., 2001a; Bons et al., 2008; Piazolo et al., 2010). ELLE has been used to simulate a variety of microstructural processes, including dynamic recrystallisation (Piazolo et al., 2002, Montagnat et al., 2013), grain growth (Jessell et al., 2001b, Jessell et al., 2003, Roessiger et al., 2011), strain localisation (Jessell et al., 2005; Griera et al., 2011), porphyroclast rotation (Griera et al., 2013), deformation of two phase materials (Jessell et al., 2009) and folding (Llorens et al., 2013a; Llorens et al., 2013b).

In this study, grain boundary migration and recovery processes are used in order to simulate the microstructural evolution by recrystallisation. Grain boundary migration covers the motion or displacement of high-angle boundaries (HAGB), whereby lattice distortions in swept regions are restored. Recovery is the decrease in intracrystalline heterogeneities by means of local rotation of the lattice without motion of high angle grain boundaries.

2.2.2.1. Grain boundary migration

The model aims to simulate grain boundary migration that is driven by reduction of the grain boundary energy and stored strain energy resulting from lattice distortions (i.e. dislocation density). For a single-phase, polycrystalline aggregate, the velocity of a grain boundary is expressed by

$$\overrightarrow{v} = M \Delta f \overrightarrow{n} \tag{2.8}$$

where M corresponds to the boundary mobility, Δ_f to the driving stress (force divided by grain-boundary area it acts on), and $\overrightarrow{n}$ to the unit vector normal to the boundary in the direction of movement. The grain boundary mobility is highly dependent on temperature and can be expressed using an Arrhenius or exponential equation

$$M = M_0 exp^{(-Q/RT)} \tag{2.9}$$

where M_0 is the intrinsic mobility, Q is the boundary-diffusion activation energy, R is the universal gas constant (e.g. Gottstein and Mecking, 1985). The driving stress Δ_f is defined as

$$\Delta f = \Delta H - \frac{2\gamma_s}{r} \tag{2.10}$$

where ΔH corresponds to the difference in stored strain energy density across the grain boundary, γ_s to the boundary energy and r to the local radius of curvature of the grain

boundary. The stored energy ΔH is calculated using the difference in dislocation density $\Delta \rho$ across a grain boundary and the energy of a dislocation per unit length E_ρ (Cottrell, 1953; Karato, 2008)

$$\Delta H = \sum_{s=1}^{N_s} (\Delta_\rho E_\rho)_s = \sum_{s=1}^{N_s} \left(\rho \frac{Gb^2}{4\pi P} \log \frac{R_e}{b_0} \right)_s \sim \Delta \rho G b^2 \tag{2.11}$$

where G is the shear modulus, P is a constant that depends on dislocation type and Poisson's ratio, b_0 is the radius of the dislocation core, R_e is the upper limit for integration of the distance from the dislocation line. As the dislocation density for each slip system is unknown, we made the assumption that the elastic energy is isotropic and equation 2.11 can be approximated to $\Delta H \sim \Delta \rho G b^2$.

Grain boundary migration is simulated using a front-tracking approach based on the algorithm by Becker et al. (2008) and recently used by Roessiger et al. (2012) to simulate grain growth of ice with air bubbles. In this algorithm the motion of boundaries is driven by minimisation of the Gibbs free energy, according to equation 2.10. Each time increment, each *bnode* is moved over a small distance assuming that the velocity does not change during the small time increment. In order to predict the direction and magnitude of the *bnode* displacement, four orthogonal trial positions at very small distance to the current node position are chosen. The change of total energy (E_j) for each trial position is due to (1) the change in total boundary length, and therefore the change of total boundary energy, and (2) the decrease of dislocation density due to the removal of all dislocations in the swept area,

$$E_j = A_j \bar{\rho}_J E_\rho - \gamma \sum_{i=1}^{N} l_i \tag{2.12}$$

where A_j, $\bar{\rho}_J$ and l_i correspond to the swept area, to the average dislocation density of the swept area and the length of the boundary segments due to the j-th trial position, respectively. N is the number of segments (two or three) that connect at the node under consideration. From the four E_j values, the spatial gradient in free energy can be calculated using a central finite difference approach. The direction of *bnode* displacement is thus determined by the direction of maximum energy reduction. Then, the velocity of a boundary is calculated using equation 2.8 assuming that the rate of energy dissipation is equal to the sum of the rates of work done by each individual boundary segment linked to the moving node. A more detailed description of this node movement algorithm can be found in Becker et al. (2008) and Bons et al. (2008).

During each time step, *bnodes* are sequentially moved in randomised order. The movement is calculated and applied immediately for each individual *bnode*. After each displacement, the topology of the grain network is examined and modified as needed. When a boundary sweeps across a *unode*, the local information stored in this material

point is updated with the following rules: (1) its dislocation density value is set to zero and (2) its lattice orientation is reassigned to that of the nearest *unode* in the grain it now belongs to (Fig. 2.2).
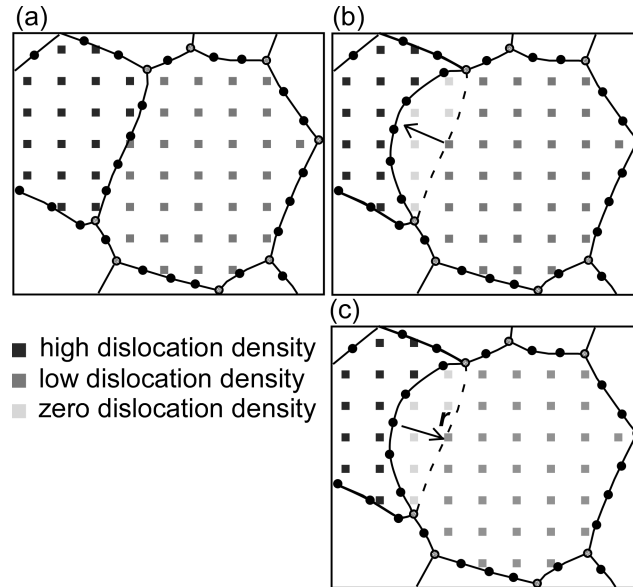
Figure 2.2: (a) Example of the simulation of grain boundary migration using two neighbouring grains with different dislocation densities, stored in the unconnected nodes (squares). (b) The difference in dislocation density drives the grain boundary into the grain with the highest dislocation density. The dislocation density in swept nodes is set to zero. (c) Surface energy strives to reduce grain boundary length, which is achieved by moving the boundary in the direction r towards the centre of curvature. Actual movement in one calculation step are much smaller, less than 1% of the distance between boundary nodes.

2.2.2.2. Recovery

In this study, the term recovery refers to intragranular reduction of the stored energy in a deformed crystal by annihilation of distributed dislocations and their rearrangement into lower-energy configurations in the form of regular arrays or low-angle subgrain boundaries, i.e. polygonisation (Sellars, 1978; McQueen and Evangelista, 1988; Urai et al., 1986; Borthwick et al, 2013; Faria et al., 2014b). To simulate this numerically, the approach by Borthwick et al. (2013) is implemented in the ELLE modelling platform. The numerical approach was validated using results from intracrystalline evolution during annealing experiments of deformed salt single crystals (Borthwick and Piazolo, 2010; Borthwick et al., 2013). Briefly, the model assumes that the rotation rate of a crystallite/subgrain is proportional to the torque (Q') generated by the change of surface energy associated with the reduction in misorientation (e.g. Li, 1962; Erb and Gleiter, 1979; Randle, 1993). Analogous to grain boundaries, where the velocity is proportional to a driving force, a linear relationship between the angular velocity ω and a driving torque Q' is assumed

$$\omega = M'Q' \tag{2.13}$$

where M' is the rotational mobility (Moldovan et al., 2002). Considering a 2D microstructure, the torque acting on a subgrain delimited by sb subgrain boundaries is given by

$$Q' = \sum_{sb} l_{sb} d\gamma_{sb}/d\theta_{sb} \tag{2.14}$$

where l_{sb} denotes the boundary length with grain boundary energy γ_{sb} and misorientation angle θ_{sb} across the boundary between the reference subgrain and a neighbouring subgrain sb. For low-angle boundaries, the boundary energy as a function of misorientation angle is calculated with the Read-Shockley equation (Read and Shockley, 1950). For this misorientation angle, the equivalent rotations by crystal symmetry are considered in order to obtain the minimum misorientation θ between two crystallite/subgrains.

Note that Equation 2.14 assumes that the torque is calculated with respect to an axis through the centre of mass of the subgrain. If grain rotation is assumed as a viscous process and it is accommodated by either cooperative motion/rearrangement of dislocations in the boundary (Li, 1962) and/or by boundary and lattice diffusion (Moldovan et al., 2001, 2002), M' can be expressed as:

$$M' = D_{gb}\frac{\delta\Omega}{KT}\frac{1}{d^p} \tag{2.15}$$

where D_{gb} is the grain boundary self-diffusion, δ the diffusion width of (sub-)grain boundary, Ω is the atomic volume, K the Boltzmann's constant, T is the temperature and d is the (sub-)grain-size. The exponent p varies according to the assumed accommodation process. Results from atomistic simulations and phase-field models by Upmanyu et al. (2002) indicated a value of exponent $p = 3$. The assumption of crystallite geometry as columnar with unit column height includes a geometric factor that raises p to 5. For a temperature of 243 K, the rotational mobility M' is $5.5 \cdot 10^{-7}$ Pa^{-1} s^{-1} m^{-2} (please see list of values in Table 2.1).

Recovery is implemented in ELLE using the unconnected nodes layer and assuming that each *unode* is a potential subgrain. As previously indicated, the goal of this routine is to reduce the intracrystalline heterogeneities by means of local rotation of the crystal lattice at each *unode* resulting in a decrease of the local misorientation, development of areas of homogeneous lattice orientations and the evolution of subgrain boundaries (Borthwick et al, 2013). Briefly, the process follows the same philosophy as for grain boundary migration. However, instead of using trial positions, trial rotations of the lattice are now used. The algorithm starts by choosing a random *unode* and finding the neighbouring unodes that belong to the same grain. Then, the average misorientation ($\tilde{\theta}_i$) and boundary energy ($\tilde{\gamma}_i$) between the reference *unode i* and the neighbour *unodes j* are calculated:

$$\tilde{\theta}_i = \sum_{j=1}^{N} \theta_{ij}, \tilde{\gamma}_i = \sum_{j=1}^{N} \frac{\gamma(\theta_{ij})}{N} \tag{2.16}$$

where θ_{ij} is the minimum misorientation angle after taking the symmetry operators into account.

A number of potential rotation axes are initially selected according to the potential specific active slip-system during deformation. During the routine, the predefined crystallographic axes are selected sequentially and a very small angle of rotation is carried out. Then, the new $\tilde{\gamma}_i$ is calculated and compared with the initial energy: The crystal orientation of the reference *unode* is rotated towards the value that results in the maximum reduction in energy. If all trials result in an increase in the energy of the neighbourhood, the crystal orientation at the datum point is left unchanged. A difference to the original Borthwick et al. (2013) approach where a constant rotation rate is applied independently of the torque component, here the rotation rate is calculated using the torque as a driving force according to equation 2.13. To simplify the routine, the boundary length of all data points is considered to be equal. This procedure is repeated for each *unode* in a random order.

Finally dislocation density in the model is updated as a change of misorientation angle implies a modification of them following a proportional relationship between both variables.

2.2.3 Program flow and coupling the viscoplastic FFT code and ELLE

A resolution of 256 x 256 Fourier points (*unodes*) is used to map lattice orientations, resulting in a unit cell defined by 65,536 discrete nodes. Each *unode* represents a small area or crystallite with a certain lattice orientation and dislocation density. The lattice orientation is defined by three Euler angles. The FFT module uses these *unodes*, not the grain-boundary network. The data structure of ELLE is fully periodic wrapping: grains touching one side of the model continue on the other size. This feature not only reduces boundary effects, but is a requirement for the FFT code. The shape of grains changes by changing the position of *bnodes*, either according to the velocity field (deformation) or by grain boundary migration. Distances between nodes are kept between $5.5 \cdot 10^{-3}$ and $2.5 \cdot 10^{-3}$ the unit distance, by removing double nodes when their neighbours are too close or adding double nodes when two nodes are too far apart. When two triple nodes approach each other within a distance of $2.5 \cdot 10^{-3}$, a neighbour switch is carried out. Small two- or three-sided grains are removed when they are defined by triple nodes only and their distance become less than $2.5 \cdot 10^{-3}$ the unit distance.

In ELLE, each process is simulated with a separate module that acts on the data structure (Jessell et al., 2001a). Each process is activated sequentially in a loop that represents a small time increment (Δt). The optimal Δt depends on the process. To avoid using a small Δt, required by one process, for a computationally expensive process that

allows a larger Δt, processes may be called a different number of times within each loop. An experimental run consists (Fig. 2.3) of iterative applications of small increments of 2% of shortening of vertical coaxial compression by viscoplastic deformation (FFT), followed by grain boundary migration and recovery. To avoid large steps during simulation of recrystallisation, grain boundary migration and recovery were simulated using a sub-loop where both processes are combined using small time increments ($\Delta t/5$). This methodology avoids the influence of order in running the recrystallisation processes and increases the stability of the numerical solution. Each coupled simulation of deformation and recrystallisation begins with a viscoplastic deformation step (FFT numerical convergence).

Each simulation of coupled deformation and recrystallisation begins with a viscoplastic deformation step. After numerical convergence of the viscoplastic FFT, the new position of Fourier points are updated using the equation 2.17. As Fourier points and unconnected nodes (*unodes*) in ELLE are equivalent, the position and material properties (i.e. Euler angles, dislocation density) of *unodes* are directly updated. During transfer information between programs, we assumed that the micromechanical fields are constant during the incremental step. Based on the velocity field, the new locations of boundary nodes (*bnodes*) are calculated using a linear inverse weighted interpolation,

$$x_i^{t+\Delta t} = x_i^t + \Delta t \sum_{i=1}^{n} \frac{\sum_{i=1}^{n} d(x_i - x_j)}{d(x_i - x_j)} \nu_j \tag{2.17}$$

where only the velocity ν_j from *unodes* located at a distance $d(x_i\text{-}x_j)$ below a threshold is taken account. After an increment of deformation, the unconnected nodes no longer defines a regular grid and a new regular mesh of Fourier points is required in order to run the next step. A particle-in-cell approach is used to remap all properties from current configuration to a new regular Fourier grid. In order to avoid unrealistic lattice orientations, Euler angles of new Fourier nodes are not interpolated and they are defined using the lattice orientation of the nearest unode that belongs to the same grain. For the case of viscoplastic materials, as simulated here, the constitutive relations are defined by means of quantities defined in the current configuration only and the approach allows us to run numerical simulation up to high strains. The approach was verified by Griera et al (2011; 2013) using Eshelby's problem (Eshelby, 1957; 1959) of deformation of a hard inclusion in a softer matrix.
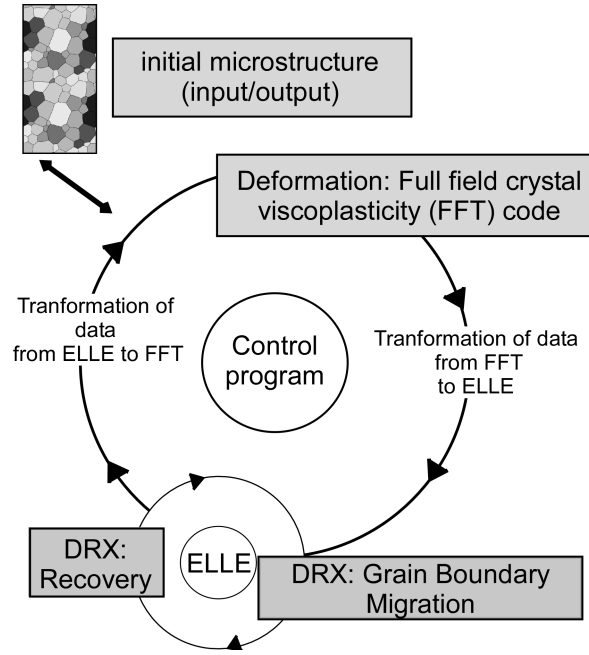
Figure 2.3: Schematic program flow. The initial microstructure is subjected to a closed loop of two alternating processes or modules: viscoplastic deformation (FFT) and dynamic recrystallisation (*DRX*). The *DRX* step itself consists of a number of alternating grain boundary migration (*GBM*), and recovery calculations.

Table 2.1: Explanation of symbols used in the text. Values used in the current models are given in brackets.

Symbol	Explanation
A	Ratio of critical resolved shear stress for basal vs non-basal slip systems [20]
A_k	Area of a grain k [m^2]
$a^{(2)}$	Second order orientation tensor
$a_1^{(2)}$, $a_2^{(2)}$, $a_3^{(2)}$	Eigenvalues associated to the base vectors of R^{sym}
α^s	Anti-symmetric Schmid tensor
b	Magnitude of Burgers vector [m]
b_0	Radius of the dislocation core [m]
c^k	Crystal orientation for a crystal k
d	Subgrain-crystallite size [$3.91 \cdot 10^{-4}$ m]
D_{gb}	Grain boundary self-diffusion [$5 \cdot 10^{-8}$ m^2 s^{-1} at 243K]
δ	Diffusion width of subgrain boundary [$9 \cdot 10^{-10}$ m]
E	Youngs modulus [$9{\cdot}10^9$ Pa]
$(\dot{E}_{ij})$	Symmetric strain rate
E	Energy of a dislocation per unit length [Jm^{-3}]
e_1, e_2, e_3	Eigenvectors corresponded to a$_1^{(2)}$, a$_2^{(2)}$, a$_3^{(2)}$
$\dot{\varepsilon}$	Strain rate [s^{-1}]

Continued on next page...

Table 2.1 – continued from previous page

Symbol	Explanation
f_k	Volume of a grain k [m3]
ϕ_0	Angle between c-axis and the unique stress axis
G	Shear modulus [$3 \cdot 10^9$ Pa]
γ_s	Grain boundary surface energy [0.065 J m^{-2}; Ketcham and Hobbs, 1969]
γ	Shear strain
$\dot{\gamma}^s$	Shear-rate [s^{-1}]
$\dot{\gamma}_0$	Reference strain rate [s^{-1}]
$\tilde{\gamma}_i$	Average boundary energy [Jm^{-2}]
H	Stored strain energy
$h^{ss'}$	Hardening matrix
η^p	Effective plastic strain gradient [m^{-1}]
φ_k	Longitude of c^k [rad]
K	Boltzmann's constant [$1.38 \cdot 10^{-23}$ JK^{-1}]
k	Growth rate [mm/year]
l	Length of boundary segment [m]
M_0	Intrinsic mobility [$1 \cdot 10^{-10}$ m^{2}kg^{-1}s^{-1}; Nasello et al., 2005]
M	Grain boundary mobility [m^{2}kg^{-1}s^{-1}]
M'	Rotational mobility [$5.5 \cdot 10^{-7}$ Pa^{-1}s^{-1}m^{-2}]
m^s	Symmetric Schmid tensor
μ	Dislocation energy constant [0.35; Mohammed and Bacroix, 2000]
N_s	Number of slip systems
N_g	Total number of non-intersecting crystals in A_k
N_p	Total number of *unodes* in A_k
n	Stress sensitivity [n=3, Glen 1958]
Q	Thermal activation energy [40 KJ mol^{-1}; Thorsteinsson, 2002]
Q'	Driving torque [J rad]
θ	Misorientation angle [rad]
θ_k	Tilt angle of a c^k [rad]
$\tilde{\theta}_i$	Average misorientation [rad]
R	Universal gas constant [J mol^{-1}K^{-1}]
R^{sym}	Principal crystal orientation reference frame
RS	Reference system
r	Local radius of curvature [m]
ρ	Dislocation density [m^{-2}]

Table 2.1 – continued from previous page

Symbol	Explanation
s	Slip system
sb	Subgrain boundary
S_g	Schmid factor
σ	Deviatoric stress [Pa]
σ_{ij}	Stress tensors [MPa]
T	Temperature [K]
t	Time [s]
τ^s	Critical resolved shear stress [Pa]
ω	Angular velocity [rad s^{-1}]
Ω	Atomic volume [$3.27 \cdot 10^{-29}$ m^{3}mol^{-1}]

2.2.4   Experimental setup

The 20x10 cm^2 initial microstructure with 3264 grains, each with an initially homogeneous, random lattice orientation (Fig. 2.1c), was deformed up to 70% of shortening in plane-strain pure shear. Dislocation glide of ice single-crystal was defined by slip on the basal plane {0001}{11-20}, prismatic plane {1-100}{11-20} an the pyramidal systems {11-22}{11-2-3}. This approach is similar than used by other authors. In the simulations, the ratio of critical resolved shear stress for non-basal versus basal slip systems was set to A=20. This value, less than the A=60-100 known for *Ih* ice was chosen as a compromise between calculation time (dependent on A) and accuracy of the simulations. Tests showed that the effect of increasing A diminishes strongly for A>10. A constant stress exponent of n=3 was set for all slip systems. Grain boundary properties were assumed isotropic, i.e. independent of the lattice orientation of the adjacent grains.

The FFT calculation is numerically the most expensive of all. Each deformation step was thus kept at a constant strain increment during calculation. Different strain rates were achieved by varying the number of steps, each equal to 20 years, in the recrystallisation loop, giving strain rates from $1.27 \cdot 10^{-12}$ to $3.17 \cdot 10^{-11}$ s^{-1} for 1 to 25 *DRX* steps per numerical time step, respectively (Table 2.2). One simulation (Experiment 0) with no *DRX* is included for reference.

2.2.5   Postprocessing

Crystallographic preferred orientation data are presented as pole figures. Furthermore, LPO data were plotted in inverse pole figures, where the sample x, y and z directions of

Experiment name	DRX/FFT ratio	Initial average grain area [mm²]	Final average grain area [mm²]	Final number of grains	strain rate [s⁻¹]
Experiment 0	0	6.12	6.02	3321	-
Experiment 1	1	6.12	10.26	1949	$3.17 \cdot 10^{-11}$
Experiment 10	10	6.12	54.80	365	$3.17 \cdot 10^{-12}$
Experiment 25	25	6.12	137.94	145	$1.27 \cdot 10^{-12}$

Table 2.2: Numerical experiment setup

are projected with respect to the crystallographic directions. These data were plotted using the texture analysis software MTEX (http://mtex.googlecode.com) (Bachmann et al., 2010; Mainprice et al., 2011) from the orientation distribution function (ODF).

The c-axis orientation of the crystal-axis orientation c^k can be determined by two angles: the colatitude or tilt angle θ_k, and the longitude or azimuth φ_k, both in a range [0-2 π], considering a reference system RS where the third axis is perpendicular to the xy plane. c^k can expressed as (Durand et al., 2006):

$$c^k = (\cos \varphi_k \sin \varphi_k, \quad \sin \varphi_k \sin \varphi_k, \quad \cos \varphi_k) \tag{2.18}$$

The second-order orientation tensor $a^{(2)}$ was used to characterise the c-axis orientation distribution. Following Woodcock, 1977, $a^{(2)}$ is defined as:

$$a^{(2)} = \sum_{k=1}^{N_g} f_k c^k \otimes c^k \tag{2.19}$$

where f_k is the volume of a grain k from a 2D section, that is proportional to its measured cross-sectional area A_k and the areas of containing non-intersecting crystals N_g (Gagliardini et al., 2004). For these simulations, we assumed that this volume is proportional to the total number of unodes N_p over which the c^k is obtained:

$$a^{(2)} = \frac{1}{N_p} \sum_{k=1}^{N_p} c^k \otimes c^k \tag{2.20}$$

Assuming that $a^{(2)}$ is symmetric, there is a principal reference system R^{sym} in which the second order orientation tensor is diagonal. Then, we can define $a_i^{(2)}$ ($i = 1, 2, 3$) and e_i ($i = 1, 2, 3$) as the expression of the three eigenvalues and their corresponding eigenvectors, associated to the three base vectors of the R^{sym}. The eigenvectors give the axis direction of the ellipsoid that best fits the density distribution of the grain orientations.

In this study, ice crystal preferred orientation symmetry is expressed as the proportion of point, girdle and random components of the [0001] crystallographic axis (Zaffarana et al., 2014). These fabric-type indices were calculated from the three eigenvalues ($a_1^{(2)}$, $a_2^{(2)}$, $a_3^{(2)}$) as P = $a_1^{(2)}$ - $a_3^{(2)}$, G =$2a_2^{(2)}$ - $2a_3^{(2)}$, and R = $3a_3^{(2)}$ (Vollmer, 1990).

2.3 Results

2.3.1 Experiment 0: viscoplastic deformation without recrystallisation

The initial microstructure underwent viscoplastic deformation without dynamic recrystallisation. The resulting microstructure has irregular grains, elongated parallel to the stretching direction (i.e. sample y direction). The deformation is localised into conjugate high-strain bands of strongly elongated grains, with an aspect ratio of approximately 15:1, surrounded by low-strain areas or "microlithons" (Passchier and Trouw, 2005), where grains are moderately elongated (aspect ratio in the order of 5:1) (Fig. 2.5a). Due to the high difference of CRSS of basal versus non-basal slip systems in ice, the ability to deform of a grain depends on the angle ϕ_0 between the c-axis and the tensile stress axis, expressed by the Schmid factor S_g (Azuma and Higashi, 1985)

$$S_g = \cos \phi_0 \sin \phi_0 \qquad (2.21)$$

S_g is at a maximum when the c-axis is oriented at $\phi_0 = 45°$ (soft) and at a minimum when $\phi_0 = 0°$ or $90°$ (hard) with respect to the tensile axis. The high-strain bands affected soft grains with low resistance to the flow rate (S_g). In the absence of recrystallisation all grains are preserved throughout the experiment. Pinching of extremely stretched grains leads to a small increase of the number of grains and concomitant reduction in mean grain size (Table 2.2). Deformation produced intragranular kinkbands, and misorientation was increased in grain boundaries and triple junctions (Fig. 2.4a-b).

From an initially random c-axis distribution (Fig. 2.6a), LPO evolved into a cone distribution with an opening angle of 90° at 30% shortening (Fig. 2.6b). C-axes rotated towards the compression axis. The LPO further evolved into a strong single maximum pattern (Fig. 2.6c, cone opening angle about 60°). In general, the LPO evolves from a random to a point-maximum distribution, with a small girdle component (Fig. 2.7). Crystallographic orientations that deviate significantly from the point maximum are mostly found in low-strain regions (Fig. 2.5a).

2.3.2 Experiments 1, 10, 25: viscoplastic deformation with recrystallisation

Three different ratios between dynamic recrystallisation (grain boundary migration and recovery processes) and deformation were modelled (1, 10 or 25 steps of dynamic recrystallisation per deformation step), to observe the influence of recrystallisation on the structure evolution. The final grain boundary geometry was interlobate, with irregular lobate grain boundaries (Fig. 2.5b-d) as expected for high temperature deformation (Passchier and
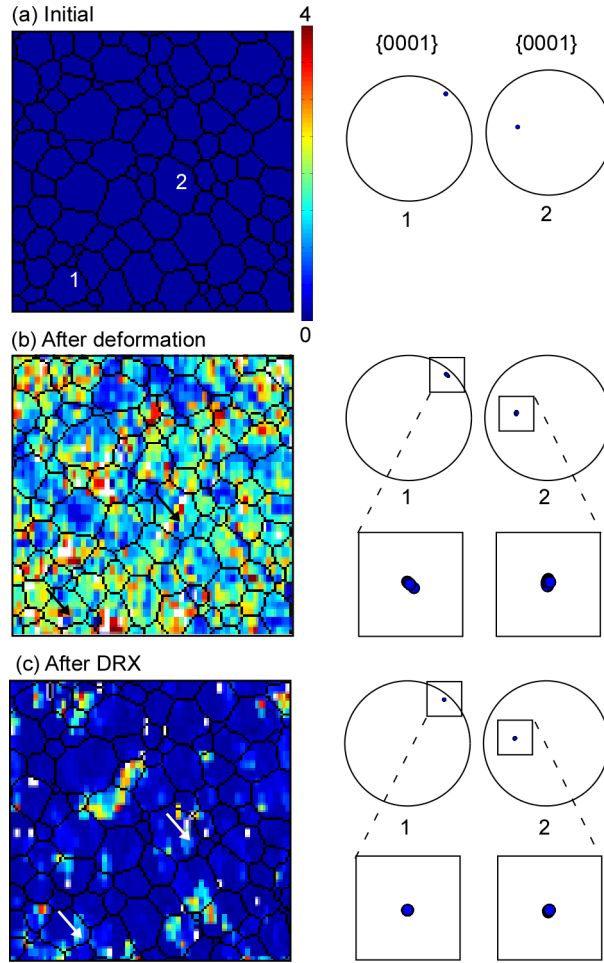
Figure 2.4: Kernel Average Misorientation (KAM) map for (a) initial, (b) after viscoplastic deformation and (c) after 25 steps of *DRX*, showing intragranular heterogeneities for grains 1 and 2. Right column shows the polar figures at the three steps of the simulation, shown as lower hemisphere stereographic projections. The KAM is defined as the average misorientation of a given *unode* with all of its neighbours *unodes*.

Trouw, 2005). The curved shapes of boundaries indicate the direction of *GBM* such that regions with high dislocation densities were swept away. Despite the amount of recrystallisation, grains remain elongated parallel to the stretching direction. The main differences caused by dynamic recrystallisation in comparison with Experiment 0 are: (1) larger grains, with smooth boundaries, and (2) a more equidimensional microstructure, (3) without localisation bands of strongly elongated grains (Fig. 2.5b-d).

The mean grain area increased, however not proportionally to the number of grain boundary migration steps (Table 2.2). The final mean grain area is 5.3 and 13.4 times larger in Experiment 10 and Experiment 25 compared to Experiment 1. For a linear increase in grain area with time as expected for *NGG* one could expect factors of 10 and 25. At 70% strain, 41% of the initial grains have disappeared in Experiment 1, and only the 11% and 5% of grains have survived in Experiment 10 and 25 (Table 2.2). The recovery process produced high-misorientation areas ($>15°$), resulting in the development of subgrains in Experiments 10 and 25 (Fig. 2.5g-h). With active *DRX*, the internal
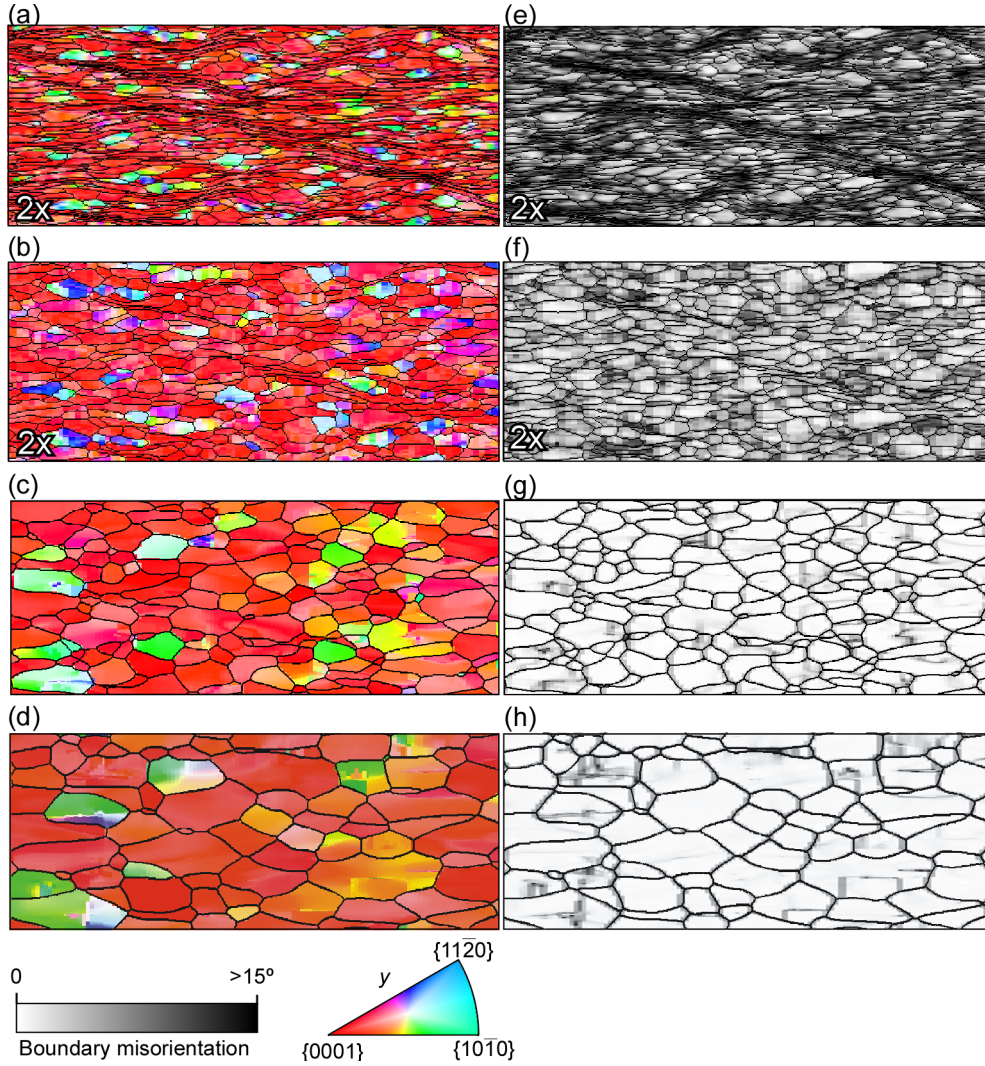
Figure 2.5: Grain network and c-axis orientation (a-b-c-d) and boundary misorientation (e-f-g-h) at 70% of shortening for simulations with (a, e) no recrystallisation, (b, f) 1 step, (c, g) 10 steps, and (d, h) 25 steps of recrystallisation per deformation step. The original size is double than the images shown. For better visibility images for Experiments 0 and 1 have been enlarged (2x). Crystal orientations are shown as shortening direction y in crystal reference frame (IPF).

boundary misorientation in general first increased, followed by a reduction when grains start to disappear (grey shading in Fig. 2.5f-h). Misorientation remained high at grain boundaries and triple junctions after *DRX* (Fig. 2.4c).

Although activation of recrystallisation causes a remarkable change in grain boundary microstructure, it does not significantly modify the development of a single maximum distribution of c-axes compared to Experiment 0 (Fig. 2.5b-d). The single-maximum c-axes LPO at low angles to the shortening direction (parallel to the compression axis) develops at medium strains (Fig. 2.6b), leading to a strong single maximum at 70% strains (Fig. 2.6c). With increasing *DRX* the c-axes maxima develop a small angle with respect to the shortening direction. Figure 2.7 shows that c-axes LPO evolves quicker than in the case of no *DRX* and first shows a point-to-girdle distribution, followed by a decreasing girdle component. The a-axes distribution shows a stronger effect of *DRX* with the development

of two sets of 3 distinct point maxima (3 axes <11-20> and 3 prism plane normal axes 10-10), distributed around a girdle in the yz-plane (Fig. 2.6d).
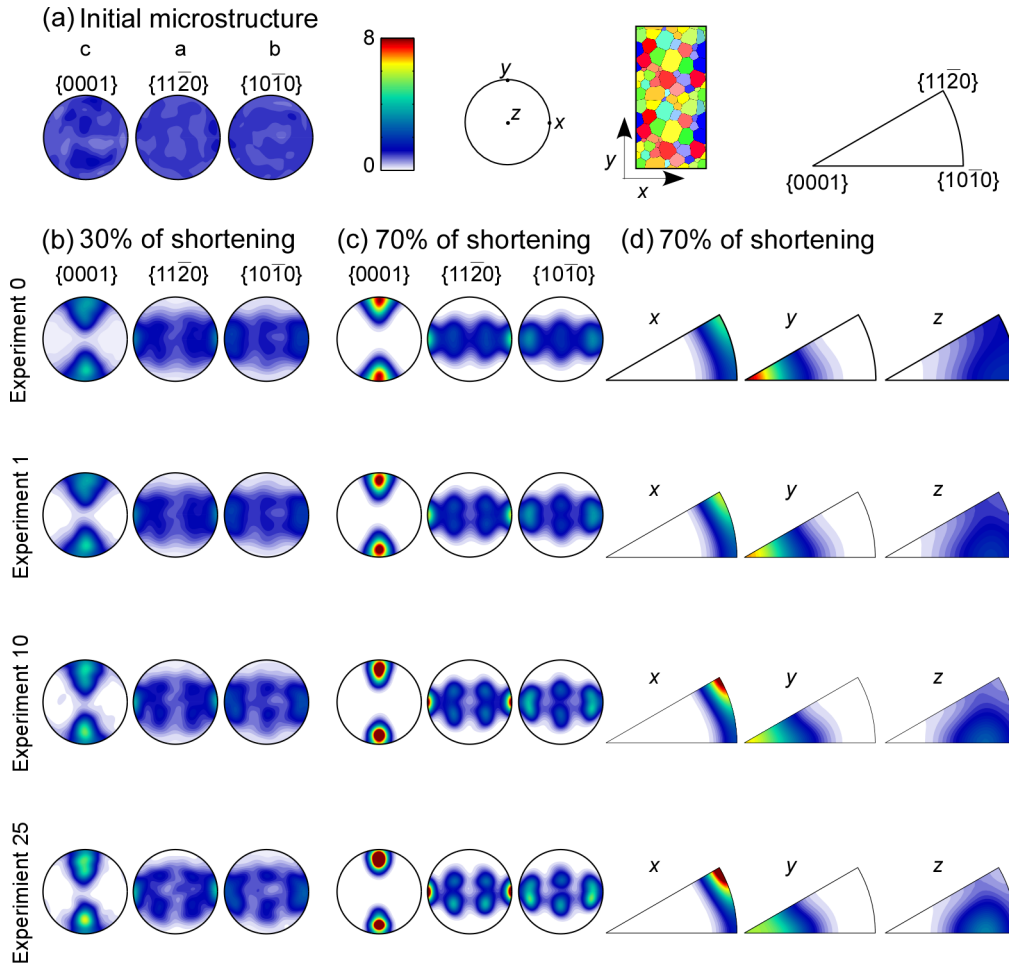
Figure 2.6: Pole figures of lattice preferred orientation (LPO) for all the simulations performed in this study, showing (a) the initial random distribution, (b) at 30% of shortening and (c) 70% of shortening. (d) shows the inverse polar figures of the x, y and z axis of the sample with respect to crystal orientations.

2.4 Discussion

We have applied a FFT formulation to model viscoplastic deformation by dislocation glide, together with grain boundary migration and recovery processes, in order to simulate the development of the microstructure and LPO in ice. Results of four experiments that represent deformation at different strain rates were compared. Our approach serves to predict the viscoplastic behaviour of an isotropic polycrystal on the microscopic scale.

2.4.1 Microstructure evolution

In Experiment 0 (only deformation) there is no grain growth, as *GBM* (static and dynamic) is not allowed and, therefore, all grains survive (Table 2.2). A slight increase on total
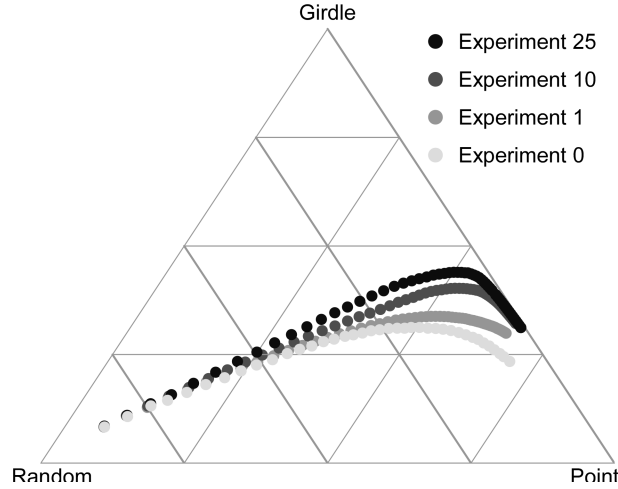
Figure 2.7: Ice LPO symmetry expressed as the proportion of single maximum, girdle and random components for the c-axes <0001>. Different grey values represent simulations with different amounts of dynamic recrystallisation: 0, 1, 10 and 25 grain boundary migration steps per deformation step.

number of grains is observed at the end of the experiment (Table 2.2) due to splitting by topological changes of the grain network during simulations. Grain growth is clearly observable in Experiments 1, 10 and 25, with the final grain size increasing with number of *DRX* steps (Fig. 2.8a). In all experiments the grain-growth rate initially follows that for normal grain growth (i.e. dominated by boundary energy) (k=0.04 mm^2/yr), followed by a stage of faster growth (Fig. 2.8c). This effect is stronger at a high strain rate (Experiment 1, k=0.08 mm^2/year) than at the lowest strain rate (Experiment 25, k=0.064 mm^2/year). The difference on the strain stored energy produces higher bulk effective mobilities with increasing the strain rate. The increase in grain- growth rate is caused by *GBM* driven by strain energy, which is strongest at high strain rates where recovery has less time to recover internal strains. It should, however, be borne in mind that grain size reduction by polygonisation is not fully implemented in the model.

The evolution of grain morphology depends on the ratio between deformation and *DRX*. Deformation without recrystallisation produces elongated grains, while *DRX* leads to larger and equidimensional grains. In Experiment 0 the average grain area remains constant during deformation, while aspect ratios of grains range from 5:1 in low-strain regions (or microlithons) to 15:1 in high-strain localisation bands (Fig. 2.8). These low values of grain's aspect ratio highly contrast with the theoretical aspect ratio of 11 at 70% of shortening, which thus cannot be due to the highly intrinsic anisotropy of the ice but due to extensive *DRX* and associated *GBM*.

Figure 2.8b shows the influence of the amount of *DRX* in the relationship between grain size and grain elongation. When *DRX* is activated, grain elongation is strongly reduced, even in Experiment 1 where the grain aspect ratio only reaches a value of <3 at 70% shortening (Figs. 2.5b, 2.8b). Shear localisation is difficult to discern in the
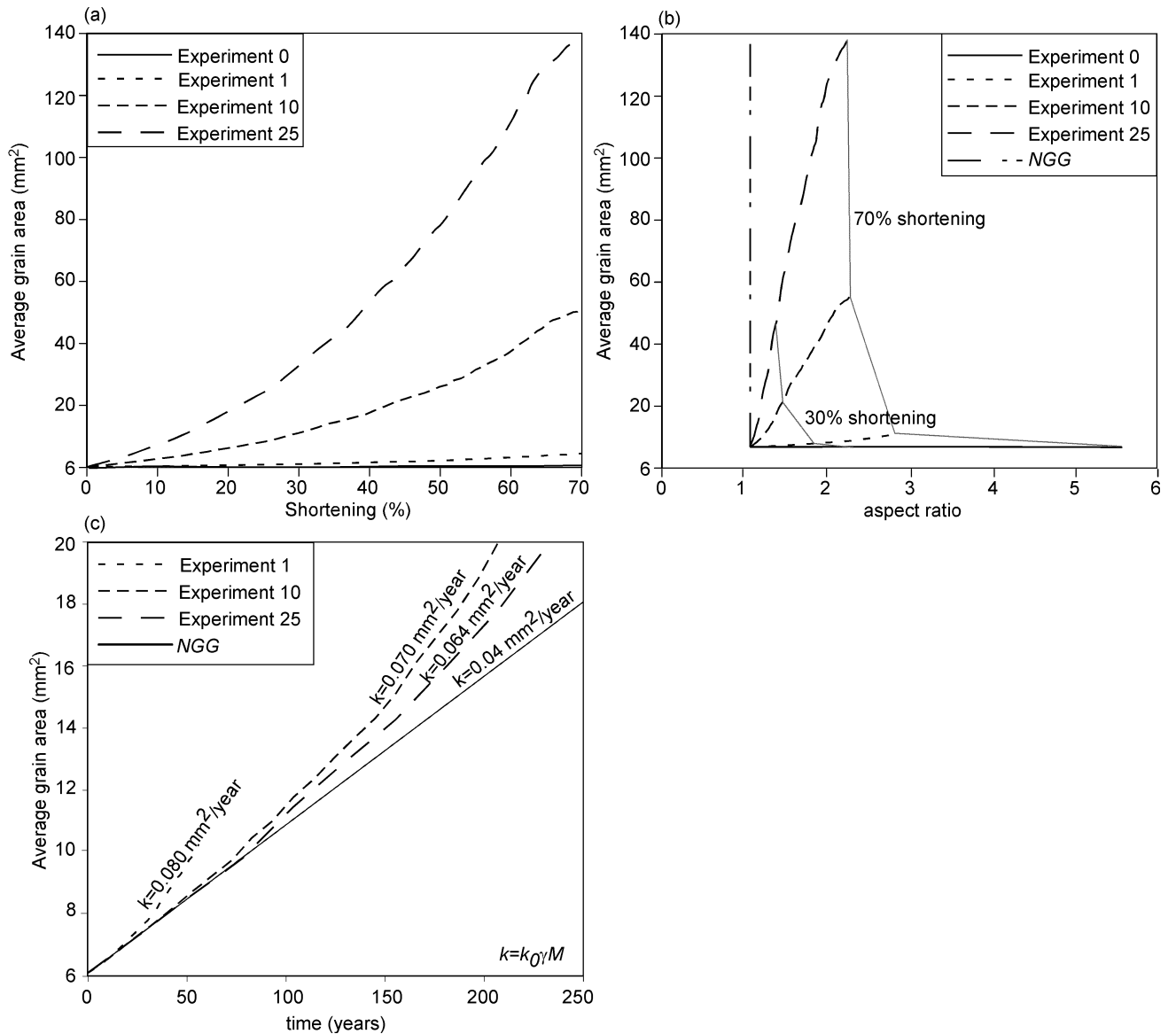
Figure 2.8: Average grain area evolution for all experiments with respect to the amount of shortening (a), and (b) aspect ratio evolution during deformation, showing in grey lines the vertical shortening. The average grain area increases with time, being the effective mobility higher in Experiment 1, than in Experiment 10 and 25, compared with the mobility for a normal grain growth experiment (*NGG*) (c). Only normal grain growth curve (*NGG* experiment) and only deformation curve (Experiment 0) are considered the two extreme cases.

microstructure in Experiment 1 and completely masked by *DRX* and associated *GBM* in the lower strain-rate experiments (Fig. 2.5c-d).

In pure ice, *GBM* inhibits the development of strong grain elongations at natural strain rates. Very elongated grains are only found in polar ice cores with a very high content of impurities, which reduces grain-boundary mobility. In the GRIP (central Greenland) and Vostok (east Antartica) ices cores, the aspect ratio of grains observed has an average value of about 1.35 (Thorsteinsson, 1995) and 1.5 (Lipenkov et al., 1989), respectively. Slightly higher values (avg. 1.8 to max. 2.2; unpublished data) were observed in the EDML core (Antarctica). This suggests that *DRX* in polar ice is at least as important as

in our Experiment 25.
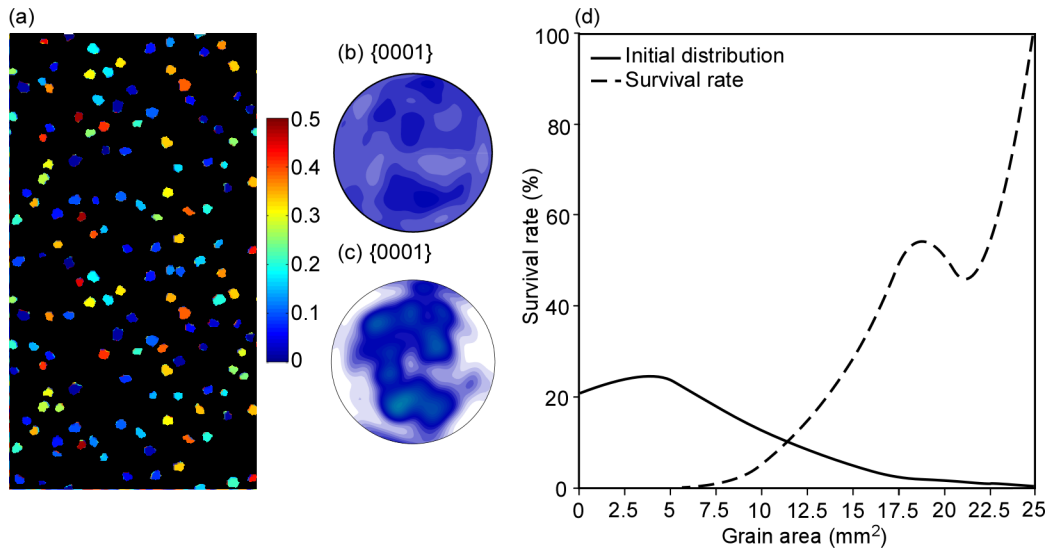
Figure 2.9: Initial grain boundary network for Experiment 25, showing the Schmid factor for grains that survive until the end of the experiment. Initial pole figures of (b) all grains, and (c) surviving grains. (d) Initial average grain area distribution and survival rate at the end of the Experiment 25. Larger grains have a higher probability to survive, while small grains disappear.

When intense *DRX* (experiments 10 and 25) is activated intragranular kink bands, developed by folding of the basal plane due to the highly anisotropy of ice crystal, disappear with increasing strain and grains tend to reduce the internal misorientation (Fig. 2.4). Therefore, *DRX* reduces the internal misorientation and sweeps away the kink bands produced by deformation. This observation contrast with experimental observations and previous predictions by numerical simulations where kink bands are preserved (Lebensohn et al., 2008; Montagnat et al., 2011; Piazolo et al., 2015), mainly due to the limited shortening and high strain rate of the experiments, or because *DRX* processes were not numerically simulated. In contrast, kink band structures are not observed in polar ice cores. A plausible simple explanation of this is that intragranular recovery relaxes these structures and/or evolves to develop subgrain boundaries.

Heterogeneous distribution of stored strain energy and differences in grain curvature are the driving forces to explain the dynamics of growth/shrinkage of grains during the simulations. A summary of surviving grains is shown in Table 2.2. The number of grains disappearing during deformation increases with increasing *DRX*, as a result of grain growth. In general, grains oriented with low Schmid factors (equation 2.21) (i.e. soft orientations) are expected to deform strongly and increase their internal stored strain energy (Thorsteinsson, 2002). Therefore, these soft grains are expected to be be overgrown by grains with high Schmid factors (i.e. hard orientations). In our experiments, the survival of grains seems to be only weakly dependent on their initial lattice orientation relative to the stress field (S_g): only grains oriented with their c-axes parallel to the *xy* plane have a slightly enhanced chance of disappearing than grains with other orientations (Fig. 2.9a-c).

The initial Schmid factor thus appears to play a minor role in the survival chances of grains possibly due to the heterogeneous strain distribution within the polycrystal which is consistent with findings by Thorsteinsson (2002). Initial grain size, however, is found to be a primary factor in determining grain-survival chances. As grain-boundary energy is a dominant driving force for *GBM*, grain survival probability is highly correlated with the initial grain size (Fig. 2.9d). This effect is observable in growth curves (Fig. 2.8c), where all the experiments follow the normal grain growth curve at the beginning of the simulations.

In terms of the numerical model, a larger grain size implies larger regions of homogeneous lattice orientation, and therefore, regions where incompatibilities of strain field are expected to be minimised. Therefore, deformation can be distributed more homogeneously without developing large strain gradients. In the other extreme, regions of small grains and/or high internal misorientation are associated with high strain gradients and, therefore, high values of stored strain energy. Although our models are limited because nucleation of new grains, and therefore grain size reduction, was not simulated, our observation can be used to interpret situations where grain coarsening is dominant (e.g. during initial grain coarsening in the upper levels of ice sheets).

2.4.2 LPO evolution

In all simulations the initially random c-axis orientation distribution of grains is destroyed, and c-axes rotate towards the maximum shortening direction (Fig. 2.5 and Fig. 2.6). This evolution has been observed before in laboratory experiments of Jacka and Maccagnan (1984), where ice samples deformed at -3°C in compression develop circle girdle fabrics around the compression axis (Castelnau et al., 1996). However, in experiments with a large number of recrystallisation steps (Experiments 10 and 25), the a-axes simultaneously rotate towards the maximum elongation axis. When *DRX* is activated the c-axes start to develop an angle with the *xy* plane (Fig. 2.6c-d). The influence of the amount of recrystallisation on the LPO evolution can be observed in figure 2.7, where the initial random c-axis orientation distribution is destroyed first, followed by the formation of a combined girdle- and single-maximum fabric and finally tending towards a single maximum pattern. The girdle fabric is most pronounced at a high number of *DRX* steps, where the random orientations are also destroyed earlier than in experiments with little or no *DRX*.

The FFT algorithm allows tracking of the relative activity of individual slip systems. Although the LPO development in the different experiments is qualitatively similar (Fig. 2.7), the amount of *DRX* causes significant differences in the relative activities of the slip systems (Fig. 2.10). Basal slip activity decreases with strain, compensated by non-basal slip (Fig. 12.10). *DRX* amplifies this behaviour up to maximum shortening of 70%. The highest amounts of *DRX* (Experiment 25) exhibit the extreme case: pyramidal slip

becomes the most important slip system at ca. 55% shortening. At higher strains this behaviour may be reverted at differing strain thresholds, indicated by changing inflection point of curves in Fig. 2.10.

The decrease of basal slip activity, and its replacement by pyramidal slip has been described before in simulations using a VPSC approach in uniaxial compression (Castelnau et al., 1996). However, the rise of pyramidal slip activity with more *DRX* does not significantly affect the final c-axis distribution, which is similar for all experiments, but instead produces an anisotropic distribution in a- and prism plane normal axes (<11-20> and <10-10>, Fig. 2.6). Such an anisotropic distribution of a-axes is difficult to observe in ice cores, as full crystal orientation measurements of statistically significant numbers of grains are not standard. In spite of these difficulties, it has been described in one ice core (Miyamoto et al., 2005): in the deep part of the GRIP ice core (with a strong single-maximum region of c axis). A significant concentration of a-axis is observed at certain depths. The anisotropy of slip along different crystallographic directions on the basal plane is proposed as a possible explanation (Miyamoto et al., 2005). Alternatively, the a-axes distribution could indicate a simple shear component to an overall compressional strain regime: a preferred glide direction in the basal plane will then cause alignment of a-axes along the simple shear direction perpendicular to the c-axes. However, as our simulations were performed in pure shear the first explanation proposed by Miyamoto et al. (2005) may hold: if a slip system on a prismatic or/and pyramidal plane is active, a-axes may be able to concentrate gradually with depth (Miyamoto et. al, 2005).

2.4.3 Stress evolution

Pure shear simulations are characterised by an initial strain hardening stage followed by a steady state at large strain (Fig. 2.11d). This hardening is associated with the alignment of c-axes close to the compression axis (Fig. 2.6 and 2.11). The plateau is reached at lower normalised equivalent stress (Duval et al., 1983) for experiments with more *DRX*, and is still not reached at 70% shortening in Experiment 1. With more *DRX* steps the strain hardening stage is contracted, so that simulations reach a steady state at 60% of shortening in Experiment 10 and 50% of shortening in Experiment 25. In Figure 2.11a-c the evolution of the stress tensors during deformation shows how σ_{xx} and σ_{yy} (extension and compression direction) evolve differently. At the beginning, the out-of-plane stress (σ_{zz}) is approximately zero. As the material hardens, this σ_{zz} increases in absolute magnitude to maintain plane strain deformation. If we assume that the macroscopic stress exponent can be calculated for the same amount of shortening for simulations at different strain rates, in order to compare material of similar states (e.g. similar anisotropy), we can observe an increase of the stress exponent during deformation (Fig. 2.11e). The exponent increases from the initial *n*=3, imposed by the exponent used in the constitutive equation
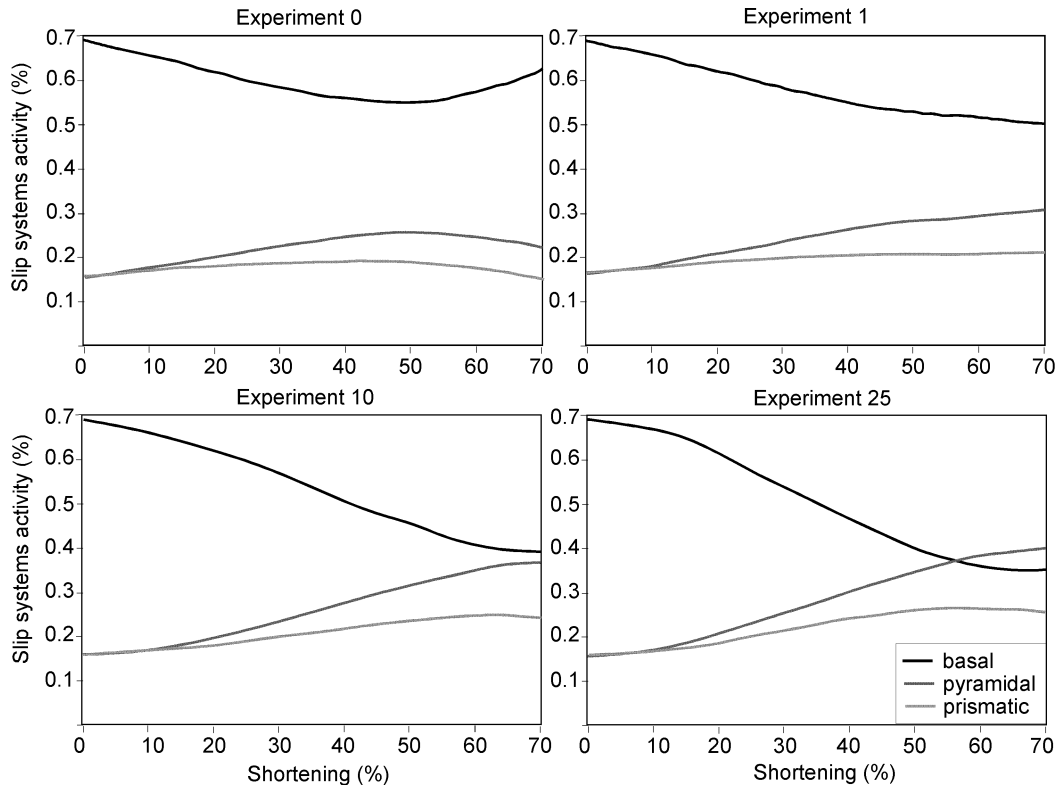
Figure 2.10: Relative activity of basal and non-basal slip systems during deformation for all the simulations.

for the individual slip systems (Equation 2.2) to ~3.5 at the end of the experiments. An explanation for this increase of the bulk stress exponent is the *DRX*-dependent activation of the pyramidal slip system and ensuing strain hardening. It should be noted that the strain hardening is not caused by an imposed hardening law for slip on individual systems, but emerges owing to the development of an LPO, and possible a shape-preferred orientation (SPO) as well. An SPO with grains elongated perpendicular to the shortening direction has been shown to produce strain hardening (Takeda and Griera, 2006; Treagus and Lan, 2004).
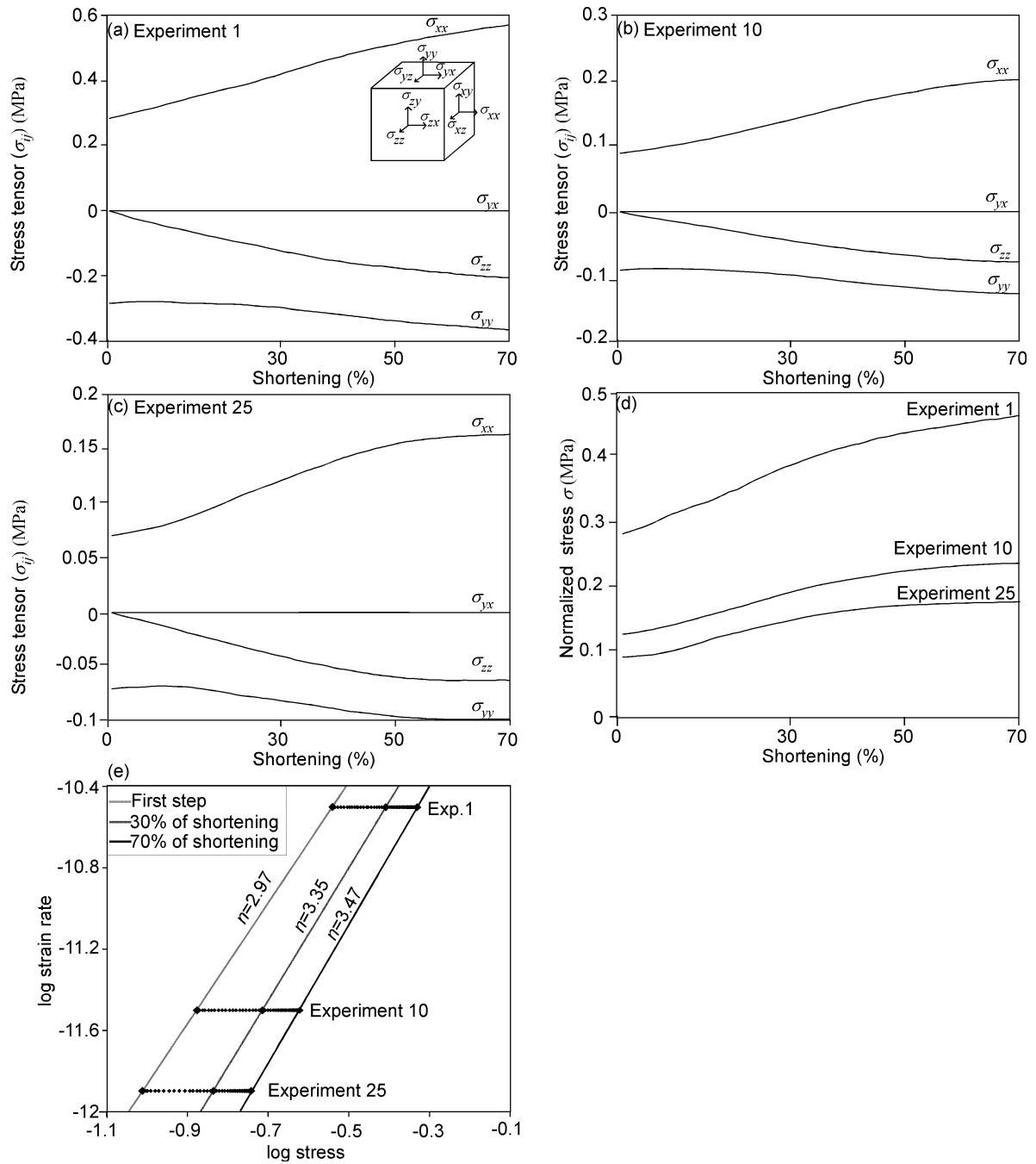
Figure 2.11: Stress tensors evolution during deformation for Experiments (a) 1, (b) 10 and (c) 25. Normalised equivalent stress vs bulk shortening for Experiments 1, 10 and 25 in (d). Equivalent stress in (d) has been normalised respect to the equivalent stress from Duval et al. (1983), assuming an average grain size of 1 mm, a temperature of -30°C and the correspondent strain rate for each experiment. Logarithmic relationship between strain rate and equivalent stress for all simulations performed with *DRX* in (b). The macroscopic stress exponent n resulting from the first step (i.e. 0.02%), 30% and 70% of shortening are indicated.

2.4.4 Limitations

In our simulations nucleation, in the sense of formation of new grain boundaries is not implemented yet, but has to be considered for natural ice (*RRX* and *SIBM-N)* (Faria et

al. 2014b). Due to the initial very fine microstructure, the expected behaviour during first stages of simulations is to a general coarsening and potentially new nucleated grains will have very small probability to survive by dominant control of grain boundary migration in the evolution of the microstructure. For Experiments 10 and 25, the size of the nucleated grains by *RXX* (Poirier, 1985; Alley, 1992) would be small (as observed by misorientations in Fig. 2.5g-h) compared to the average grain size, which increases very fast, being destroyed by the *GBM*, that mainly depends on grain size. As strain stored energy is not expected to be enough to balance the reduced grain size, probably most of the new grains will be overgrowth by fast motion of grain boundaries. In Experiment 1, nucleated grains have chances to survive, as grain size is increasing much during deformation, resulting in a grain size reduction. We can assume that the possibility to reach a grain-size steady state depends on the relative amounts of nucleation of new grains by splitting versus grain boundary migration (*RXX/SIBM*), as explained in Faria et al., 2014b. If creation of new grains is controlled by polygonisation polygonisation (i.e. progressive rotation of subgrains up to develop high misorientation boundaries), we should not expect an influence on LPO development, as new grains maintain very similar crystal orientations. However, grains nucleating spontaneously would be oriented at favourable positions, avoiding orientations with c-axes parallel to the *xy* plane. The steady state may be reached earlier with the *RX* suite, which can be tested implementing nucleation by *RRX*.

With nucleation, we should expect a softer behaviour. Laboratory creep deformation experiments showed a hardening process with a peak of strength at few % of strain, followed by a steady-state at 10-20%, in either uniaxial compression or simple shear experiments (Treverrow et al., 2012). Our results differ from this evolution, such that steady-state creep cannot yet be reached at 70% of shortening. Even though our simulations have been performed at constant strain rate and cannot be directly compared to models with 3 creep regimes, we can hypothesize that this difference could be caused by the nucleation effect on the microstructure, where a steady state is associated with an equilibrium grain size (Jacka and Li, 1994). Another hypothesis is that even more *GBM* by *DRX* results in a softer behaviour. Simulations may still underestimate amount of *GBM* to reach deformation and recrystallisation behaviour of real ice in experiment and nature at very high homologous temperature.

2.4.5 Implications on interpretation of natural polar ice microstructures

Experiment 0 is an end-member simulation, in the sense that ice being at high homologous temperatures (up to 1) on Earth will not deform without a significant contribution of recrystallisation. This experiment illustrates the effect of formation mechanisms of lattice preferred orientations in polycrystals of the highly anisotropic ice. Dislocation glide,

preferably along basal planes leads to continuous rotation of crystals towards the bulk compression axis. LPOs are typically most acknowledged microstructural feature in observations in ice cores and experiments (e.g. Rigsby, 1951, Thorsteinson et al., 1997, Wang et al., 2003, Azuma et al., 1999, DiPrinzio et al., 2005, Treverrow et al., 2012, Montagnat et al., 2014; more refs in Faria et al., 2014a). The strains reached in the simulations (up 70% shortening) nominally correspond to ice sheet depths down to roughly 1000m (e.g. Huybrechts et al., 2007). Faria et al., 2014c review that typically in these depth ranges evolution from random c-axes distributions to strong LPO becomes significant. Strength of this evolution is more slowly increasing with depth in most drilling locations however, which probably depends on the site-specific stress configurations, but also on the pervasive recrystallisation in ice on Earth. Another important reason for the evolution of strong LPO at lower strains in our simulations are the still missing *RX* processes nucleation (sponatnous and splitting). In Experiments 1, 10 and 25 we demonstrate the influence of *RX* on LPO: *GBM* does not modify the single maximum pattern of c-axes (Fig. 2.5b-d). LPO evolution is very similar in the only viscoplastic deformation case (Experiment 0) compared to simulations with active *DRX*. This is in accordance with the observations in ice cores that LPO is continuously developing with depth while other *RX* measures (grain shape, subgrain boundary density; Weikusat et al. 2009) do not change systematically with depth.

Despite the high anisotropy of ice, we do not observe *DRX*-induced LPO development (Urai et al., 1986, Karato, 1987, Jessell 1988a, 1988b). This could be expected when grains grow at the expense of grains with unfavourable orientations (Karato, 2008), related to the strong orientation dependence of dislocation densities resulting from the highly anisotropic behaviour of ice. In our models we observe deformation-induced LPO (Karato, 2008).

Recrystallisation is the cause for dynamic grain growth (*DGG*) in natural ice usually observed in ice cores if considering the same type of ice (e.g. "clean" interglacial ice) (e.g. Faria et al., 2014c). DGG being the grain growth process is reflected by the constant grain size (Fig. 2.8a-b) in Experiment 0 simulating purely viscoplastic deformation. Thus a general evaluation of Experiment 0 with respect to the general appearance of microstructures from natural polar ice emphasises the necessity to include recrystallisation processes to the deformation by dislocation glide. Particularly interesting is the question concerning the dominance or relative speed of deformation vs recrystallisation which was investigated in Experiments 1, 10 and 25. Grain growth occurs when *DRX* is activated. Although *DGG* increment is not proportional to the amount of *GBM*, grain size and grain elongation depend on the amount of *DRX* (Fig. 2.8b).

The *GBM* module includes static and dynamic driving forces, which calculates the motion of boundaries according to the local energy field calculated by the grain boundary curvature and the difference in dislocation density (stored strain energy) across the grain boundary. Previous authors already mentioned that a difference in strain between the

considered grains and bulk values is needed to model the LPO evolution in ice (van der Veen and Whillans, 1994), however the strictly local consideration of our simulations is necessary for a realistic *GBM* as grain boundaries do not "see" far into the neighbouring grain. This conclusion was derived from grain shape and subgrain boundary data in ice core microstructures (Weikusat et al. 2009) and creep deformation samples (Hamann et al. 2007). Applying this approach of local driving forces for *GBM* our simulations derive increasing grain growth with increasing amount of *RX*, which in principle confirms the concept of dynamic grain growth being able to describe ice grain size evolution (Faria et al. 2014b). All microstructural studies on polar ice cores so far report certain amounts of grain growth with depth thus time and deformation – at least as long as we observe similar types of ice (e.g. "clean" interglacial ice) (e.g. refs in Faria et al. 2014a). Most of these studies so far argue for "normal grain growth" as the only concept to describe grain size evolution in polar ice. Results shown here may indicate a misconception in the interpretations assuming only movement of GB due to curvature reduction being the cause for grain growth. However, nucleation and formation of new GB are not yet implemented into the suite of simulations presented here and will change the GS evolution again, of course. Our model is so far able to simulate grain size evolution in the grain growth field of the recrystallisation diagram of Faria et al., 2014b (below the attractor surface Dss).

2.5   Conclusions

Observations of microstructure and LPO evolution during numerical simulations at different strain rates have been presented which provide new information about influence of recrystallisation during deformation. *DRX* can significantly increase grain size, avoiding elongation of grains and masking the deformation and strain localisation. *DRX* does not modify the c-axes LPO evolution, which in all cases is oriented parallel to the shortening direction. However, in experiments at low strain rates, the a-axes rotate towards the maximum elongation axis simultaneously. The anisotropic distribution of a-axes is related to the increment of activity of non-basal slip systems. Although *GBM* is driven by stored strain and boundary energy reduction, the grains' survival probability is highly related to the initial grain size, and only slightly related to the crystal orientation with respect to the flow rate. Grain growth in experiments at high strain rate is faster than experiments performed at low strain rate, due to the stored strain energy.

2.6   References

- Alley RB (1988) Fabrics in polar ice sheets: development and prediction. Science, 240(4851), 493-495.

- Alley RB (1992) Flow-law hypotheses for ice-sheet modeling. Journal of Glaciology, 38(129), 245-256.

- Azuma N (1994) A flow law for anisotropic ice and its application to ice sheets. Earth and Planetary Science Letters, 128(3), 601-614.

- Azuma N, Higashi A (1985) Formation processes of ice fabric pattern in ice sheets. Annals of Glaciology, 6, 130 - 134.

- Azuma N, Wang Y, Mori K, Narita H, Hondoh T, Shoji H and Watanabe O (1999) Textures and fabrics in theDomeF (Antarctica) ice core. Ann. Glaciol. 29,163e168.

- Azuma N, Miyakoshi T, Yokoyama S and Takata M (2012) Impeding effect of air bubbles on normal grain growth of ice. Journal of Structural Geology, 42, 184-193.

- Ashby MF (1970) The deformation of plastically non-homogeneous materials. Philosophical Magazine, 21(170), 399-424.

- Ashb, MF and Duval P (1985) The creep of polycrystalline ice. Cold Regions Science and Technology, 11(3), 285-300.

- Bachmann F, Hielscher R and Schaeben H (2010) Texture Analysis with MTEX – Free and Open Source Software Toolbox. Solid State Phenomena 160, 63-68.

- Becker R (1991) Analysis of texture evolution in channel die compression. 1. Effects of grain interaction. Acta Metallurgica et Materialia, 39(6), 1211–1230.

- Becker JK, Bons PD and Jessell MW (2008) A new front-tracking method to model anisotropic grain and phase boundary motion in rocks. Computer & Geosciences, 34(3), 201-212.

- Bons PD, Koehn D and Jessell MW (2008) Lecture notes in earth sciences. In: Bons P, Koehn D, Jessell M, editors. Microdynamic Simulation. Springer, Berlin; number 106. 405pp.

- Borthwick VE and Piazolo S (2010) Complex temperature dependent behaviour revealed by in-situ heating experiments on single crystals of deformed halite: New ways to recognize and evaluate annealing in geological materials. Journal of Structural Geology 32, 982-996.

- Borthwick VE, Piazolo S, Evans L, Griera A and Bons PD (2013) What happens to deformed rocks after deformation? A refined model for recovery based on numerical simulations. Geological Society London, Special Publications, 394(1), 215 – 534.

- Brinckmann S, Siegmund T and Huang Y (2006) A dislocation density based strain gradient model. International Journal of Plasticity, 22(9), 1784-1797.

- Budd W and Jacka T (1989) A review of ice rheology for ice sheet modelling. Cold Regions Science and Technology, 16(2), 107-144.

- Budd WF, Warner RC, Jacka TH, Jun LI and Treverrow A (2013) Ice flow relations for stress and strain-rate components from combined shear and compression laboratory experiments. Journal of Glaciology, 59(214), 374-392.

- Castelnau O, Duval P, Lebensohn RA and Canova GR (1996) Viscoplastic modeling of texture development in polycrystalline ice with a self-consistent approach: Comparison with bound estimates. Journal of Geophysical Research: Solid Earth (1978–2012), 101(B6), 13851-13868.

- Cottrell AH (1953). Theory of dislocations. Progress in Metal Physics, 4, 205-264.

- Cuffey KM and Kavanaugh JL (2011) How nonlinear is the creep deformation of polar ice? A new field assessment. Geology, 39(11), 1027-1030.

- De La Chapelle S, Castelnau O, Lipenkov V and Duval P (1998) Dynamic recrystallization and texture development in ice as revealed by the study of deep ice cores in Antarctica and Greenland. Journal of Geophysical Research: Solid Earth (1978–2012), 103(B3), 5091-5105.

- Delannay L, Logé RE, Chastel Y, Signorelli JW and Van Houtte P (2003) Measurement of in-grain orientation gradients by EBSD and comparison with finite element results. Advanced Engineering Materials, 5(8), 597–600.

- DiPrinzio CL, Wilen LA, Alley RB, Fitzpatrick JJ, Spencer MK and Gow AJ (2005) Fabric and texture at siple dome, antarctica. Journal of Glaciology, 51(173), 281-290.

- Diard O, Leclercq S, Rousselier G and Cailletaud G (2005) Evaluation of finite element based analysis of 3D multicrystalline aggregates plasticity. Application to crystal plasticity model identification and the study of stress and strain fields near grain boundaries. International Journal of Plasticity, 21(4), 691-722.

- Drury MR and Urai, JL (1990) Deformation-related recrystallization processes. Tectonophysics, 172(3), 235-253.

- Durand G (2004) Microstructure, recristallisation et deformation des glaces polaires de la carotte EPICA, Dôme Concordia, Antartique. Thèse de doctorat.

- Durand G, Gagliardini O, Thorsteinsson T, Svensson A, Kipfstuhl J and Dahl-Jensen, D (2006) Ice microstructure and fabric: an up to date approach to measure textures. Journal of Glaciology, 52(179), 619–630.

- Durand G, Persson A, Samyn D, and Svensson A (2008) Relation between neighbouring grains in the upper part of the NorthGRIP ice core—Implications for rotation recrystallization. Earth and Planetary Science Letters, 265(3), 666-671.

- Duval P, Ashby M and Anderman I (1983) Rate controlling processes in the creep of polycrystalline ice. The Journal of Physical Chemistry 87(21), 4066-4074.

- Duval P and Castelnau O (1995) Dynamic recrystallization of ice in polar ice sheets. Le Journal de Physique IV, 5(C3), C3-197.

- Duval P, Arnaud L, Brissaud O, Montagnat M, and de La Chapelle S (2000) Deformation and recrystallization processes of ice from polar ice sheets. Annals of Glaciology, 30(1), 83-87.

- Erb U, and Gleiter H (1979) The effect of temperature on the energy and structure of grain boundaries. Scripta Metallurgica 13.1: 61-64.

- Eshelby JD (1957) The determination of the elastic field of an ellipsoidal inclusion, and related problems. Proceedings of the Royal Society of London A241, 376–396.

- Eshelby JD (1959) The elastic field outside an ellipsoidal inclusion. Proceedings of the Royal Society of London 252 (1271), 561–569.

- Estrin Y and Kim HS (2007) Modelling microstructure evolution toward ultrafine crystallinity produced by severe plastic deformation. Journal of materials science, 42(5), 1512-1516.

- Faria HG, Weikusat I and Azuma N (2014a) The microstructure of polar ice. Part I: Highlights from ice core research. Journal of structural geology 61, 21 – 49.

- Faria HG, Weikusat I and Azuma N (2014b) The microstructure of polar ice. Part II: State of the art. Journal of structural geology 61, 21 – 49.

- Faria SH, Kipfstuhl S and Lambrecht A (2014c) The EPICA-DML Deep Ice Core. Springer, Heidelberg

- Fleck NA and Hutchinson JW (1997) Strain gradient plasticity. Adv Appl Mech 33:295–361

- Gagliardini O, Durand G and Wang Y (2004) Grain area as a statistical weight for polycrystal constituents. Journal of Glaciology, 50(168), 87–95.

- Gao H, Huang Y, Nix WD and Hutchinson JW (1999) Mechanism-based strain gradient plasticity - I. theory. Journal of the Mechanics and Physics of Solids, 47(6), 1239 - 1263.

- Gillet-Chaulet F, Hindmarsh RC, Corr HF, King EC and Jenkins A (2011) In-situ quantification of ice rheology and direct measurement of the Raymond Effect at Summit, Greenland using a phase-sensitive radar. Geophysical Research Letters, 38(24).

- Glen JW (1955) The creep of polycrystalline ice. Proc. Roy. Soc. Lond. A 228, 519- 538.

- Glen JW (1958) The flow law of ice: A discussion of the assumptions made in glacier theory, their experimental foundations and consequences. IASH Publ, 47: 171-183.

- Goldsby DL and Kohlstedt DL (2001) Superplastic deformation of ice: Experimental observations. Journal of Geophysical Research: Solid Earth (1978–2012), 106(B6), 11017-11030.

- Gottstein G and Mecking H (1985) Recrystallization. Preferred Orientation in Deformed Metals and Rocks: An Introduction to Modern Texture Analysis, 183-218.

- Griera A, Bons PD, Jessell MW, Lebensohn RA, Evans L and Gomez-Rivas E (2011) Strain localization and porphyroclast rotation. Geology 39, 275-278.

- Griera A, Llorens M-G, Gomez-Rivas E, Bons PD, Jessell MW, Evans LA, Lebensohn RA, (2013) Numerical modelling of porphyroclast and porphyroblast rotation in anisotropic rocks. Tectonophysics 587, 4-29.

- Gudmundson P (2004) A unified treatment of strain gradient plasticity. Journal of the Mechanics and Physics of solids, 52(6), 1379 – 1406. Hamann I, Weikusat C, Azuma N and Kipfstuhl S (2007). Evolution of ice crystal microstructure during creep experiments. Journal of Glaciology, 53(182), 479-489.

- Hamann, I., Weikusat, C., Azuma, N., Kipfstuhl, S., May 2007. Evolution of ice crystal microstructures during creep experiments. J. Glaciol. 53 (182), 479–489.

- Huybrechts P, Rybak O, Pattyn, F, Ruth U and Steinhage D (2007) Ice thinning, upstream advection, and non-climatic biases for the upper 89% of the EDML ice core from a nested model of the Antarctic ice sheet. Climate of the Past Discussions, 3(3), 693-727.

- Idiart MI, Moulinec H, Ponte Castaneda P and Suquet P (2006) Macroscopic behavior and field fluctuations in viscoplastic composites: second-order estimates versus full-field simulations. Journal of the Mechanics and Physics of Solids 54(5), 1029–1063.

- Jacka, TH (1984) Laboratory studies on relationships between ice crystal size and flow rate. Cold Regions Science and Technology, 10(1), 31-42.

- Jacka, TH and Maccagnan, M (1984) Ice crystallographic and strain rate changes with strain in compression and extension. Cold Regions Science and Technology, 8(3), 269-286.

- Jacka TH and Li J (1994) The steady-state crystal size of deforming ice. Annals of Glaciology 20, 13-28

- Jacka TH and Li J (2000) Flow rates and crystal orientation fabrics in compression of polycrystalline ice at low temperature and stresses. Physics of ice core records, 83-113.

- Jessel MW (1988a) Simulation of fabric development in recrystallizing aggregates – I. Description of the model. Journal of Structural Geology 10, 771–778.

- Jessel MW (1988b) Simulation of fabric development in recrystallizing aggregates – II. Example model runs. Journal of Structural Geology 10, 779–793.

- Jessell MW, Bons PD, Evans L, Barr T and Stüwe K (2001a) Elle: the numerical simulation of metamorphic and deformation microstructures. Computers & Geosciences 27, 17 - 30.

- Jessell MW, Evans L, Barr T and Stüwe K (2001b) Modeling of anisotropic grain growth in minerals. Tectonic Modeling: A Volume in Honor of Hans Ramberg, 193, 39.

- Jessell MW, Kostenko O and Jamtveit B (2003) The preservation potential of microstructures during static grain growth. Journal of Metamorphic Geology, 21(5), 481–491.

- Jessell MW, Siebert E, Bons PD, Evans L and Piazolo S (2005) A new type of numerical experiment on the spatial and temporal patterns of localization of deformation in a material with a coupling of grain size and rheology. Earth and Planetary Science Letters, 239(3), 309 - 326.

- Jessell MW, Bons PD, Griera A, Evans LA and Wilson CJL (2009) A tale of two viscosities. Journal of Structural Geology 31, 719 - 736.

- Karato SI (1987) Seismic anisotropy due to lattice preferred orientation of minerals: kinematic or dynamic? In High- Pressure Research in Geophysics (ed. M. H. Manghnani and Y. Syono), pp. 455–471. American Geophysical Union.

- Karato SI (2008) Deformation of earth materials: an introduction to the rheology of solid earth. Cambridge University Press.

- Kennicutt II, Chown SL, Cassano JJ, Liggett D, Massom R, Lloyd S and Peck LS (2014) Six priorities for Antarctic science. Nature, 512(7512), 23-25.

- Ketcham WM and Hobbs PV (1969) An experimental determination of the surface energies of ice. Philosophical Magazine, 19(162), 1161 -1173.

- Kipfstuhl S, Hamann I, Lambrecht A, Freitag J, Faria SH, Grigoriev D, Azuma N (2006) Microstructure mapping: a new method for imaging deformation-induced microstructural features of ice on the grain scale. J. Glaciol. 52 (178), 398-406.

- Kipfstuhl S, Faria SH, Azuma N, Freitag J, Hamann I, Kaufmann P and Wilhelms, F (2009) Evidence of dynamic recrystallization in polar firn. Journal of Geophysical Research: Solid Earth (1978–2012), 114(B5).

- Kocks UF, Tomé CN and Wenk HR (2000) Texture and anisotropy: preferred orientations in polycrystals and their effect on materials properties. Cambridge University Press.

- Kröner E (1962) Dislocations and continuum mechanics. Applied Mechacnics Reviews, 15(8), 599-606.

- Lebensohn RA (2001) N-site modelling of a 3D viscoplastic polycrystal using fast Fourier transform. Acta Materialia, 49(14), 2723–2737.

- Lebensohn RA, Liu Y and Castañeda PP (2004) Macroscopic properties and field fluctuations in model power-law polycrystals: full-field solutions versus self-consistent estimates. Proceedings of the Royal Society of London. Series A: Mathematical, Physical and Engineering Sciences, 460(2045), 1381-1405.

- Lebensohn RA, Castelnau O, Brenner R and Gilormini P (2005) Study of the antiplane deformation of linear 2-D polycrystals with different microstructures. International journal of solids and structures, 42(20), 5441-5459.

- Lebensohn RA, Brenner R, Castelnau O, Rollett AD (2008) Orientation image-based microme-chanical modelling of subgrain texture evolution in polycrystalline copper. Acta Materialia, 56(15), 3914–3926.

- Lebensohn RA and Tomé CN (1993) A selfconsistent approach for the simulation of plastic deformation and texture development of polycrystals: application to Zirconium alloys. Acta Metallurgica et Materialia, 41(9), 2611-2624.

- Li JCM (1962) Possibility of subgrain rotation during recrystallization. Journal of Applied Physics 33.10: 2958-2965.

- Lipenkov VY, Barkov NI, Dural P and Pimenta P (1989) Crystalline texture of the 2083 m ice core at Vostok Station, Antarctica. J. Glaciol, 35.

- Llorens M-G, Bons PD, Griera A, Gomez-Rivas E and Evans LA (2013a) Single layer folding in simple shear. Journal of Structural Geology, 50, 209-220

- Llorens M-G, Bons PD, Griera A and Gomez-Rivas E (2013b) When do folds unfold during progressive shear?. Geology, 41, 563-566.

- Mathiesen J, Ferkinghoff-Borg J, Jensen MH, Levinsen M, Olesen P, Dahl-Jensen D, and Svensson A (2004) Dynamics of crystal formation in the Greenland NorthGRIP ice core. Journal of Glaciology, 50(170), 325-328.

- Ma A, Roters F, and Raabe D (2006) A dislocation density based constitutive model for crystal plasticity FEM including geometrically necessary dislocations. Acta Materialia 54.8: 2169-2179.

- McQueen HJ and Evangelista E (1988) Substructures in aluminium from dynamic and static recovery. Czechoslovak Journal of Physics B, 38(4), 359–372.

- Mainprice D, Hielscher R and Schaeben H (2011) Calculating anisotropic physical properties from texture data using the MTEX open source package. Geological Society, London, Special Publications, 360(1), 175-192.

- Michel JC, Moulinec H and Suquet P (2000) A computational method based on augmented Lagrangians and fast Fourier transforms for composites with high contrast. Computer Modelling in Engineering and Sciences, 1(2), 79-88.

- Michel JC, Moulinec H and Suquet P (2001) A computational scheme for linear and non-linear com-posites with arbitrary phase contrast. International Journal for Numerical Methods in Engineering, 52(1-2), 139-160.

- Miyamoto A, Shoji H, Hori A, Hondoh T, Clausen HB and Watanabe O (2005) Ice fabric evolution process understood from anisotropic distribution of a-axis orientation on the GRIP (Greenland) ice core. Annals of Glaciology, 42(1), 47-52.

- Mika DP and Dawson PR (1998) Effects of grain interaction on deformation in polycrystals. Materials Science and Engineering A, 257(1), 62-76.

- Mohamed G and Bacroix B (2000) Role of stored energy in static recrystallization of cold rolled copper single and multicrystals. Acta Materialia 48(13), 3295-3302.

- Moldovan D, Wolf D and Phillpot SR (2001) Theory of diffusion-accommodated grain rotation in columnar polycrystalline microstructures. Acta materialia, 49(17), 3521-3532.

- Moldovan D, Wolf D, Phillpot SR and Haslam AJ (2002) Role of grain rotation during grain growth in a columnar microstructure by mesoscale simulation. Acta Materialia, 50(13), 3397-3414.

- Montagnat M and Duval P (2004) The viscoplastic behaviour of ice in polar ice sheets: experimental results and modelling. Comptes Rendus Physique, 5(7), 699-708.

- Montagnat M, Diard M, Weiss J, Chevy J, Duval P, Brunjail H, Bastie P and Gil Sevillano J (2006) The heterogeneous nature of slip in ice single crystals deformed under torsion. Philosophical Magazine, 86(27), 4259 - 4270.

- Montagnat M, Blackford JR, Piazolo S, Arnaud L and Lebensohn RA (2011) Measurements and full-field predictions of deformation heterogeneities in ice. Earth and Planetary Science Letters, 305(1-2), 153 - 160.

- Montagnat M, Castelnau O, Bons PD, Faria SH, Gagliardini O, Gillet-Chaulet F, Grennerat F, Griera A, Lebensohn RA, Moulinec H, Roessiger J and Suquet P (2013) Multiscale modeling of ice deformation behavior. Journal of Structural Geology, 61, 78 – 108.

- Montagnat, M, Azuma N, Dahl-Jensen D, Eichler J, Fujita S, Gillet-Chaulet F, Kipfstuhl S, Samyn D, Svensson A and Weikusat I (2014) Fabric along the NEEM ice core, Greenland, and its comparison with GRIP and NGRIP ice cores. The Cryosphere 8, no. 4: 1129-1138.

- Moulinec H and Suquet P (1994) A fast numerical method for computing the linear and nonlinear mechanical properties of composites. Comptes rendus de l'Académie des sciences. Série II, Mécanique, physique, chimie, astronomie, 318(11), 1417-1423.

- Moulinec H and Suquet P (1998) Numerical method for computing the overall response of nonlinear composites with complex microstructure. Computer methods in applied mechanics and engineering, 157(1), 69-94.

- Nasello OB, Di Prinzio CL and Guzán PG (2005) Temperature dependence of "pure" ice grain boundary mobility. Acta Materialia, 53 (18), 4863 – 4869.

- Nye J (1953) Some geometrical relations in dislocated crystals. Acta Materialia, 1(2), 153-162.

- Passchier CW and Trouw RAJ (2005) Deformation Mechanisms. Microtectonics: 25-66.

- Piazolo S, Jessell MW, Bons PD, Evans L and Becker JK (2010) Numerical simulations of microstructures using the Elle platform: a modern research and teaching tool. Journal of the Geological Society of India, 75(1), 110-127.

- Piazolo S, Bons PD, Jessell MW, Evans L and Passchier CW (2002) Dominance of microstructural processes and their effect on microstructural development: insights from numerical modelling of dynamic recrystallization. Geological Society, London, Special Publications, 200(1), 149-170.

- Piazolo S, Borthwick V, Griera A, Montagnat M, Jessell MW, Lebensohn RA and Evans L (2012) Substructure dynamics in crystalline materials: new insight from in situ experiments, detailed EBSD analysis of experimental and natural samples and numerical modelling. Materials Science Forum, 715, 502-507.

- Piazolo S, Montagnat M, Grennerat F, Moulinec H and Wheeler J (2015). Effect of local stress heterogeneities on dislocation fields: Examples from transient creep in polycrystalline ice. Acta Materialia, 90, 303-309.

- Prakash A and Lebensohn RA (2009) Simulation of micromechanical behavior of polycrystals: finite elements versus fast Fourier transforms. Modelling and Simulation in Materials Science and Engineering 17.6: 064010.

- Poirier JP (1985) Creep of Crystals. Cambridge University Press, New York.

- Raabe D, Sachtleber M, Zhao Z, Roters F and Zaefferer S (2001) Micromechanical and macromechanical effects in grain scale polycrystal plasticity experimentation and simulation. Acta Materialia 49(17), 3433–3441.

- Randle V (1993) Microtexture investigation of the relationship between strain and anomalous grain growth. Philosophical Magazine A 67.6: 1301-1313.

- Read WT and Shockley W (1950) Dislocation models of crystal grain boundaries. Physical Review 78.3: 275.

- Rigsby GP (1951) Crystal Fabric Studies on Emmons Glacier Mount Rainier, Washington. The Journal of Geology, 590-598.

- Roessiger J, Bons PD, Griera A, Jessell MW, Evans L, Montagnat M, Kipfstuhl S, Faria SH and Weikusat I (2011) Competition between grain growth and grain size reduction in polar ice. Journal of Glaciology, 57(205), 942 - 948.

- Roessiger J, Bons PD and Faria SH (2012) Influence of bubbles on grain growth in ice. Journal of Structural Geology, 61, 123 – 132.

- Roters F, Eisenlohr P, Bieler TR and Raabe D (2011) Crystal Plasticity Finite Element Methods: In Materials Science and Engineering. John Wiley & Sons.

- Roters F, Eisenlohr P, Hantcherli L, Tjahjanto DD, Bieler TR and Raabe D (2010) Overview of constitutive laws, kinematics, homogenization and multiscale methods in crystal plasticity finite-element modeling: Theory, experiments, applications. Acta Materialia, 58(4), 1152-1211.

- Sachs G (1928) On the derivation of a condition of flowing. Zeitschrift des Vereins Deutscher Ingenieure für Maschinenbau und Metallbearbeitung, 72, 734–736.

- Schulson EM and Duval P (2009) Creep and fracture of ice (p. 432). Cambridge: Cambridge University Press.

- Sellars CM (1978) Recrystallization of metals during hot deformation. Philosophical Transactions of the Royal Society of London A, 288(1350), 147–158.

- Stipp M and Tullis J (2003) The recrystallized grain size piezometer for quartz. Geophysical Research Letters, 30(21).

- Takeda YT, and Griera A (2006) Rheological and kinematical responses to flow of two-phase rocks. Tectonophysics 427.1: 95-113.

- Taylor GI (1938) Plastic strain in metals. Journal of the Institute of Metals, 62, 307–324.

- Thorsteinsson T, Kipfstuhl J, Eicken H, Johnsen SJ and Fuhrer K (1995) Crystal size variations in Eemian-age ice from the GRIP ice core, central Greenland. Earth and Planetary Science Letters, 131(3), 381-394.

- Thorsteinsson T, Kipfstuhl J and Mille H (1997) Textures and fabrics in the GRIP ice core. J. Geophys. Res. 102, 26583–26599

- Thorsteinsson T (2002) Fabric development with nearest-nieghbour interaction and dynamic recrystallization. Journal of Geophysical Research 107(B1), 2014.

- Treagus SH and Lan L (2004) Deformation of square objects and boudins. Journal of Structural Geology 26.8: 1361-1376.

- Treverrow A, Budd WF, Jacka TH and Warner RC (2012) The tertiary creep of polycrystalline ice: experimental evidence for stress-dependent levels of strain rate enhancement. Journal of Glaciology, 58(208), 301-314.

- Tullis J, Dell'Angelo L and Yund RA (1990) Ductile shear zones from brittle precursors in feldspathic rocks: the role of dynamic recrystallization. The brittle-ductile Transition in Rocks, 67-81.

- Upmanyu M, Srolovitz DJ, Shvindlerman LS and Gottstein G (2002) Molecular dynamics simulation of triple junction migration. Acta materialia, 50(6), 1405-1420.

- Urai JL, Means WD and Lister GS (1986) Dynamic recrystallization of minerals. Mineral and Rock Deformation: Laboratory Studies: The Paterson Volume, 161-199.

- Van der Veen CJ and Whillans IM (1994). Development of fabric in ice. Cold regions science and technology, 22(2), 171-195.

- Vollmer FW (1990) An application of eigenvalue methods to structural domain analysis. Geological Society of America Bulletin, 102(6), 786-791.

- Wang Y, Kipfstuhl S, Azuma N, Thorsteinsson T and Miller H (2003) Ice-fabrics study in the upper 1500 m of the Dome C (East Antarctica) deep ice core. Annals of glaciology, 37(1), 97-104.

- Weikusat I, Kipfstuhl S, Faria SH, Azuma N and Miyamoto A (2009) Subgrain boundaries and related microstructural features in EDML (Antarctica) deep ice core. Journal of Glaciology, 55(191), 461-472.

- Wen J, Huang Y, Hwang KC, Liu C and Li M (2005) The modified Gurson model accounting for the void size effect. International Journal of Plasticity, 21(2), 381 – 395.

- Wilson CJL (1986) Deformation induced recrystallization of ice; the application of in situ experiments. Mineral and Rock Deformation: Laboratory Studies: The Paterson Volume, 213-232.

- Wilson CJ and Zhang Y (1996) Development of microstructure in the high-temperature deformation of ice. Annals of Glaciology, 23, 293-302.

- Wilson CJL, Peternell M, Piazolo S and Luzin V (2013) Microstructure and fabric development in ice: lessons learned from in situ experiments and implications for understanding rock evolution. Journal of Structural Geology, 61, 50 – 77.

- Woodcock NH (1977) Specification of fabric shapes using an eigenvalues Method. Geological Society of America Bulletin, 88(9), 1231-1236.

- Zaffarana C, Tommasi A, Vauchez A and Grégoire M (2014) Microstructures and seismic properties of south Patagonian mantle xenoliths (Gobernador Gregores and Pali Aike). Tectonophysiscs, 621, 175 – 197.

Chapter 3

Full-field predictions of pure ice dynamic recrystallisation under simple shear conditions

Maria-Gema Llorens[a,b], Albert Griera[c], Paul D. Bons[a], Ricardo Lebensohn[d] and Ilka Weikusat[a,b]

[a]Departament of Geosciences, Eberhard Karls University Tübingen, Germany
[b]Alfred Wegener Institute for Polar and Marine Research, Bremerhaven, Germany
[c]Departament de Geologia, Universitat Autònoma de Barcelona, Cerdanyola del V., Spain
[d]Material Science and Technology Division, Los Alamos National Laboratory, USA

Abstract

The understanding of ice microstructural response is necessary to improve our knowledge of ice sheet dynamics and to interpret climate signals from the ice sheet record. Ice in polar ice sheets flows and behaves anisotropically affecting the passive particles that can be stored in it. We present a series of numerical simulations of ice deformation coupling full-field viscoplastic deformation (FFT) with dynamic recrystallisation processes in simple shear boundary conditions. The model predicts the morphology of local misorientations within ice grains and the internal stresses produced by deformation. Analyses of the evolution of grain sizes and lattice preferred orientations of models performed at different strain rates demonstrate that recrystallisation has a strong influence on the resulting microstructure. An increase of grain boundary migration produces larger and more equidimensional grains, but does not significantly influence c-axis distributions and the development of lattice preferred orientations. The intrinsic anisotropy developed in ice due to lattice preferred orientation of the polycrystalline aggregate, produces strain localisation that can be masked by the recrystallisation, being not possible to recognise the real amount of deformation by only looking at the microstructure. The results of this study reveal that the probability of grains to survive is strongly related to their initial grain size, and does not significantly depend on their orientation with respect to the flow field.

Keywords

3.1   Introduction

Polar ice sheets are considered a valuable record of the past climate. They archive changes in atmospheric temperature, humidity and dust particles such as volcanic activity or pollution. The study of the ice composition, air bubbles and dust from ice core allows us to reconstruct the paleoclimate record (e.g. Buiron et al., 2011; Greenland ice core project (GRIP) members, 1993), since ice is organised in chronologically ordered strata. However, post-depositional factors such as ice deformation by ice sheet flow or recrystallisation processes of the microstructure, can produce a mixture of ice, particles and dust from different origins and thus altering climate signal (e.g. Faria et al., 2009). Therefore, a quantitative understanding of ice dynamics and their microstructures is crucial in order to properly interpret the paleoclimate record. For this reason it is essential to know how deformation and dynamic recrystallisation processes affect the microstructures and mechanics of polar ice (Castelnau et al., 1996; Durand et al., 2007).

The only natural type of ice in the Earth is the hexagonal crystal form *Ih* which presents highly anisotropic viscoplastic behaviour when it is deformed. This is because deformation

is mostly accommodated by dislocation glide along the basal plane, while the other slip systems are much harder to activate (Duval and Castelnau, 1995). The anisotropy of the crystal (A) is determined by the ratio of critical resolved shear stress ($CRSS$) required to activate slip along non-basal versus basal systems. This value ranges between 60 and 100 in hexagonal ice (Duval et al., 1983; Montagnat et al., 2013). It is observed in ice cores that ice crystals tend to be oriented with their basal planes perpendicular to the principal compressive stress (Azuma and Higassi, 1985; Alley 1992).

The orientation of ice crystals is usually defined according to the orientation of their c-axis, which is perpendicular to the basal plane. Polycrystalline ice with c-axes randomly oriented is considered to behave isotropically. However, ice crystals in polar ice sheets typically appear aligned at a certain depth, thus forming a lattice preferred orientation (LPO) and developing an intrinsic anisotropy (Kennedy et al., 2013). It has been found that ice presenting a strong LPO deforms up to an order of magnitude faster than isotropic ice. Therefore ice flow strongly depends on the orientation of polycrystalline ice (Azuma, 1994; Castelnau et al., 1996; Thorsteinsson, 2001).

Ice microstructure is affected by different processes, depending on the temperature and strain rate (Faria et al., 2014). Normal grain growth (NGG) reduces the boundary energy by increasing the grain size, while strain induced migrational recrystallisation ($SIBM$) reduces the stored strain energy by migration of boundaries. Poligonisation is a recovery process that results in the rotation of subgrains developing tilt walls (Alley, 1992). Dynamic recrystallisation is very efficient in ice due to the natural deformation conditions of this mineral, i.e. temperatures close to its pressure melting point and deformation at very low strain rates (Jacka and Li, 1994; Kipfstuhl et al., 2006; Montagnat et al., 2009).

Ice tends to deforms under compression in the vertical direction and extension in the horizontal direction (pure shear boundary conditions) near the divide of ice sheets. On the contrary, simple shear boundary conditions dominates in zones away from the divide and close to the bedrock (Cuffey and Paterson, 2010). It is therefore crucial for understanding bulk polar ice behaviour to study its fabrics and microstructural evolution in response to stress and time under different types of deformation (i.e. under different strain rates and vorticities).

The aim of this contribution is to systematically study the effects of dynamic recrystallisation on the mechanical behaviour and resulting microstructures of polar ice under simple shear deformation by means of numerical simulations. We focus on the evolution of fabric and microstructure in response to finite strain and time, and specially study the development of intrinsic polycrystalline anisotropies and how they produce finite strain localisation that can potentially affect the spreading of climate signals at the small scale (NEEM comunity, 2013).

3.2   Experimental procedure and data analysis

We use a two-dimensional numerical model that simulates viscoplastic deformation coupled with dynamic recrystallisation in order to investigate the microstructural evolution of an aggregate of pure ice grains. The numerical software platform ELLE is used (Bons et al., 2008; http://www.elle.ws). The numerical approach is based on the coupling of a full-field viscoplastic code using the Fast Fourier Transform algorithm (FFT; Lebensohn 2001; Lebensohn et al., 2008) and several ELLE modules (Jessell et al., 2001; Bons et al., 2008) that simulate recrystallisation processes such as recovery and grain boundary migration. The FFT formulation provides a solution of the micromechanical problem by finding a strain rate and stress field that minimises the average local work-rate under the compatibility and equilibrium constraints (see Lebensohn, 2001). The deformation induced lattice rotation and the estimation of geometrically necessary dislocations densities calculated from the stress and velocity field provided by the FFT approach, are used to simulate intra-crystalline recovery and grain boundary migration. ELLE has previously been successfully used to simulate several deformation microstructure processes, including grain growth (Bons et al., 2001; Jessell et al., 2003; Roessiger et al., 2011), dynamic recrystallisation (Piazolo et al., 2002; Montagnat et al., 2013), strain localisation (Jessell et al., 2005; Griera et al., 2011; Griera et al., 2013) or folding (Llorens et al., 2013a; Llorens et a., 2013b), among many others. In this study, grain boundary migration (*GBM*) is simulated using a front-tracking approach based on the algorithm by Becker et al. (2008). Grain boundary migration is driven by reduction of grain boundary energy and stored strain energy, reproducing the motion or displacement of high-angle grain boundaries (*HAGB*), whereby lattice distortions in swept regions are restored. Recovery reduces the intra-granular stored energy in a deformed crystal, simulating annihilation of dislocations and their rearrangement into low-angle subgrains (Urai et al. 1986; Borthwick et al, 2013; Faria et al., 2014).

The data structure of the models consists of two basic layers (Fig. 3.1): (a) a contiguous set of polygons (termed *flynns*) that are themselves defined by boundary nodes (*bnodes*) and connected by straight boundary segments, and (b) a set of unconnected nodes (*unodes*) that provide a high-resolution grid for storing physical properties within grains. A resolution of 256 x 256 Fourier points (*unodes*) was used to map lattice orientations, resulting in a unit cell defined by 65,536 discrete *unodes*. Each *unode* represents a small area or crystallite with a certain lattice orientation, defined by three Euler angles, and a dislocation density. The FFT code uses these *unodes* for the viscoplastic deformation calculations. The change of the position of *bnodes* is calculated according to the deformation velocity field and grain boundary migration. The data structure of ELLE is fully wrapping: grains touching one side of the model continue on the other size. This feature not only reduces boundary effects, but also allows repositioning the model into a square grid every time step, and

therefore, high strain can be reached (Fig. 3.1e). FFT and ELLE codes use periodic boundary conditions and the physical space is discretised into a regular mesh of nodes (Fourier points), being possible the direct mapping of all the variables and to share the same data structures by both codes.

Each process in ELLE is performed sequentially in a loop that represents a small time increment (Δt; Jessell et al., 2001). An experimental run reproduces first viscoplastic deformation (FFT) by the application of dextral shear strain increment of γ=0.04 (Fig. 3.1f). After this deformation step, the microstructure is affected by a sub-loop of dynamic recrystallisation processes: grain boundary migration and recovery. This sub-loop may be called more than once to simulate deformation at different strain rates, varying the balance between deformation and recrystallisation.

The input microstructure has 1632 grains and a dimension of 10x10 cm^2. Grains have an initially homogeneous random lattice orientation (Fig. 3.1d), representing a bulk isotropic material. The ratio of critical resolved shear stress for non-basal versus basal slip systems was set to A=20 and a value of stress exponent n=3 was chosen for all slip systems (e.g. Castelnau et al 1996). The value of A is assumed to range between 60 and 100 for hexagonal ice (Ih). However, previous tests showed that the effect of increasing A is not clearly observable with our approach at values of A above 10, and it only increases the calculation time (Llorens et al., in review). Therefore, this value was chosen to be a compromise between calculation time (dependent on A) and accuracy of the simulations.

The initial microstructure was deformed up to a shear strain of γ=3 in plane-strain simple shear, by small constant steps of dextral shear strain of γ=0.04. Four experiments at different strain rates were simulated by varying the number of steps in the recrystallisation loop (Table 3.1). Grain boundary mobility is the same value for all the simulations, and therefore different ratios between DRX and FFT steps reproduce deformation at different strain rates.

Experiment name	DRX/FFT ratio	Initial average grain area [mm^2]	Final average grain area [mm^2]	Final number of grains	strain rate [s^{-1}]
Experiment 0	0	6.12	6.11	1636	-
Experiment 1	1	6.12	11.63	873	$6.34 \cdot 10^{-11}$
Experiment 10	10	6.12	63.29	156	$6.34 \cdot 10^{-12}$
Experiment 25	25	6.12	136.06	61	$2.54 \cdot 10^{-12}$

Table 3.1: Numerical experiment setup

Figure 3.1: ELLE data structure and program flow. Microstructures consist of three layers: (a) boundary nodes that define polygons (grains), (b) a regular mesh of unconnected nodes to store dislocation density and lattice orientations used for the FFT calculation, and (c) a passive marker grid used to track the finite deformation. The initial model (d) is affected by a closed loop of processes (f): deformation by small increments of $\gamma=0.04$, reposition that brings the model back into the unit cell (e), and a subloop of (*GBM*) and recovery processes.

3.3   Results

3.3.1   Microstructure evolution

Experiment 0 represents a case where polar ice is deformed in simple shear without recrystallisation and (i.e. *DRX* processes are not active). Deformation of this model produced irregular elongated grains oriented parallel to the stretching direction at the end of the simulation (at a shear strain of $\gamma=3$). In the absence of *GBM* the average grain size remained constant through the experiment (Table 3.1). Deformation localised in this model in conjugate high-strain bands of strongly elongated grains, separated by low strain areas or microlithons (Fig. 3.2b) (Passchier and Trouw, 2005). There is a general tendency to increase intergranular heterogeneities and the development of subgrains, as indicated by the progressive increase of the local misorientation (Fig. 3.2a). Experiments 1, 10 and 25 simulate systems with different degrees of dynamic recrystallisation. In these cases, grains were still elongated parallel to the stretching direction at the end of deformation, despite the amount of dynamic recrystallisation. Grain boundary migration decreases the degree of grain elongation, so that dynamic recrystallisation produced larger and more equidimensional grains. High-strain bands are not easy to recognize from the grain network (Fig. 3.2d,e). The initial average grain size increased according to the amount of dynamic recrystallisation (Table 3.1). We could expect that the final average grain size in Experiments 10 and 25 would be 10 and 25 times larger than that of Experiment 1. However, the grain size increment was not proportional to the number of dynamic recrystallisation steps, being the final average grain size 5.4 and 11.7 times larger in

Experiments 10 and 25 than that in Experiment 1, respectively.

Figure 3.2: Local misorientation field, crystal orientations with respect to the y direction in crystal reference frame (IPF), shear strain rate field normalised with respect to the bulk strain, and passive marker grid at $\gamma=3$ for models with (b) no recrystallisation, (c) 1 step, (d) 10 steps, and (e) 25 steps of DRX per deformation step, respectively. The initial microstructure is showed in (a). Images for Experiments 0 and 1 have been enlarged (2x) for better visibility.

3.3.2 LPO evolution

All simulations present a similar evolution of c-axis orientations, regardless of the amount of dynamic recrystallisation. They start with an initial microstructure with randomly oriented c-axes (Figs. 2a and 3a), and evolve to a configuration where c-axes are orientated approximately perpendicular to the shear plane (red and purple colours in Fig. 3.2b,c,d,e; Fig. 3.3c). The preferred c-axis orientation is clearly visible at a shear strain of $\gamma=1.5$ (Fig. 3.3b), where c-axes are defining an open cone which evolve further into a strong single maximum pattern. The maximum density progressively moves towards the centre of the cone (Fig. 3.3c). The maximum concentration of c-axes tends to be normal to the shear plane, but there is still an obliquity between both directions at $\gamma=3.0$. The increase of dynamic recrystallisation produces a relative strength of the c-axis maximum and an increase of the obliquety of the maximum with respect to the *xy* plane (Experiments 1, 10 and 25; Fig. 3.3c). Another observable effect of dynamic recrystallisation on the final crystal orientation is the anisotropic distribution of a-axes, which tend to be aligned to the shear direction when *DRX* is active (Fig. 3.3c).

The evolution of the LPO symmetry during deformation is similar in all the experiments, and evolves from a random to a point distribution. The random component is minimised with increasing dynamic recrystallisation. Additionally, we can observe that a girdle component on the LPO symmetry arises in Experiments 10 and 25 with progressive deformation (Fig. 3.4), being it a clear effect of dynamic recrystallisation.

3.3.3 Strain rate field

The ratio of the critical resolved shear stress between basal and non-basal slip systems (pyramidal and prismatic) determines the heterogeneous response of the mineral aggregate. One of the parameters governing strain localisation is the anisotropic viscoplastic behaviour of the crystalline material. In all the experiments, the anisotropy parameter *A* was set to 20. In all cases, strain field becomes increasingly heterogeneous with progressive strain, and synthetic shear bands oriented at low angle to the imposed shear plane develop (see the shear strain rate field column of Fig. 3.2).

Dynamic recrystallisation reduces the amount and intensity of shear bands, as it can be observed in the map of equivalent strain rate for Experiment 10 and Experiment 25 (Fig. 3.2d,e). The strain partitioning pattern is clearly visible from the geometry of the grain shapes in models with zero or small amounts of dynamic recrystallisation (Experiments 0 and 1). Bands of extremely stretched grains are observable surrounding lozenge-shaped domains with more equidimensional grains. However, when dynamic recrystallisation is active (i.e. grain boundary migration operates) there is a decrease of grain elongation and more equidimensional grains are possible to recognise. In these situations, strain partitioning from the grain shapes is more difficult to be recognised (Fig. 3.2c,d,e).
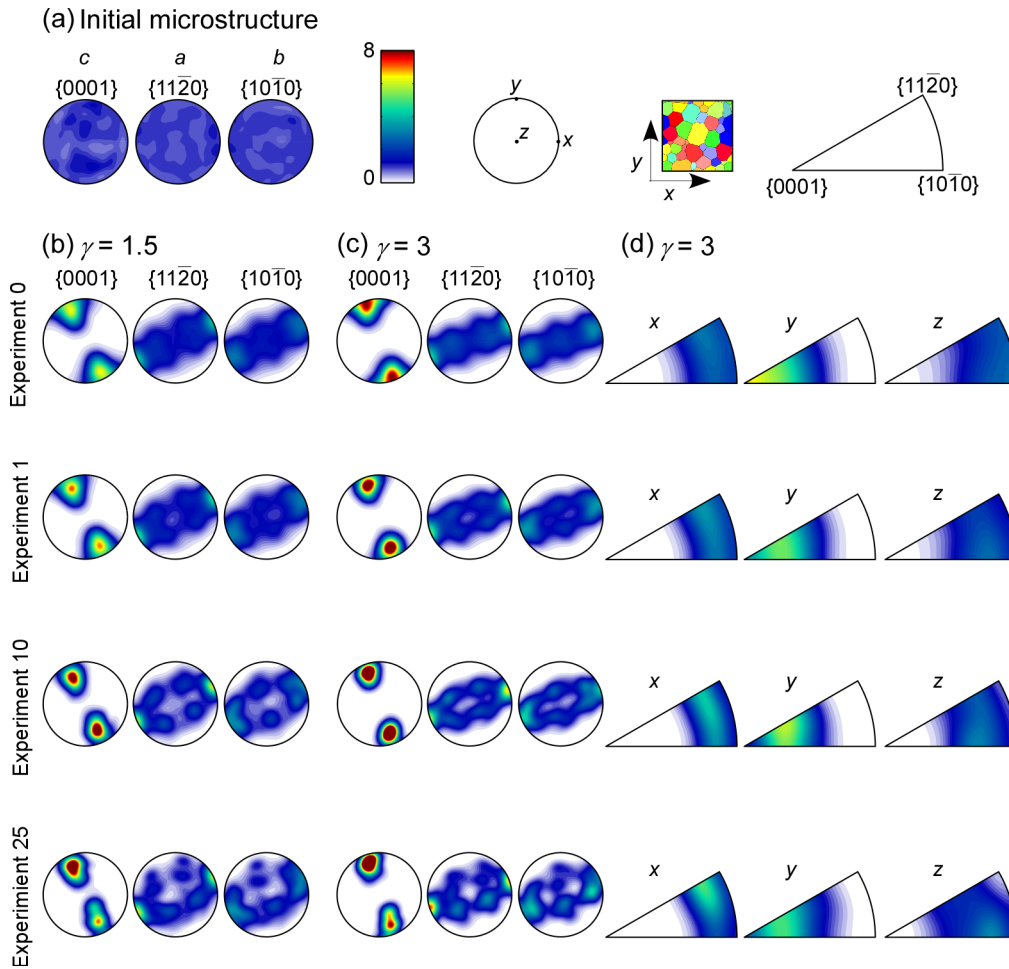
Figure 3.3: Pole figures of lattice orientation for all the simulations performed in this study, at the initial step (a) and at shear strain of γ=1.5 (b) and γ=3 (c). Rightmost three columns show the inverse polar figures of the x, y and z axes of the sample respect to crystal orientations.
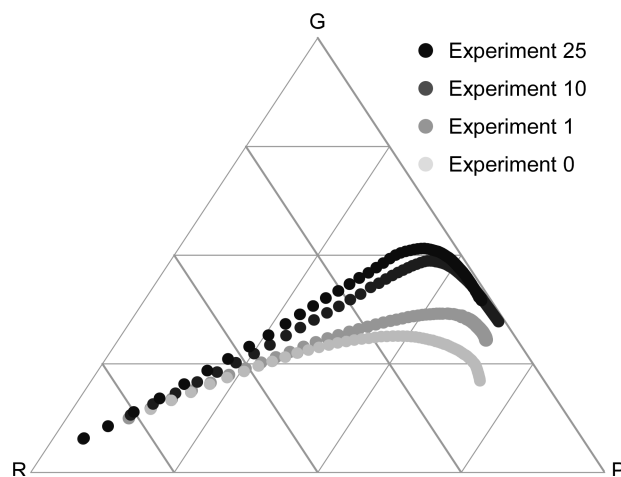
Figure 3.4: Ice LPO symmetry for all the experiments performed in this study, expressed as the proportion of point (P), girdle (G) and random (R) components for c-axes <0001>.

3.3.4   Finite strain localisation

Finite deformation patterns can be imaged from the models using an orthogonal marker grid of vertical and horizontal lines (Fig. 3.2a, rightmost column; only horizontal lines shown). This grid is computed from the velocity flow and it is assumed deform passively. This allows us to track finite deformation, even when the intensity of dynamic recrystallisation is high enough to mask strain heterogeneities (Experiments 10 and 25; Fig. 3.2d,e). Qualitative observations confirm the development of highly heterogeneous strain fields, which is qualitatively more heterogeneous than can be detected by looking grain geometries.

Strain localisation is clearly recognisable with the help of the passive marker grid. This grid displays bands where markers are stretched and parallelised to extension direction, and relative low strain regions where markers are smooth and folded (Fig. 3.2b-e). Recrystallisation reduces the intensity and amount of shear bands, as shown in Fig. 3.2c-e. In all cases, marker lines rotate synthetically with the imposed shearing, and asymmetric folds and synthetic shear bands develop with progressive strain at approximately 45° with respect to the macroscopic shear plane. A second set of shear bands almost parallel to the shear plane develops in Experiment 0 (without recrystallisation) with increasing strain (Fig. 3.2b). This set coincides with the bands defined by stretched grains.

3.4   Discussion

3.4.1   Effects of dynamic recrystallisation on the microstructure evolution

The results described above show that dynamic recrystallisation has a strong influence on grain growth. When grain boundary migration is not active, the grain size does not vary and 100% of the grains survive through time (Table 3.1). These results are somehow expected. However, when dynamic recrystallisation is active, strain stored energy from dislocation densities and grain boundary energy are driving the forces for grain boundary migration (Fig. 3.5a). It can be observed in such cases that grains do not grow proportionally to the amount of dynamic recrystallisation, because the effective mobility is different depending on the applied strain rate (Fig. 3.5c). By comparing grain growth (k) for all the experiments, it is possible to recognise that grains in experiments deformed at high strain rate (i.e. with low number of dynamic recrystallisation steps) grow faster than that of the experiments deformed at low strain rates (i.e. with high number of dynamic recrystallisation steps). All simulations initially follow the grain growth curve (normal grain growth, *Normal GG* simulation), but there is a progressive deviation with increasing amount of stores strain energy from the static grain growth curve until exponential grain growth is reached (Fig. 3.5c). This deviation from linear to exponential growth, is observed

early for simulations with reduced dynamic recrystallisation (Experiment 1). If the energy of the system was similar in all simulations, the expected behaviour would be a grain size relationship proportional to the number of dynamic recrystallisation steps (10 and 25 times larger than in Experiment 1). However as previously explained, higher macroscopic growth rates are observed in Experiment 1 than in Experiment 10 and 25. This is related to the local strain stored energy, which is higher than in other experiments.

The simulation results indicate that the evolution of grain morphology is significantly affected by dynamic recrystallisation. Deformation produces bands of extremely stretched grains that bound lozenge-shaped low-strain domains, while dynamic recrystallisation results in larger and more equidimensional grains. The average grain elongation in models deformed only by viscoplastic deformation is close to 5:1 (Fig. 3.5b). When dynamic recrystallisation is active, grain boundary migration masks deformation, being the grain elongation ratio strongly reduced. At low strain rates (Experiments 10 and 25) the elongation is less than 2:1 (Fig. 3.5b).

3.4.2   Localisation of deformation

The results presented in this contribution reveal that polar ice can be strongly deformed and yet it is almost impossible to detect and quantify such amount of deformation (Fig. 3.2c-e). This might have severe consequences if we consider that impurities and other climate signals can behave in natural ice as passive markers, which only move passively with ice flow. This fact is usually not considered when performing paleoclimate reconstructions using polar ice core. These numerical simulations demonstrate that strain localisation of can potentially redistribute impurities heterogeneously within ice at the microscale. Impurities are difficult to visualise with microstructural analysis methods in natural ice. Only visual stratigraphy line scanning (Svensson et al., 2005) reveals a sum effect of the impurities, grain boundaries and bubbles as scattering surfaces forming "cloudy bands", using a dark-field microscopy method. As localisation bands become more and more parallel to each other with increasing amount of dynamic recrystallisation, and as spacing of localisation bands cannot be evaluated with confidence in our simulations, an alternative formation mechanisms for cloudy bands in deep ice can be anticipated here. This finding shows that understanding the effects of impurities on the microstructure (e.g. pinning) is essential in order to properly capture the distribution of climate signals in polar ice. This process has to be included in the presented FFT/ELLE models. The coupling of these codes could potentially lead to a re-visualisation of localisation bands by anisotropic concentration of impurities.
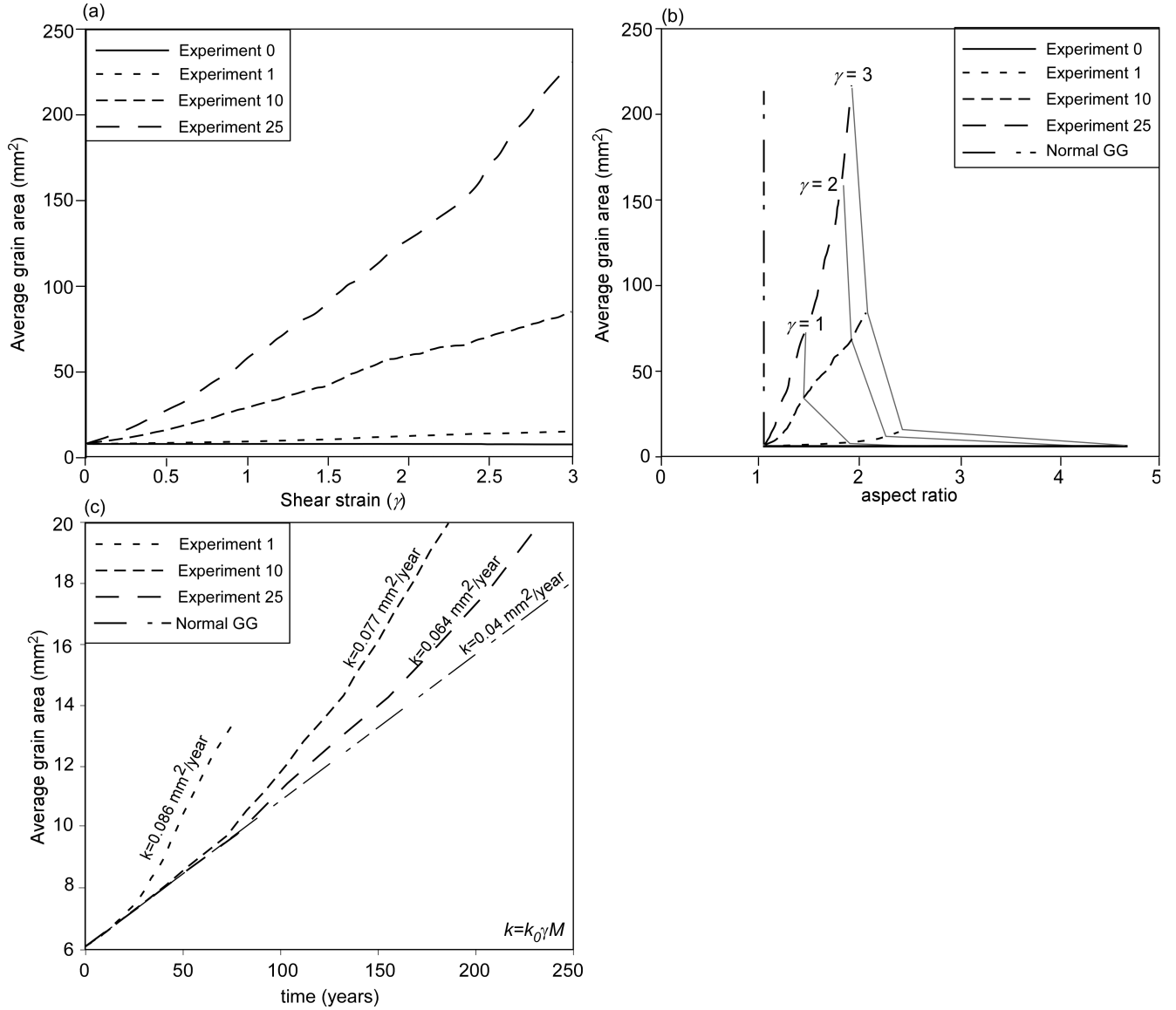
Figure 3.5: Average grain area evolution for all the experiments with respect to the bulk shear strain (a), and (b) to the grain elongation. The curves comparing grain growth through time (years) (c) reveal that the effective mobility is higher in Experiment 1 than in Experiments 10 and 25, compared to the mobility for a normal grain growth experiment (*NGG*).

3.4.3 Effects of dynamic recrystallisation on the evolution of lattice preferred orientation

The results of the present simulations indicate that fabrics evolve as expected in simple shear boundary conditions. This evolution is typically characterised by a strong single maximum almost perpendicular to the shear plane (Bouchez and Duval., 1982; Wenk and Tomé, 1999), as predicted by torsion experiments (Rigsby, 1960; Bouchez and Duval 1982) and ice core descriptions (Hudleston, 1977; Russell-head and Budd, 1979; Bouchez and Duval, 1984 (quitar); Wang 2002; Durand et al., 2009). A strong LPO rapidly develops with increasing strain in all simulations, independently of whether dynamic recrystallisation is active, and regardless of the applied strain rate (Fig. 3.2 and 3). At lower shear strain

(γ =1.5 Fig. 3.3b) the initial randomly oriented basal planes are quickly distributed into a preferred orientation. Polar figures show that the single maxima is located at about the pole of a plane oriented at an angle approximately α=10° with respect to the shear plane in all cases at high strain (γ=3) (Fig. 3.3c).

Recrystallisation produces a girdle component at the LPO symmetry (Fig. 3.3b-d), which is more pronounced at low strain rates (Fig. 3.3c,d) (Budd and Jacka 1989). This effect is clearly observable from a Random-Point-Girdle diagram (Fig. 3.4), where Experiments 10 and 25 develop a girdle component that forms at low shear strain (less than γ=0.5), despite the fact that all the experiments follow the same random to pointed LPO symmetry evolution.

Our simulations demonstrate that LPO distributions are coincident with that described by Lister and Hobbs (1980) for quartz with an easy basal glide and a CRSS of basal vs. basal and prismatic slip systems of 3. This process of LPO development is similar to that described for ice from field observations and laboratory experiments (Rigsby, 1960; Bouchez and Duval 1982). However, some slight differences can be observed at low deformation conditions when our results are compared with experimental simple shear tests (Steinemann, 1958; Duval, 1981; Bouchez and Duval 1982; Kamb 1964; 1972). These studies showed that the LPOs are sometimes accompanied by a secondary maxima rotated away in a reverse sense of shearing. Our simulations, both with and without dynamic recrystallisation, display a unique single maximum that is initially developed at approximately 45° with respect to the shear plane, thus reflecting the predominant slip activity along the basal plane. When deformation increases, the LPO concentrates and the simple shear boundary conditions imposes a rotation of the basal planes producing a final LPO almost perpendicular to the shear plane. This result is coincident with previous numerical simulations at lows strain, like the ones reported by Van der Veen and Whillans (1994), where crystals are oriented in a single maximum fabric at 45° with respect to the shear plane when dynamic recrystallisation is not active. However, these authors considered that it is necessary to activate recrystallisation in order to develop a fabric almost perpendicular to the shear plane, like the one observed in nature at high strain. Our simulations show very similar results as the ones presented by Azuma (1995), where simple shear simulations produce a single maximum that rotates clockwise during deformation, evolving in a final LPO almost perpendicular to the shear plane at high strains. Therefore, our models are coincident with the conclusion that it is not necessary to activate dynamic recrystallisation in order to develop the simple shear LPO observed in nature (Azuma 1995).

The experimental and natural observed bimodal LPO distribution has been explained by different processes. Bouchez and Duval (1982) proposed that dynamic recrystallisation destroys grains unfavourably oriented for further slip at high strains, while simple shear deformation produces c-axis rotation. Other authors, such as Kizaki (1969) or Budd (1972),

proposed that c-axis preferred orientations with multiple maxima could be produced by grain boundary migration, so that these distributions are indeed characteristic of ice with coarse irregular grains, while the c-axes of fine-grained ice should develop a single maximum. However, when dynamic recrystallisation is active in our simulations grains are more regular and their survival is only slightly dependent on their orientation (Fig. 3.6a). In this case, only few grains with their c-axes oriented parallel to the *xy* plane disappeared (Fig. 3.6c). The numerical results indicate that the selection of grains to survive is mainly determined by their initial size (Fig. 3.6d,e) and not by their crystal orientation. This is coherent with the highly heterogeneous intra- and intergranular field expected for highly anisotropic polycrystalline aggregates. The experimental values were used of grain mobility, surface energy and dislocation density energy, do not allow the development of high enough anisotropic energy to induce a LPO controlled by preferred grain boundary migration.

It should be also noted that indicate that the geometry of grain boundaries tends to vary between straight and lobate. We do not observe short-scale length bulging or highly serrated boundaries. This is related to the relative balance between dislocation and boundary energies used. If higher dislocation line energies were used, we could expect to see bulging and serrated grain boundaries. This means that the classical range of values expected from lab experiments indicate that highly lobate/bulging are not expected in the physical polar ice sheet conditions.

The results show that a-axes in simulations performed at low strain rates (Experiments 10 and 25) rotate towards the maximum elongation axis at the same time as c-axes rotate towards the compression axis (Fig. 3.3c,d). This a-axis LPO development can be related to the increment of the activity of non-basal slip systems (Fig. 3.7). The results show that when dynamic recrystallisation is active (Experiments 10 and 25) the deformation accommodated along the basal slip system decreases, being increased the part of the deformation accommodated along the pyramidal and prismatic slip systems.

3.4.4 Microshear

The macroscopic softening behaviour of ice-age ice has serious implications for ice core dating and paleoclimate record interpretation. It was assumed that the glacial ice softening behaviour was produced by preferred orientations of the crystal lattice (Paterson et al., 1991). However, investigations of glacial ice microstructures from the EDML deep ice core (Faria et al., 2009) revealed the development of microshear as a deformation mechanism that operates in combination with dislocation glide and producing a reduction of the material hardness. This interpretation was based on analogue experiments by Bons and Jessell (1999) using OCP at high homologous temperature. These authors observed that small bands of intense deformation, measured by means of digital correlation, did not produce
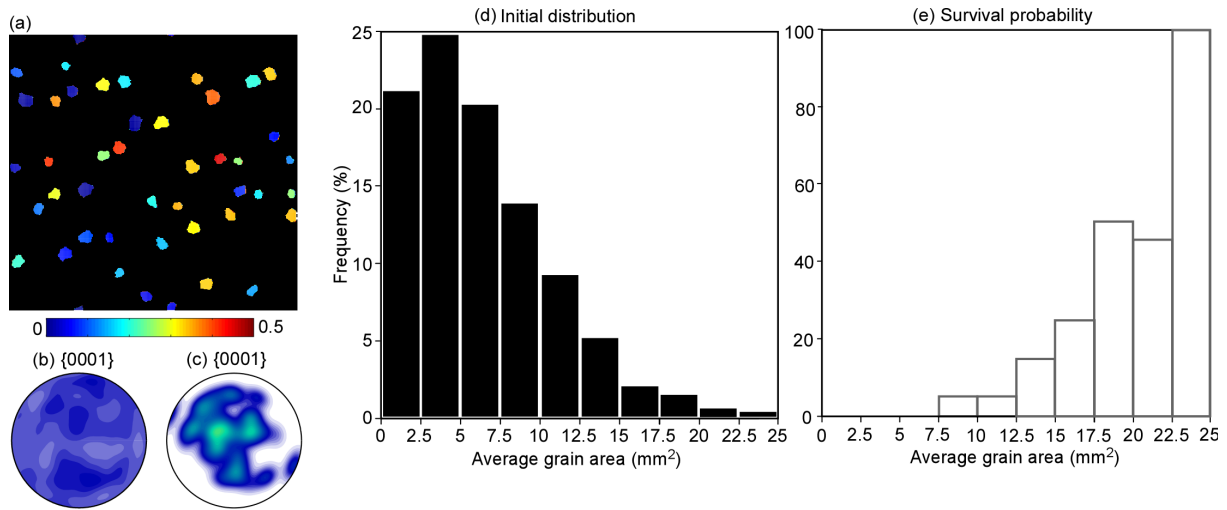
Figure 3.6: Initial grain boundary network for Experiment 25, showing: (a) the Schmid factor for the grains that survive at the end of the experiment, (b) initial pole figures of all grains, and (c) grains that will survive at the end of the experiment. A comparison between the initial average grain area distribution (d) and survival probability at the end of the Experiment 25 (c) reveal that larger grains have a higher chance to survive while small grains tend to disappear.
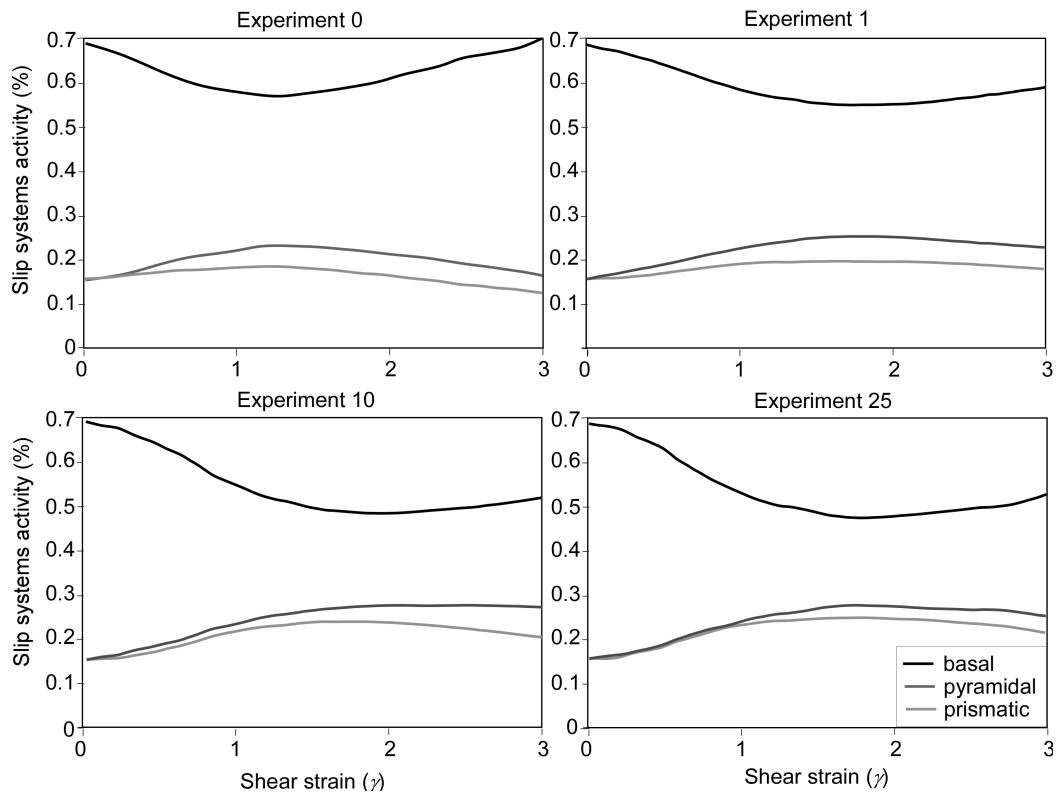
Figure 3.7: Activity of basal and non-basal slip systems during deformation for all the presented simulations.

an apparent grain size reduction or microstructural modification, but correlate with the development of stepped grain boundaries. They interpreted these stepped geometries as indicators of microshearing. These results were used by Faria et al (2009) to interpret

81

observations from EDML deep ice core. The development of dynamic grain boundary structures formed by microshear was proposed as the explanation of the softening behaviour of the ice-age ice, in of small grain size, high temperature and moderate stress conditions. Our simulations reveal the development of microshear boundaries related to the shear strain rate field (Fig. 3.8). The accommodation of deformation by microshear reduces the stress concentration without modifying the crystallographic texture evolution. Dislocation activity within grains produces microshear zones along grain boundary chains, splitting grains developing a subgrain boundary (Faria et al., 2009).
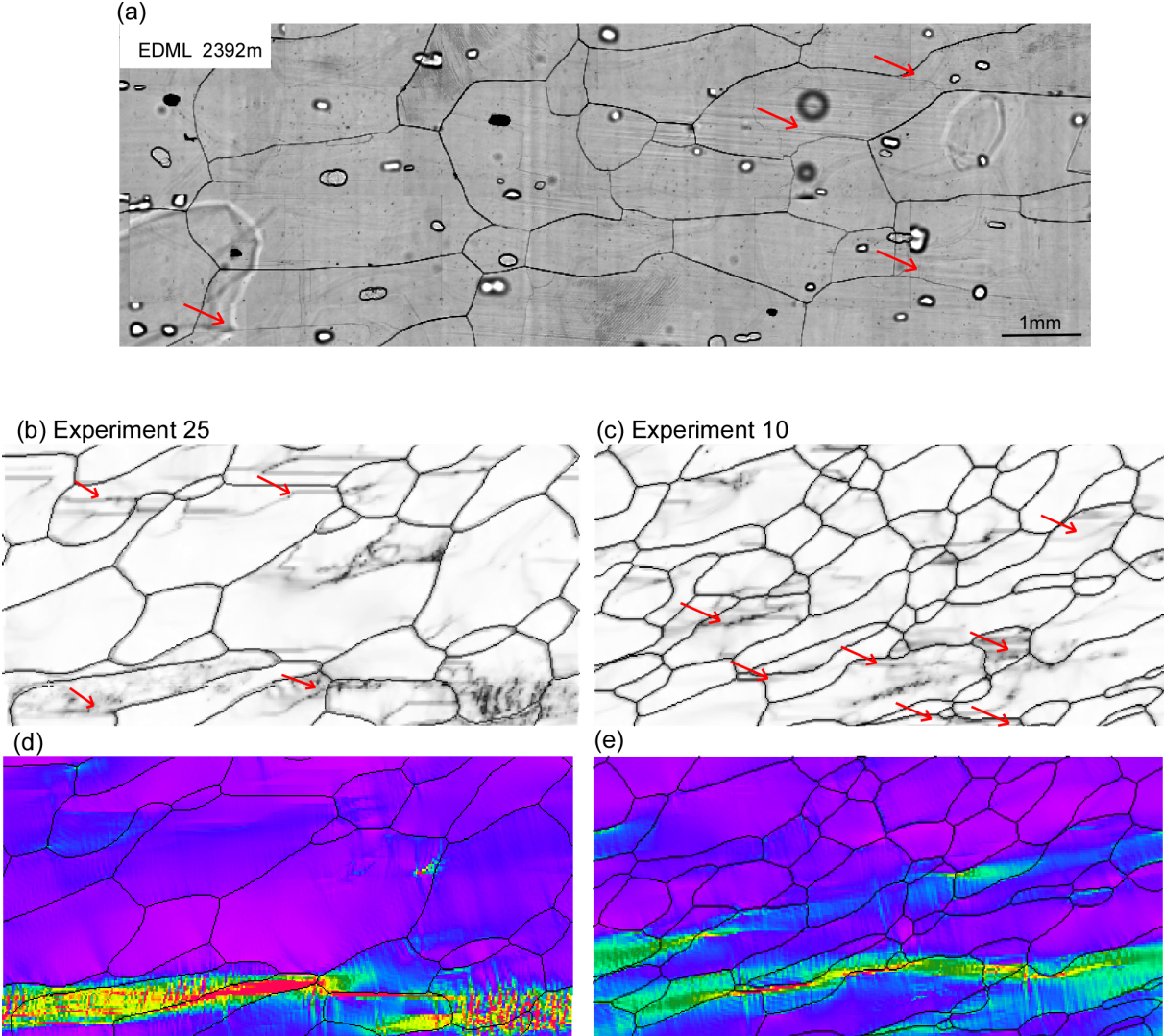
Figure 3.8: Boundary misorientation and grain boundary network compared with shear strain rate field for Experiments 25 (b-d) and 10 (c-e). Arrows indicate subgrain boundaries developed by microshear, compared with natural example of a thin section of EDML core at 2392 m depth.

3.5 Conclusions

New results on the influence of recrystallisation on the microstructures and deformation behaviour of polar ice in simple shear boundary conditions at different strain rates have been presented. Observations of microstructure and LPO evolution show that dynamic recrystallisation can significantly increase ice grain size, and produce more equidimensional grains, masking the deformation and strain localisation produced by the high intrinsic anisotropy of the crystals. The strain rate at which ice is deformed does not modify the evolution of c-axes lattice preferred orientation, which in our simulations show a single maxima oriented almost parallel to the shortening direction. At low strain rates, the activity of non-basal slip systems increases, and produces a rotation of the a-axes towards the maximum elongation axis. The selection of grains that will survive during grain boundary migration is highly related to the initial grain size, and only slightly related to the crystal orientation with respect to the flow rate. Stored strain energy is higher in experiments performed at low strain rates, producing a faster growth of grains than in experiments at low strain rates.

3.6 References

- Alley RB (1992) Flow-law hypotheses for ice-sheet modeling. Journal of Glaciology, 38(129), 245-256.

- Azuma N (1994) A flow law for anisotropic ice and its application to ice sheets. Earth and Planetary Science Letters, 128(3), 601-614.

- Azuma N (1995) A flow law for anisotropic polycrystalline ice under uniaxial compressive deformation. Cold Reg. Sci. Technol. 23 (2), 137–147.

- Azuma N and Higashi A (1985) Formation processes of ice fabric pattern in ice sheets. Annals of Glaciology, 6, 130 - 134.

- Becker JK, Bons PD and Jessell MW (2008) A new front-tracking method to model anisotropic grain and phase boundary motion in rocks. Computer & Geosciences, 34(3), 201-212.

- Bons PD and Jessell MW (1999) Micro-shear zones in experimentally deformed octachloropropane. J. Struct. Geol. 21, 323-334.

- Bons PD, Jessell MW, Evans L, Barr TD and Stüwe K (2001) Modelling of anisotropic grain growth in minerals. Geol. Soc. Am. Mem. 193, 39–49.

- Bons PD, Koehn D and Jessell MW (2008) Lecture notes in earth sciences. In: Bons P, Koehn D, Jessell M, editors. Microdynamic Simulation. Springer, Berlin; number 106. 405pp.

- Borthwick VE, Piazolo S, Evans L, Griera A and Bons PD (2013). What happens to deformed rocks after deformation? A refined model for recovery based on numerical simulations. Geological Society London, Special Publications, 394(1), 215 – 534.

- Bouchez JL and Duval P (1982). The fabric of polycrystalline ice deformed in simple shear: experiments in torsion, natural deformation and geometrical interpretation. Texture, Stress, and Microstructure, 5(3), 171-190.

- Budd W F (1972) The development of crystal orientation fabrics in moving ice. Z. Gletscherkunde Glazialgeol. 8 (1–2), 65–105.

- Budd W F and Jacka TH (1989) A review of ice rheology for ice sheet modelling. Cold Regions Science and Technology, 16(2), 107-144.

- Buiron D, Chappellaz J, Stenni B, Frezzotti M, Baumgartner M, Capron E and Landais A (2011) TALDICE-1 age scale of the Talos Dome deep ice core, East Antarctica. Climate of the Past 7, 1: 1-16.

- Castelnau, O, Duval, P, Lebensohn, RA and Canova, GR (1996). Viscoplastic modeling of texture development in polycrystalline ice with a self-consistent approach: Comparison with bound estimates. Journal of Geophysical Research: Solid Earth (1978–2012), 101(B6), 13851-13868.

- Cuffey K and Paterson WSB (2010) The physics of glaciers. Academic Press.

- Durand G, Gillet-Chaulet F, Svensson A, Gagliardini O, Kipfstuhl S, Meyssonnier J, Parrenin F, Duval P and Dahl-Jensen D (2007) Change in ice rheology during climate variations–implications for ice flow modelling and dating of the EPICA Dome C core. Climate of the Past 3, 1:155-167.

- Durand G, Svensson A, Persson A, Gagliardini O, Gillet-Chaulet F, Sjolte J, Montagnat M, Dahl-Jensen D (2009) Evolution of the texture along the EPICA Dome C Ice Core. Low Temp. Sci. 68, 91-105.

- Duval P (1981) Creep and fabrics of polycrystalline ice under shear and compression. J. Glaciol., 27: 129-140.

- Duval P, Ashby M and Anderman I (1983) Rate controlling processes in the creep of polycrystalline ice. The Journal of Physical Chemistry 87(21), 4066-4074.

- Duval P and Castelnau O (1995) Dynamic recrystallization of ice in polar ice sheets. Le Journal de Physique IV, 5(C3), C3-197.

- Faria SH, Kipfstuhl S, Azuma N, Freitag J, Hamann I, Murshed MM and Kuhs WF (2009) The multiscale structure of Antarctica. Part I: inland ice. Low Temp. Sci. 68, 39-59.

- Faria HG, Weikusat I and Azuma N (2014) The microstructure of polar ice. Part II: State of the art. Journal of structural geology 61, 21 – 49.

- Greenland Ice-core Project (GRIP) members (1993) Climate instability during the last interglacial period recorded in the GRIP ice core. Nature 364, 203–207.

- Griera A, Bons PD, Jessell MW, Lebensohn RA, Evans L and Gomez-Rivas E (2011). Strain localization and porphyroclast rotation. Geology 39, 275-278.

- Griera A, Llorens M-G, Gomez-Rivas E, Bons PD, Jessell MW, Evans LA and Lebensohn RA, (2013) Numerical modelling of porphyroclast and porphyroblast rotation in anisotropic rocks. Tectonophysics 587, 4-29.

- Hudleston PJ (1977) Similar folds, recumbent folds, and gravity tectonics in ice and rocks. J. Geol. 85, 113–122.

- Jacka TH and Li J (1994) The steady-state crystal size of deforming ice. Annals of Glaciology 20, 13-28

- Jessell MW, Bons PD, Evans L, Barr T and Stüwe K (2001) Elle: the numerical simulation of metamorphic and deformation microstructures. Computers & Geosciences 27, 17 - 30.

- Jessell MW, Kostenko O and Jamtveit B (2003) The preservation potential of microstructures during static grain growth. Journal of Metamorphic Geology, 21(5), 481–491.

- Jessell MW, Siebert E, Bons PD, Evans L and Piazolo S (2005) A new type of numerical experiment on the spatial and temporal patterns of localization of deformation in a material with a coupling of grain size and rheology. Earth and Planetary Science Letters, 239(3), 309 - 326.

- Kamb WB (1964) Glacier geophysics. Science 146 (3642), 353–365.

- Kamb WB (1972) Experimental recrystallization of ice under stress. In: Heard,

- Heard HC, Borg IY, Carter NL, Raleigh CB (Eds.) (1972) Flow and Fracture of Rocks. No. 16 in Geophysical monograph. American Geophysical Union, Washington DC, 211-241.

- Kennedy JH, Pettit EC and Di Prinzio CL (2013) The evolution of crystal fabric in ice sheets and its link to climate history. Journal of Glaciology, 59(214), 357-373.

- Kipfstuhl S, Hamann I, Lambrecht A, Freitag J, Faria SH, Grigoriev D and Azuma N (2006) Microstructure mapping: a new method for imaging deformation-induced microstructural features of ice on the grain scale. J. Glaciol. 52 (178), 398e406.

- Kizaki K (1969) Ice-fabric study of the Mawson region, East Antarctica. J. Glaciol. 8 (53), 253–276.

- Lebensohn RA (2001) N-site modelling of a 3D viscoplastic polycrystal using fast Fourier transform. Acta Materialia, 49(14), 2723–2737.

- Lebensohn RA, Brenner R, Castelnau O, Rollett AD (2008) Orientation image-based micromechanical modelling of subgrain texture evolution in polycrystalline copper. Acta Materialia, 56(15), 3914–3926.

- Lister GS and Hobbs BE (1980) The simulation of fabric development during plastic deformation and its application to quartzite: the influence of deformation history. Journal of Structural Geology, 2(3), 355-370.

- Llorens M-G, Bons PD, Griera A, Gomez-Rivas E and Evans LA (2013a) Single layer folding in simple shear. Journal of Structural Geology, 50, 209-220

- Llorens M-G, Bons PD, Griera A and Gomez-Rivas E (2013b) When do folds unfold during progressive shear?. Geology, 41, 563-566.

- Llorens M-G, Griera A, Bons PD, Roessiger J, Lebensohn R and Weikusat, I (submitted to Journal of Glaciology) Dynamic recrystallization of ice aggregates during co-axial viscoplastic deformation: a numerical approach.

- Montagnat M, Durand G and Duval P (2009) Recrystallization processes in granular ice. Low Temperature Science 68.Supplement : 81-90.

- Montagnat M, Castelnau O, Bons PD, Faria SH, Gagliardini O, Gillet-Chaulet F, Grennerat F, Griera A, Lebensohn RA, Moulinec H, Roessiger J and Suquet P (2013) Multiscale modeling of ice deformation behavior. Journal of Structural Geology, 61, 78 – 108.

- NEEM Community Members (2013) Eemian interglacial reconstructed from a Greenland folded ice core. Nature, 493, doi:10.1038/nature11789.

- Passchier CW and Trouw RAJ (2005) Deformation Mechanisms. Microtectonics: 25-66.

- Paterson WSB (1991) Why ice-age ice is sometimes "soft". Cold Regions Science and Technology 20.1: 75-98.

- Piazolo S, Bons PD, Jessell MW, Evans L and Passchier CW (2002) Dominance of microstructural processes and their effect on microstructural development: insights from numerical modelling of dynamic recrystallization. Geological Society, London, Special Publications, 200(1), 149-170.

- Rigsby GP (1960) Crystal orientation in glacier and in experimentally deformed ice. J. Glaciol. 3 (27), 589e606.

- Roessiger J, Bons PD, Griera A, Jessell MW, Evans L, Montagnat M, Kipfstuhl S, Faria SH and Weikusat I (2011) Competition between grain growth and grain size reduction in polar ice. Journal of Glaciology, 57(205), 942 - 948.

- Russell-Head DS and Budd WF (1979) Ice-sheet flow properties derived from bore-hole shear measurements combined with ice-core studies. Journal of Glaciology, 24, 117-130.

- Steinemann S (1958) Experimentelle Untersuchungen zur Plastizität von Eis. Beitr. Geol. Schweiz. Hydrol. 10, 1-72. Also as Ph.D. Thesis, Swiss Federal Institute of Technology (ETH) Zurich.

- Svensson A, Nielsen SW, Kipfstuhl S, Johnsen SJ, Steffensen JP, Bigler M, Ruth U and Röthlisberger R (2005) Visual stratigraphy of the North Greenland Ice Core Project (NorthGRIP) ice core during the last glacial period. J. Geophys. Res. 110, D02108.

- Thorsteinsson T (2001) An analytical approach to deformation of anisotropic ice-crystal aggregates. Journal of Glaciology, 47(158), 507-516.

- Urai JL, Means WD and Lister GS (1986) Dynamic recrystallization of minerals. Mineral and Rock Deformation: Laboratory Studies: The Paterson Volume, 161-199.

- Van der Veen CJ and Whillans IM (1994) Development of fabric in ice. Cold regions science and technology, 22(2), 171-195.

- Wang Y, Thorsteinsson T, Kipfstuhl J, Miller H, Dahl-Jensen D and Shoji H (2002) A vertical girdle fabric in the NorthGRIP deep ice core, North Greenland. Ann. Glaciol. 35, 515-520.

- Wenk HR and Tomé CN (1999) Modeling dynamic recrystallization of olivine aggregates deformed in simple shear. Journal of Geophysical Research: Solid Earth (1978–2012), 104(B11), 25513-25527.

Chapter 4

Small-scale disturbances in the stratigraphy of the NEEM ice core: observations and numerical simulations

Daniela Jansen[a], **Maria-Gema Llorens[a,b]**, Julien Westhoff[b], Florian Steinbach[b], Sepp Kipfstuhl[a], Paul D. Bons[b], Albert Griera[c] and Ilka Weikusat[a,b]

[a]Alfred Wegener Institute for Polar and Marine Research, Bremerhaven, Germany
[b]Departament of Geosciences, Eberhard Karls University Tübingen, Germany
[c]Departament de Geologia, Universitat Autònoma de Barcelona, Cerdanyola del V., Spain

At the time of submission of this thesis this manuscript was in its final stages of completion for submission to the journal The Cryosphere. The reader should note that the final manuscript may deviate slightly from the version printed here.

Abstract

Disturbances on the centimetre scale in the layering of the NEEM ice core (North Greenland) can be mapped by means of visual stratigraphy as long as the ice does have a visual layering, such as, for example, cloudy bands. Different focal depths of the visual stratigraphy method allow, to a certain extent, a three dimensional view of the structures. In this study we present a structural analysis of the visible folds, discuss their characteristics and frequency and present examples of typical fold structures. With this study we aim to quantify the potential impact of small-scale folding on the integrity of climate proxy data. We also analyse the structures with regard to the stress environment under which they formed. The structures evolve from gentle waves at about 1500 m to overturned z-folds with increasing depth. Occasionally, the folding causes significant thickening of layers. Their shape indicates that they are passive features and are probably not initiated by rheology differences between alternating layers. Layering is heavily disturbed and tracing of single layers is no longer possible below a depth of 2160 m. Lattice orientation distributions for the corresponding core sections were analysed where available in addition to visual stratigraphy. The data show axial-plane parallel strings of grains with c-axis orientations that deviate from that of the matrix, which shows a single-maximum fabric at the depth where the folding occurs. We conclude from these data that folding is a consequence of deformation along localised shear planes and kink bands. The findings are compared with results from other deep ice cores. The observations presented are supplemented by microstructural numerical modelling using a code that reproduces crystal viscoplastic deformation, applying a Fast Fourier Transform (FFT), coupled dynamic recrystallisation processes. The model results reproduce the development of bands of grains with a tilted orientation relative to the single maximum fabric of the matrix, and also the associated local deformation.

Keywords

4.1 Introduction

The drilling site for the NEEM (North Greenland Eemian Ice drilling) ice core is 77° 27' N 51° 3.6' W, and it has been drilled between June 2009 and July 2010. It is located on a topographic ridge, which dips towards the northwest so that the surface velocities on the ice divide have a non-negligible component of along ridge flow of 5 m a^{-1} (NEEM community members, 2013). In July 2010 the bedrock was reached at 2537.36 m depth. The site has been chosen in order to recover an undisturbed Eem warm period ice layer, however, it

was found later that the ice below 2200 m was heavily disturbed and probably folded on a larg scale (NEEM community, 2013). Visible stratigraphy of the NEEM ice core also showed folding on a small scale, with fold amplitudes varying from less than 1 cm to few decimetres. Similar structures have been found in other ice cores, and have been described in the literature (Alley et al., 1997; Svensson et al., 2005; Faria et al., 2010; Fitzpatrick et al., 2014). These disturbances are of particular interest in terms of their influence on the integrity of the climatic record (Faria et al., 2010). Waddington (2001), and Thorsteinsson and Waddington (2002) explored the amplification of small disturbances in the layering of ice cores for isotropic and anisotropic conditions, investigating the potential for the existence of overturned folds near ice sheet centres. However, the initial formation of the disturbances has not been fully understood yet.

Here we present a characterisation and inventory of the small-scale folding observed in the NEEM ice core. We also discuss possible folding mechanisms and the link to the so called "Alley-stripes" visible in the stratigraphy as well as in the crystal fabric of grains. Microstructural numerical modelling with ELLE reproduces similar fabrics and fold structures to the ones we observe in the NEEM ice core.

4.2 Methods

The data used in this study have been obtained by different observational methods, which will be introduced only briefly in the following section. For technical details we recommend the reader to check the original literature.

4.2.1 Linescan visual stratigraphy

The visual stratigraphy of the NEEM ice core has been recorded by means of an automated linescan instrument (see Svensson et al. (2005) for a detailed description of the instrument and data from the North GRIP ice core). An indirect light source is illuminating the ice core, leading to black pixels if the ice is clear. If dust particles or bubbles are included in the ice core they cause scatter of light and thus are visible in the linescan image. A clear correlation between backscatter and dust content has been found in the North Grip ice core (Svenson et al., 2005). The method can be applied directly in the field and in the case of the NEEM ice core has been applied continuously for the entire core, with a gap between 860 m and 1150 m due to technical difficulties. For the NEEM ice core the linescan images were recorded with a standardised exposure time and three focal planes within the ice core section with a vertical distance of 1 cm (Kipfstuhl, 2010). This allows to a certain degree a three-dimensional mapping of the visible layering in the ice core. The data is stored in high-resolution (118 pixel per centimetre) tiff images. One drawback of this method is of course that it only shows disturbances in the ice if scattering particles

are included. However, it is possible by means of image processing and filtering to reveal structures also at low dust content.

4.2.2 Automated Fabric Analyser

The crystal fabric orientation of discrete samples has been measured using an Automatic Fabric Analyser (Wilson type) (Weikusat and Kipfstuhl, 2010). Samples from the physical properties part of the NEEM core have been cut to 250 nanometer thin sections and crystal fabric orientation has been measured using the polarimetric method. The data coverage is much better than in previous ice cores with continuous sampling of selected core sections (bags) to investigate meter-scale variations in fabric through the core. However, due to the time-consuming preparation of the samples it was not possible to produce a continuous record. The physical properties section of the core is at the opposite side, so that due to three-dimensional variations it is not always possible to assign features from each data set to one another.

4.2.3 Microstructural modelling with ELLE and full field crystal plasticity (FFT)

To investigate the development of strain localisation in simple shear deformation we used a 2-D numerical modelling technique. The simulation approach couples a full field method based on the fast Fourier transform (FFT) that simulates viscoplastic deformation, and two codes that simulate dynamic recrystallisation processes, both included within the open-source numerical modelling platform ELLE (http://www.elle.ws; Bons et al., 2008). ELLE has been successfully used to simulate evolution of microstructures during deformation, as dynamic recrystallisation (Piazolo et al., 2002) or strain localisation (Jessell et al., 2003; Griera et al., 2011, 2013). The full-field crystal plasticity (FFT) code (Lebensohn, 2001; Lebensohn et al., 2008) simulates deformation by pure viscoplastic dislocation glide. An experimental run consists of iterative applications of small increments of shear strain $\gamma=0.04$ of simple shear deformation, followed by a sub-loop of processes simulating dynamic recrystallisation (grain boundary migration - *GBM* and recovery). The recrystallisation sub-loop may be called more than once to simulate the different balance between deformation and recrystallisation as a function of strain rate, since all simulations are performed with the same intrinsic mobility value (M_0) and boundary-diffusion activation energy (Q) (Llorens et al., in review). A direct one-to-one importation of data between both codes is possible, as ELLE and FFT use periodic boundary conditions and the physical space is discretised into a shared regular node mesh.

The ELLE data structure consists of three layers: (1) a network of nodes (boundary nodes or *bnodes*) that are connected by straight boundary segments that define the high-angle grain boundaries that enclose individual ice grains, (2) a set of unconnected nodes

(*unodes*) to map lattice orientations and dislocation densities, used for the FFT calculation, and (3) a passive marker grid utilised to track finite strain. Distances between nodes are kept between 5.5 x 10^{-3} and 2.5 x 10^{-3} the unit distance (in a 1x1 bounding box), by removing *bnodes* when their neighbours are too close or adding *bnodes* when two nodes are too far apart. The space is discretised in a mesh of 256x256 Fourier points, resulting in a unit cell defined by 65.536 discrete nodes. Each *unode* represents a small area or crystallite with a certain lattice orientation, defined by three Euler angles, and a dislocation density value. The ELLE data structure has fully wrapping boundaries. The 10x10 cm^2 initial microstructure has 1632 grains, each with a homogeneous lattice orientation, showing a lattice preferred orientation (LPO) almost perpendicular to the shear plane, in order to simulate an intrinsic anisotropic material. The misorientation between grains has been set at <5° (i.e. initial noise). In these simulations, the ratio of critical resolved shear stress (*CRSS*) for non-basal versus basal slip systems is set to $A = 20$. The same stress exponent (*n*=3) is set for all slip systems. The physical values used for recrystallisation are: mobility M (7.5 x 10^{-5} m^{2}kg^{-1}s^{-1}; Schulson and Duval, 2009), intrinsic mobility M_0 (1 x 10-10 m^{2}kg^{-1}s^{-1}; Nasello et al., 2005), boundary-diffusion activation energy Q (40 KJ mol^{-1}; Thorteinsson, 2002) and isotropic surface energy γ_e (0.065 Jm^{-2}; Ketcham and Hobbs, 1969). Please see Llorens et al. (in review) for a complete description of the methods. Starting with the same initial microstructure, models with two different ratios between dynamic recrystallisation (*GBM* and recovery) and viscoplastic deformation were performed: 1 and 10 DRX steps per deformation (FFT) step.

4.3 Results

4.3.1 Stratigraphy and fold classification

The stratigraphy data has been visually inspected for all parts of the ice core containing cloudy bands, in order to categorise disturbances of the visible layers. It has to be noted that that this method is only appropriate where sufficient layers are visible, since clear ice may have also been deformed. Fig. 4.1 shows an overview of the layering structures we find in the NEEM ice core. The panels display the scans of entire core sections, which were cut into segments of 0.55 m after the scanning. The top always represents the upper part of the core segment. The segments vary in length as the recovered core pieces are not always exactly 1.10 m long. Some of the pieces also fractured during the recovery process or during preparation. The images have been partly processed by applying a Gauss filter to enhance the visibility of the layering, and therefore the grey values are no indication of impurity content (or of other parameters which could influence the backscatter within the ice).
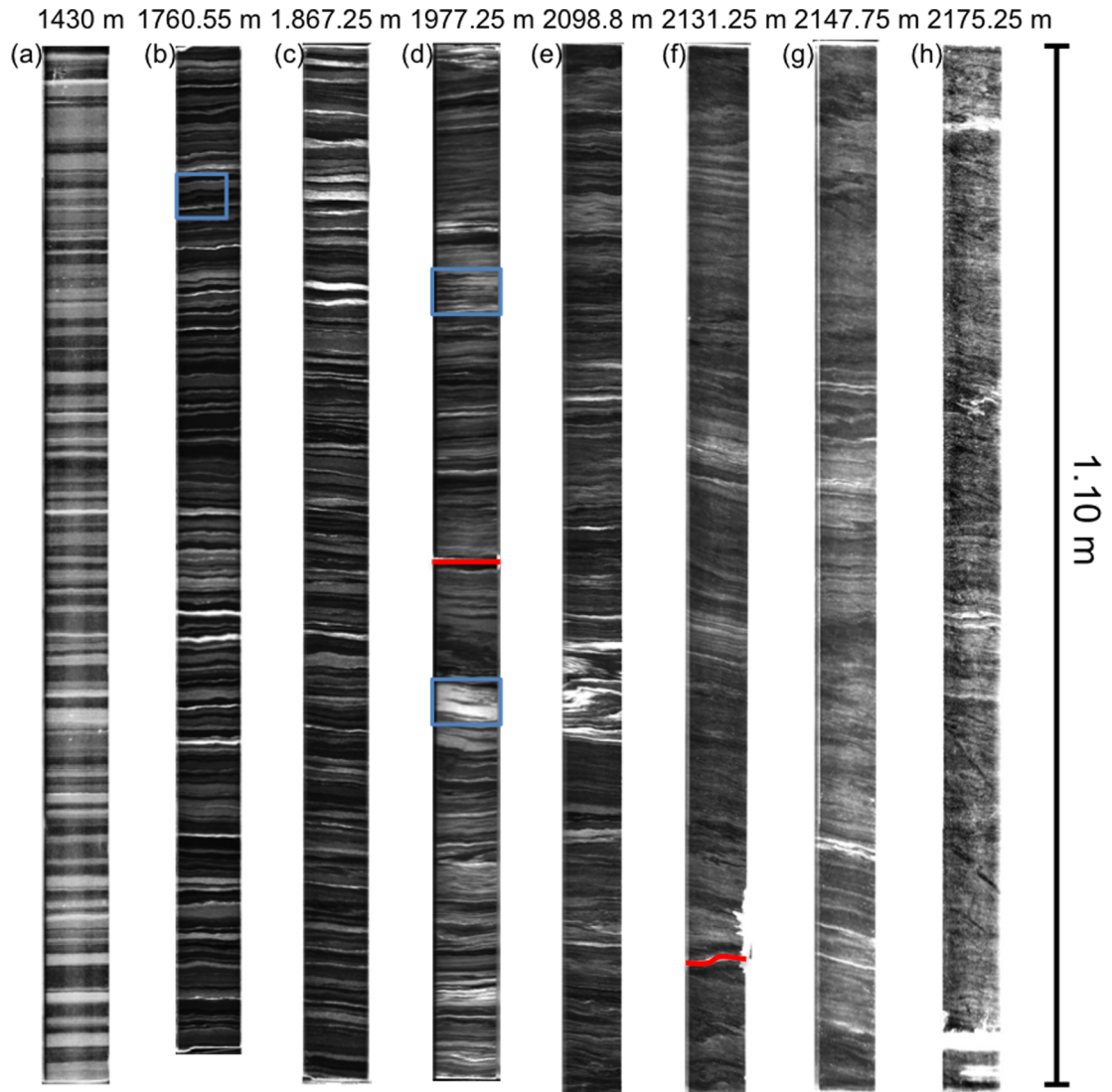
Figure 4.1: Visual stratigraphy overview. Linescan images from different depths. A Gauss filter was applied to images shown in panel (a), (d), (e), (f), (g), and (h) to enhance the visibility of the layers. Red lines indicate fractures. Blue squares indicate location of enlargements shown in Figure 4.2.

The upper part of the NEEM ice core shows little or no disturbances. Fig. 4.1a shows an example from 1430 m depth with perfectly horizontal layers. The layer thickness and opacity does vary in the core segment, the single layers do have a constant thickness throughout the section. A close up of one of the layers shows no particular structure within the cloudy band (Fig. 4.2). Below a depth of about 1700 m the layering begins to show disturbances. Fig. 4.1b,c show examples from depths of approximately 1760 m and 1867 m. Wave-like disturbances with cm-scale amplitudes and wavelength in the order of the core diameter can be observed. In parts of the core segments these disturbances can be clearly followed through several layers. Fig. 4.2 shows an enlarged section of Fig. 4.1b, showing a well-developed asymmetric z-fold. The shape of the fold indicates sinistral shear and it is beginning to overturn. The fold axis is a sharp feature, which can be followed

over several layers. The enlargements in Fig. 4.2 also show that the layers themselves appear to be laminated.
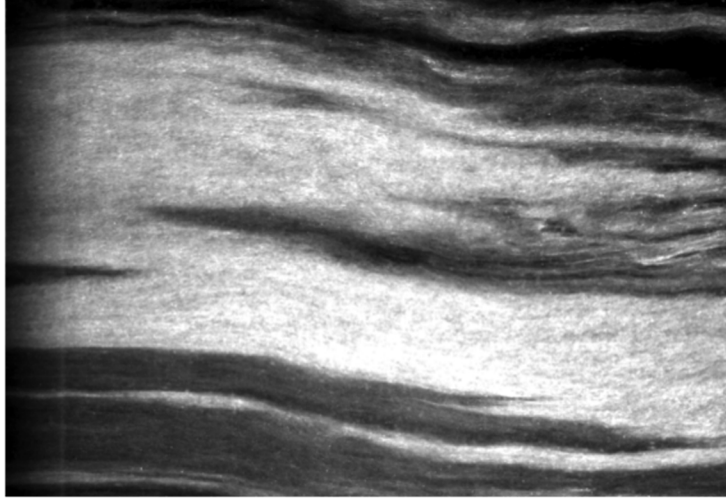
Figure 4.2: Close-ups from the overview Fig. 4.1. (a) angular z fold consistent throughout layering (from Fig. 4.1 panel (b)). (b) Strongly disturbed layer significantly thickened (from Fig. 4.1 panel (d)). (c) Different generation of folds (from Fig. 4.1 panel (d)).

For the core sections shown in Fig. 4.2b,c the layers do already vary in thickness, as can be clearly seen in Fig. 4.2a, where the central greyish layer nearly doubles its thickness in the centre. Fig. 4.1d,e show examples from 1977 m and 2098 m depth. Here the layering is significantly more disturbed. The vertical scale of the disturbances has risen to the scale of ten centimetres. In between the larger-scale folds the layering appears to be more regular again, however the limited width of the core sections also limits our interpretation here, as the layers could have been flattened out by shear deformation. There are also new generations of folds standing out through their well-defined and steeper fold axes (Fig. 4.2c).

At even greater depth the layering becomes less distinct (Fig. 4.1f,g,h). In some parts of these sections the layers appear to be undisturbed but inclined, which might indicate that they are part of a larger deformation structure. The now very thin layers still show new generation of folds. Below a depth of approximately 2200 m it is no longer possible to see fold structures in the visual stratigraphy data as the ice is mostly clear.

4.3.2   Crystal fabric orientation anomalies connected to folds

The general evolution of the fabric of the NEEM ice core has been described in Montagnat et al. (2014). The c-axis orientation distribution develops from an isotropic fabric more or less linearly to a single maximum at a depth of about 1500 m, which also represents the transition from the Holocene to the last glacial (Rasmussen et al., 2013). Within the well-developed single maximum fabric we found inclined bands of grains with a deviating c-axis orientation. We assume that the bands are planar features, but as the thin section

are vertical cuts through the cylindrical core section the inclination of the bands is not necessarily equal to the inclination of the planes. These bands have been found before in the GISP2 ice core (Alley et al., 1997), but for NEEM there is significantly more fabric data available which enables us to follow these structures through entire core sections.

One of the first examples of such a band, shown in Fig. 4.5a, appears at a depth of 1800 m. The c-axis orientation of the bands is tilted to the left relative to the single maximum, which is indicated by the blue-greenish colours in the colour wheel used to illustrate c axis orientation (inset in Fig. 4.5a). Their grain size does not differ from the average grain size of the sample. The subgrain boundary density in these grains does not change from the surrounding ones, thus they are most likely not newly nucleated (4.3b). However, while the subgrain structures in the vertically orientated grains are mostly parallel to the basal planes, they are mainly perpendicular in the grains of the band, indicating the onset of rotation recrystallisation.

The direct comparison of these data with that arising from visual stratigraphy reveals that these bands are connected with disturbances in the layering. Their inclination is in agreement with the sense of shear. Dextral folds in layers are connected with bands tilted to the left and vice versa (Figs. 4.5,4.6) However, not everywhere disturbances are visible in the linescan image we find anomalies in the fabric. If the bands occur in several parts in one core section, their inclination and orientation appears to be consistent throughout (Fig. 4.4).
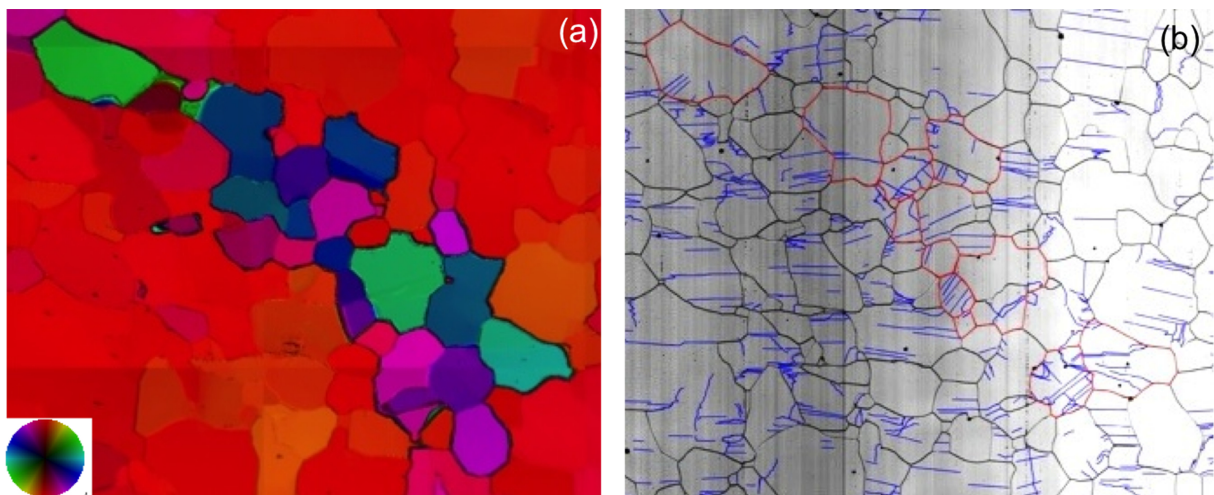
Figure 4.3: (a) close-up of a kink band grains at approximately 1803 m depth (bag 3276). Inset shows the colour code for c-axes orientation (b) subgrain structures (blue) visible on LASM data. Black lines indicate grain boundaries, the red outlines highlight the kink band grains.

4.3.3 Model results

To understand the development of the observed fabric anomalies and the related disturbances in the layering, we simulated the evolution under simple shear with an initially well
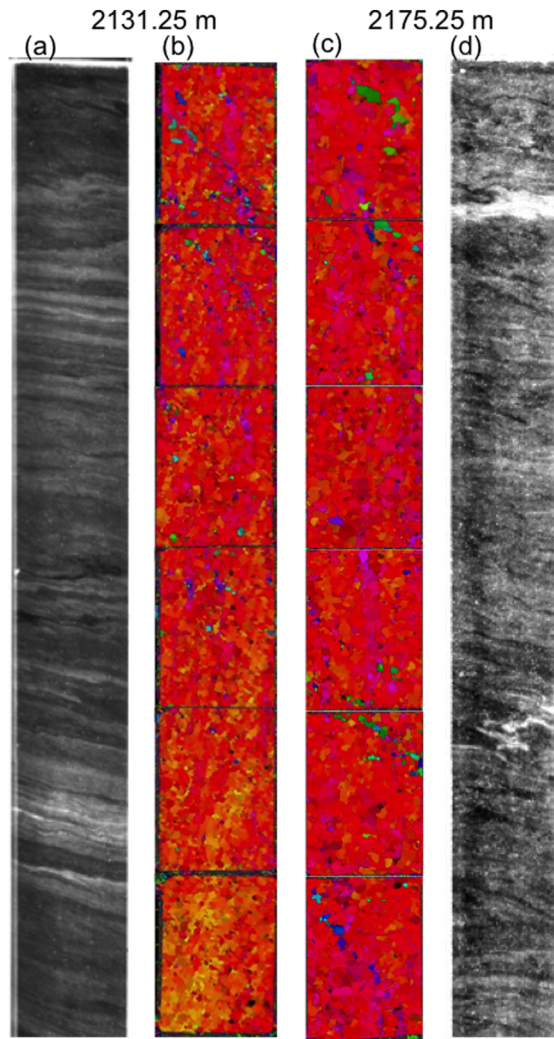
Figure 4.4: Comparison of entire core sections of linescan (a,d) and fabric data (b,c).
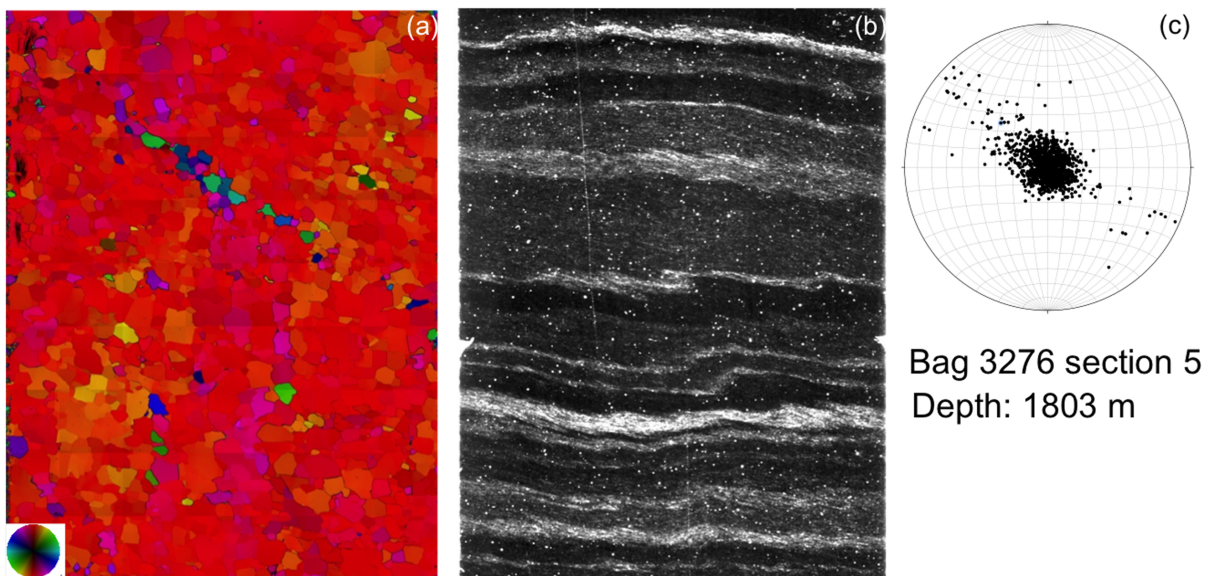
Figure 4.5: Comparison fabric data and visual stratigraphy in detail, Bag 3276, approximate depth 1803 m. (a) fabric data, (b) linescan image, (c) stereoplot of c-axes orientations.
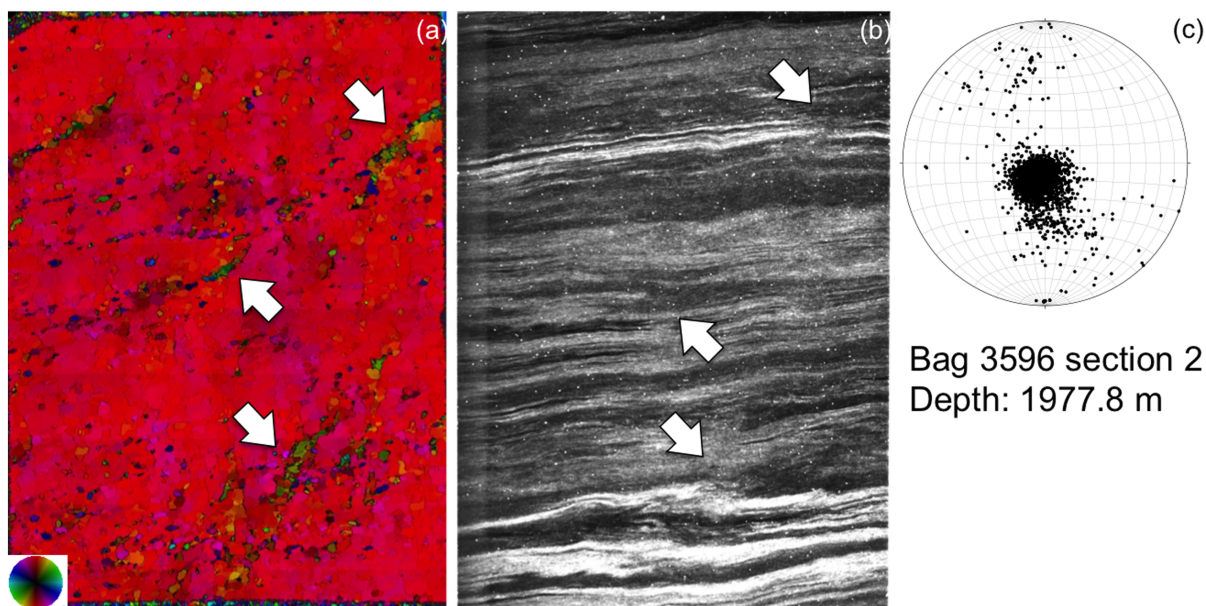
Figure 4.6: Comparison fabric data and visual stratigraphy in detail, Bag 3596, approximate depth 1977.8 m. (a) fabric data, (b) linescan image, (c) stereoplot of c-axes orientations.
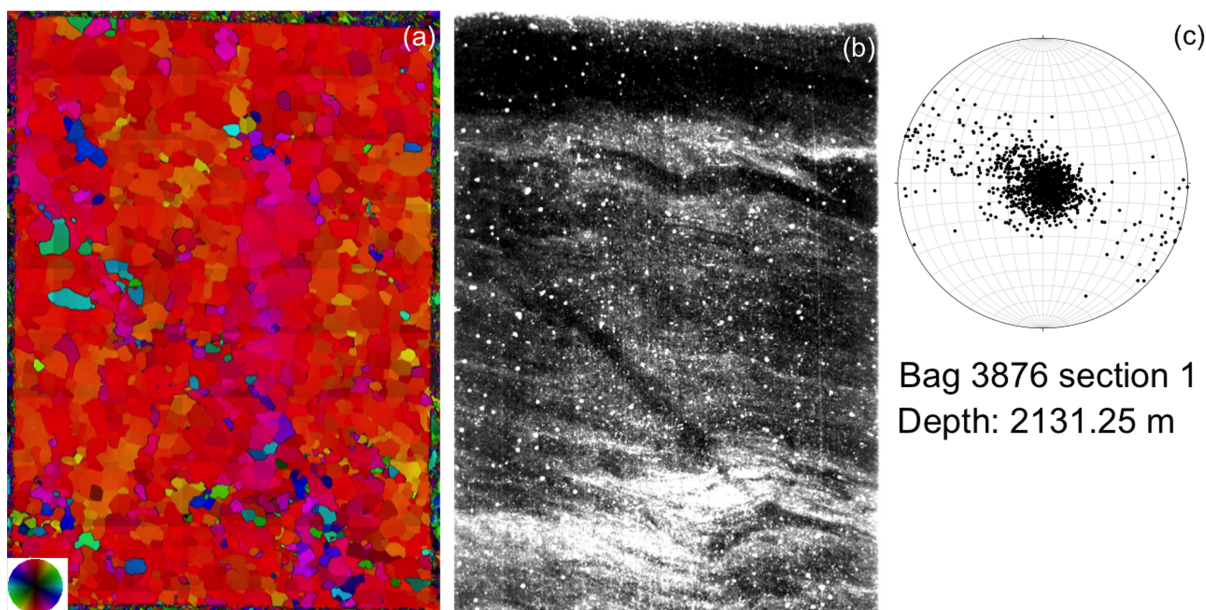
Figure 4.7: Comparison fabric data and visual stratigraphy in detail, Bag 3876, approximate depth 2131.25 m. (a) fabric data, (b) linescan image, (c) stereoplot of c-axes orientations.

developed single maximum orientation distribution, with a random noise of <5°. The setup of the simulation does not fully represent the boundary conditions in the region of the ice core where we observe the structures, since a combination of vertical compression and simple shear affected this part of the ice sheet. We model these structures in simple shear for simplicity. This approach is reasonable, since there is a non-coaxial flow component in the region and fold geometries in pure and simple shear are not very different (Llorens et al., 2013a). Moreover, the choose of simple shear boundary conditions is also justified by the fact that the bands start to appear in the lower third of the ice core where shear

stress becomes the dominant driver for deformation.

Already after the first five modelling steps (shear strain of $\gamma=0.2$) vertical bands of grains develop, with c-axes are slightly tilted to the left. These bands intensify during the next steps and begin to tilt due to the continuing shear deformation (Fig. 4.10). Also the c-axis orientation of the bands is further tilted under continuing shearing. Fig. 4.9a-c shows the c-axis orientation for the sample after shear strains of $\gamma=1$, $\gamma=2$ and $\gamma=3$. The bands seem to develop in different generations, which can be distinguished by their inclination because the new bands are steeper. The orientations of c-axes between the bands rotate towards the opposite direction (orange-yellow colours), but on a larger scale and not in narrow bands. In later stages of the simulation the oldest bands begin to disintegrate with the grains recrystallizing back to a vertical c-axis fabric. The results shown here are calculated with 10 steps of recrystallisation per deformation step. In the case of the simulation with one step recrystallisation per deformation step the kink bands formed in the same places but presented lower intensities and slower change of orientation of the grains within the bands.
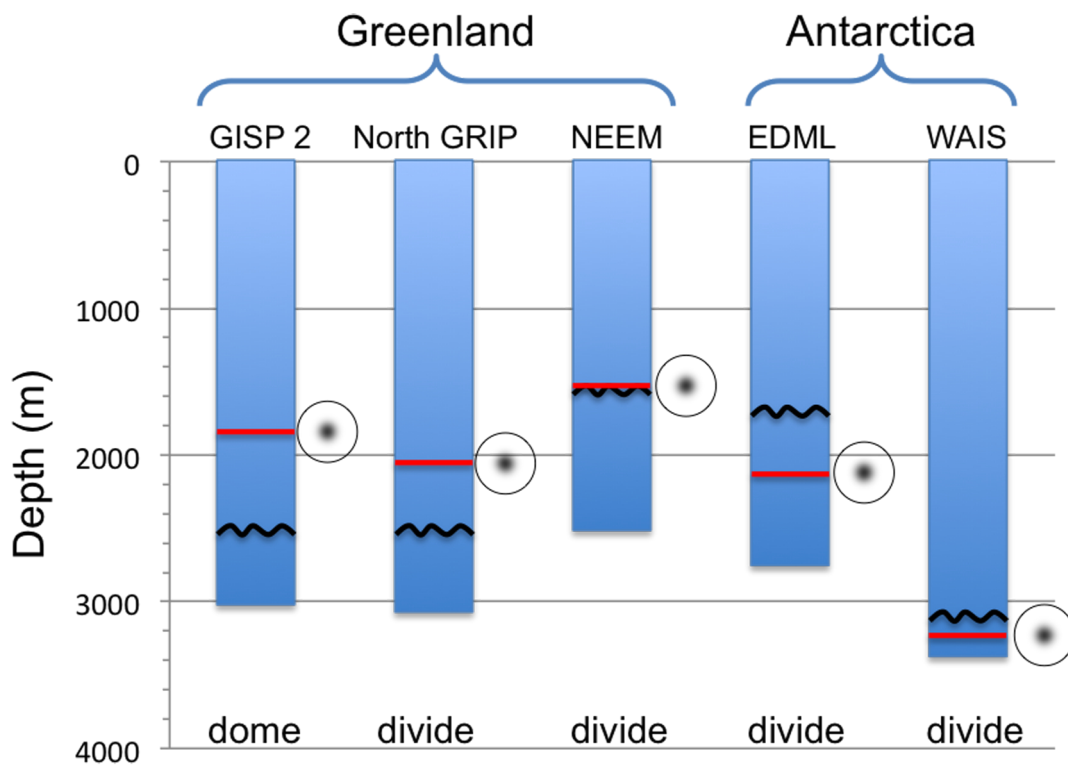
Figure 4.8: Comparison of the onset of visible folding in ice cores with published visual stratigraphy. The red line indicates single maximum fabric, the black line indicates onset of folding.

Fig. 4.9d-e displays the development of a passive marker grid during the simulations. The blue lines were perfectly horizontal at the beginning of the simulation and can be regarded as an analogue to the stratigraphic layering observed in the ice core. It is apparent that the bands described above are connected with kinks in the layering. At

first these kinks appear as small steps, but they develop into overturned folds with a short and steep limb with progressive deformation. They correspond to the well-developed bands in the fabric, and to a long, less inclined limb, representing the area in between the bands. The deformation step in the passive layering is larger when the grains in the bands are orientated in a way that the easy glide direction is oriented along the band. This leads to intensification and narrowing of the bands, and to a larger step of localised deformation along the bands (Fig. 4.11). In the following steps the bands are increasing their inclination further due to progressive shearing, and also the orientation is tilting more, but the combination of both is no longer orientated for easy glide along the bands. Thus, the fold amplitude in the passive grid is not increased further, but subject to a passive overturning. Moreover, in the passive grid the different generations of the bands are distinguishable, which interfere with each other. The disturbances in the layering are permanent, and therefore the bands are visible in the passive grid even when they no longer exist in the orientation plot. The development of the kink bands is represented in the model run, but the flattening out of the structures probably takes place faster in reality in a way folds become recognizable. This might be a possible explanation for the existence of a layered structure in the deeper parts of the NEEM ice core.
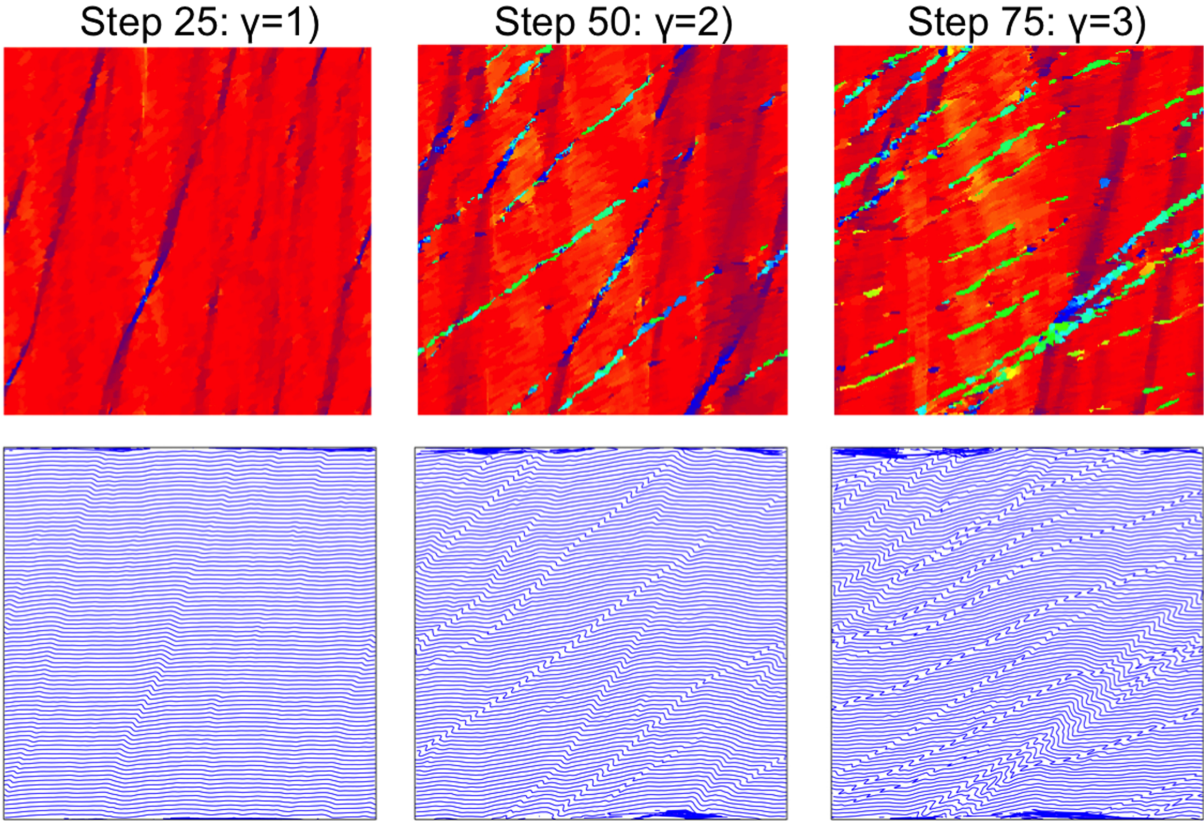
Figure 4.9: Elle model results for the simple shear experiment. Panels (a), (b) and (c) show c-axes orientations. Panels (d), (e) and (f) show the distortion of the passive grid marker.

4.4 Discussion

4.4.1 General discussion of folds

The shape of the observed folds in the NEEM ice core is typical for similar folds, as the layers are thickened in the hinge region and thinned in the fold limbs. Similar folds are typical passive features, where all layers of the package are deformed in a similar way. In contrast to parallel folds, where the thickness of the layer remains constant along the observed feature, no competence contrast is required for their formation. Although there might be changes in the softness of the ice between the layers due to different impurity content, the observed folding appears to be consistent over several stacks of layers (Figs.1 and 2). These folds can be initiated by simple shear and can develop from small-scale perturbations. Under continuing shear they can evolve to become overturned z-folds. In the case of parallel or buckle folding the more competent layer is folded, while the softer embedding layers accommodate the strain by deformation on smaller scales and do not necessarily maintain integrity. This is not what we do observe in the NEEM ice core. The formation of these buckle folds requires a high viscosity contrast between the layers (factor 25, see Llorens et al. 2013a,b), a variation which is not realistic at this small-scale in ice.

Comparison with data from EDML (Faria et al., 2010) and WAIS (Fitzpatrick et al., 2014), from Antarctica and with GISP2 (Alley et al., 1997) and North Grip (Svensson et al., 2005) from Greenland reveal that the onset of visible folding is dependent on the relation between vertical strain rates and shear strain rates (Fig. 4.8). As an approximation we can assume that in the upper two thirds of the ice column the vertical compression is dominant, while the shear component is large in the lower third (Dansgaard Johnson). The later onset of folding in the deeper ice cores shows that higher shear strain is required to produce visible folding due to the higher overburden pressure. This has been theoretically described by Waddington (2001). If vertical compression is high, fold structures are flattened out before they overturn, and are thus no longer visible.

The scale of the disturbances found in the visual stratigraphy of the NEEM ice core is very similar to the ones observed at EDML by Faria et al. (2010). Thorsteinsson and Waddington (2002) numerically explored the influence of anisotropy to folding in ice cores and found that anisotropy and the occurrence of "regions of unadjusted fabric" can facilitate folding in ice due to local flow anomalies. However they stated that the source of the anomalous fabric is still unclear.

4.4.2 Kink bands as a source for folding

We also find from the observation and modelling results that a strong anisotropy is required to produce folds in ice. We further suggest that the initial disturbance is similar to kinking in single crystals. Kinking has been observed in single ice crystals as well as

in polycrystalline aggregates under compression (Wilson et al., 1986). The ELLE model results show a similar feature: for the single maximum fabric vertical stripes develop already in the first deformation stages, which only show a slight deviation of the c-axis from the vertical orientation. Kink bands are usually associated with a compressional regime. The developing bands under vertical compression would be inclined to the vertical at an angle, which is related to the angular shift in the orientation (Frank and Stroh, 1952). In the model we do have a simple shear environment, corresponding to compressive stress at an angle of 45° to the vertical direction. We assume that this leads to near vertical kink bands to start with instead of inclined bands. In this first step, the kinking and the disturbance for the layering are hardly visible. However, once established, the modelled kink bands rotate further as described above. The orientation of the grains in the band is tilting further, their c-axes rotating in the opposite direction relative to the rotation of the band itself.

As described in section 4.3.3 the effect of the anomalous fabric bands on deformation is highest when the basal planes are aligned with the inclination of bands. This configuration enables sliding along the band direction, which is visible in the passive marker gird as a significant increase of the amplitude of the disturbance. Thus, the rotated kink bands act as a shear plane, localizing shear deformation. When the bands rotate further due to progressive deformation, the grains are no longer aligned for gliding along the bands, which leads to a further passive deformation of the disturbances in the passive grid. However, the disturbances in the passive grid stay visible because recrystallisation of the kink bands gradually erodes them and they begin to disappear.

In summary, the model results indicate that the kink bands are active as shear planes only for a short period of time, initiating local disturbances of the layering similar to thrust faults. Thus it is difficult to find an active shear band in the observations, since the ice core samples only represent a snapshot in time. The fabric data of most of the analysed examples indicates that the rotation of the c-axis orientation within the kink bands exceeds 90° from the vertical direction, and the band do have gaps due to recrystallisation to a single maximum fabric. In cases where the kink bands can be associated with strong disturbances in the layering, the shearing along the plane of the bands must have already taken place.

Another difficulty with the observational data is that we can only capture a 2-dimensional section of a 3-dimensional process. Assuming the kink bands are planar features, the angle at which the cylinder of the ice core is cut relative to the inclination of the plane determines its appearance on the 2-dimensional section. Thus, the inclination of the bands in the plane is not sufficient to describe the full orientation of the kink plane. This also has to be taken into account when interpreting the fold structures on the linescan images.

Within one section of the ice core (bag) the cutting plane through the core is consistent

and thus the samples used to prepare the thin sections for the fabric measurements. Fig. 4.4 shows that within one bag the inclinations of the kink bands are consistent as well, strengthening the assumption that they are connected to the local stress environment and to the sense of shear, projected onto the plane of the thin section or linescan image.

The mechanism of kinking as a trigger for stratigraphic disturbances has already been suggested by Samyn et al. (2011). However, together with the microstructural model results the observations can be seen in a different light. While Samyn et al. (2011) stated that the c-axes of the bands in the grain are aligned with the inclination of the plane, the model results suggest that this is only a later stage in the evolution of the kink bands and that the shearing along this bands take place at an earlier time, when the basal planes are aligned with the kink band inclination. Alley et al. (1997), who described similar bands in the GISP2 ice core state that they are most likely not kink bands, as they would require a compressional regime in the horizontal direction. However, the model results clearly show that thrust-like structures can form in simple shear conditions. At the moment it is not clear why the bands sometimes appear dark in the linescan images, however from deeper parts of the core where the crystals are larger in size the linescan images give indication the backscattering can be subject to the crystal orientation.

4.5   Summary and Conclusions

The onset of small-scale folding can be observed at the start of the lower third of the NEEM ice core, which is similar to the fold evolution observed in EDML (Faria et al., 2010). Below a depth of about 2160 m it is no longer possible to track stratigraphic layers. The shape of the observed structures indicate that they are no buckle folds, which means that they are not originated by a competence contrast between alternating layers. The amounts of folding as well as the state of disturbance increase with depth.

Folding causes thickening of cloudy bands and reduces the resolution of climate data extracted from ice cores. It also produces doubling of layers within the scale of ten centimetres below a depth of about 2100 m. In some core sections the layering appears to be intact in between larger folds in the linescan data. However, it is difficult to identify regions where the climate signal could be disturbed due to the limited diameter of the ice core.

Microstructure numerical modelling results indicate that the observed folding is due to localized deformation along kink bands. To produce the initial disturbances of the fabric, a single maximum fabric is required. The localized shear is at its maximum when the basal planes of the kink band planes are parallel to the inclination of the bands. The kink bands are eventually eroded through recrystallisation processes, thus we do not see bands in every fold axis.

Kinking appears to be an important deformation mechanism for ice. Although the

kinking itself does not contribute much to total strain, the inclined c-axes on the kink band enable easy glide and localize strain. Even if the kink bands are no longer active they have been recrystallizing to a single maximum fabric, while the disturbance of the layers remains.

Acknowledgements

4.6   References

- Alley, R. B., Gow, A. J., Meese, D. A., Fitzpatrick, J. J., Waddington, E. D. and Bolzan, J. F., (1997). Grain-scale processes, folding, and stratigraphic disturbance in the GISP2 ice core. J. Geophys. Res., 102 (C12), 26819-26830.

- Bons, P.D., Koehn, D. and Jessell, M.W., (2008). Lecture notes in earth sciences. In: Bons P., Koehn D., Jessell M., editors. Microdynamic Simulation. Springer, Berlin; number 106. 405 pp.

- Faria, S. H., Freitag, J. and Kipfstuhl S., (2010). Polar ice structure and the integrity of ice-core paleoclimate records. Quaternary Science Reviews, 29, 338-351.

- Fitzpatrick, J. J., Voigt, D.E., Fegyveresi, J.M., Stevens, N.T;, Spencer, M.K., Cole-Dai, J., Alley, R.B., Jardine, G.E., Cravens, E.D., Wilen, L.A., Fudge, T.J. and McConnell, J.R., (2014). Physical Properties of the WAIS Divide ice core, J. Glac., 60 (224), 1181-1198, doi: 10.3189/2014JoG14J100

- Frank, F. C. and Stroh A.N., (1952). On the theory of kinking. Proceedings of the Physical Society (Section B), 65(10), 811-821.

- Griera, A., Bons, P.D., Jessell, M.W., Lebensohn, R.A., Evans, L. and Gomez-Rivas, E., (2011). Strain localization and porphyroclast rotation. Geology 39, 275-278.

- Griera, A., Llorens, M.-G., Gomez-Rivas, E., Bons, P.D., Jessell, M.W., Evans, L. and Lebensohn, R.A., (2013). Numerical modeling of porphyroclast and porphyroblast rotation in anisotropic rocks. Tectonophysics 587, 4-29.

- Jessell, M.W., Kostenko, O. and Jamtveit, B., (2003). The preservation potential of microstructures during static grain growth. Journal of Metamorphic Geology, 21(5), 481-491.

- Ketcham, W. M., and Hobbs, P. V. (1969). An experimental determination of the surface energies of ice. Philosophical Magazine, 19(162), 1161-1173.

- Kipfstuhl, J. (2010). Visual stratigraphy of the NEEM ice core with a linescanner. Alfred Wegener Institute, Helmholtz Center for Polar and Marine Research, Bremerhaven, Unpublished dataset #743062

- Lebensohn, R. A., Montagnat, M., Mansuy, P., Duval, P., Meysonnier, J. and Phillip, A., (2008). Modeling viscoplastic behaviour and heterogeneous intracrystalline deformation of columnar ice polycrystals. Acta Materialia, 57, 1405-1415.

- Lebensohn, R. A. (2001). N-site modeling of a 3D viscoplastic polycrystal using Fast Fourier Transform. Acta Materialia, 49, 2723-2737.

- Llorens, M.-G., Griera, A., Bons, P.D., Roessiger, J., Lebensohn, R. and Weikusat, I., (submitted to Journal of Glaciology). Dynamic recrystallization of ice aggregates during co-axial viscoplastic deformation: a numerical approach.

- Llorens, M.-G., Bons, P.D., Griera, A., Gomez-Rivas, E. and Evans, L.A. (2013a). Single layer folding in simple shear. Journal of structural Geology, 50, 209-220.

- Llorens, M-.G., Bons, P.D., Griera, A. and Gomez-Rivas, E. (2013b). When do folds unfold during progressive shear?. Geology, 41, 563-566.

- Montagnat, M., Azuma, N., Dahl-Jensen, D., Eichler, J., Fujita, S., Gillet-Chaulet, F., Kipfstuhl, S., Samyn, D., Svensson, A. and Weikusat, I., (2014). Fabric along the NEEM ice core, Greenland, and its comparison with GRIP and NGRIP ice cores. The Cryosphere, 8, 1129-1138, doi:10.5194/tc-8-1129-2014.

- Nasello, O.B., Di Prinzio C.L. and Guzman, P.G., (2005). Temperature dependence of "pure" ice grain boundary mobility. Acta Materialia, 53 (18), 4863-4869.

- NEEM Community Members (2013). Eemian interglacial reconstructed from a Greenland folded ice core. Nature, 493, doi:10.1038/nature11789.

- Piazolo, S., Bons, P.D., Jessell, M.W., Evans, L. and Passchier, C.W., (2002). Dominance of microstructural processes and their effect on microstructural development: insights from numerical modelling of dynamic recrystallization. Geological Society, London, Special Publications, 200(1), 149-170.

- Rasmussen, S. O., Abbott, P. M., Blunier, T., Bourne, A.J., Brook, E., Buchardt, S.L., Buizert, C., Chappellaz, J., Clausen, H.B., Cook, E., Dahl-Jensen, D., Davies, S.M., Guillevic, M., Kipfstuhl, S., Laepple, T., Seierstad, I.K., Severinghaus, J. P., Steffensen, J.P., Stowasser, S., Svensson, S., Vallelonga, P., Vinther, B.M., Wilhelms, F. and Winstrup, M., (2013). A first chronology for the North Greenland Eemian Ice Drilling (NEEM) ice core. Clim. Past, 9, 2713-2730, doi:10.5194/cp-9-2713-2013.

- Samyn, D., Weikusat, I., Svensson, A., Azuma, N., Montagnat, N. and Kipfstuhl, S., (2011). Microstructure of the NEEM deep ice core: towards quantifying stratigraphic disturbances. Geophysical Research Abstracts, 13, EGU2011-12563-1, EGU General Assembly 2011.

- Schulson, E. M., and Duval, P. (2009). Creep and fracture of ice (p. 432). Cambridge: Cambridge University Press.

- Svensson, A., Wedel Nielsen, S., Kipfstuhl, S., Johnsen, J., Steffensen, J.P., Bigler, M., Ruth, U. and Röthlisberger, R., (2005). Visual Stratigraphy of the North Greenland Ice Core Project (NorthGRIP) ice core during the last glacial period. J. Geophys. Res, 110, D02108, doi:10.1029/2004JD005134

- Thorsteinsson, T., and Waddington, E.D., (2002). Folding in strongly anisotropic layers near ice-sheet centers. Annals of Glaciology, 35, 480-486.

- Thorsteinsson, T., (2002). Fabric development with nearest-neighbour interaction and dynamic recrystallization. Journal of Geophysical Research 107 (B1), 2014.

- Waddington, E. D, Bolzan, J.F. and Alley, R.B., (2001). Potential for stratigraphic folding near ice-sheet centres. J. Glac., 47(159), 639-648.

- Weikusat, I., and Kipfstuhl, J., (2010). Crystal c-axes (fabric) of ice core samples collected from the NEEM ice core. Alfred Wegener Institute, Helmholtz Center for Polar and Marine Research, Bremerhaven, Unpublished dataset #744004

- Wilson, C. J. L., Burg, J.P. and Mitchell, J.C., (1986). The origin of kinks in polycrystalline ice. Tectonophysics, 127, 27-48.
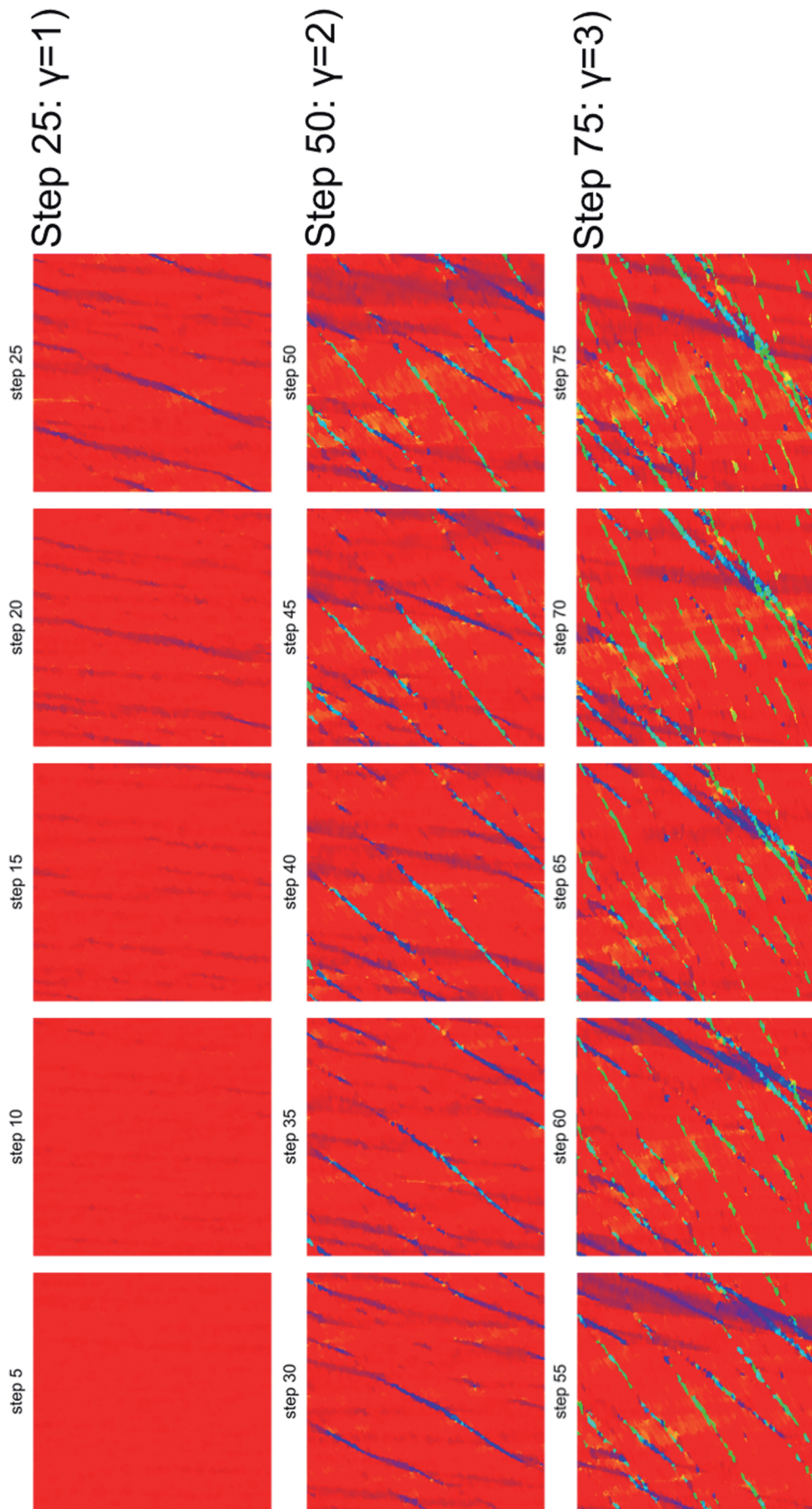
Figure 4.10: crystal orientations respect to the y direction in crystal reference frame (IPF), for a dextral simple shear simulation with 10 steps of dynamic recrystallisation per deformation step.
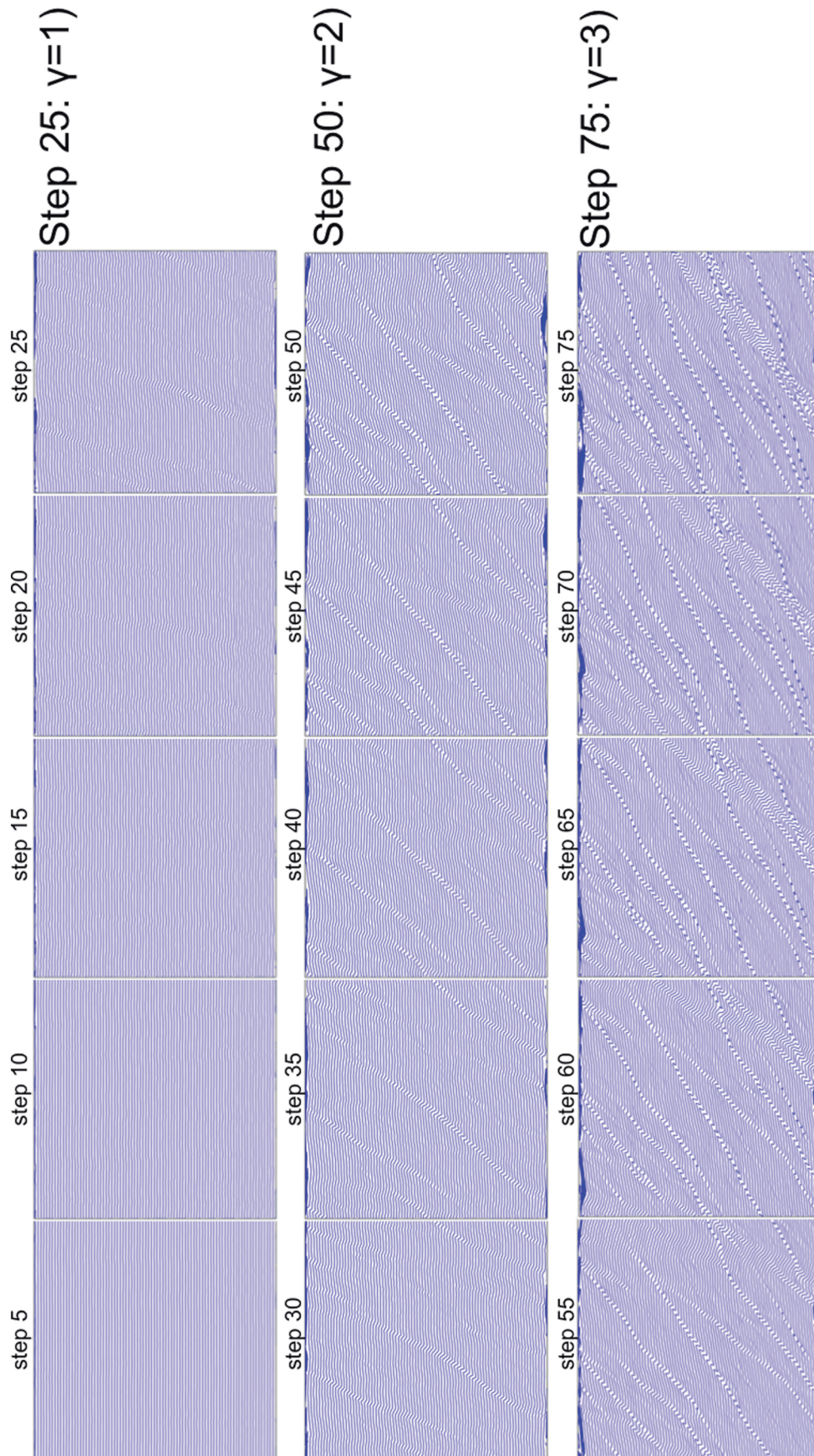
Figure 4.11: Passive marker grid evolution for a dextral simple shear simulations with 10 steps of dynamic recrystallisation per deformation step. Deformation produces the development of bands due the intrinsic anisotropy.

Chapter 5

Single layer folding in simple shear

Maria-Gema Llorens[a], Paul D. Bons[a], Albert Griera[b], Enrique Gomez-Rivas[a] and Lynn A. Evans[c]

[a]Departament of Geosciences, Eberhard Karls University Tübingen, Wilhemstr. 56, 72074 Tübingen, Germany

[b]Departament de Geologia, Universitat Autònoma de Barcelona, 08193 Bellaterra (Barcelona), Spain

[c]School of Geosciences, Monash University, Clayton, Victoria 3800, Australia

Abstract

Despite the common occurrence of simple shear deformation, laboratory and numerical simulations of folding have so far been almost exclusively in pure shear. Here we present a series of finite-element simulations of single layer folding in simple shear up to high shear strains ($\gamma \leq 4$, and up to 75% shortening of the folding layer). In the simulations we vary the viscosity contrast between layer and its surroundings (25–100), the stress exponent (1 or 3) and the kinematics of deformation (pure- versus simple shear). In simple shear fold trains do not show a clear asymmetry, axial planes form perpendicular to the developing fold train and rotate along with the fold train. Differences in geometries between folds formed in simple and pure shear folds are thus difficult to distinguish visually, with simple shear folds slightly more irregular and with more variable axial plane orientation than in pure shear. Asymmetric refraction of an axial planar cleavage is a clearer indication of folding in simple shear. The main effect of an increase in stress exponent is an increase in effective viscosity contrast, with only a secondary effect on fold geometry. Naturally folded aplite dykes in a granodiorite are found in a shear zone in Roses, NE Spain. Comparison of the folded dykes with our numerical simulations indicates a viscosity contrast of around 25 and a stress exponent of 3. The natural folds confirm that at this moderate viscosity contrast, a significant amount of shortening (20–30%) is achieved by layer thickening instead of folding.

Keywords

Simple shear; Folding; Strain analysis; Vorticity; Non-linear rheology; Numerical modelling

5.1   Introduction

Folds are very common and usually conspicuous structures in rocks that are therefore widely used to unravel rock deformation. They are classical indicators of shortening direction and amount (Treagus, 1982; Hudleston, 1986; Ramsay and Huber, 1987; Hudleston and Lan, 1993; Hudleston and Treagus, 2010 and references therein). However, folds potentially contain much more relevant information, for example on the kinematics of deformation or rock properties. Viscosity or competence contrast between a folding layer and its matrix is usually assumed to have a first order control on fold geometry, as this contrast determines the initial wavelength and amplification rate of developing folds (Biot, 1961; Ramberg, 1961; Ghosh, 1966; Sherwin and Chapple, 1968; Fletcher, 1974, 1977; Smith, 1975; Johnson and Fletcher, 1994; Schmalholz and Podladchikov, 2001). Apart from studies that focussed on fold amplification from initial perturbations, many studies also investigated the question whether fold geometry may reveal the rheology of folding layers

and their matrix. Most studies have focused on power-law rheology, where strain rate is proportional to stress to the power n (Fletcher, 1974; Smith, 1975, 1977; Abassi and Mancktelow, 1992; Mühlhaus et al., 1994; Hudleston and Lan, 1994; Lan and Hudleston, 1995; Kenis et al., 2005; Hudleston and Treagus, 2010). One problem in cases where $n \neq 1$ is that there is no single or constant viscosity contrast. This issue will be addressed further below. Other factors that may influence fold geometry are strain-dependent rheology (Lan and Hudleston, 1991; Tackley, 1998; Huismans and Beaumont, 2003; Schmalholz et al., 2005), mechanical anisotropy (Hudleston et al., 1996; Toimil and Griera, 2007; Kocher et al., 2008) or, recently, thermal effects (Hobbs et al., 2008; but see discussion by Treagus and Hudleston, 2009).

The kinematics of deformation can potentially also be deduced from the analysis of folds. Folds are common structures in many ductile shear zones, where they commonly show a strong asymmetry that can be used as a shear sense indicator (Hudleston, 1977; Quinquis et al., 1978; Ramsay et al., 1983; Passchier and Williams, 1996; Alsop and Holdsworth, 2006; Carreras et al., 2005). Strongly asymmetric folds are common at very high strains in non-coaxial deformation, where their formation has been explained with passive shearing of existing folds (Ghosh, 1966; Cobbold and Quinquis, 1980; Hudleston and Lan, 1993), although active buckling probably plays a role as well (Bons and Urai, 1996; Alsop and Carreras, 2007). Other studies, however, indicate that non-coaxial deformation does not necessarily produce asymmetric fold shapes (Ghosh, 1966) and that asymmetries arise during the final stages of fold amplification (Schmid, 2002). Several studies have pointed out that the asymmetry of cleavage patterns associated with folding is a better indicator of non-coaxial folding than the fold shape itself (Manz and Wickham, 1978). These authors observed that strain is not necessarily symmetrically distributed about fold axial planes, and that asymmetries between the two limbs arise in single layer simple shear experiments. In linear viscous simple shear models, Viola and Mancktelow (2005), however, did not observe a marked asymmetry in fold shape, but a clear difference in refraction of a developing cleavage. A complicating factor here is that layers originally oblique to the maximum shortening direction could potentially also develop asymmetric folds even in coaxial deformation (Treagus, 1973; Anthony and Wickham, 1978; Viola and Mancktelow, 2005).

Apart from theoretical and field studies (e.g. Biot, 1961; Flinn, 1962; Sherwin and Chapple, 1968; Treagus, 1973, 1981; Fletcher, 1977; Ramsay and Huber, 1987; James and Watkinson, 1994; Schmalholz and Podladchikov, 2000; Ormond and Hudleston, 2003), most of our current knowledge of fold mechanics is derived from experiments (e.g. Ghosh, 1966; Hudleston, 1973; Cobbold, 1975; Shimamoto and Hara, 1976; Manz and Wickham, 1978; Abassi and Mancktelow, 1992; Bons and Urai, 1996; Tikoff and Peterson, 1998) and numerical simulations (e.g. Chapple, 1968; Dieterich, 1970; Parrish, 1973; Stephansson and Berner, 1971; Parrish et al., 1976; Shimamoto and Hara, 1976; Hudleston and Stephansson,

1973; Anthony and Wickham, 1978; Casey and Huggenberger, 1985; Hudleston and Lan, 1994; Lan and Hudleston, 1995; Zhang et al., 1996, 2000; Mancktelow, 1999; Viola and Mancktelow, 2005; Frehner and Schmalholz, 2006; Schmid and Podladchikov, 2006; Schmalholz, 2008; Hobbs et al., 2008; Kocher et al., 2008; etc.). By far most of the studies deal with folding of single or multiple layers in pure shear parallel to the maximum shortening direction. Only a few have considered general shear or folding of a layer oblique to the maximum shortening direction (Anthony and Wickham, 1978; Schmid, 2002; Viola and Mancktelow, 2005). Considering that simple shear deformation is likely to be common in the crust, a numerical study on folding in true simple shear is long overdue.

In this paper, we present a series of numerical simulations of folding in simple and pure shear of viscous single layers. Layers are initially oriented oblique to the shear plane in the case of simple shear simulations, and parallel to the compression x-direction for pure shear models. This study aims to determine the difference, if any, in fold patterns between the two kinematic end-members.

5.2 Methods and experimental setup

5.2.1 The numerical model

Simulations were carried out with the software packages ELLE (Jessell et al., 2001, 2005; 2009; Bons et al., 2008) and the finite-element module BASIL (Barr and Houseman, 1996; Bons et al., 1997; Houseman et al., 2008 and references therein). ELLE is an open-source modelling platform used to simulate the development of (micro-) structures during tectonic and/or metamorphic processes. In ELLE, the model is defined by a contiguous set of polygons that are defined by nodes that link straight segments (Fig. 5.1). The spatial resolution of the model is constant as additional nodes are inserted or removed when boundaries are stretched or shortened. The spacing of nodes (set between 0.005 and 0.011, at a model size of 1 x 1) not only determines the resolution of the shape of the folding layer, but also determines the resolution of the triangulation for the finite-element routine (see below). A series of tests with different node spacings (between 0.00125 and 0.005 to 0.00275–0.011) was carried out to ensure that it did not influence the results.

Properties can be assigned to polygons. In this case, the only property assigned to a polygon is its viscosity (see definition below), which is constant within a polygon and remains unchanged throughout the simulation (no strain hardening or softening is considered). We define a single, more competent layer with a constant viscosity, which is embedded in a matrix with a lower viscosity. To track the finite deformation field we use a passive marker grid.

In our simulations the model is a unit cell that it is repeated infinitely in all directions. For this, ELLE uses both horizontally and vertically wrapping boundaries. A polygon

that is truncated by the right boundary thus continues on the left side. For simple shear deformation, an initially square model remains square, which significantly reduces the boundary effects that would arise if the model were to shear into a parallelogram. In pure shear simulations boundaries are also periodic, but the unit cell does not remain square.

All simulations presented here are for the folding of a single competent layer in a homogeneous isotropic matrix. The layer is originally inclined with respect to the shear plane in simple shear. The initial layer thickness is 0.025 for all simulations, 1 being the size of the simulation bounding box in simple shear. It should be noticed though, that due to the wrapping boundaries, the initial model in simple shear effectively consists of multiple layers that finally shear into a single vertical layer (see Fig. 5.1a).

The simulations presented below address two main questions: (i) What is the difference in fold geometry between pure shear and simple shear? and (ii) What is the difference between folding in linear ($n = 1$) and non-linear ($n = 3$) materials? For this we varied (a) the viscosity contrast ($m = 25, 50, 100$), (b) the stress exponent ($n = 1, 3$), (c) the boundary conditions and (d) the amount of finite shortening (Table 5.1):

- Horizontal dextral simple shear up to a shear strain of $\gamma = 2$ and $\gamma = 4$, with a square unit cell of dimensions 1 x 1. For $\gamma = 2$, the folding layer was initially inclined 27° and shortened 59%, while for $\gamma = 4$, it was inclined 14° and shortened 75%. At the end of the simulation, the layer is oriented normal to the shear plane.

- Vertical pure-shear shortening by 59% (starting as $\sqrt{5}$ by $\frac{1}{\sqrt{5}}$ rectangle) and 75% (starting as $\sqrt{17}$ by $\frac{1}{\sqrt{17}}$ rectangle) to end up with a square model of dimensions 1 x 1. The layer is oriented parallel to the maximum compression x-direction for all deformation stages.

5.2.2 Finite-element method

BASIL is a 2D finite element (FEM) package that calculates non-linear viscous deformation in plane strain (Houseman et al., 2008). BASIL is used to compute viscous strain rates and the associated stress fields. An incompressible, viscous constitutive law is assumed for both folding layer and matrix. Here the deviatoric stress tensor (τ_{ij}) is related to the strain rate tensor ($\dot{\varepsilon}_{ij}$) with:

$$\tau_{ij} = 2\eta\dot{\varepsilon}_{ij} = \eta \left[\frac{\partial u_i}{\partial x_j} + \frac{\partial u_j}{\partial x_i} \right] \tag{5.1}$$

where u is the velocity in either the x or y direction, and η is the viscosity which is defined by:

$$\eta = \left(\frac{B}{2} \right) \dot{E}^{((\frac{1}{n})-1)} \tag{5.2}$$
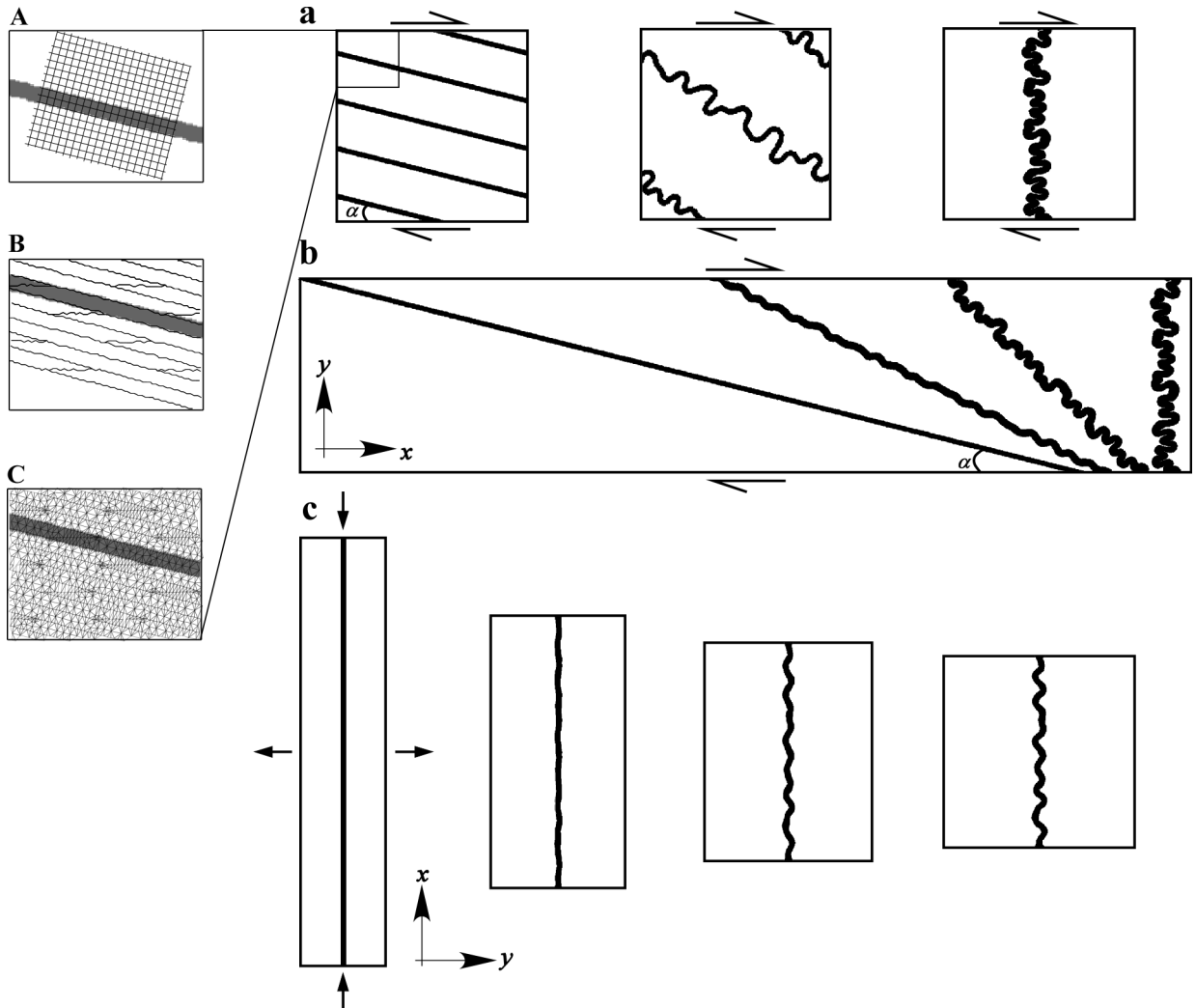
Figure 5.1: Example of the initial configuration and evolution of the simulations in (a) - (b) simple shear, (c) pure shear. Black and white represent the layer and matrix, respectively. The model is defined in three ways: A: a passive and initially square grid parallel and perpendicular to layering used to trace the local accumulative deformation; B: a segment network used to define layers and matrix; and C: a Delaunay triangulation mesh preserving the layer boundaries is used for FEM calculations. A new mesh is created every time step. (a) Three stages of folding in simple shear shown as the square ELLE model. (b) Unwrapping the wrapping boundaries allows visualisation of the shortening of a single layer.

where B is the strength coefficient, n denotes the stress exponent, and $\dot{E}$ is the second invariant of the strain rate tensor. In the simulations, the stress exponent was either n = 1 (i.e. Newtonian viscous) or n = 3, but always equal for layer and matrix. A stress exponent of 3 was chosen as it is in the range of values expected for dislocation creep in minerals, such as quartz (e.g. Kirby, 1983). Higher stress exponents could have been used, but would have significantly increased the runtime of simulations. The viscosity contrast (m) is defined as the ratio between the strength coefficient (B) of the layer and of the matrix. A triangular mesh is generated using the nodes and respecting the polygon boundaries and the velocity field is represented using quadratic functions on this mesh. Viscosity contrasts of up to 100 were used, as the code would not converge at higher viscosity contrasts in combination with non-linear rheologies.

5.2.3 Boundary conditions

Although ELLE uses fully periodic boundaries in x and y directions, the finite-element module BASIL only has periodic boundaries in the horizontal direction. For simple shear, rigid-plate velocity conditions (i.e. $u_x = \pm\gamma_{inc}$, $u_y = 0$) are applied to the horizontal top and bottom boundaries to achieve a shear strain increment (γ_{inc}) of 0.025 per calculation step. Traction and velocity are continuous across the periodic boundaries. After each strain increment, all nodes (and hence polygons) are repositioned into the square unit cell. These boundary conditions have the disadvantage that rotation of the folding layer is inhibited at the top and bottom boundary. To counteract this numerical artefact, the model is shifted upwards by a random distance (S) before every deformation calculation, after which BASIL carries out the strain increment. The model is subsequently shifted down the same amount S and repositioned again into the unit cell. This way, the boundary conditions are applied to a different level each time and the resulting artefacts are delocalized. A similar procedure was used by Jessell et al. (2009) with identical boundary conditions.

For pure shear, velocity boundary conditions, representing 1% vertical shortening, were applied to all four sides of the model. We also shifted the model perpendicular to the x-axis a random distance S before every strain increment. The initial shape of the model was rectangular with dimensions such that a square shape was achieved at the end of a simulation.

5.2.4 Initial perturbations

Folds essentially form by selective amplification of irregularities in the folding layer. Whereas such irregularities are always present in natural rocks, they have to be introduced in numerical models. The choice of initial perturbations is not a trivial matter as these can potentially have significant effect on fold development (Zhang et al., 1996, 2000; Mancktelow, 1999).

We applied an initial uncorrelated noise by randomly shifting the position of nodes of the competent layer perpendicular to the layer boundary. The distance of each shift is a random distance between $\pm D$, where D is the ratio between the layer width (H) and the maximum shift. D-values of 10, 20, 30, 40 and 50 and viscosity ratios of $m = 10, 25, 50, 100, 150$ and 250 were tested in pure shear simulations up to 70% shortening. To allow comparison, the A/λ versus H/λ data for different viscosity contrasts and initial noise are plotted in Fig. 5.2 together with those of the analytical model of Schmalholz and Podladchikov (2001). As our $D = 40$ simulations are closest to their analytical model, we chose this noise for all subsequent simulations. It should however be noted that although the A/λ versus H/λ curves show a close match, the strains to achieve these in our numerical simulations differ from those predicted by the analytical model of Schmalholz and Podladchikov (2001). Strain contours obtained by Schmalholz and Podladchikov (2001) are those accumulated after the amplification of an initial sinusoidal fold has reached the nucleation threshold (i.e. when amplification by kinematic layer thickening and dynamic folding are equal). On the contrary, our strain values account for total strain accumulated from the beginning of shortening.

Experiment name	Viscosity ratio m	Initial layer orientation (α)	Stress exponent (n)	Boundary conditions	Bulk shear strain (γ)	Max. % short.
25_n1_ssh	25	14°	1	Simple shear	4	75%
50_n1_ssh	50	14°	1	Simple shear	4	75%
100_n1_ssh	100	14°	1	Simple shear	4	75%
25_n1_ssh_g2	25	27°	1	Simple shear	2	59%
50_n1_ssh_g2	50	27°	1	Simple shear	2	59%
25_n3_ssh	25	14°	3	Simple shear	4	75%
50_n3_ssh	50	14°	3	Simple shear	4	75%
25_n3_ssh_g2	25	27°	3	Simple shear	2	59%
50_n3_ssh_g2	50	27°	3	Simple shear	2	59%
25_n1_psh	25	90°	1	Pure shear	0	75%
50_n1_psh	50	90°	1	Pure shear	0	75%
100_n1_psh	100	90°	1	Pure shear	0	75%
25_n3_psh	25	90°	3	Pure shear	0	59%
50_n3_psh	50	90°	3	Pure shear	0	59%
100_n3_psh	100	90°	3	Pure shear	0	59%

Table 5.1: Settings of the simulations presented in this paper
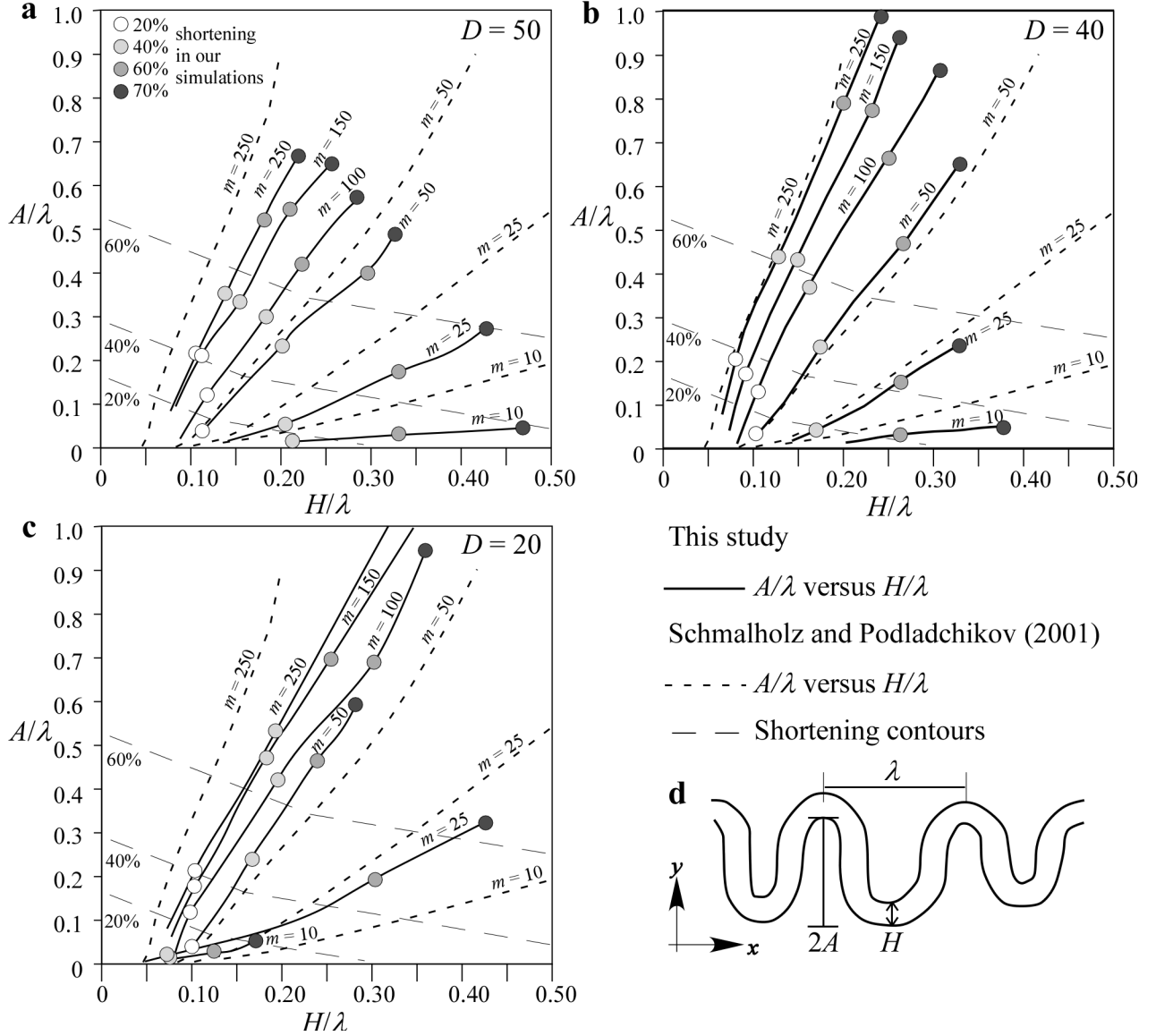
Figure 5.2: Ratios of A/λ and H/λ from measured folds of simulations of viscous folding in pure shear plotted in the strain contour map of Schmalholz and Podladchikov (2001). Dashed lines mark the analysis by Schmalholz and Podladchikov (2001). Closed lines mark the results of our simulations. Sub-horizontal dashed lines are contours of layer shortening in percent of Schmalholz and Podladchikov (2001). Dots indicate layer shortening in percent of our models. Magnitude of the initial perturbations was set at (a) $D = 20$, (b) $D = 40$ and (c) $D = 50$. (d) definition of the parameters A, H and λ.

5.3 Experimental results

5.3.1 Linear ($n = 1$) viscosity models: comparison of single layer folding in simple and pure shear

To compare the evolution of single layer fold geometries in simple shear and pure shear, we used simulations with the same starting layer length and thickness, linear viscosity ($n = 1$) of both layer and matrix, and 75% finite shortening of the folding layer. We varied the boundary conditions (pure versus simple shear) and viscosity contrast ($m = 25$, 50, 100).

In both pure and simple shear fold trains develop consisting of a dozen individual folds (Fig. 5.3). As expected, layer thickening decreases and amplitude increases with increasing viscosity contrast. Layer thickening occurs in particular at the early stages, while buckling instabilities are still developing. There is a noticeable difference in the onset of folding between pure and simple shear simulations. Folds are already clearly noticeable at 20% layer shortening in pure shear, but only at about 30% in simple shear. Otherwise, the folds in pure and simple shear are quite similar at first sight. Most importantly, there is no clear asymmetry in simple shear folds. Axial planes of the folds develop approximately perpendicular to the folding layer. As the layer shortens and rotates during simple shear, the axial planes rotate as well and maintain their orientation roughly perpendicular to the fold train.

There is, however, a difference in fold geometry between pure and simple shear. Folds are more irregular in simple shear, with a higher tendency to form "box-folds" and "double hinge folds" (Fig. 5.4). Wavelength, amplitude and axial plane orientations are all more irregular in simple shear than in pure shear.

Both simple shear and pure shear develop a single dominant wavelength without the development of second order, parasitic folds. The wavelength increases with increasing viscosity contrast and is roughly in accordance with that predicted by the Biot's theory (Biot, 1961). However, at around 60% shortening, the whole fold train begins to buckle to form larger wavelength folds. This is probably the result of the folds "locking up" and the whole fold train begins to act as a single competent layer. As this composite layer is thicker than the original single layer, the resulting wavelength is larger. Original folds keep tightening during this process, but their axial planes are rotated passively in the limbs of the larger-scale fold, resulting in a fanning of axial planes. This effect appears more pronounced in simple shear than in pure shear.

The above indicates that differences in fold geometry between pure and simple shear are relatively minor and probably not enough to determine flow kinematics from analyses of the geometry of natural folds. Additional information on kinematics can, however, be derived from the orientation of cleavage that is commonly associated with folding (Manz and Wickham, 1978; Viola and Mancktelow, 2005). Cleavages often show cleavage
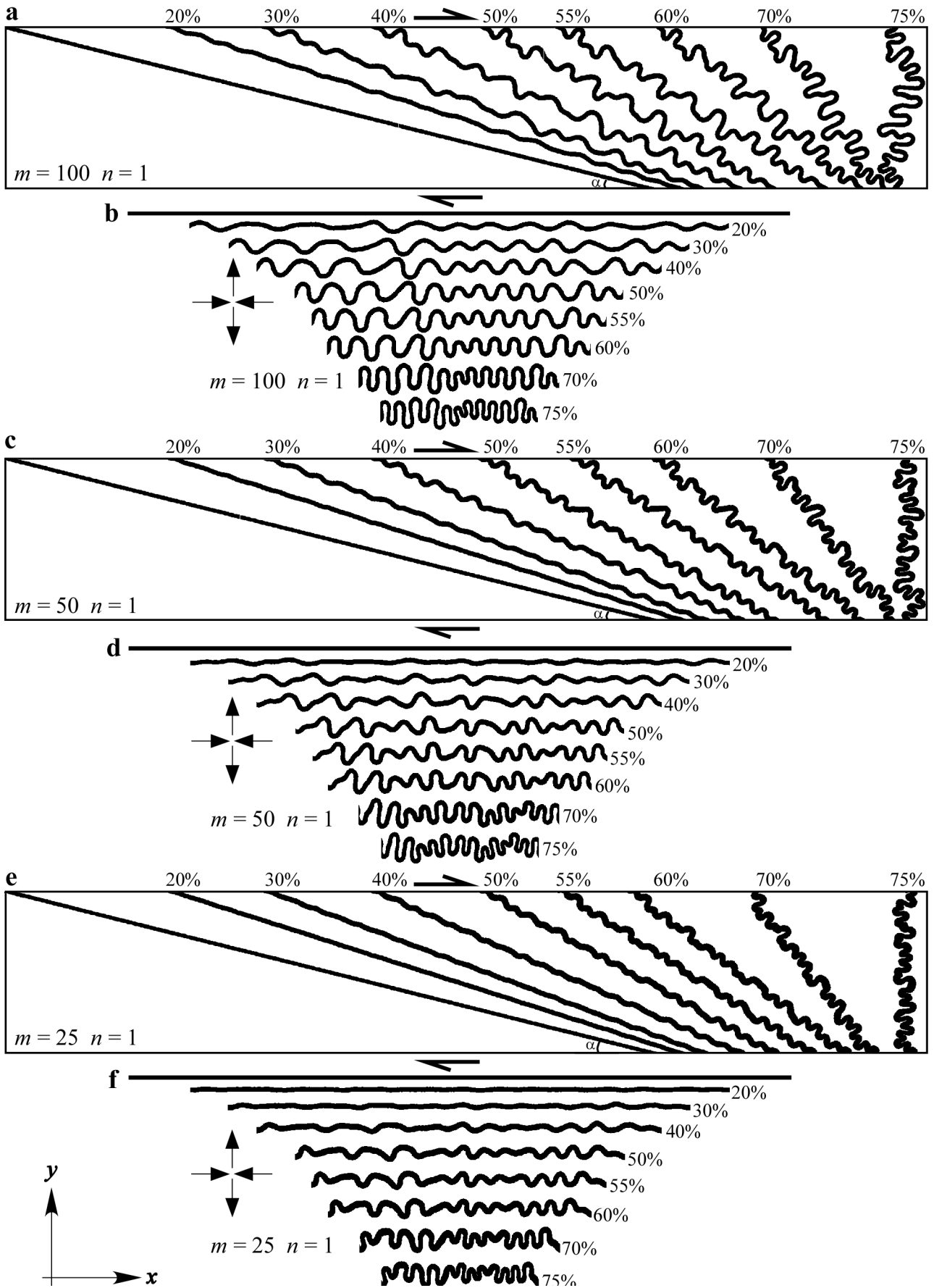
Figure 5.3: Progressive shortening of a single layer that is folding in (a), (c) and (e) simple shear, and (b), (d) and (f) pure shear. Viscosity contrast (m) varies from 100 (a–b), 50 (c–d) to 25 (e–f) at a stress exponent of $n = 1$.

117
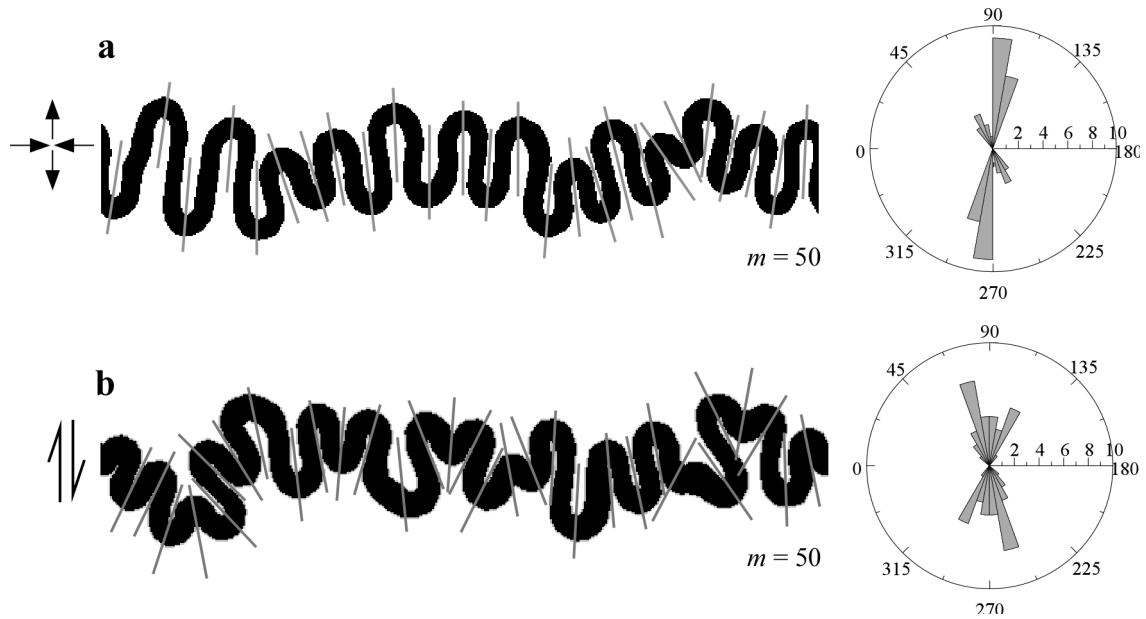
Figure 5.4: Axial plane orientation distribution at 75% of shortening in (a) pure shear and (b) simple shear simulations, with linear viscosity ($n = 1$) and viscosity contrast (m) of 50. Axial plane orientations are clearly more variable in simple than in pure shear.

refraction, where the cleavage typically makes a larger angle with layering in competent layers than in incompetent layers, which can be used to estimate viscosity contrast (e.g. Treagus, 1983, 1988, 1999; Treagus and Treagus, 2002).

An axial planar cleavage is usually expected to develop parallel to the long axis of the finite strain ellipse. The current numerical code, however, does not allow us to record the orientation distribution of the finite strain ellipse. To predict the orientation and refraction of an axial planar cleavage, we assumed that this cleavage formed by passive rotation of the orientation of the initial incremental maximum stretching direction (i.e. perpendicular to shortening for pure shear and initially perpendicular to the layers for simple shear). Even though this may not give an accurate prediction of the expected cleavage development, it serves as a qualitative proxy. Using the marker grid the reorientation of this direction could be tracked during progressive folding (Fig. 5.5). Strong differences between pure and simple shear are observed. In pure shear the axial planes of the folds are parallel to the cleavage in the matrix (Fig. 5.5a), and cleavage refraction is symmetric. In simple shear, the axial planes are at an angle to the cleavage in the matrix away from the folds (Fig. 5.5b–c). This is because the axial planes keep a large angle to the fold train, while the cleavage away from the fold train changes its orientation relative to the rotating fold train. As a result, refraction patterns are different in opposite limbs, consistent with the observation of Manz and Wickham (1978) and Viola and Mancktelow (2005).
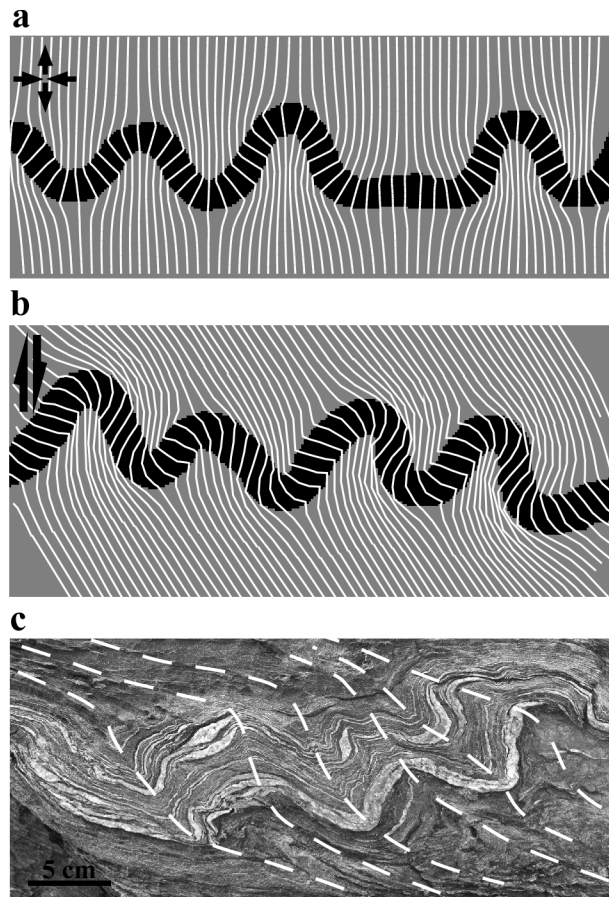
Figure 5.5: Comparison of the foliation refraction in the competent layer (represented by a passive marker grid) between models deformed under (a) pure and (b) simple shear boundary conditions, at the same amount of layer shortening (59%). (c) Example of asymmetry in cleavage in a folded set of quartz veins from Puig Culip (Cap de Creus, NE Spain).

5.3.2 Non-linear ($n = 3$) viscosity models: comparison of single layer folding in simple and pure shear

A series of simulations with the same initial configuration as the linear viscosity models ($n = 1$) were carried out in order to investigate the effect of the stress exponent ($n = 1$ versus $n = 3$) on the developing fold shapes in both simple and pure shear (Fig. 5.6 and Fig. 5.7, respectively).

The most noticeable difference between the linear and non-linear viscous simulations is the more irregular fold shapes in the latter case (Fig. 5.8). The irregularity already develops at the earliest folding stages and becomes visible at 20–30% shortening. As in the linear viscous models, folds nucleate and become visible at a lower strain in pure shear compared to simple shear. An increase in stress exponent - effectively increases the viscosity contrast (Jessell et al., 2009) compared to the linear case. This higher effective viscosity contrast is reflected in less thickening, higher amplitudes and more irregular folds. The $n = 1$, $m = 100$ simulation, for example, is thus comparable with the $n = 3$, $m = 50$ simulation (Fig. 5.8). Higher-order folds already form at high strains for $m = 25$ when $n = 3$, but not when the viscosity is linear. Higher-order folds, however, did not develop in pure shear at $n = 3$.
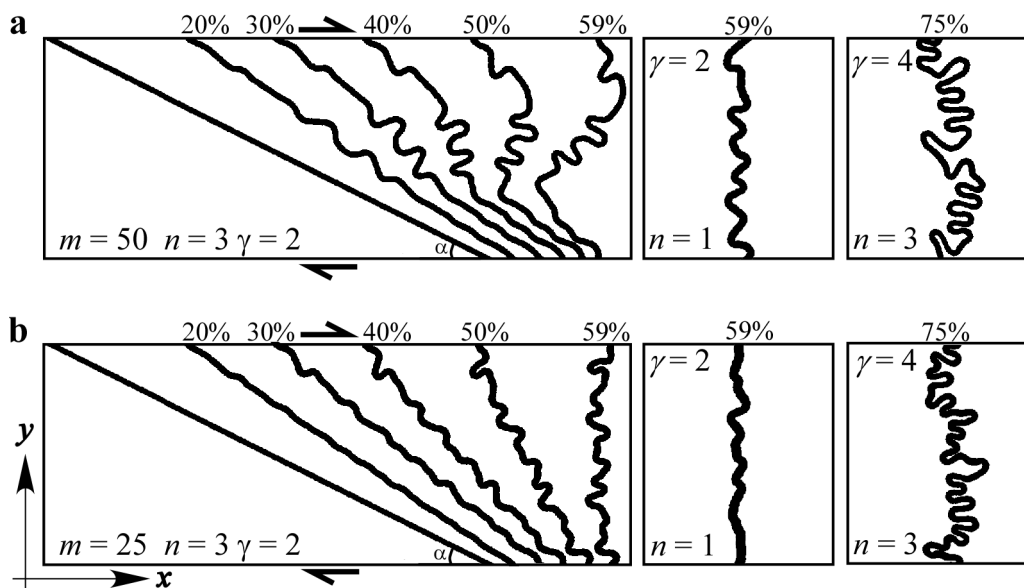
Figure 5.6: Progressive shortening of a single layer that is folding in simple shear up to a shear strain of $\gamma = 2$, where both layer and matrix have a stress exponent of $n = 3$ and a viscosity contrast of $m = 50$ (a) and $m = 25$ (b). The final fold shape for $n = 1$, and for $n = 3$ for simulations deformed up to $\gamma = 4$ is shown for comparison.
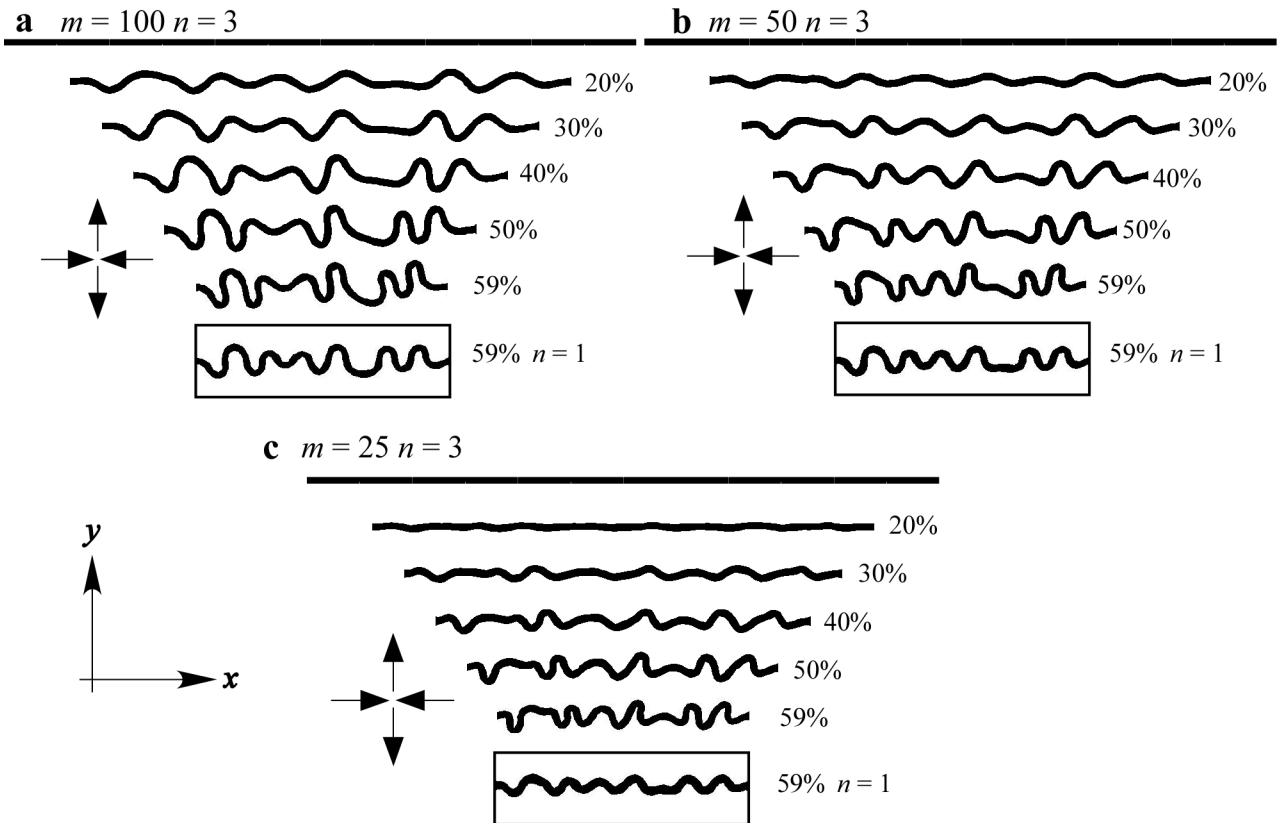
Figure 5.7: Progressive shortening of a single layer that is folding in pure shear, where both layer and matrix have a stress exponent of $n = 3$ and a viscosity contrast of $m = 100$ (a), $m = 50$ (b) and $m = 25$ (c). The final fold shape for $n = 1$ is shown for comparison.

5.4   Discussion

Amount of shortening, competence contrast between layer and matrix, degree of non-linearity of the flow law, and boundary conditions all determine the final shape of folded layers (Currie et al., 1962; Chapple, 1968; Johnson, 1970; Hudleston and Lan, 1994; Fletcher, 1995; Lan and Hudleston, 1996; Treagus, 1997; Schmalholz and Podladchikov, 1999, 2000). It is the aim of our and other studies to determine parameters that can be measured in the field to reconstruct the conditions of folding and potentially gain insight in material properties. The most straightforward quantitative parameters that can be measured in the field are layer thickness (H), fold amplitude (A) and wavelength (λ) (Fig. 5.2d). As long as folds are regular, this can be done relatively accurately, but in cases of irregular, ptygmatic folds, such measurements are more difficult and may be subject to observer bias (Adamuszek et al., 2011). Based on our simulations we address two main questions: what information do measurable fold parameters contain to constrain the kinematics of deformation (i.e. pure versus simple shear) or rheology (i.e. linear versus non-linear viscosity)? and secondly, how well can the real amount of shortening be determined from folds?
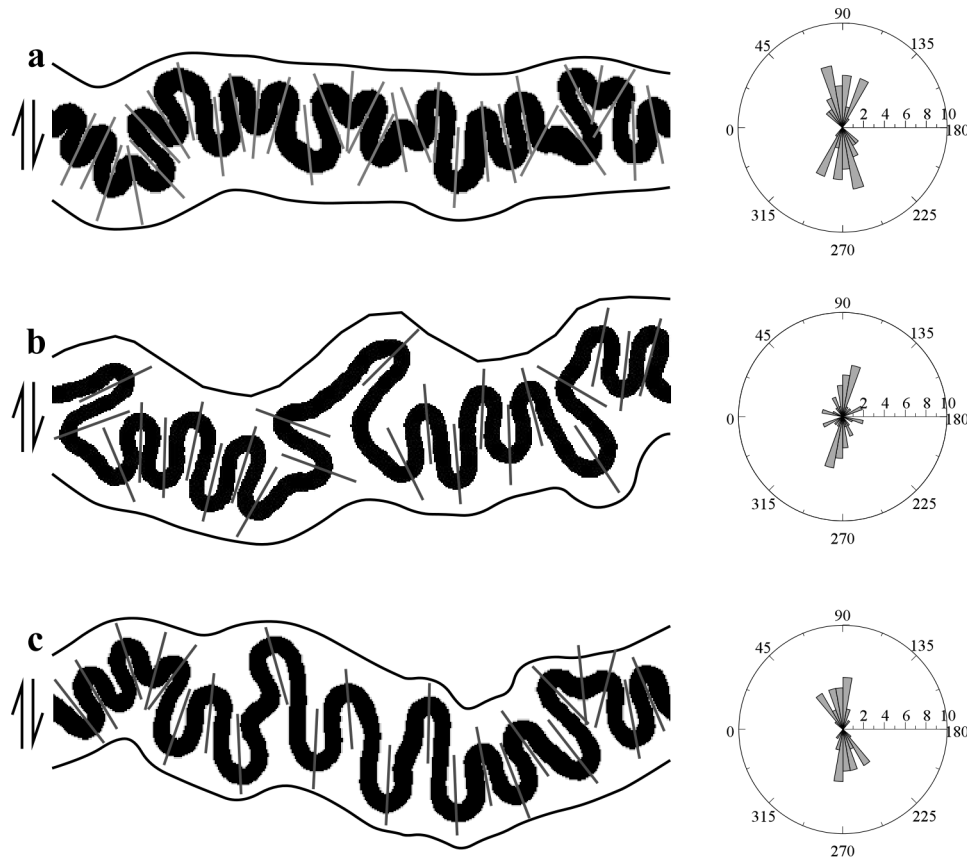
Figure 5.8: Axial plane orientations distribution at 75% of shortening in simple shear simulations, with (a) $m = 50$ and $n = 1$, (b) $m = 50$ and $n = 3$ and (c) $m = 100$ and $n = 1$. The non-linear case (b) clearly shows the higher effective viscosity contrast with (b) more similar to (c) than (a). The higher effective viscosity contrast is expressed in the form of less thickening, more irregular folds and a larger variation in axial plane orientations, partly related to the enhanced development of higher-order folds.

Wavelength-normalised amplitude versus thickness graphs (Schmalholz and Podladchikov, 2001) are a simple way to plot the three measurable parameters in a single graph. Rather than aiming to find a single best fit value for the three parameters for a fold train (Adamuszek et al., 2011), we choose to measure each individual fold to also gain insight in the variation in the three parameters. All data combined (Fig. 5.9 and Fig. 5.10) show several trends.

It is obvious that layer thickening decreases and therefore amplitude increases with increasing viscosity contrast. As non-linearity increases the effective viscosity contrast, it is not possible to distinguish from these graphs whether a folding layer had a high viscosity contrast but a low stress exponent, or a low viscosity contrast and a high stress exponent, and hence a high effective viscosity contrast.

There, however, appears to be a distinct difference between pure and simple shear, with folds formed in simple shear showing (i) more thickening and (ii) a higher variability in A/λ and H/λ than in pure shear. In our simulations this is due to a slower nucleation of folds in simple shear. As a layer preferentially thickens as long as folds have not yet

nucleated to amplify, the slower nucleation in simple shear leads to a shift to the lower-right in the A/λ versus H/λ graphs. The reason remains unclear, because we have used identical initial random perturbations in both pure and simple shear simulations to allow stress and strain perturbations to develop (comparable to Schmalholz and Podladchikov, 2001).
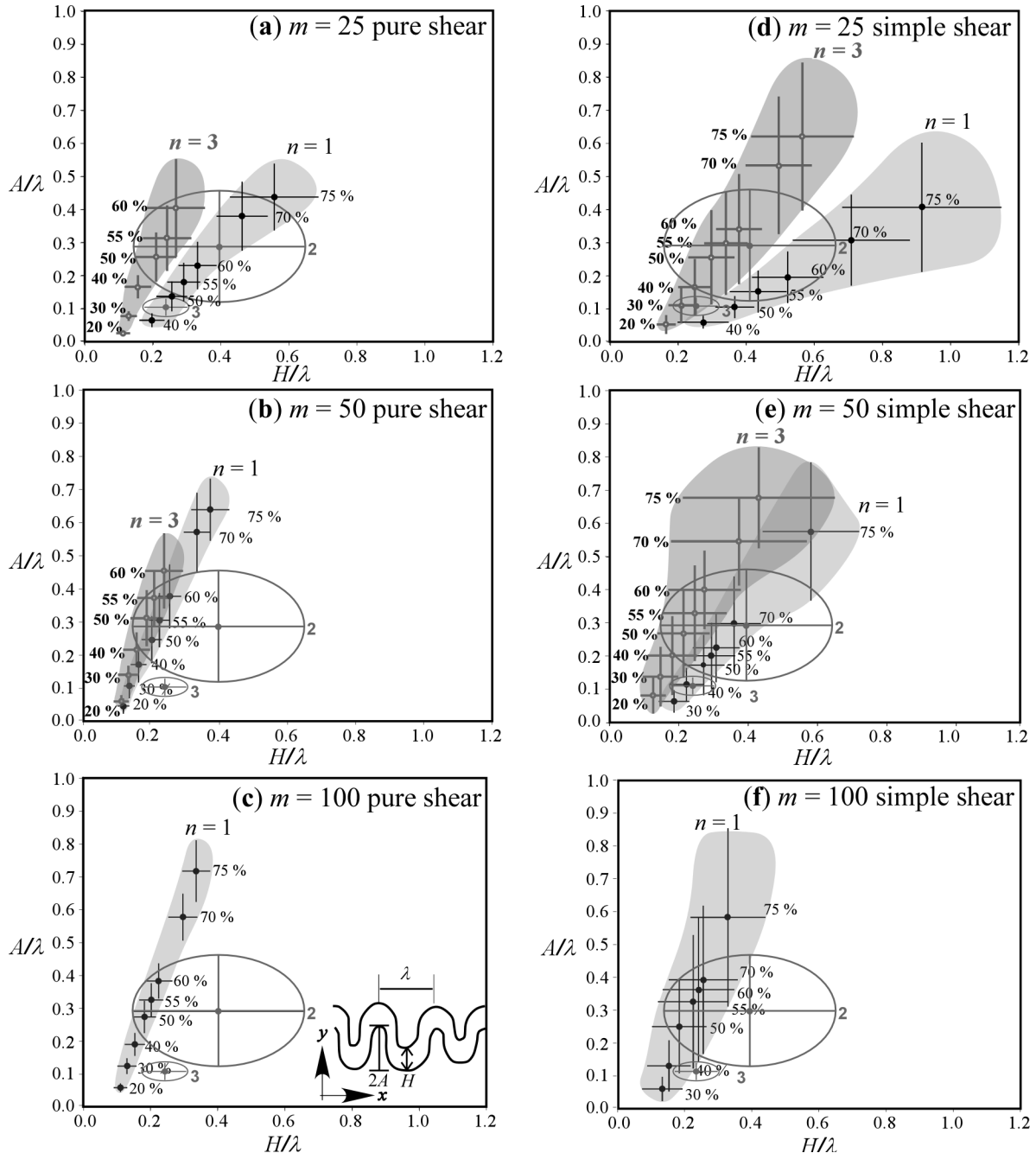
Figure 5.9: Comparison of fold parameters in the form of ratios of A/λ and H/λ for $n = 1$ (light shading) and $n = 3$ (dark shading) between pure shear (a–c) and simple shear (d–f) at different viscosity contrasts (m). Data from naturally deformed aplite dykes at Roses, Spain (dyke 2 and 3, see text) are shown as ellipses.

5.5 Natural example

The numerical simulations were compared with folded aplite dykes in the Roses Granodiorite at Roses on the Cap de Creus Peninsula, north-eastern Spain. This peninsula forms the most easterly outcrop of Variscan basement exposed in the axial zone of the Pyrenees. The granodiorite is transected by numerous shear zones, described in detail by Simpson et al. (1982), Segall and Simpson (1986), Carreras et al. (2004) and Montmoli et al. (2008). The folded aplite dykes are exposed in a sub-horizontal wave platform (Fig. 5.11). As both dykes and shear zones are subvertical and the stretching lineation in the shear zone approximately horizontal, the platform is ideally suited for accurate strain analysis. The amount of strain could be determined with the *Rf/ϕ*-method on mafic enclaves (Carreras et al., 2004) and from rotation of the dyke in the shear zone.

The whole outcrop experienced a broad and highly heterogeneous dextral simple shear. The lowest shear strain of $\gamma = 0.7$ (based on *Rf/ϕ*-method) is found on the right side of the outcrop (dyke 1), while the left side experienced a finite strain of $\gamma = 2.2$ (based on angular relationship between dykes 1 and 2, which are the same, and also on enclave geometries). In between these zones, dextral shearing was very strong ($\gamma > 10$). Later sinistral reactivation of this zone brought dyke 2 opposite to dyke 1 again. With this, a total shortening of 60% is inferred for dyke 2. Two more dykes are found in the moderate strain region at a lower angle to the shear zone. Due to this, the amount of shortening is less: 30% for the weakly folded dyke 3 and 20% for dyke 4, which appears not folded. These shortening estimates were calculated by constructing Mohr circles for strain (Means, 1982).

The amplitude, thickness and wavelength data of dyke 2 and 3 can be compared with our model results. As could be expected from the known shear zone kinematics, the field data best fit folding in simple shear. The viscosity contrast between dyke and granodiorite appears to be approximately 25 at a stress exponent of 3 (Fig. 5.9d) and 50 at a stress exponent of one (Fig. 5.9e). However, the calculated amount of shortening for dyke 2 (60%) and dyke 3 (30%) are only consistent with the $m = 25$ and $n = 3$ trend graph. Non-linear creep would be expected in the case of deformation under greenschist facies metamorphic conditions. (Kirby, 1983; Carter, and Tsenn, 1987; Luan and Paterson, 1992; Tullis, 2002; Bürgmann and Dresen, 2008).

Estimates of shortening of the dykes by the arc-length method are significantly lower than actual shortening values: 40% versus 60%, 13% versus 30% and 0% versus 20% for dykes 2, 3 and 4, respectively. This is consistent with the numerical models that show almost no visible folding up to about 30% shortening in simple shear at viscosity contrasts of 25 or less.

Although the different trends in Fig. 5.9 show some overlap, the example shows that they can be used to estimate the deformation boundary conditions, stress exponent, and

viscosity contrast. If only fold geometry data (A, H, λ) are available, this estimate can only be approximate. If other data are available to constrain the kinematics (cleavage refraction) or true amount of layer-parallel shortening, the stress exponent and viscosity contrast can be further constrained.
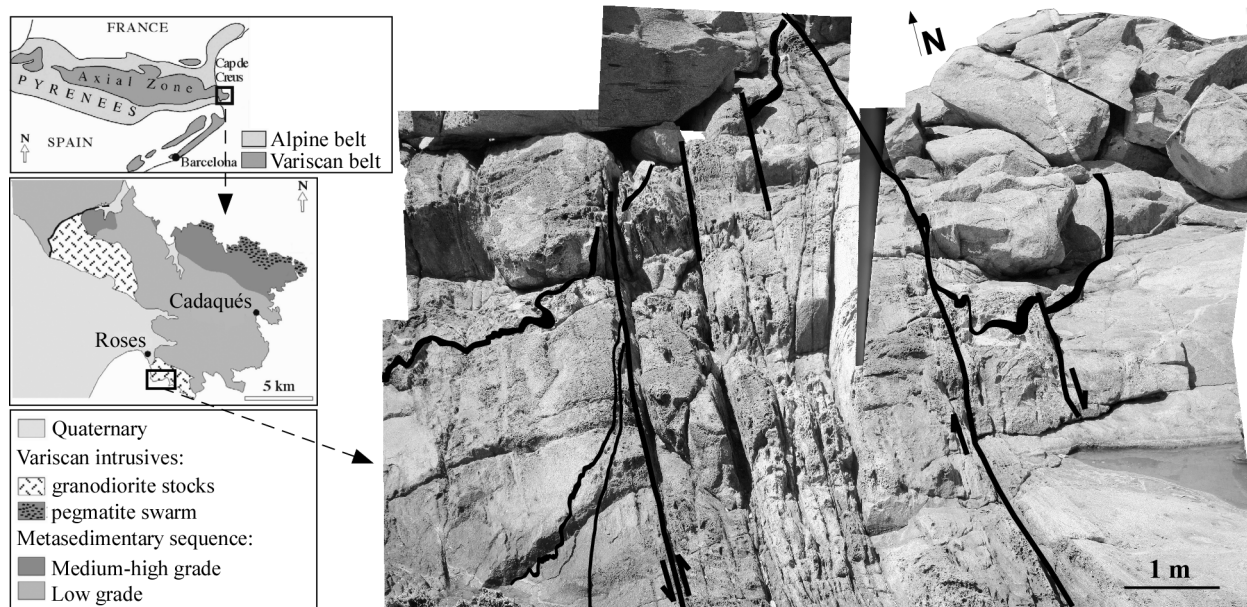
Figure 5.10: Aplite dykes in granodiorite measured for this study located at the Roses Lighthouse (Spain). (Cap de Creus, NE Spain; Coordinates: 42.245299°N, 3.182890°E).
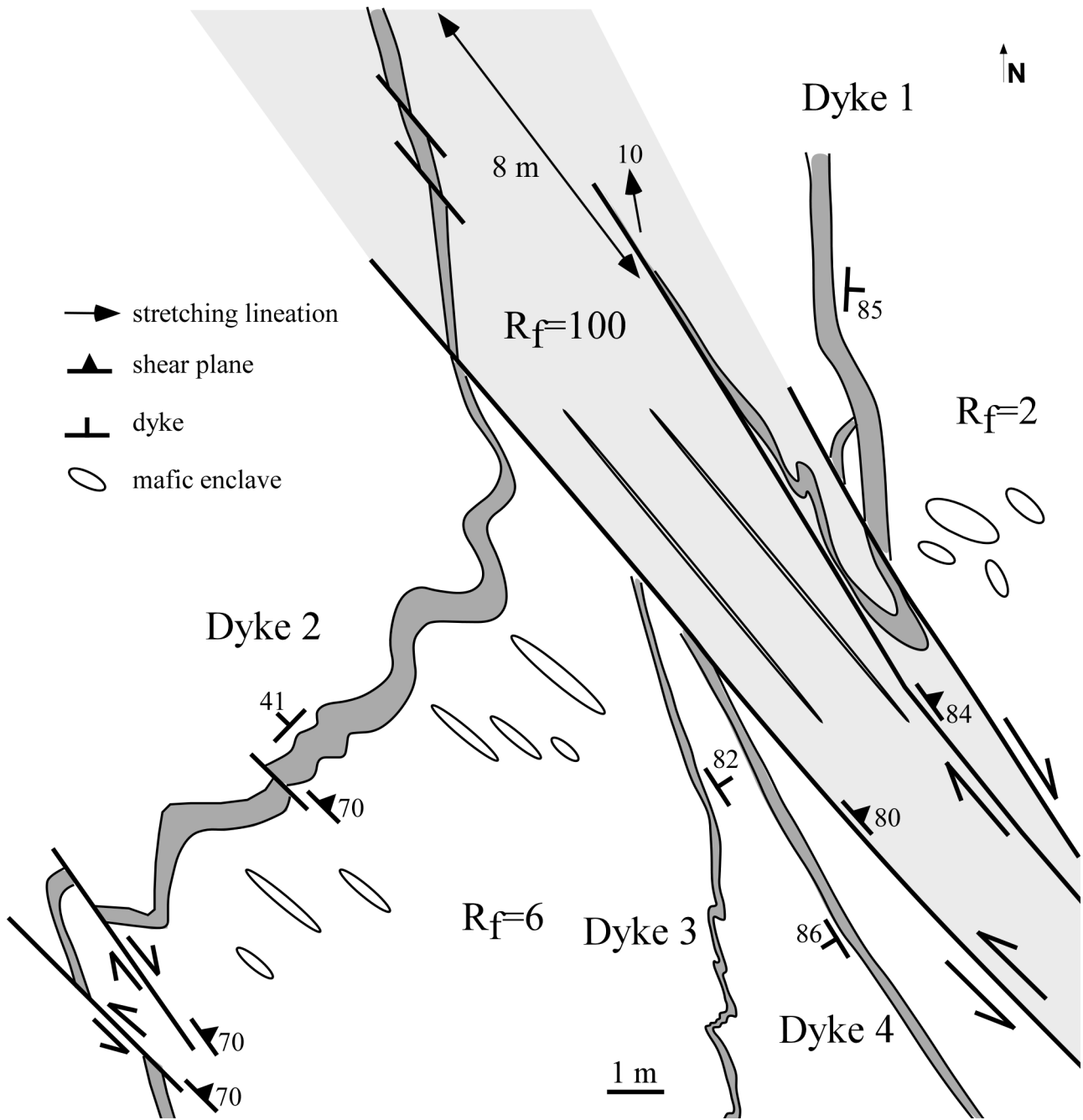
Figure 5.11: Aplite dyke sketch showing the less deformed part (dyke 1) cut by a dextral shear zone that affect the dykes 2, 3 and 4 with different intensities depending on the angle with the shear zone. Ellipses indicate the geometry of the enclaves described by Carreras et al. (2004). Shaded area indicates the high strain zone ($Rf \sim 100$).

5.6 Conclusions

This contribution presents the first systematic simulations of folding in simple shear to allow a comparison of fold development in single layers deformed in pure versus simple shear. The use of different numerical tools has allowed us to simulate folds up to a shear strain of $\gamma = 4$. We have run series of simulations varying the viscosity contrast between layer and matrix (m), the stress exponent (n) of the power-law viscous materials and the deformation conditions. With this approach we can compare fold patterns, the refraction of foliation and the distribution of axial plane orientations. The analysis of the resulting fold geometries led to the following main conclusions:

1. There is no distinct visual difference between folds that formed in pure and simple shear linear viscous simulations, except that axial plane orientations are more variable under simple-shear conditions. However, visual assessment of fold geometry alone is not sufficient to readily determine whether folds formed under simple- or pure-shear conditions. The most noticeable difference is the development of a more complicated foliation refraction pattern in simple shear.

2. Comparison of folds developed in linear and non-linear materials show that the effective viscosity contrast increases with non-linearity. This leads to the formation of folds with higher amplitudes and less thickening than in equivalent linear models. Fold envelopes are curved for all non-linear viscosities in simple shear, while they remain straight for linear cases, except for very high viscosity contrast ($m > 100$).

3. The use of graphs of layer thickness versus fold amplitude (both normalised against the fold wavelength) allows an estimate of the viscosity contrast and vorticity from folds. Data dispersion is highest for low viscosity contrast, low stress exponent, and for simple shear deformation.

4. The numerical simulations are compared with aplite dykes from Roses (Cap de Creus, Spain) that were folded in simple shear. The natural folds give a best match to our simulations for simple shear, a viscosity contrast of 25 and a stress exponent of 3. The folds confirm the observations from the numerical simulations that visible folding only initiates after considerable shortening ($\geq 30\%$ at $m = 25$). The arc-length method can thus significantly underestimate the true amount of strain.

Acknowledgements

5.7 References

- Adamuszek, M., Schmid, D.W., Dabrowski, M., 2011. Fold geometry toolboxeAutomated determination of fold shape, shortening, and material properties. Journal of Structural Geology 33, 1406-1416.

- Abassi, M.R., Mancktelow, N.S., 1992. Single layer buckle folding in non-linear materials - I. Experimental study of fold development from an isolated initial perturbation. Journal of Structural Geology 14, 85-104.

- Alsop, G.I., Holdsworth, R.E., 2006. Sheath folds as discriminators of bulk strain type. Journal of Structural Geology 28, 1588-1606.

- Alsop, G.I., Carreras, J., 2007. The structural evolution of sheath folds: a case study from Cap de Creus. Journal of Structural Geology 29, 1915-1930.

- Anthony, J.M., Wickham, J.S., 1978. Finite-element simulation of asymmetric folding. Tectonophysics 47, 1-14.

- Barr, T.D., Houseman, G.A., 1996. Deformation fields around a fault embedded in a non-linear ductile medium. Geophysical Journal International 125, 473-490.

- Biot, M.A.,1961. Theory of folding of stratified viscoelastic media and its implication in tectonics and orogenesis. Geological Society of America Bulletin 72, 1595-1632.

- Bons, P.D., Urai, J.L., 1996. An apparatus to experimentally model the dynamics of ductile shear zones. Tectonophysics 256, 145-164.

- Bons, P.D., Barr, T.D., ten Brink, C.E., 1997. The development of d-clasts in non-linear viscous materials: a numerical approach. Tectonophysics 270, 29-41.

- Bons, P.D., Koehn, D., Jessell, M.W. (Eds.), 2008. Microdynamics Simulation. Lecture Notes in Earth Sciences, vol. 106. Springer-Verlag.

- Bürgmann, R., Dresen, G., 2008. Rheology of the lower crust and upper mantle:evidence from rock mechanics, geodesy, and field observations. Annual Review of Earth and Planetary Sciences 36, 531-567.

- Carreras, J., Druguet, E., Griera, A., Soldevilla, J., 2004. Strain and deformation history in a syntectonic pluton. The case of the Roses granodiorite (Cap deCreus, Eastern Pyrenees). In: Alsop, G.I., Holdsworth, R.E. (Eds.), Flow Processes in Faults and Shear Zones. Geological Society of London Special Publication,pp. 307-319.

- Carreras, J., Druguet, E., Griera, A., 2005. Shear zone-related folds. Journal ofStructural Geology 27, 1229-1251.

- Carter, N.L., Tsenn, M.C., 1987. Flow properties of the continental lithosphere. Tectonophysics 136, 27-63.

- Casey, M., Huggenberger, P., 1985. Numerical modelling of finite-amplitude similar folds developing under general deformation histories. Journal of Structural Geology 7, 103-114.

- Chapple, W.M., 1968. A mathematical theory of finite amplitude rock-folding. Geological Society of America Bulletin 79, 47-68.

- Cobbold, P.R., 1975. Fold propagation in single embedded layers. Tectonophysics 27, 333-351.

- Cobbold, P.R., Quinquis, H., 1980. Development of sheath folds in shear regimes: shear zones in rocks. Journal of Structural Geology 2, 119-126.

- Currie, J.B., Patnode, H.W., Trump, R.P., 1962. Development of folds in sedimentary strata. Geological Society of America Bulletin 73, 655-674.

- Dieterich, J.H.,1970. Computer experiments on mechanics of finite-amplitude folds.Canadian Journal of Earth Sciences 7, 467-476.

- Fletcher, R.C., 1974. Wavelength selection in the folding of a single layer with power-law rheology. American Journal of Science 274, 1029-1043.

- Fletcher, R.C., 1977. Folding of a single viscous layer: exact infinitesimal-amplitude solution. Tectonophysics 39, 593-606.

- Fletcher, R.C., 1995. 3-dimensional folding and necking of a power-law layer - are folds cylindrical, and if so, do we understand why? Tectonophysics 247, 65-83.

- Flinn, D., 1962. On folding during three-dimensional progressive deformation. Quarterly Journal Geological Society London 118, 385-433.

- Frehner, M., Schmalholz, S.M., 2006. Numerical simulations of parasitic folding in multilayers. Journal of Structural Geology 28, 1647-1657.

- Ghosh, S.K., 1966. Experimental tests of buckling folds in relation to strain ellipsoid in simple shear deformations. Tectonophysics 3, 169-185.

- Hobbs, B., Regenauer-Lieb, K., Ord, A., 2008. Folding with thermal-mechanical feedback. Journal of Structural Geology 30, 1572-1592.

- Houseman, G., Barr, T., Evans, L., 2008. Basil: stress and deformation in a viscous material. In: Bons, P.D., Koehn, D., Jessell, M.W. (Eds.), 2008. Microdynamics Simulation. Lecture Notes in Earth Sciences, vol. 106.Springer, Berlin, p. 405.

- Hudleston, P.J., 1973. An analysis of "single-layer" folds developed experimentally in viscous media. Tectonophysics 16, 189-214.

- Hudleston, P.J., Stephansson, O., 1973. Layer shortening and fold shape development in the buckling of single layers. Tectonophysics 17, 299-321.

- Hudleston, P.J., 1977. Similar folds, recumbent folds, and gravity tectonics in ice and rocks. Journal of Geology 85, 113-122.

- Hudleston, P.J., 1986. Extracting information from folds in rocks. Journal of Geological Education 34, 237-245.

- Hudleston, P.J., Lan, L., 1993. Information from fold shapes. Journal of Structural Geology 15, 253-264.

- Hudleston, P.J., Lan, L., 1994. Rheological controls on the shapes of single-layer folds. Journal of Structural Geology 16, 1007-1021.

- Hudleston, P.J., Treagus, S.H., Lan, L., 1996. Flexural flow folding: does it occur in nature? Geology 24, 203-206.

- Hudleston, P.J., Treagus, S.H., 2010. Information from folds: a review. Journal of Structural Geology 32, 2042-2071.

- Huismans, Beaumont, R.S., 2003. Symmetric and asymmetric lithospheric extension: relative effects of frictional-plastic and viscous strain softening. Journal ofGeophysical Research 108. doi:10.1029/2002JB002026.

- James, A.I., Watkinson, A.J., 1994. Initiation of folding and boudinage in wrench shear and transpression. Journal of Structural Geology 16, 883-893.

- Jessell, M.W., Bons, P.D., Evans, L., Barr, T., Stüwe, K., 2001. Elle: a micro-process approach to the simulation of microstructures. Computers and Geosciences 27, 17-30.

- Jessell, M.W., Siebert, E., Bons, P.D., Evans, L., Piazolo, S., 2005. A new type of numerical experiment on the spatial and temporal patterns of localization of deformation in a material with a coupling of grain size and rheology. Earth and Planetary Science Letters 239, 309-326.

- Jessell, M.W., Bons, P.D., Griera, A., Evans, L.A., Wilson, C.J.L., 2009. A tale of two viscosities. Journal of Structural Geology 31, 719-736.

- Johnson, A.M., 1970. Physical Processes in Geology. Freeman, Cooper and Company, San Francisco.

- Johnson, A.M., Fletcher, R.C., 1994. Folding of Viscous Layers. Columbia University Press, New York.

- Kenis, I., Urai, J.L., van der Zee, W., Hilgers, C., Sintubin, M., 2005. Rheology of fine-grained siliciclastic rocks in the middle crust - evidence from structural and numerical analysis. Earth and Planetary Science Letters 233, 351-360.

- Kirby, S.H., 1983. Rheology of the lithosphere. Reviews of Geophysics and SpacePhysics 21, 1458-1487.

- Kocher, T., Mancktelow, N.S., Schmalholz, S.M., 2008. Numerical modelling of the effect of matrix anisotropy orientation on single layer fold development. Journal of Structural Geology 30, 1013-1023.

- Lan, L., Hudleston, P.J., 1991. Finite-element models of buckle folds in non-linear materials. Tectonophysics 199, 1-12.

- Lan, L., Hudleston, P.J., 1995. The effects of rheology on the strain distribution in single layer buckle folds. Journal of Structural Geology 17, 727-738.

- Lan, L., Hudleston, P.J., 1996. Rock rheology and sharpness of folds in single layers.Journal of Structural Geology 18, 925-931.

- Luan, F.C., Paterson, M.S., 1992. Preparation and deformation of synthetic aggregates of quartz. Journal of Geophysical Research 97, 301-320.

- Mancktelow, N.S., 1999. Finite-element modelling of single-layer folding in elasto-viscous materials; the effect of initial perturbation geometry. Journal of Structural Geology 21, 161-177.

- Manz, R., Wickham, J., 1978. Experimental analysis of folding in simple shear. Tectonophysics 44, 79-90.

- Means, W.D., 1982. An unfamiliar Mohr circle construction for finite strain. Tectonophysics 89, T1-T6.

- Montmoli, Ch., Carosi, R., Frassi, Ch., Ardito, N., Carreras, J., Druguet, E., 2008. Shear partitioning across two parallel shear zones in Roses Granodiorite (EasternPyrenees, Spain). Rendiconti della Società Geologica Italiana 3, 569-570.

- Mühlhaus, H.B., Hobbs, B.E., Ord, A., 1994. The role of axial constraints on the evolution of folds in single layers. In: Siriwardane, H.J., Zaman, M.M. (Eds.),1994. Computer Methods and Advances in Geomechanics, vol. 1. A. A. Balkema, Rotterdam, pp. 223-231.

- Ormond, C.J., Hudleston, P.J., 2003. Strain paths of three small folds from theAppalachian Valley and Ridge, Maryland. Journal of Structural Geology 25,1841-1854.

- Parrish, D.K., 1973. A non linear finite-element fold model. American Journal ofScience 273, 318-334.

- Parrish, D.K., Krivz, A.L., Carter, N.L., 1976. Finite-element folds of similar geometry. Tectonophysics 32, 183-207.

- Passchier, C.W., Williams, P.R., 1996. Conflicting shear sense indicators in shear zones; the problem of non-ideal sections. Journal of Structural Geology 18, 1281-1284.

- Quinquis, H., Audren, C., Brun, J.P., Cobbold, P.R., 1978. Intense progressive shear in the Ile de Groix blue schists and compatibility with subduction or obduction. Nature 273, 43-45.

- Ramberg, H., 1961. Contact strain and folding instability of a multilayered body under compression. Geologische Rundshau 51, 405-439.

- Ramsay, J.G., Casey, M., Kligfield, R., 1983. Role of shear in development of theHelvetic fold-Thrust belt of Switzerland. Geology 11, 439-442.

- Ramsay, J.G., Huber, M.I., 1987. The Techniques of modern structural geology. In:Folds and Fractures, vol. II. Academic Press, London.

- Schmalholz, S.M., Podladchikov, Y.Y., 1999. Buckling versus folding: importance of viscoelasticity. Geophysical Research Letters 26, 2641-2644.

- Schmalholz, S.M., Podladchikov, Y.Y., 2000. Finite amplitude folding: transition from exponential to layer length controlled growth. Earth and Planetary Science Letters 181, 619-633.

- Schmalholz, S.M., Podladchikov, Y.Y., 2001. Strain competence contrast estimation from fold shape. Tectonophysics 340, 195-213.

- Schmalholz, S.M., 2008. 3D numerical modelling of forward and reverse folding of a viscous single-layer: implications for the formation of fold and fold patterns. Tectonophysics 446, 31-41.

- Schmalholz,S.M., Podladchikov, Y.Y., Jamtveit, B., 2005. Structural softening of the lithosphere. Terra Nova 17, 66-72.

- Schmid, D.W., 2002. Finite and infinite heterogeneities under pure and simple shear. PhD thesis, ETH Zurich. doi:10.3929/ethz-a-004447477.

- Schmid, D.W., Podladchikov, Y.Y., 2006. Fold amplification rates and dominant wavelength selection in multilayer stacks. Philosophical Magazine 86, 3409-3423.

- Segall, P., Simpson, C., 1986. Nucleation of ductile Shear zones on dilatant fractures. Geology 14, 56-59.

- Sherwin, J.-A., Chapple, W.M., 1968. Wavelengths of single layer folds: a comparison between theory and observation. American Journal of Science 266, 167-179.

- Shimamoto, T., Hara, I., 1976. Geometry and strain distribution of single-layer folds. Tectonophysics 30, 1-34.

- Simpson, C., Carreras, J., Losantos, M., 1982. Inhomogeneous deformation in Roses granodiorite. Acta Geol[ó]gica Hisp[á]nica 17, 219-226.

- Smith, R.B., 1975. Unified theory of the onset of folding, boudinage, and mullion structure. Geological Society of America Bulletin 86, 1601-1609.

- Smith, R.B., 1977. Formation of folds, boudinage, and mullions in non-Newtonian materials. Geological Society of America Bulletin 88, 312-320.

- Stephansson, O., Berner, H., 1971. The finite-element method in tectonic processes. Physics of the Earth and Planetary Interiors 4, 301-321.

- Tackley, P.J., 1998. Self-consistent generation of tectonic plates in three-dimensional mantle convection. Earth and Planetary Science Letters 157, 9-22.

- Tikoff, B., Peterson, K., 1998. Physical experiments of transpressional folding. Journal of Structural Geology 20, 661-672.

- Toimil, N.C., Griera, A., 2007. Influence of viscosity contrast and anisotropy on strain accommodation in competent layers. Journal of Structural Geology 29, 787-801.

- Treagus, S.H., 1973. Buckling stability of a single-layer system, oblique to the principal compression. Tectonophysics 19, 271-289.

- Treagus, S.H., 1981. A theory of stress and strain variations in viscous layers, and its geological implications. Tectonophysics 72, 75-103.

- Treagus, S.H., 1982. A new isogon-cleavage classification and its application to natural and model fold studies. Geological Journal 17, 49-64.

- Treagus, S.H., 1983. A new theory of finite strain variation through contrasting layers, and its bearing on cleavage refraction. Journal of Structural Geology 5, 351-358.

- Treagus, S.H., 1988. Strain refraction in layered systems. Journal of Structural Geology 10, 517-527.

- Treagus, S.H., 1997. Modelling deformation partitioning in folds. In: Sengupta, S.(Ed.), Evolution of Geological Structures in Micro to Macro-scales. Chapman & Hall, London, pp. 341-372.

- Treagus, S.H., 1999. Are viscosity ratios of rocks measurable from cleavage refraction? Journal of Structural Geology 20, 895-901.

- Treagus, S.H., Hudleston, P.J., 2009. Folding with thermal-mechanical feedback: discussion. Journal of Structural Geology 31, 749-751.

- Treagus, S.H., Treagus, J.E., 2002. Studies of strain and rheology of conglomerates. Journal of Structural Geology 24, 1541-1567.

- Tullis, J., 2002. Deformation of granitic rocks: experimental studies and natural examples. Reviews in Mineralogy and Geochemistry 51, 51-95.

- Viola, G., Mancktelow, N.S., 2005. From XY tracking to buckling: axial plane cleavage fanning and folding during progressive deformation. Journal of Structural Geology 27, 409-417.

- Zhang, Y., Hobbs, B.E., Ord, A., Mühlhaus, H.B., 1996. Computer simulation of single-layer buckling. Journal of Structural Geology 18, 643-655.

- Zhang, Y., Mancktelow, N.S., Hobbs, B.E., Ord, A., Mühlhaus, H.B., 2000. Numerical modelling of single-layer folding: clarification of an issue regarding the possible effects of computer codes and the influence of initial irregularities. Journal of Structural Geology 22, 1511-1522.

Chapter 6

Mechanics of fold development in pure- and simple shear

Maria-Gema Llorens[a], Paul D. Bons[a], Albert Griera[b] and Enrique Gomez-Rivas[a]

[a]Departament of Geosciences, Eberhard Karls University Tübingen, Wilhemstr. 56, 72074 Tübingen, Germany
[b]Departament de Geologia, Universitat Autònoma de Barcelona, 08193 Bellaterra (Barcelona), Spain

Abstract

Folds not only help to determine the orientation and magnitude of shortening, but contain much more information on deformation mechanics, kinematics and rheology. The use of folds for strain analysis requires a first-order quantification of the relationships between parameters that determine fold geometry. We present series of 2-dimensional simulations of single-layer folding under pure and simple shear using the software packages ELLE and BASIL. The orientation of the competent layer, the competence contrast between layer and matrix, the stress exponent of the power-law viscous material as well as the boundary conditions are systematically varied to observe the influence of these parameters on fold development. Analyses of stress heterogeneities show that stress localizations are not regularly distributed at the initial stages of folding. Folding of a competent layer requires lower energy (work) in simple shear than in pure shear conditions.

Keywords

Folding; Simple shear; Pure shear; Stress; Non-linear rheology.

6.1   Introduction

Folds are structures commonly used to unravel rock deformation history. They typically indicate orientation and amount of shortening (e.g., Hudleston, 1986; Hudleston and Lan 1993, Bobillo-Ares et al., 2004; Bastida et al., 2005). However, much more information can potentially be extracted from fold analysis, like the viscosity contrast between folded layers and matrix, kinematic vorticity and non-linearity of the viscosity Llorens et al. (2013a). Additionally, one can find indications on whether folds have been shortened and stretched again (Means, 1999; Llorens et al. 2013b). In this contribution we investigate the relationships between the different parameters that determine fold geometries and their mechanical implications, in order to be able to improve the use of folds to unravel rock mechanics, kinematics and rheology.

The viscosity or competence contrast between folding layers and matrix (m) is assumed to be the main factor determining the initial wavelength and amplification rate of the developing folds (Biot, 1961; Ghosh, 1966; Fletcher, 1974). Additionally, non-linear viscous behaviour when the strain rate is proportional to the stress to the power n, also influences fold geometry (Fletcher, 1974; Abassi and Mancktelow, 1992; Mühlhaus et al., 1994;).

6.2 Numerical simulation method and experimental setup

We use the 2D numerical modeling platform ELLE, including the finite-element module BASIL (Bons et al., 2008), to simulate the development of single-layer folds. Layer and matrix are defined by a contiguous set of polygons, to which mechanical properties are assigned. All the boundaries of the model are periodic, so that it is a unit cell that can be repeated infinitely in all directions. In simple shear experiments, rigid-plate velocity conditions are applied to the horizontal boundaries with a constant incremental shear strain of $\Delta\gamma$=0.025. Contrary to simple-shear simulations, the pure-shear models are initially not square but rectangular. Velocity boundary conditions ($\sim$1% incremental shortening) are applied to all boundaries. All the simulations presented in this paper have an initial random noise of layer thickness to noise amplitude ratio of 40, as in [5, 7], a constant viscosity contrast of m=50 and a strain-independent, power-law viscous rheology with a stress exponent (n) of either 1 or 3.

In simple shear simulations, the layer is originally inclined 14° with respect to the shear plane, and sheared to γ=4, which results in 75% shortening of the layer. In pure shear it is parallel to the maximum shortening direction. Simulations with a linear viscosity (n=1) reached 75% shortening and those with n=3 reached 55% shortening.

6.3 Results

Stress distribution for n=1 simulations are shown in Fig. 1A-B (simple shear) and Fig. 1C-D (pure shear), and the maximum deviatoric stress in the layer as a function of layer shortening is shown in Fig. 2A. Maximum deviatoric stresses are higher in power-law materials than in linear-viscosity materials. Maximum deviatoric stress in pure shear is initially double than that of simple-shear folding, but decreases markedly towards the simple-shear value after about 20% strain. In case of n=3 (Fig. 1E-F, simple shear, and Fig. 1G-H, pure shear) the difference in maximum deviatoric stress between pure shear and simple shear is less pronounced and both decrease steadily during the first 30% of shortening (Fig. 2B).

Stress localizations are not regularly distributed at the initial stages of folding. After a certain amount of shortening stress concentrations determine the future fold hinges.
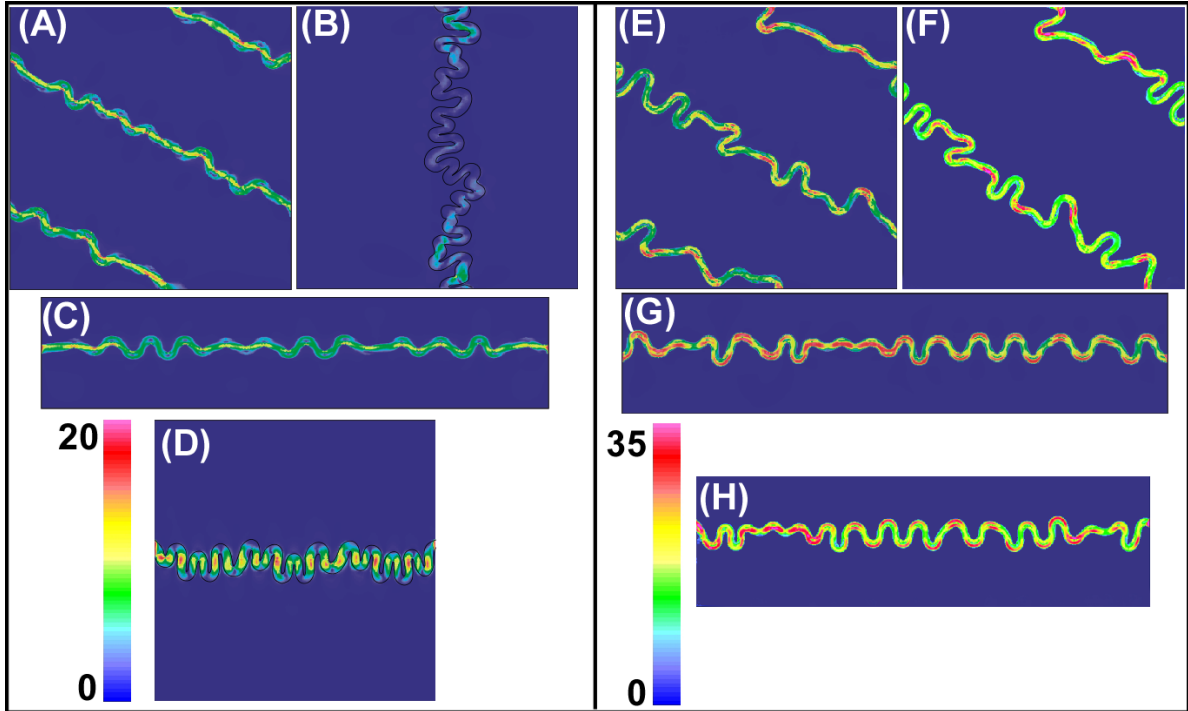
Figure 6.1: Plots of maximum deviatoric stress of the simple shear experiment with linear viscosity at (A) 35% and (B) 75% of shortening. Pure-shear experiment with linear viscosity at (C) 35% and (D) 75% of shortening. Simple shear with non-linear viscosity at (E) 35% and (F) 55% of shortening and the same for pure shear at (G) 35% and (H) 55% of shortening.

6.4   Discussion and conclusions

Although similar final fold geometries are developed in simple and pure shear conditions (Fig. 1), differences in stress evolution can be observed (Fig. 2). Pure shear is characterized by an initial stage of high stress followed by a strong weakening after fold perturbations develop. An increase of stress at large strain indicates that folds become locked and shortening is now accommodated by fold limb stretching. In case of pure shear, the folded layer is always parallel to the maximum shortening direction, whereas the fold train rotates relative to the maximum shortening direction in simple shear. Folding in simple shear shows relative lower stresses and the geometrical strain weakening is less pronounced. For the linear case, a strain hardening-softening behavior in the stress evolution is observed. Peak stresses are not observed at the beginning, but when the layer envelope is at $\sim$45°, the maximum shortening strain rate is reached. The non-linear case shows an evolution similar to the pure shear cases, without a stress maximum at $\sim$45°, maybe due to the strain-rate softening behavior of power law materials with $n>1$. Further studies are still required.

Although similar in geometry, the folds are less regular in simple shear than in pure shear. This appears to be related to the organization of stress perturbations that seed the folds. In pure shear, the folded layer maintains a constant orientation with respect to the

bulk deformation. Stress perturbations are organized earlier and more regularly than in simple shear, where the folding layer continuously changes its orientation relative to the bulk deformation.
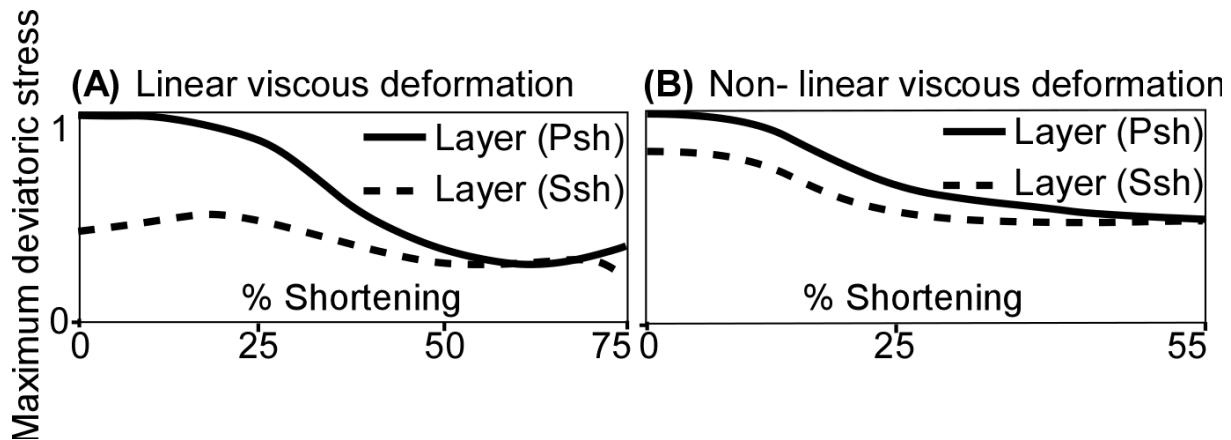
Figure 6.2: Maximum deviatoric stress in the folded layer as a function of layer shortening in Psh and Ssh, and for (A) linear (n=1) and (B) power-law (n=3) viscosity models. Stress values are normalized with respect to the maximum layer-averaged deviatoric stress in the linear and non-linear simulations, respectively.

6.5   References

- Adamuszek, M., Schmid, D.W., Dabrowski, M., 2011. Fold geometry toolboxeAutomated determination of fold shape, shortening, and material properties. Journal of Structural Geology 33, 1406-1416.

- Hudleston, P.J., 1986. Extracting information from folds in rocks. Journal of Geological Education 34, 237-245.

- Hudleston, P.J., Lan, L., 1993. Information from fold shapes. Journal of Structural Geology 15, 253-264.

- Bobillo-Ares, N. C., Toimil, N. C., Aller, J. and Bastida, F. 2004. FoldModeler: a tool for the geometrical and kinematical analysis of folds. Computer and Geosciences 30, 147-159.

- Bastida, F., Aller, J., Bobillo-Ares, N. C. and Toimil, N. C., 2005. Fold geometry: a basis for their kinematical analysis. Earth-Science Reviews 70, 129-164.

- Llorens, M.-G., Bons, P.D., Griera, A., Gomez-Rivas, E., and Evans, L. A., 2013, Single layer folding in simple shear: Journal of Structural Geology 50, 209-220.

- Means, W. D., 1999, Reversed structures and bounce structures: Are they recognizable? Are they real?: Journal of Structural Geology, 21, 917-921.

- Llorens, M.-G., Bons, P.D., Griera, A., and Gomez-Rivas, E., 2013, When do folds unfold during progressive shear?: Geology 41, 563-566.

- Biot, M.A., 1961. Theory of folding of stratified viscoelastic media and its implication in tectonics and orogenesis. Geological Society of America Bulletin 72, 1595–1632.

- Ghosh, S.K., 1966. Experimental tests of buckling folds in relation to strain ellipsoid in simple shear deformations. Tectonophysics 3, 169-185.

- Fletcher, R.C., 1974. Wavelength selection in the folding of a single layer with power-law rheology. American Journal of Science 274, 1029–1043.

- Abassi, M.R., Mancktelow, N.S., 1992. Single layer buckle folding in non-linear materials - I. Experimental study of fold development from an isolated initial perturbation. Journal of Structural Geology 14, 85-104.

- Muühlhaus, H.B., Hobbs, B.E., Ord, A., 1994.The role of axial constraints on the evolution of folds in single layers. In: Siriwardane HJ, Zaman MM (eds) Computer methods and advances in geomechanics 1, A. A. Balkema, Rotterdam, 223-231.

- Bons, P.D., Koehn, D. and Jessell, M.W. (Eds.), 2008. Microdynamics Simulation. Lecture Notes in Earth Sciences 106. Springer-Verlag.

Chapter 7

When do folds unfold during progressive shear?

Maria-Gema Llorens[a], Paul D. Bons[a], Albert Griera[b] and Enrique Gomez-Rivas[a]

[a]Departament of Geosciences, Eberhard Karls University Tübingen, Wilhemstr. 56, 72074 Tübingen, Germany
[b]Departament de Geologia, Universitat Autònoma de Barcelona, 08193 Bellaterra (Barcelona), Spain

Abstract

Folded layers in rocks can be stretched again, potentially unfolding the folds back to straight layers. Little is known, however, about how to recognize partly or even entirely unfolded layers. When folded layers can unfold, what determines their mechanical behavior, and how can we recognize them in the field? In order to address these questions, we present a series of numerical simulations of the stretching of previously folded single layers and multilayers in simple shear. Layers do not completely unfold when they undergo softening before or during the stretching process, or when adjacent competent layers prevent them from unfolding. Intrafolial folds and cusp-like folds adjacent to straight layers as well as variations in fold amplitudes and limb lengths of irregular folds are indicative of stretching of a fold train.

7.1   Introduction

Can a straight layer or vein in a deformed rock have been folded before, or could a folded layer or vein once have had tighter folds? If so, how can one tell? When rocks deform, some planar elements (e.g., veins, layers, dikes, cleavage) are shortened parallel to their long axis, while others are stretched, depending on their orientation relative to the applied deformation. Folds tend to form when the structure is shortened and the structure is more competent than its surrounding matrix (Biot, 1961; Ramberg, 1962, 1963; Chapple, 1968; Hudleston and Stephansson, 1973; Fletcher, 1974, 1977; Smith, 1975, 1977, 1979; Treagus, 1983, 1993; Hudleston and Lan, 1994; Johnson and Fletcher, 1994; Lisle, 1997; Mancktelow 1999, 2001; Schmid et al., 2004). Structures that are stretched become thinner or are pulled apart in lenses or blocks, called boudins or pinch-and-swell structures (e.g., Ramberg, 1955; Lloyd and Ferguson, 1981; Lloyd et al., 1982; Malavieille and Lacassin, 1988; DePaor et al., 1991; Swanson, 1992; Ghosh and Sengupta, 1999). A fold can become stretched again if (1) it is subjected to extension under a new and differently oriented deformation (Hudleston and Lan, 1993), or (2) during the same deformation event that caused folding it rotates into the extensional field (Ramsay, 1980; Passchier, 1988; Bons and Urai, 1996; Carreras et al., 2005; Sengupta et al., 2005). The latter can be expected in shear zones, where the localized high strain can cause significant rotation of structures (Ramberg and Ghosh, 1977; Ramsay, 1980; Skjernaa, 1980; Ghosh and Sengupta, 1987; Passchier, 1988; Harris, 2003; Carreras et al., 2005).

In the geological record, boudins are far less common than folds, although one can expect planar structures to have about equal chances to be shortened or stretched. This suggests that in most cases, stretching structures tend to thin, rather than be boudinaged, because ductile necking requires strong nonlinearity and high competence contrast (Talbot, 1970; Smith, 1977; Talbot and Sokoutis, 1992; Schmalholz and Fletcher, 2011). In most

studies boudinage is assumed as the structure developed in the extensional field, but stretching folds may thus not always be boudinaged, which means that they must either unfold or the entire fold train must thin. The question of what happens when folds get stretched, and how we can recognize this, has hardly been addressed in the literature (Kelley and Del Mar, 1958; Klein, 1980; Means, 1999).

Because of the reversibility of the Stokes equations for slow viscous flow, reversing the deformation that caused folding will unfold a folded layer, provided that the viscosity ratio remains the same (Schmalholz, 2008; Lechmann et al., 2010). A retrodeformation is, however, not necessarily identical to ongoing deformation that may bring a folded layer into the stretching field. In this case, although the layer changes from shortening to extensional field, shear strain components are not reversed. Furthermore, viscosity ratios may change during deformation due to strain-dependent rheologies, or changes in strain rate or metamorphic conditions during deformation (e.g., Klein, 1980; Hobbs et al., 1990; Tullis et al., 1991; Talbot, 1999). In this paper we investigate stretching of folds during progressive deformation and the effect of changes in viscosity ratio during the process.

7.2 Unfolding a single layer

Folding and subsequent unfolding in simple shear was simulated with the two-dimensional numerical modeling platform Elle, including the finite-element module Basil (Barr and Houseman, 1996; Jessell et al., 2001, 2009; Bons et al., 2008, 2009; Griera et al., 2011). Horizontal, dextral simple shear was applied to the model in incremental steps of shear strain, $\gamma = 0.025$. Lateral boundary conditions are periodic, while rigid-plate velocity conditions were applied to the top and bottom. As a result, the model remains square at all times (Fig. 7.1). This boundary condition is applied at different levels within the model each deformation step, to suppress artifacts at the top and bottom boundary (Jessell et al., 2009). Layers and matrix were defined by polygons with homogeneous, time-independent linear viscosity. In the first series of experiments, a single layer with a viscosity ratio $m = 50$, relative to the matrix, and an inclination of 14° to the shear zones was first sheared to a shear strain of 4. This caused 75% shortening and folding of the layer (Llorens et al., 2012). This configuration was used as the start for a series of simulations of further shearing. To investigate the effect of a change in viscosity ratio during shearing, viscosity ratios from $\gamma = 4$ onward were varied from 100 down to 3.125. Such a sudden change in viscosity ratio is not realistic. However, it is impossible to fully investigate the infinite number of potential viscosity ratio histories. Control tests with a continuously decreasing viscosity ratio showed that results are only marginally different from those presented here.

Figure 7.2 shows that once the layer has regained its original length, it is unfolded into a straight layer, as long as the viscosity ratio is ≥50, which was the one used to create the starting configuration. If the viscosity ratio between layer and matrix is less than that

during formation of the folds (here $m = 50$), the layer does not completely unfold. This is because some folds do not widen, but become tighter. In the end, the stretched fold train has asymmetric isoclinal folds with a vergence opposite to the applied shear sense. With decreasing viscosity ratio, more folds remain and the geometry approaches that of pure passive shearing of the fold train (Carreras et al., 2005). Applying the arc-length method (Fletcher and Sherwin, 1978) at an additional strain of $\gamma' = 2$ would overestimate the amount of shortening, especially when the viscosity ratio decreased significantly. At the end of the experiments, the layer has undergone an additional shear strain of $\gamma' = 4$, and therefore has been brought back to its original length, but folds remain if the viscosity ratio was reduced.
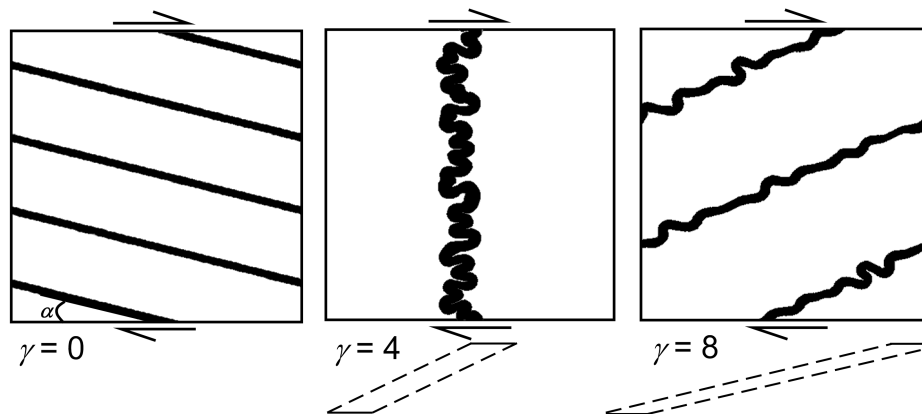
Figure 7.1: Elle-Basil model (see text). Inclined layer is sheared to shear strain, $\gamma = 4$, resulting in vertical fold train at 75% shortening, which is used as starting configuration for Figure 7.2. Model is laterally wrapping, and inclined single layer therefore reappears several times in the square model. Further shear to $\gamma = 8$ brings layer back to its original length.

Partial unfolding due to a reduced viscosity ratio thus leads to irregular, asymmetric folds, natural examples of which can be found at Roses and Puig Culip (Cap de Creus) at the easternmost extent of the Pyrenees in northeast Spain. At Puig Culip, ptygmatically folded quartz veins are found in strongly deformed, amphibolite facies metaturbidites (Carreras and Druguet, 1994; Druguet and Griera, 1998). Across a fold in the metaturbidite layers, folds in the vein shown in Figure 7.3A change from tight and symmetrical in the short limb (A' section) to irregular and asymmetric in the long limb (A" section). The thinner long limb underwent more dextral shearing than the short limb; the amount of shortening (assuming no thickening and thinning of the vein) is 56% and 22%, respectively. The vein section with the least apparent shortening underwent the most shearing, which supports the assertion that the vein shown in the A" section is partly unfolded. The partly unfolded vein section has distinct variations in thickness, implying that the strain estimate is incorrect: finite shortening is overestimated. Comparison with the numerical simulations suggests that the viscosity ratio between quartz vein and matrix was reduced during the partial unfolding. Formation of the veins and folding occurred during progressive metamorphism (Druguet et al., 1997; Druguet, 2001), which could cause a reduction in

viscosity ratios, as the activation energy for deformation of phyllite (∼98 kJ/mol; Shea and Kronenberg, 1992) is lower than that of quartz aggregates (e.g., 223 kJ/mol according to Gleason and Tullis, 1995).

The second example is of a partially unfolded aplite dike in a granodiorite shear zone (Simpson et al., 1982; Segall and Simpson, 1986; Carreras et al., 2004; Montmoli et al., 2008). The aplite dike (Fig. 7.3B), oriented at a small angle to the shear zone, underwent a shear strain of $\gamma \sim 13$ (Llorens et al., 2012, their figure 11), which would have first shortened the dike by 60% and subsequently stretched it to a finite stretch of ∼400%. The dike did not completely unfold, even though its finite length is much larger than the initial length. A few asymmetric, tight folds remained between strongly thinned sections (Figs. 7.3C and 7.3D), very similar to those in our numerical simulations (Fig. 7.2B); this suggests that the viscosity ratio was reduced during progressive shearing, possibly by shear weakening, as observed in experimentally deformed aplite (Dell'Angelo and Tullis, 1996).
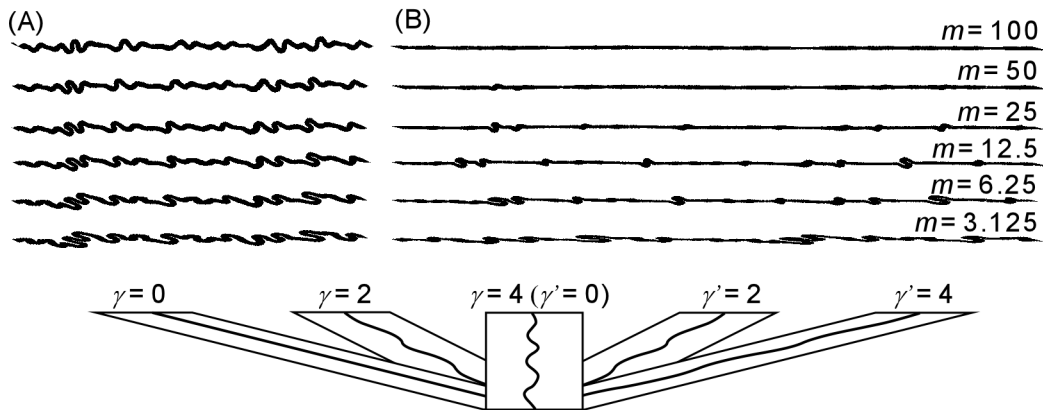
Figure 7.2: Result of stretching fold train of Figure 1 by additional shear strain, γ (m is viscosity ratio). A: $\gamma' = 2$. B: $\gamma' = 4$. Prime signifies amount of shearing after maximum layer-parallel shortening was reached (i.e., $\gamma = 4$ is equivalent to $\gamma' = 0$) that brings layer back to its original length. Layer envelope is initially oriented 14° to shear plane.

7.3   Unfolding multilayers

The preceding discussion showed that a layer can unfold and become straight again if the viscosity ratio remains the same, or increases. How can we know whether a straight layer was once folded? This is possible if the matrix is not completely homogeneous, but contains layers with different viscosities. Figure 7.4 shows a sample of the rich variety of geometries that can form in multilayers with various viscosity ratios that remained constant throughout the simulations. In all cases, one layer has a constant viscosity of 100, while the other layers have viscosities of 5, 10, or 25 times the matrix. While the central stiff layer straightens completely, adjacent layers do not; they form cusp-like folds and intrafolial folds (Ramsay, 1967; Ez, 2000; Carreras et al., 2005). Intrafolial folds are common in strongly deformed rocks, where they are usually interpreted as intensely
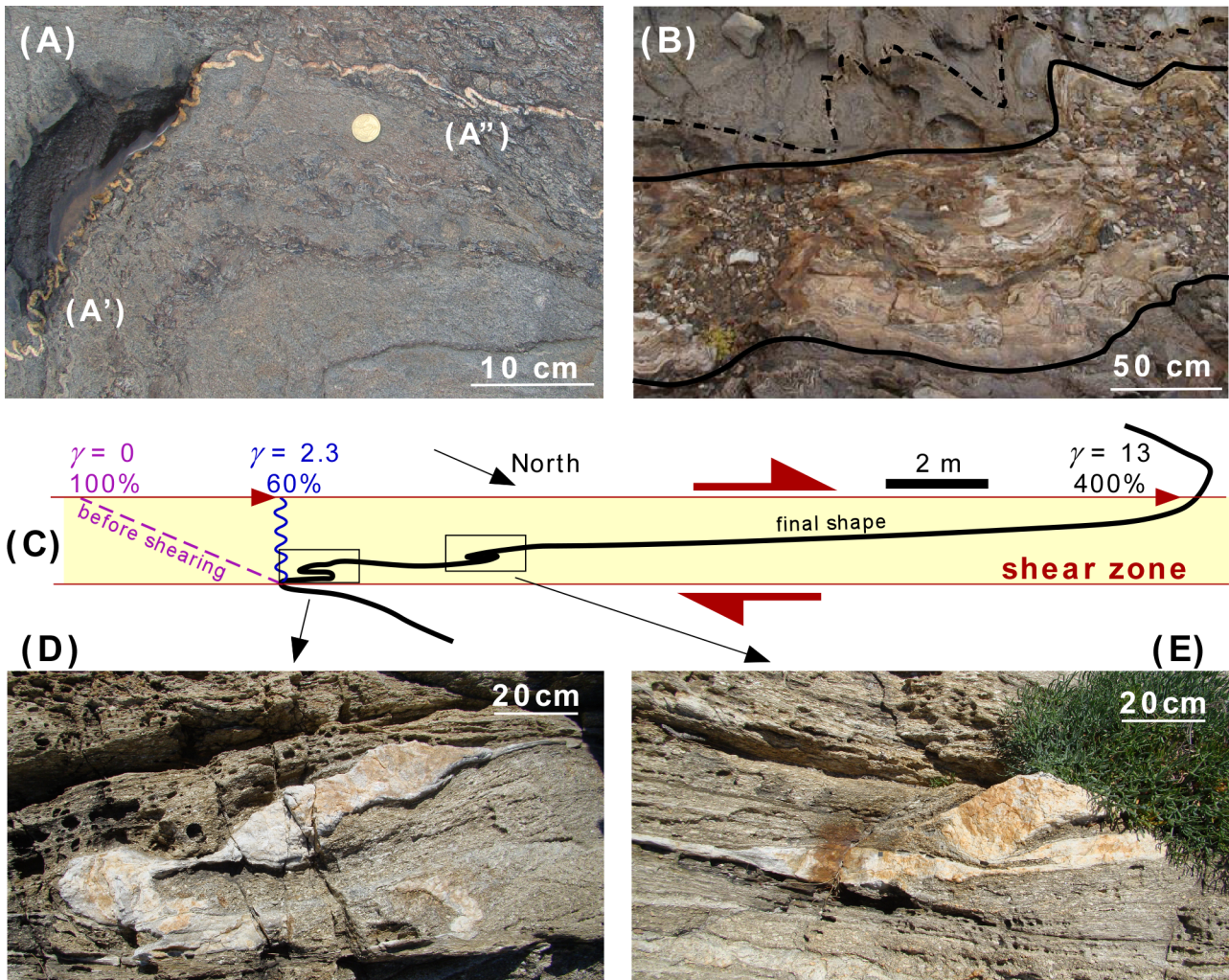
Figure 7.3: A: Quartz vein embedded in folded metaturbidite layers at Puig Culip (Cap de Creus, northeast Spain, Universal Transverse Mercator, UTM, coordinates 525.083, 4685.853). In left fold limb (A'), vein shows regular folds and is probably at its maximum shortening. In right limb (A"), irregular fold geometry indicates stretching by dextral shearing after initial shortening. B: Aplite dikes in granodiorite at Roses Lighthouse (Cap de Creus, northeast Spain, UTM coordinates 515.114, 4677.024; see Llorens et al., 2012, their figures 10 and 11). Dike is affected by dextral shear zone. Dike section inside shear zone first shortened 60% from initial length of ∼4.25 m and then stretched to length of 22 m, 400% of its original length. Although mostly sheared into thin layer, a few asymmetric folds with sinistral vergence remained. C, D: Asymmetric folds with sinistral vergence remaining. E: Straight but internally folded quartzite layer at Puig Culip (UTM coordinates 525.113, 4685.719). Adjacent metaturbidite layers show conspicuous cusp-like folds that indicate that competent quartzite layer was once more intensely folded. Dashed yellow line in E indicates fold train in the metaturbidite layers.

flattened remnants of an early deformation stage (Ez, 2000). Our simulations show that they can be alternatively interpreted as flattened fold trains that did not fully unfold, while the adjacent straight layers are fully unfolded and thus straight. A straight quartzite layer at Puig Culip (Fig. 7.3E) is probably an example of a straightened, but once folded layer. In nearby lower strain regions these sedimentary quartzite layers are folded, but here it is straight, though internally folded. Quartz veins and bedding in the adjacent

144

metaturbidites show the same conspicuous wavy or cusp-like folds as in our numerical simulations.

7.4 Discussion and conclusions

When isolated fold trains are stretched, they unfold to straight layers if their viscosity ratio with the matrix is not reduced between the shortening stage and the stretching stage (Fig. 7.2). In the case of multilayers, folds may not completely unfold again even without a change in viscosity ratio, if the unfolding is hampered by adjacent layers (Fig. 7.4). This was investigated numerically for linear viscous rheologies. Our numerical simulations (not shown here) indicated that a nonlinear, power law rheology does not significantly modify folding and unfolding behavior, but only increases the effective viscosity ratio (Jessell et al., 2009; Llorens et al., 2012). Boudinage or pinch-and-swell structures are enhanced by strain-dependent behavior (Hobbs et al., 1990), very high stress exponents or exponential flow (Smith, 1977; Schmalholz and Fletcher, 2011; Schmalholz and Maeder, 2012), or brittle failure (Goscombe et al., 2004). We did not include these effects in our simulations and therefore did not induce boudinage, which we regard as permissible considering the relative scarcity of boudins compared to folds in nature (Schmalholz and Fletcher, 2011).

Our simulations are a reminder that folds may once have been tighter, and that even straight layers may once have been folded (Kelley and Del Mar, 1958; Means, 1999). To our knowledge, no unambiguous structures have so far been recognized that could be used as indicators for straightening or unfolding. The simulations show that intrafolial folds and cusp-like folds adjacent to straight layers are such indicators. Irregular folds, with variations in fold amplitude and limb lengths, also appear characteristic, but not indicative, of stretching of folds (Schmalholz and Schmid, 2012). A reduction in viscosity ratio from shortening to extension leads to an additional variation in layer thickness. In this case, stretching does not necessarily result in complete straightening. This is an important consideration for strain analysis. The classical arc-length method (Fletcher and Sherwin, 1978) would significantly overestimate the amount of shortening, as fold trains may actually be longer than the original layer.

Acknowledgements
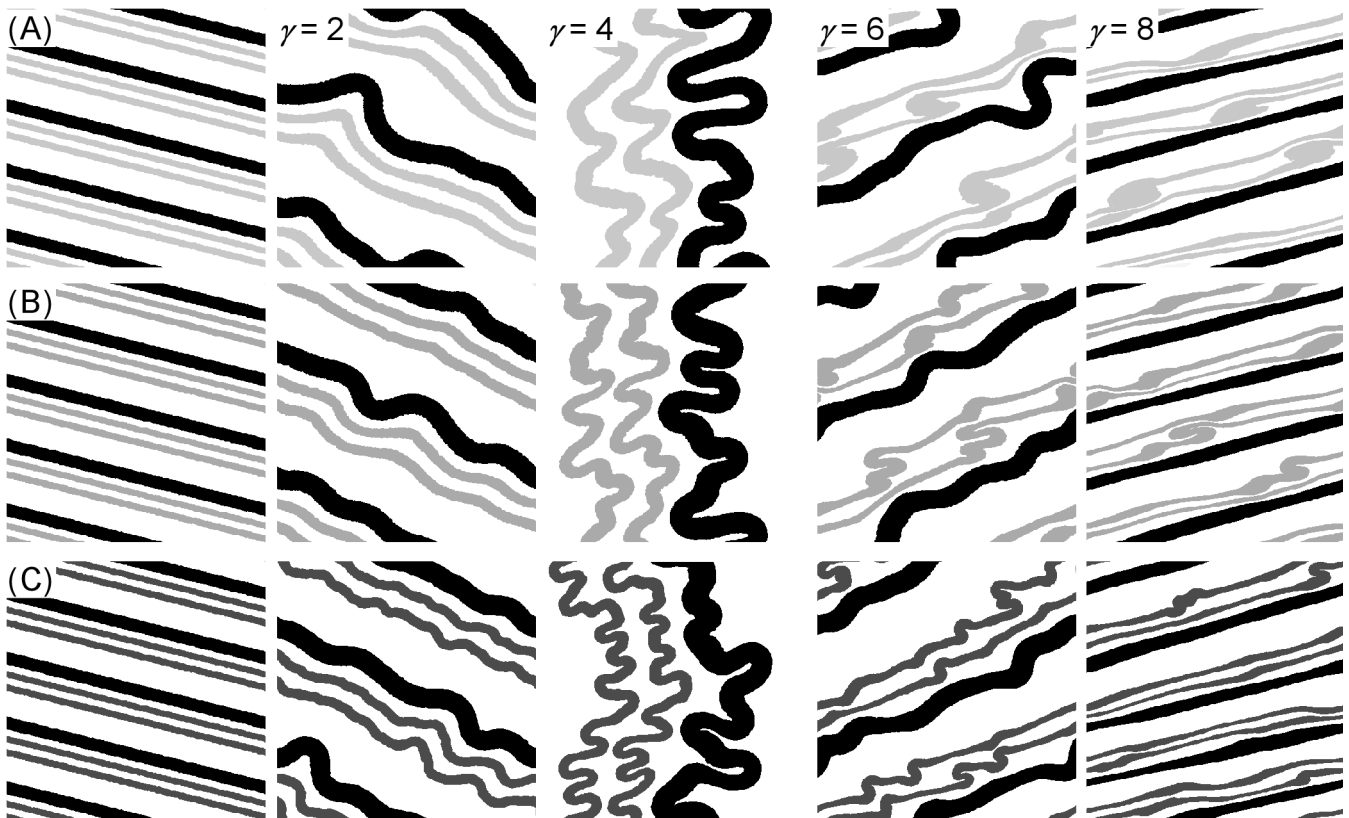
Figure 7.4: Multilayer simulations with layer with viscosity ratio $m = 100$ (black) and two surrounding layers (gray); γ is shear strain. A: With $m = 5$. B: With $m = 10$. C: With $m = 25$. Viscosity ratio is not changed during entire simulations. Folding in gray layers is party controlled by that of most competent layer, which leads to incomplete unfolding of gray layers, including cusp-like folds and intrafolial folds.

7.5 References

- Barr T.D., Houseman G.A., 1996, Deformation fields around a fault embedded in a non-linear ductile medium: Geophysical Journal International, v. 125, p. 473–490.

- Biot M.A., 1961, Theory of folding of stratified viscoelastic media and its implication in tectonics and orogenesis: Geological Society of America Bulletin, v. 72, p. 1595–1632.

- Bons P.D., Urai J.L., 1996, An apparatus to experimentally model the dynamics of ductile shear zones: Tectonophysics, v. 256, p. 145–164.

- Bons P.D., Koehn D., Jesell M.W., eds., 2008, Microdynamics simulation: Berlin, Springer, 406 p.

- Bons P.D., Jessell M.W., Griera A., 2009, Porpyroblast rotation versus nonrotation: Conflict resolution!: Comment: Geology, v. 37, p. e182–e188.

- Carreras J., Druguet E., 1994, Structural zonation as a result of inhomogeneous non-coaxial deformation and its control on syntectonic intrusions: An example from the Cap de Creus area (eastern-Pyrenees): Journal of Structural Geology, v. 16, p. 1525–1534.

- Carreras J., Druguet E., Griera A., Soldevilla J., 2004, Strain and deformation history in a syntectonic pluton. The case of the Roses granodiorite (Cap de Creus, Eastern Pyrenees), in Alsop G.I., et al., eds., Flow processes in faults and shear zones: Geological Society of London Special Publication 224, p. 307–319.

- Carreras J., Druguet E., Griera A., 2005, Shear zone–related folds: Journal of Structural Geology, v. 27, p. 1229–1251.

- Chapple W.M., 1968, A mathematical theory of finite amplitude rock-folding: Geological Society of America Bulletin, v. 79, p. 47–68.

- Dell'Angelo L.N., Tullis J., 1996, Textural and mechanical evolution with progressive strain in experimentally deformed aplite: Tectonophysics, v. 256, p. 57–82.

- DePaor D.G., Simpson C., Bailey C.M., McCaffrey K.J.W., Beam E., Robert J.W., Aziz G., 1991, The role of solution in the formation of boudinage and transverse veins in carbonate rocks at Rheems, Pennsylvania: Geological Society of America Bulletin, v. 103, p. 1552–1563.

- Druguet E., 2001, Development of high thermal gradients by coeval transpression and magmatism during the Variscan Orogeny: Insights from the Cap de Creus (Eastern Pyrenees): Tectonophysics, v. 332, p. 275–293.

- Druguet E., Griera A., 1998, Strain analysis using deformed quartz veins: Geogaceta, v. 24, p. 119–122.

- Druguet E., Passchier C.W., Carreras J., Victor P., den Brok S., 1997, Analysis of a complex high-strain zone at Cap de Creus, Spain: Tectonophysics, v. 280, p. 31–45.

- Ez V., 2000, When shearing is a cause of folding: Earth-Science Reviews, v. 51, p. 155–172.

- Fletcher R.C., 1974, Wavelength selection in the folding of a single layer with power-law rheology: American Journal of Science, v. 274, p. 1029–1043.

- Fletcher R.C., 1977, Folding of a single viscous layer: Exact infinitesimal-amplitude solution: Tectonophysics, v. 39, p. 593–606.

- Fletcher R.C., Sherwin J., 1978, Arc lengths of single layer folds: A discussion of the comparison between theory and observation: American Journal of Science, v. 278, p. 1085–1098.

- Ghosh S.K., Sengupta S., 1987, Progressive evolution of structures in a ductile shear zone: Journal of Structural Geology, v. 9, p. 277–287.

- Ghosh S.K., Sengupta S., 1999, Boudinage and composite boudinage in superposed deformations and syntectonic migmatization: Journal of Structural Geology, v. 21, p. 97–110.

- Gleason G.C., Tullis J., 1995, A flow law for dislocation creep of quartz aggregates determined with the molten salt cell: Tectonophysics, v. 247, p. 1–23.

- Goscombe B.D., Passchier C.W., Hand M., 2004, Boudinage classification: End-member boudin types and modified boudin structures: Journal of Structural Geology, v. 26, p. 739–763.

- Griera A., Bons P.D., Jessell M.W., Lebensohn R.A., Evans L., Gomez-Rivas E., 2011, Strain localization and porphyroclast rotation: Geology, v. 39, p. 275–278.

- Harris L.B., 2003, Folding in high-grade rocks due to back-rotation between shear zones: Journal of Structural Geology, v. 25, p. 223–240.

- Hobbs B.E., Muhlhaus H.B., Ord A., 1990, Instability, softening and localization of deformation, in Knipe R.J., Rutter E.H., eds., Deformation mechanisms, rheology and tectonics: Geological Society of London Special Publication 54, p. 143–165.

- Hudleston P.J., Lan L., 1993, Information from fold shapes: Journal of Structural Geology, v. 15, p. 253–264

- Hudleston P.J., Lan L., 1994, Rheological controls on the shapes of single-layer folds: Journal of Structural Geology, v. 16, p. 1007–1021.

- Hudleston P.J., Stephansson O., 1973, Layer shortening and fold shape development in the buckling of single layers: Tectonophysics, v. 17, p. 299–321.

- Jessell M.W., Bons P.D., Griera A., Evans L.A., Wilson C.J.L., 2009, A tale of two viscosities: Journal of Structural Geology, v. 31, p. 719–736,

- Jessell M.W., Bons P.D., Evans L., Barr T., Stüwe K., 2001, Elle: A micro-process approach to the simulation of microstructures: Computers & Geosciences, v. 27, p. 17–30.

- Johnson A.M., Fletcher R.C., 1994, Folding of viscous layers: New York, Columbia University Press, 461 p.

- Kelley V.C., Del Mar R., 1958, Unfolding; a bending process: American Association of Petroleum Geologists Bulletin, v. 42, p. 1094–1099.

- Klein J., 1980, Evolution of the first generation folds in a marble unit (Damara Orogenic Belt, Namibia): International Journal of Earth Sciences, v. 69, p. 770–800.

- Lechmann S.M., Schmalholz S.M., Burg J.-P., Marques F.O., 2010, Dynamic unfolding of multilayers: 2D numerical approach and application to turbidites in SW Portugal: Tectonophysics, v. 494, p. 64–74.

- Lisle R., 1997, A fold classification scheme based on polar plot of inverse layer thickness, in Sengupta S., ed., Evolution of geological structures in micro to macro-scales: London, Chapman and Hall, p. 323–339.

- Llorens M.-G., Bons P.D., Griera A., Gomez-Rivas E., Evans L.A., 2013, Single layer folding in simple shear: Journal of Structural Geology, v. 50, p. 209-220.

- Lloyd G.E., Ferguson C.C., 1981, Boudinage structure—Some new interpretations based on elastic-plastic finite element simulations: Journal of Structural Geology, v. 3, p. 117–128.

- Lloyd G.E., Ferguson C.C., Reading K., 1982, A stress transfer model for the development of extension fracture boudinage: Journal of Structural Geology, v. 4, p. 355–372.

- Malavieille J., Lacassin R., 1988, "Bone-shaped" boudins in progressive shearing: Journal of Structural Geology, v. 10, p. 335–345.

- Mancktelow N.S., 1999, Finite-element modelling of single-layer folding in elastoviscous materials; the effect of initial perturbation geometry: Journal of Structural Geology, v. 21, p. 161–177.

- Mancktelow N.S., 2001, Single-layer folds developed from initial random perturbations; the effects of probability distribution, fractal dimension, phase, and amplitude, in Koyi H.A., Mancktelow N.S., eds., Tectonic modeling: A volume in honor of Hans Ramberg: Geological Society of America Memoir 193, p. 69–87.

- Means W.D., 1999, Reversed structures and bounce structures: Are they recognizable? Are they real?: Journal of Structural Geology, v. 21, p. 917–921.

- Montmoli C., Carosi R., Frassi H., Ardito N., Carreras J., Druguet E., 2008, Shear partitioning across two parallel shear zones in Roses Granodiorite (Eastern Pyrenees, Spain): Rendiconti della Società Geologica Italiana, v. 3, p. 569–570.

- Passchier C.W., 1988, Analysis of deformation paths in shear zones: Geologische Rundschau, v. 77, p. 309–318.

- Ramberg H., 1955, Natural and experimental boudinage and pinch-and-swell structures: Journal of Geology, v. 63, p. 512–526.

- Ramberg H., 1962, Contact strain and folding instability of a multilayered body under compression: Geologische Rundschau, v. 51, p. 405–439.

- Ramberg H., 1963, Fluid dynamics of viscous buckling applicable to folding of layered rocks: American Association of Petroleum Geologists Bulletin, v. 47, p. 484–505.

- Ramberg H., Ghosh S.K., 1977, Rotation and strain of linear and planar structures in three-dimensional progressive deformation: Tectonophysics, v. 40, p. 309–337

- Ramsay J.G., 1967, Folding and fracturing of rocks: New York, McGraw-Hill, 568 p.

- Ramsay J.G., 1980, Shear zone geometry: A review: Journal of Structural Geology, v. 2, p. 83–99

- Schmalholz S.M., 2008, 3D numerical modelling of forward folding and reverse folding of a viscous single-layer: Implications for the formation of folds and fold patterns: Tectonophysics, v. 446, p. 31–41

- Schmalholz S.M., Fletcher R.C., 2011, The exponential flow law applied to necking and folding of a ductile layer: Geophysical Journal International, v. 184, p. 83–89.

- Schmalholz S.M., Maeder X., 2012, Pinch-and-swell structure and shear zones in viscoplastic layers: Journal of Structural Geology, v. 37, p. 75–88.

- Schmalholz S.M., Schmid D.W., 2012, Folding in power-law folding multi-layers: Royal Society of London Philosophical Transactions, ser. A, v. 370, p. 1798–1826.

- Schmid D.W., Podladchikov Y.Y., Marques F.O., 2004, Folding of a finite length power law layer: Journal of Geophysical Research, v. 109, B03407, doi:10.1029/2003JB002421.

- Segall P., Simpson C., 1986, Nucleation of ductile shear zones on dilatant fractures: Geology, v. 14, p. 56–59.

- Sengupta S., Ghosh S.K., Deb S.K., Khan D., 2005, Opening and closing of folds in superposed deformations: Journal of Structural Geology, v. 27, p. 1282–1299.

- Shea W.T., Kronenberg A.K., 1992, Rheology and deformation mechanisms of an isotropic mica schist: Journal of Geophysical Research, v. 97, p. 15,201–15,237.

- Simpson C., Carreras J., Losantos M., 1982, Inhomogeneous deformation in Roses granodiorite: Acta Geológica Hispánica, v. 17, p. 219–226.

- Skjernaa L., 1980, Rotation and deformation of randomly oriented planar and linear structures in progressive simple shear: Journal of Structural Geology, v. 2, p. 101–109.

- Smith R.B., 1975, Unified theory of the onset of folding, boudinage, and mullion structure: Geological Society of America Bulletin, v. 86, p. 1601–1609.

- Smith R.B., 1977, Formation of folds, boudinage, and mullions in non-Newtonian materials: Geological Society of America Bulletin, v. 88, p. 312–320.

- Smith R.B., 1979, The folding of a strongly non-Newtonian layer: American Journal of Science, v. 279, p. 272–287, doi:10.2475/ajs.279.3.272.

- Swanson M.T., 1992, Late Acadian–Alleghenian transpressional deformation: Evidence from asymmetric boudinage in the Casco Bay area, coastal Maine: Journal of Structural Geology, v. 14, p. 323–341.

- Talbot C.J., 1970, The minimum strain ellipsoid using deformed quartz veins: Tectonophysics, v. 9, p. 47–74.

- Talbot C.J., 1999, Can field data constrain rock viscosities?: Journal of Structural Geology, v. 21, p. 949–957.

- Talbot C.J., Sokoutis D., 1992, The importance of incompetence: Geology, v. 20, p. 951–953.

- Treagus S.H., 1983, A new theory of finite strain variation through contrasting layers and its bearing on cleavage: Journal of Structural Geology, v. 5, p. 351–368.

- Treagus S.H., 1993, Flow variations in power-law multilayers: Implications for competence contrast in rocks: Journal of Structural Geology, v. 15, p. 423–434.

- Tullis T.E., Horowitz F.G., Tullis J., 1991, Flow laws of polyphase aggregates from end-member flow laws: Journal of Geophysical Research, v. 96, p. 8081–8096.

Chapter 8

Numerical modelling of porphyroclast and porphyroblast rotation in anisotropic rocks

Albert Griera[a], **Maria-Gema Llorens[b]**, Enrique Gomez-Rivas[b], Paul D. Bons[b], Mark W. Jessell[c], Lynn A. Evans[d] and Ricardo Lebensohn[e]

[a]Departament de Geologia, Universitat Autònoma de Barcelona, 08193 Bellaterra (Barcelona), Spain
[b]Departament of Geosciences, Eberhard Karls University Tübingen, Wilhemstr. 56, 72074 Tübingen, Germany
[c]Université de Toulouse, UPS (SVT-OMP) & IRD, GET, 14 Av. Edouard Belin, F-31400 Toulouse, France
[d]School of Geosciences, Monash University, Clayton, Victoria 3800, Australia
[e]Materials Science and Technology Division, Los Alamos National Laboratory, Los Alamos, NM 87545, USA

Abstract

The rotational behaviour of rigid objects in a weaker rock matrix during deformation has been the subject of many field, experimental and numerical modelling studies, often centred on the question whether objects rotate or not in non-coaxial deformation. With numerical studies gaining increasing popularity and importance we here provide an overview of the results published so far and provide new simulations. Originally, shape and orientation were investigated, while the emphasis shifted to rheology and slip between object and matrix in the nineties of the last century. Due to improved numerical techniques, anisotropic rheology has become the focus of most recent studies, indicating that it is a primary factor in the rotation behaviour of objects. We present new simulations investigating the role of anisotropy on different scales relative to the object, and show how this influences the rotation rate, as well as the inclusion patterns in case of syntectonically growing porphyroblasts. These simulations showthat a variety of factors play a role to determine the rate and sense of rotation of objects. The variability of the inclusion patterns that can develop necessitates extreme caution in the kinematic interpretation of these structures when observed in the field.

Keywords

8.1   Introduction

Structural geologists use a wide range of structures, such as folds, cleavages, veins, etc., to unravel deformation histories and conditions in rocks (see text books such as Hobbs et al., 1976; Passchier and Trouw, 2005; Ramsay and Huber, 1983, 1987; Vernon, 2004). Hard inclusions (e.g. mineral grains) in a relative weaker matrix form one class of structures that have received much attention for the potential wealth of information stored in them, such as sense of shear, kinematic vorticity number, distinguishing different deformation events, finite strain, etc. (e.g. Passchier and Trouw, 2005, and references therein). The structures related to such hard inclusions fall into two main categories, which we group under the terms porphyroclasts and porphyroblasts (Fig. 8.1).

Porphyroclasts are pre-existent hard objects whose shape and orientation can be modified by deformation, resulting in the formation of structures such as sigma- and delta-clasts, and mica fish. Porphyroclasts are relatively hard and occur as large single crystals or mechanically coherent polycrystalline aggregates compared to the grains of the surrounding matrix (Passchier and Simpson, 1986). Typical examples are feldspar porphyroclasts in a finer grained, mylonitic quartz–feldspar matrix (Fig. 8.1a). Porphyroclasts often have wings

or tails of material that appear smeared off and recrystallised from the porphyroclast. Under non-coaxial deformation, winged porphyroclasts usually develop a monoclinic symmetry that is of great practical use as a shear-sense indicator (Bjørnerud, 1989a; Hammer and Passchier, 1991; Passchier and Simpson, 1986). The main winged-porphyroclast types are sigma- and delta-clasts (Fig. 8.2).

Porphyroblasts are relatively large and hard metamorphic minerals (e.g. garnet) that overgrowtheirmatrix in response to changes inmetamorphic conditions (e.g. Passchier and Trouw, 2005). Their presence influences the deformation field in their immediate vicinity. A "frozen" image of this vicinity can often be found inside the porphyroblast in the form of aligned inclusions that were incorporated during growth of the porphyroblast.While shape and orientation are of primary interest for porphyroclasts, the relationships between internal structures (internal foliation, *Si*) relative to that in the object's vicinity (external foliation, *Se*) is of importance for porphyroblasts (e.g. Bell, 1985; Bell et al., 1992b; Passchier et al., 1992; Schoneveld, 1977; Wilson, 1971).

Porphyroblasts containing sigmoidal or spiral inclusion patterns are common in deformed rocks (Fig. 8.1). They are a key tool to evaluate the relationship between deformation and metamorphism (e.g. Johnson, 1999). However, the interpretation of how these microstructures are formed has been the topic of a long and ongoing debate. Many geologists assume that the rotational component of non-coaxial deformation during porphyroblast growth will lead to the rotation of rigid objects and the development of spiral trail geometries (e.g. Rosenfeld, 1970; Schoneveld, 1977). This conceptual model is based on the analytical solution for the rotation of a stiff inclusion embedded in a linear viscous fluid developed by Einstein (1905) and extended by Jeffery (1922). Ghosh and Ramberg (1976) provided an analytical solution for elliptical inclusion rotation in general shear conditions and performed analogue models to experimentally test their solution.

A few years later, Bell (1985) proposed an alternative model where deformation is partitioned in the matrix around the hard object, so that it does not rotate and remains fixed with respect to the geographical coordinate frame. This conceptual model is based on the development of anastomosing non-coaxial strain zones around the porphyroblast. These zones can significantly reduce the vorticity induced by deformation around the object. In this approach, curved inclusion trails are interpreted by near orthogonal foliations produced by successive deformation phases (e.g. Bell et al., 1992b). Therefore, the orientation of aligned inclusions inside a porphyroblast relative to the external foliation can be interpreted in two different ways: (a) if the porphyroblast did not rotate, the internal foliation shows the orientation of an foliation older than the external foliation (Bell, 1985) or, alternatively, (b) the difference in orientation indicates porphyroblast rotation, which again provides information on the kinematics of deformation, such as sense of shear (Schoneveld, 1977; Vernon, 1978). The resulting interpretation of porphyroblasts is not trivial because it has significant tectonic implications: these models may predict an opposite sense of shear but
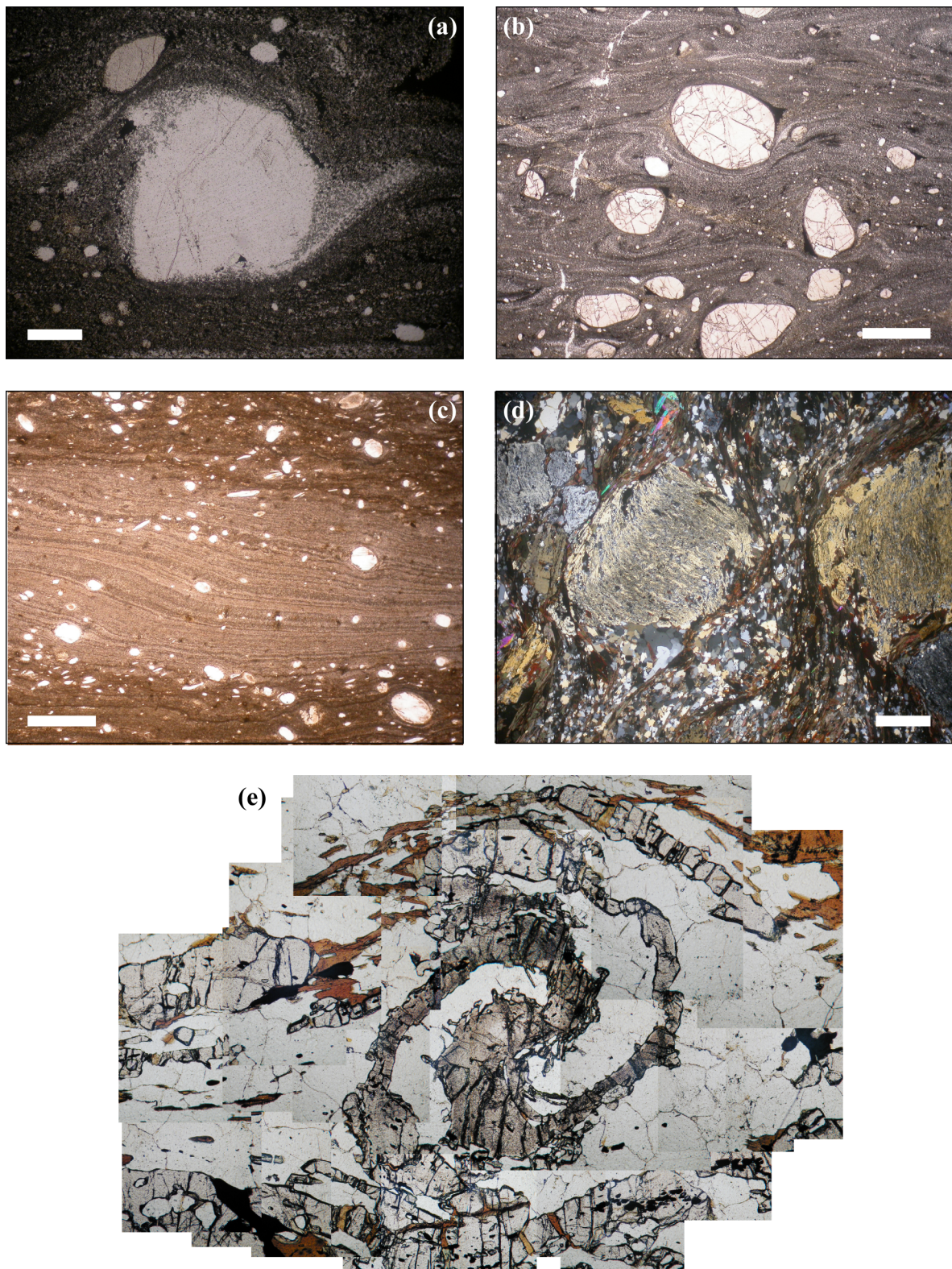
Figure 8.1: Examples of porphyroclasts and porphyroblasts: (a) mantled plagioclase δ-clast; (b) interaction between differently sized garnets clasts, decoupling between garnet and mylonite is evident in the central clast; (c) plagioclase and garnet clasts from a mylonite–ultramylonite zone with variable ratios between mylonitic layer thickness and clast size; (d) andalusite porphyroblasts with sigmoidal inclusion pattern oblique to the external foliation; (e) garnet porphyroblast with a spiral shaped inclusion trail or snow-ball inclusion pattern. Photos (a), (b) and (c) are from mylonites zone from the Ivrea–Verbano zone, (d) and (e) are from the Variscan basement of the NE-Pyrenees. Micrograph (e) is courtesy of Joan Reche Estrada (Reche Estrada and Martinez, 2002). White scale bars are 1 mm long. All views are in the *XZ* section with a dextral sense of shear.

154
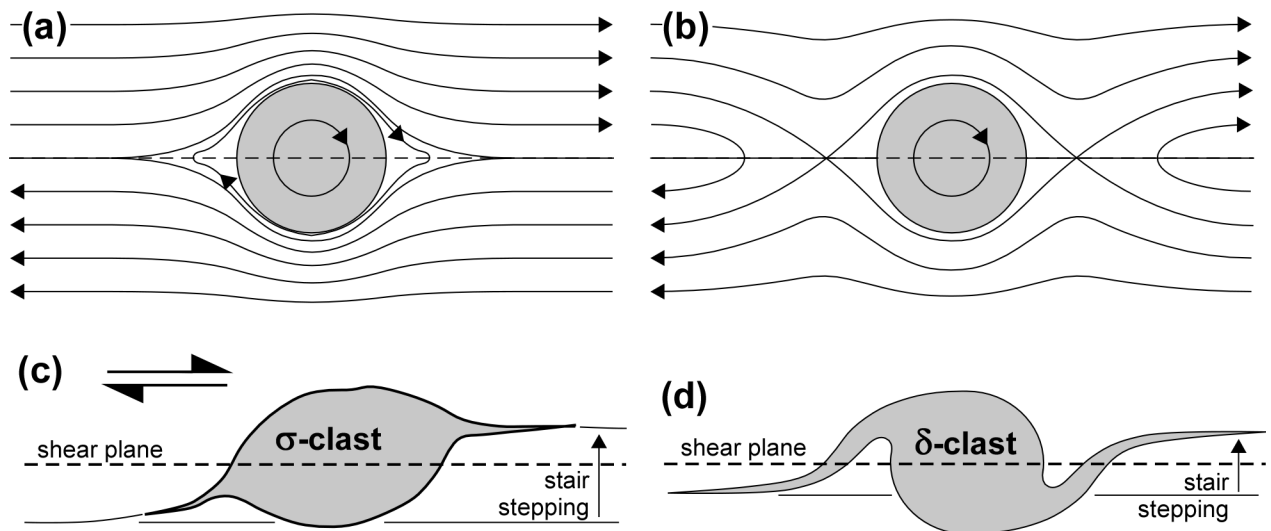
Figure 8.2: Flow patterns around a circular object in dextral simple shear: (a) Cat's eye pattern and (b) bow tie pattern. (c) Sigma- and (d) delta-clast, both with stair stepping of the wings.

also a different tectonic history (i.e.multiple deformation phases versus a single phase, e.g. Johnson, 1999; Robyr et al., 2009).

The level of this controversy is illustrated by the heated discussion and reply papers of Passchier et al. (1992) and Bell et al. (1992b). Several discussion and review papers followed these publications (e.g. Aerden, 2005; Jiang and Williams, 2004; Johnson, 1999; Williams and Jiang, 1999). Despite some publications with titles containing ambitious claims, such as "conflict resolution!" (Fay et al., 2008), or "Debate settled!" (Johnson, 2009), the discussions and replies following these papers show that the debate is still far from being settled (Bons et al., 2009; Fay et al., 2009; Johnson, 2010; Sanislav, 2010). However, this might only be an apparent conflict, as recently illustrated by several authors (e.g. Bons et al., 2009; Dabrowski and Schmid, 2011; Griera et al., 2011). Field, experimental and numerical data support the observation that rigid objects can rotate significantly, but there are several factors that can reduce or inhibit their rotation, or even cause rotation in an antithetic sense. These factors comprise incoherent matrix–inclusion interfaces (e.g. Ceriani et al., 2003; Ildefonse and Mancktelow, 1993), confined shear flow (Marques and Coelho, 2001; Marques et al., 2005a, 2005b), strain localisation in the matrix (Griera et al., 2011; ten Grotenhuis et al., 2002) or mechanical interaction between inclusions (e.g. Ildefonse et al., 1992; Jessell et al., 2009), among others.

One of the main issues for the study of rigid-object rotation is that most of the existing experiments and numerical simulations are based on homogeneous isotropic (linear) viscous matrix rheologies, whose results are coherent with the analytical solutions. However, natural rocks are generally crystalline, heterogeneous and very often anisotropic. These mechanical properties enhance heterogeneous stress and strain rate fields and favour strain localisation. Bell (1985) already proposed that rigid object rotation could be inhibited by the development of anastomosing shear band networks. Two decades of advances on

numerical modelling techniques have been necessary before this fundamental issue has been incorporated into studies (e.g. Dabrowski and Schmid, 2011; Griera et al., 2011; see below).

Two decades after the discussion of Passchier et al. (1992) and Bell et al. (1992b), and after more than 30 years of numerical modelling on this topic, we would like to take advantage of this special volume in honour to Tim Bell to contribute to the issue of porphyroclast/-blast behaviour in anisotropic materials. We present a series of numerical simulations to investigate the influence of mechanical anisotropy on rigid-object rotation behaviour and porphyroblast inclusion pattern development. We first provide a review of published numerical studies that explicitly addressed the problem of rotation and deformation in and around rigid objects in ductile rocks. We intentionally exclude field and experimental contributions related to the controversy of the rotation versus non-rotation issue, as for example the foliation inflexion axes preserved within porphyroblasts (FIAs; e.g. Bell et al., 1992b; Hayward, 1990). These aspects are widely discussed in the excellent review paper by Johnson (1999). After that, we systematically analyse the influence of the orientation, degree and type of anisotropy on rigid object rotation behaviour and porphyroblast inclusion trails. For this purpose,we use the software package Elle (Bons et al., 2008; Jessell et al., 2001). In this contribution, two main aspects are considered: (1) syntectonic growth of porphyroblasts and (2) influence of the relative ratio between the length scale of anisotropy and object size. We analyse the case of intrinsic anisotropy, in a similar way as Griera et al. (2011), and also the behaviour of objects embedded in composite materials (e.g. Treagus, 1997). Finally, we provide a brief summary and a perspective on the future of numerical modelling of porphyroblasts.

Table 8.1: Summary of publications that specifically addressed the mechanical problem of rotation behaviour of rigid objects and/or the development of spiral inclusion by means of 2D or 3D analytical or numerical studies. Please note that this table only includes studies where the kinematical or mechanical field around an inclusion are explicitly calculated. FEM: finite element method; FD: finite difference; CPFFT: crystal plastic fast Fourier transform.

Reference	Approach	Rheology	Particle behaviour	Growth kinetics	Goals
Einstein (1905, 1956)	Analytical, 3D	Isotropic linear viscous	Rigid, spherical, single	No	Flow field
Jeffery (1922)	Analytical, 3D	Isotropic linear viscous	Rigid, ellipsoidal, single	No	Rotation
Muskhelishvili (1953)	Analytical, 3D	Isotropic linear elastic	Deformable, elliptical, single	No	Elastic field distribution
Eshelby (1957)	Analytical, 3D	Isotropic linear elastic	Deformable, elliptical, single	No	Elastic field distribution

Table 8.1 – continued from previous page

Reference	Approach	Rheology	Particle behaviour	Growth kinetics	Goals
Gay (1968)	Analytical, 2D	Isotropic linear viscous	Deformable, elliptical, single	No	Rotation
Ghosh and Ramberg (1976)	Physical, analytical, 2D	Isotropic linear viscous	Rigid, ellipsoidal, single	No	Rotation, general shear
Ferguson (1979)	Physical, analytical, 3D	Isotropic linear and power-law viscous	Rigid, ellipsoidal, single	No	Rotation
Masuda and Ando (1988)	Analytical, 2D	Isotropic linear viscous	Rigid, circular, single	No	Flow and stress field, marker orientation influence
Masuda and Mochizuki (1989)	Analytical, numerical integration, 2D	Isotropic linear viscous	Rigid, spherical, single	Yes, linear	Foliation trace, inclusion pattern
Bjørnerud (1989b)	Analytical, numerical integration, 2D	Isotropic linear viscous	Rigid, spherical, single	No	Foliation trace, strain distribution
Bjørnerud and Zhang (1994)	Analytical, numerical integration, 2D	Isotropic linear viscous	Rigid, spherical, single	Yes, discontinuous growth	Foliation trace, decoupling matrix and inclusion
Gray and Busa (1994)	Analytical, 3D	Isotropic linear viscous	Rigid, spherical, single	Yes, linear and power-law growth	Foliation trace
Masuda and Mizuno (1995, 1996a, 1996b)	Analytical and FEM numerical, 2D	Isotropic linear and non-linear viscous	Rigid, circular, single	No	Flow and stress field, marker orientation influence
Beam (1996)	Analytical, numerical integration, 2D	Isotropic linear viscous	Rigid, elliptical, single	Yes, linear and power-law growth	Foliation and inclusion trace
Bons et al. (1997)	Analytical and numerical, 2D FEM	Isotropic non linear viscous	Rigid, circular, single	No	Flow pattern, influence of boundary conditions
Kenkmann and Dresen (1998)	Numerical, 2D FEM	Isotropic non-linear viscous	Deformable, circular, single	No	Stress field, influence of slip interface
Ježek et al. (1999)	Analytical, numerical integration, 3D	Isotropic linear viscous	Rigid, elliptical, single	Yes, unspecified	Flow field

Table 8.1 – continued from previous page

Reference	Approach	Rheology	Particle behaviour	Growth kinetics	Goals
Pennacchioni et al. (2000)	Numerical, 2D FEM	Isotropic non linear viscous	Rigid, circular, single	No	Flow field, influence of slip interface
Mandal et al. (2000, 2002)	Analytical, numerical integration, 2D	Isotropic linear viscous	Rigid, elliptical, single	No	Flow pattern, strain distribution, general shear
Treagus and Lan (2000, 2003, 2004)	Numerical, 2D FEM	Isotropic, linear viscous	Deformable, square, single	No	Rotation, strain
ten Grotenhius (2001)	Numerical, 2D FD	Isotropic non linear viscous and elastoplastic	Deformable, rectangular, single, soft interface	No	Rotation, strain distribution
Biermeier et al. (2001)	Numerical, 2D FEM	Isotropic non-linear viscous	Deformable, circular, single	No	Rotation, influence inclusion size and boundary conditions
Tenczer et al. (2001)	Numerical, 2D FEM	Isotropic non-linear viscous	Deformable, circular, single	No	Pressure shadows
Samanta et al. (2002a, 2002b)	Analytical, 2D numerical integration	Isotropic linear viscous	Rigid, elliptical, single	Yes, linear growth	Flow field, foliation trace, influence marker orientation
Stallard et al. (2002)	Analytical, numerical integration, 3D	Isotropic, linear viscous	Rigid spherical	Yes, constant volume rate	Inclusion trail geometry, large strain
Taborda et al. (2004)	Numerical, 2D FEM	Isotropic linear viscous	Rigid, elliptical, single	No	Rotation, strain and stress distribution
Samanta et al. (2003)	Analytical, 2D numerical integration	Isotropic linear viscous	Rigid, circular, multiple	No	Flow field
Jiang and Williams (2004)	Analytical, drawing	Isotropic linear viscous	Rigid, circular, single	No	Foliation trace
Schmid and Podladchikov (2004), Schmid and Podladchikov (2005)	Numerical, 2D FEM	Isotropic non-linear viscous	Rigid, elliptical, single, soft interface	No	Rotation and stress/strain rate distribution
Schmid (2005)	Analytical and numerical, 2D FEM	Isotropic, non-linear viscous	Deformable, polygonal, single	No	Rotation, strain and stress distribution

Continued on next page...

Table 8.1 – continued from previous page

Reference	Approach	Rheology	Particle be-haviour	Growth kinetics	Goals
Mandal et al. (2005a)	Analytical, 2D	Anisotropic, linear elastic	Rigid, elliptical, single	No	Instantaneous rotation
Mandal et al. (2005b)	Numerical, 2D FEM	Isotropic, linear viscous	Rigid, circular, single	No	Flow field, influence of boundary conditions
Marques et al. (2005a,b,c)	Numerical, 2D FEM	Isotropic, linear viscous	Rigid, elliptical and rhomboidal, single	No	Rotation, flow perturbation, strain and stress distribution
Takeda and Griera (2006)	Numerical, 2D FD	Isotropic, linear viscous	Deformable, square, multiple	No	Strain and stress distribution, bulk flow rheology
Groome and Johnson (2008), Groome et al. (2006)	Numerical, 2D front tracking FEM	Isotropic linear viscous	Deformable, polygonal, multiple	Yes, linear growth	Strain distribution, bulk flow, rheology, microstructure of matrix, large strain
Mulchrone (2007)	Analytical, 2D	Isotropic linear viscous	Rigid, elliptical, single, slip interface	No	Rotation, strain distribution, influence slip interface
Houseman et al. (2008)	Numerical, 2D front tracking FEM	Isotropic, linear viscous	Deformable, circular, single	Yes, linear growth	Strain distribution, microstructure matrix
Johnson (2008)	Numerical, 2D front tracking FEM	Isotropic, linear viscous	Deformable, circular, single, soft interface	No	Strain and stress distribution
Fay et al. (2008)	Numerical, 2D unspecified	Isotropic, elasto-plastic	Deformable, square, single	No	Rotation, strain distribution
Jessell et al. (2009)	Numerical, 2D front tracking FEM	Isotropic, non-linear viscous	Deformable, polygonal, multiple	No	Strain distribution, high strain, microstructure matrix
Wilson et al. (2009)	Numerical, 2D front tracking FEM	Isotropic, non-linear viscous	Deformable, rectangular, multiple	No	Strain and stress distribution
Johnson et al. (2009)	Numerical, 2D FEM	Isotropic, linear viscous	Rigid, elliptical, multiple, soft interface	No	Rotation and strain rate distribution

Table 8.1 – continued from previous page

Reference	Approach	Rheology	Particle behaviour	Growth kinetics	Goals
Bons et al. (2009)	Numerical, 2D	Isotropic linear viscous	Deformable, cylindrical, single	Yes, linear growth	Inclusion geometry
Fletcher (2009)	Analytical, 2D	Anisotropic, linear viscous	Rigid, cylindrical, single	No	Rotation
Griera et al. (2011)	Numerical, 2D front tracking, CPFFT	Anisotropic, non-linear viscous plastic	Rigid, cylindrical, single	No	Rotation, strain distribution, high strain, microstructure of matrix
Dabrowski and Schmid (2011)	Analytical and numerical, 2D FEM	Anisotropic linear viscous	Rigid, circular, single	No	Rotation and perturbation development
This study	Numerical, 2D front tracking, CPFFT, 2D FEM	Anisotropic, non-linear viscous plastic, anisotropic linear viscous	Rigid, circular, single	Yes, linear growth	Rotation, strain distribution, high strain, microstructure of matrix, influence of degree, type and orientation of anisotropy

8.2 Historical overview

The rotation of rigid objects during deformation is a key aspect for the interpretation of structures related to hard particles, because they provide information on the kinematics and mechanics of deformation as well as on the metamorphic history. For this reason, a wide range of numerical approaches have addressed these structures from different perspectives. For example, the orientation distribution of rigid objects is used to determine the kinematics of deformation (i.e. vorticity number) as kinematics of deformation control the object rotational behaviour (e.g. Johnson et al., 2009, Masuda et al., 1995, Passchier, 1987 and Reed and Tryggvason, 1974), the orientation and the geometry of inclusion patterns are used to infer folding mechanisms (e.g. Jiang, 2001 and Stallard and Hickey, 2001), while the shape of deformable inclusions is used as a strain indicator (e.g. *Rf/phi* method; Bilby and Kolbuszewski, 1977, Bilby et al., 1975, Jiang, 2007 and Mancktelow, 2011 and references therein). Finally, the asymmetrical geometry of rigid clasts is used to infer the shear-sense (e.g. Passchier, 1994 and Passchier et al., 1993).

Table 8.1 provides a list of studies that explicitly addressed the mechanical problem of rotation behaviour of rigid objects and/or the development of spiral inclusion by means

of 2D or 3D analytical or numerical studies. This table summarises a large number of contributions on the topic, and reflects the importance of this field for the understanding of rock deformation. Most of the listed studies focused on porphyroclast behaviour and only less 25% of them studied the deformation and growth of porphyroblasts.

8.2.1 Analytical models

Most analytical approaches are essentially based on the seminal paper by Jeffery (1922), which has been cited more than 1700 times at the time of writing this paper. Jeffery (1922) provided the basic equations for the rotation of ellipsoidal objects and the velocity field around it in a slow linear viscous flow. It is important to recognise that Jeffery (1922) is a generalisation of the work by Einstein (1905; republished in 1956) that provided the first mathematical solution of the flow field around a rigid spherical object in a slowly flowing viscous matrix. The analytical solution for a single deformable inclusion in a linear elastic matrix was developed by Muskhelishvili (1953), and later on Eshelby, 1957 and Eshelby, 1959 provided a general solution for deformation in and around an ellipsoidal inclusion that is applicable to a wide range of rheologies of inclusion and matrix. These four publications are the mathematical basis of most of the current analytical approaches in structural geology.

Around half a century later than the work by Jeffery (1922), geologists picked up these theories in order to predict orientations of single objects and populations of elongate objects as a function of applied deformation and extended solutions to arbitrarily oriented ellipsoidal objects, non-rigid objects, and even power-law viscosity (Ferguson, 1979, Gay, 1968, Ghosh and Ramberg, 1976 and Reed and Tryggvason, 1974). The earliest studies mainly focussed on the rotation of ellipsoidal objects, but not on the flow field around these objects, even though Einstein (1905) or Jeffery (1922) already provided the basic equations for this. Various solutions for the flow field around spherical and ellipsoidal objects can be found in Chwang and Wu (1975) or Masuda and Ando (1988), among others. Passchier et al. (1993) used and analytical equation for flow lines, based on the work by Chwang and Wu (1975), to explain the occurrence of stair stepping, which requires a "bow-tie" shaped flow pattern (ten Brink and Passchier, 1995) (Fig. 8.2). Their suggestion that such a flow pattern had to be the result of a power-law rheology of the matrix was refuted by later finite-element simulations (Bons et al., 1997).

Most of the numerical studies addressing the flow around a growing sphere to predict inclusion patterns inside porphyroblasts are based on the aforementioned kinematic equations (Beam, 1996, Bjørnerud and Zhang, 1994, Gray and Busa, 1994, Masuda and Mochizuki, 1989, Samanta et al., 2002a, Samanta et al., 2002b and Stallard et al., 2002). Numerical modelling was needed to integrate the analytical solutions over time to achieve the finite strain field. The work by Masuda and Mochizuki (1989) represents the first

two-dimensional numerical simulation study while Gray and Busa (1994) extended it to three dimensions. Bjørnerud and Zhang (1994) included the effect of a slipping object surface, which would reduce rotation, an aspect that would receive much attention a decade later (see below). Stallard et al. (2002) provided numerical simulations of the development of three dimensional spiral inclusion trails according to the rotational and the non-rotation models. They found that the interpretation of spiral inclusion is problematic because of the lack of diagnostic geometrical differences between the two models. Posteriori extension for general shear and different initial orientation of foliation markers was done by Samanta et al., 2002a and Samanta et al., 2002b. A major handicap of analytical models is that they are unable to address the rotation problem from a dynamic point of view because the mode of rotation is imposed by the assumptions.

8.2.2   Numerical simulations: isotropic matrix

By the nineteen-nineties, computers had developed to the stage that the stress and velocity field in and around objects could be calculated numerically, typically by the finite-element method, thus obviating the need to use simplified analytical models. Bons et al. (1997) is one of the first numerical finite-element models (FEM) of circular semi-rigid inclusions in simple shear flow in a homogenous matrix. They investigated the effect of power-law viscosity (with stress exponents 1, 3 and 5) and showed that it has little effect on the rotation rate of a circular object, nor on the flow field (cat's eye versus bow-tie pattern; Fig. 8.2). They did, however, point out that boundary conditions are important and that a change from velocity to stress boundary conditions can significantly change the flow pattern around an object. This result was confirmed by Biermeier et al. (2001), who also showed that the rotation rate is significantly reduced when the shear-zone boundaries are very close to the object. A similar effect was also observed by Marques et al., 2005a and Marques et al., 2005c using FEM simulations for conditions of confined shear flow (i.e. when inclusion size is similar to the shear zone width).

Subsequent studies extended the numerical simulations to non-circular objects (e.g. Schmid, 2005), interaction between multiple inclusions (Jessell et al., 2009) and explored the role of an incoherent interface between object and matrix (e.g. Kenkmann and Dresen, 1998, Pennacchioni et al., 2000 and Schmid and Podladchikov, 2004). This last series of studies was largely inspired by the observation that Jeffery's (1922) theory predicts that sufficiently elongate objects have stable positions in combined pure and simple shear tilted forward in the shear direction, while field observations rather show a backward tilting (Mancktelow et al., 2002, Pennacchioni et al., 2001 and ten Grotenhuis et al., 2003). Experiments showed that this behaviour could be explained by localisation of strain at the object surface (Ceriani et al., 2003, Mancktelow et al., 2002 and ten Grotenhuis et al., 2002). This localisation could be caused by the presence of a soft mantle (Passchier, 1994)

and was modelled by Schmid and Podladchikov, 2004 and Schmid and Podladchikov, 2005.

An alternative explanation is that the matrix has an intrinsic tendency to localise strain, for example if the matrix behaves as a plastic material with a yield strength. In experiments with a Mohr–Coulomb brittle matrix (approximating a plastic matrix), ten Grotenhuis et al. (2002) indeed produced the expected backward tilting object orientations, related to strong shear localisation at the object boundary. This model closely resembles the one for non-rotation of porphyroblasts of Bell et al. (1989), and an elastoplastic rheology was therefore used for numerical simulations to prove non-rotation (Fay et al., 2008 and ten Grotenhius, 2001). Not surprisingly, both "schools" achieved the desired results to support their own model. Objects rotate in a deforming (linear or power-law) viscous matrix, but a softer object mantle inhibits rotation and may lead to stable object orientations. In an elastoplastic matrix, object rotation is significantly or completely inhibited but deformation is accommodated by sliding along fracture zones. The question is of course, which rheology most closely approximates that of real rocks and not, which rheology to choose to achieve the desired result (Bons et al., 2009).

8.2.3   Numerical simulations: anisotropic matrix

It was already clear in the nineteen-eighties (e.g. Bell et al., 1989) and nineteen-nineties (e.g. Bons et al., 1997) that an anisotropic matrix rheology could be a significant factor for object (non) rotation. However, numerical methods only recently reached the stage that an anisotropic rheology could be incorporated. The analytical solution by Fletcher (2009) showed that the rotation rate of an elliptical rigid inclusion is independent of the anisotropy and equal to the observed one in an isotropic medium. However, this solution is limited because it assumes that anisotropy remains homogenous and it is not applicable to systems with high strain and heterogeneous anisotropy. One way to simulate an anisotropic matrix rheology is the use of layers with alternating (viscous) rheology (Dabrowski and Schmid, 2011). A generic finite-element model for isotropic rheology can be used, as the anisotropy emerges from the layering. Effective anisotropy of layered medium can be calculated using Biot's theory (Biot, 1965). The numerical model does, however, require a much higher resolution and computing power than could be achieved in earlier simulations. Dabrowski and Schmid (2011) augmented their numerical model with an analytical model for an anisotropic matrix, equivalent to a matrix with infinitely thin layers with isotropic rheology. They showed that anisotropy can significantly or even completely inhibit rotation of a circular inclusion.

The last hurdle to take to model the full behaviour of an object–matrix system is to take into account the strain-dependent behaviour. In nature, anisotropy (whether by aligned minerals or by crystallographic preferred orientation (CPO)) develops and evolves over time and, contrary to the configuration in Dabrowski and Schmid (2011), its initial

orientation is usually not independent of the presence of the object. Griera et al. (2011) for the first time presented numerical simulations where an anisotropy (CPO) developed during deformation, using a full-field numerical model (CPFFT; Lebensohn, 2001 and Lebensohn et al., 2008; see below). Starting with a matrix represented by an aggregate of grains and using anisotropic crystal plasticity, effective anisotropy develops by lattice rotation in the matrix, resulting in the formation of shear bands, similar to the model proposed by Bell (1985). However, contrary to Bell's (1985) model, the simulations showed that significant rotation occurs before shear bands developed to inhibit further rotation. The work of Griera et al. (2011) should certainly not be used as proof for non-rotation.

The brief review above shows that, thanks to numerical simulations, significant progress has been made from the initial analytical models of e.g. Jeffery (1922) and Ghosh and Ramberg (1976). Over time, heterogeneous rheologies, slipping object surface, proximity of the shear zone boundary, and finally anisotropy of the matrix have been incorporated in the numerical models. One thing that remains to be done is to model deformation of a porphyroblast that is simultaneously growing. This has been done manually by Schoneveld (1977) and using analytical flow fields by several authors (Beam, 1996, Bjørnerud and Zhang, 1994, Gray and Busa, 1994, Masuda and Mochizuki, 1989, Samanta et al., 2002a, Samanta et al., 2002b and Stallard et al., 2002). However this is normally simulated by (1) assuming a simplistic isotropic matrix and (2) predefining rotation behaviour of the rigid inclusion. So far, only Jessell et al. (2001), Groome and Johnson (2008), Houseman et al. (2008) and Bons et al. (2009) have published finite-element simulations of porphyroblast growth during deformation (all using effectively the same numerical scheme). The complicating factor here is that deformation and growth require very different numerical techniques, which are rarely combined in a single modelling package. An exception is the software Elle, which is specifically designed to model different, simultaneous and competing processes (Bons et al., 2008, Jessell et al., 2001 and Piazolo et al., 2010). Using this specific functionality, we present three series of numerical simulations of the deformation of object–matrix systems. Every series aims to explore the scale dependence between the length scale of anisotropy and the inclusion size, a length scale factor that also is observed in rocks (Fig. 8.1). We address two issues: (1) the rotation behaviour of objects as a function of the scale of anisotropy from layering that is coarser than the size of the object down to intrinsic anisotropy and (2) inclusion patterns inside growing porphyroblasts, an issue that has so far received relatively little attention in numerical studies.

8.3 Methods

This study made use of the software platform ELLE (Bons et al., 2008 and Jessell et al., 2001; http://www.elle.ws) to conduct three series of two-dimensional numerical experiments. The numerical platform ELLE is open-source multi-purpose and multi-scale software for the simulation of the evolution of microstructures during deformation and metamorphism. ELLE has been extensively used to simulate microstructure processes, including grain growth (Becker et al., 2008, Bons et al., 2001 and Jessell et al., 2003), dynamic recrystallization (Piazolo et al., 2002), strain localization (Jessell et al., 2005), deformation of two-phase materials (Jessell et al., 2009 and Llorens et al., 2013) and porphyroclast rotation in anisotropic materials (Griera et al., 2011), among other contributions. The Elle code used in the numerical simulations is an open source code available by download from the website http://www.elle.ws. Upgrade versions of the code will also be available through this Internet address. A mailing list to inform users on developments and improvements of the codes is available.

We simulate the behaviour of a rigid object (porphyroblast/porphyroclast) as a circular inclusion embedded within an incompressible initially homogeneous and either anisotropic or effectively anisotropic medium. The initial rigid object is circular, and simulates the nucleus of an intertectonic porphyroblast. The initial diameter of the object is defined as $2r$ (with r being the radius) and the initial layer thickness as h (Fig. 8.3). Three series of experiments were run (Table 8.2). The first series (A) simulate the deformation and growth of a rigid object embedded in an intrinsically anisotropic matrix (Fig. 8.3a), being $r \gg h$ and $h \to 0$. These models are based on the coupling of a full-field viscoplastic formulation based on the Fast Fourier Transform (CPFFT; Lebensohn, 2001) and a front-tracking approach. The second series (B) simulates a growing rigid object within an effectively anisotropic matrix constituted by a sequence of layers with alternating viscosities (Fig. 8.3b). In this case, the object radius is initially equal or larger than the layer thickness ($h \leq r$). The third series of models (C) simulates the behaviour of a rigid object that does not grow. This object is smaller than the layer thickness and it is embedded either within a hard or a soft layer (h > r; Fig. 8.3c). Deformation in the series of experiments B and C is modelled using a non-linear viscous finite-element method (BASIL, Houseman et al., 2008). With this approach we can test the influence of different kinds of anisotropy on porphyroblast development and rotation behaviour.

8.3.1 Crystal plasticity simulations with intrinsic anisotropy (series A)

The series of simulations with intrinsic anisotropy are based on a full-field crystal plasticity formulation that uses a Crystal Plastic Fast Fourier Transform technique (CPFFT) to
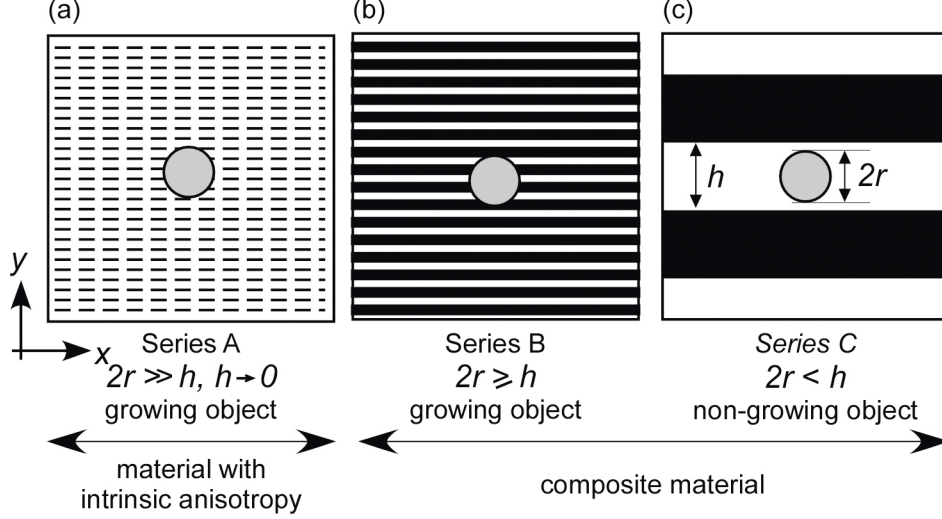
Figure 8.3: Sketch illustrating the three different series of experiments performed in this study: (a) growing objects embedded in a material with intrinsic anisotropy, (b) growing objects embedded in a composite material and (c) non-growing objects embedded either in hard or soft layers in a composite material. r denotes the radius of the circular inclusion, $2r$ its diameter and h the thickness of anisotropy (i.e. layers in composite materials).

calculate the viscoplastic deformation for a polycrystalline aggregate (Lebensohn, 2001 and Lebensohn et al., 2008). The CPFFT code solves the mechanical problem by finding the strain rate and stress fields that minimize the average local work-rate under the constraints of strain compatibility and equilibrium. The term full-field indicates that the micromechanical fields (i.e. velocity, velocity gradient and stress) are explicitly resolved and long and short-range grain interactions are considered. More detailed descriptions of the theoretical framework and numerical algorithm are given by Lebensohn (2001) and Lebensohn et al., 2008 and Lebensohn et al., 2011.

The anisotropic crystalline behaviour is defined using a nonlinear viscous rate-dependent approach, where deformation at the crystal scale is assumed to be accommodated by dislocation glide only (e.g., Lebensohn, 2001). The constitutive equation between the strain rate $\dot{\varepsilon}_{ij}(\mathbf{x})$ and the deviatoric stress $\sigma(\mathbf{x})$ at position $\mathbf{x}$ is given by,

$$\dot{\varepsilon}_{ij}(\mathbf{x}) = \sum_{s=1}^{N_s} m_{ij}^s(\mathbf{x}) \dot{\gamma}^s(\mathbf{x}) = \dot{\gamma}_0 \sum_{s=1}^{N_s} m_{ij}^s(\mathbf{x}) \left| \frac{m^s(\mathbf{x}) : \sigma'(x)}{\tau^s(\mathbf{x})} \right|^n \mathrm{sgn}(m^s(\mathbf{x}) : \sigma'(\mathbf{x})) \qquad (8.1)$$

where m^s, $\dot{\gamma}^s$ and τ^s are respectively the symmetric Schmid tensor, the shear strain rate and the critical resolved shear stress (CRSS) of the slip system s, $\dot{\gamma}_0$ is the reference strain rate, n is the rate sensitivity exponent and N_s is the number of slip systems in the crystal. A hexagonal symmetry is used to simulate the mechanical properties of the polycrystal, and deformation is allowed to be accommodated by glide along basal plane and along non-basal systems (i.e. pyramidal and prismatic). The resistance to shear of slip systems is simulated by means of the critical resolved shear stress. The basal system is assumed to be

166

the weakest slip system and used to describe the orientation of the matrix anisotropy. In this approach the grain anisotropy (a) parameter, that measures the degree of anisotropy, is characterised as the ratio between the critical stresses of the non-basal and basal slip systems (e.g., Lebensohn, 2001). For all simulations, the critical shear stress of the basal plane was set to 1. A value of $n = 3$ was assumed for all slip systems.

The dependence of the resolved shear stress in basal and non-basal slip systems on the direction of the tensile axis (σ_3) is illustrated in Fig. 8.4. This dependence is calculated using Eq. (8.1) considering that the normal plane and slip direction are coincident with the analysed 2D model. The reference system is defined to be coincident with the basal plane and φ is the angle between (σ_3) and the normal to the basal plane. The strength of the aggregate is controlled by the slip system with the minimum shear stress. The anisotropic behaviour can be derived from the yield envelope in Fig. 8.4. For conditions of shortening or extension parallel to the basal plane (i.e. $\varphi = 0°$ or $\varphi = 90°$), deformation is accommodated by slip along non-basal systems, and the effective strength of the material is the critical resolved shear stress for non-basal systems. For shear parallel to the basal plane ($\varphi = 45°$), the effective strength is defined by the critical resolved shear stress of the basal system. The transition between both conditions is controlled by the grain anisotropy parameter (a) or relative strength of the slip systems. Note that for the case of linear viscosity (i.e. $n = 1$), a is equivalent to the degree of anisotropy (δ), defined as the ratio between normal and shear viscosities, and therefore, corresponds to the limit case of a multilayered stack with $h \to 0$.

The local crystallographic orientations are updated using the following local rotation rate (e.g. Lebensohn et al., 2008),

$$\dot{\omega}_{ij}(\mathbf{x}) = \dot{\Omega}(\mathbf{x}) + \dot{\tilde{\omega}}(\mathbf{x}) - \dot{\omega}_{ij}^p(\mathbf{x}) \tag{8.2}$$

where $\dot{\Omega}(\mathbf{x})$ and $\dot{\tilde{\omega}}(\mathbf{x})$ are the average and fluctuation rotation rates, and the plastic spin $\dot{\omega}_{ij}^p(\mathbf{x})$ is given by

$$-\dot{\omega}_{ij}^p(\mathbf{x}) = \sum_{s=1}^{N_s} \alpha_{ij}^s(\mathbf{x})\dot{\gamma}^s(\mathbf{x}) \tag{8.3}$$

where $\alpha_{ij}^s(\mathbf{x})$ is the antisymmetric Schmid tensor.

The CPFFT is integrated within the ELLE package using a direct one-to-one mapping between data structures. The polycrystalline aggregate is discretised into a periodic, regular array of spaced nodes (Fourier Points or "unconnected nodes" in the ELLE package, unconnected nodes are nodes that do not define polygons). The geometry of the porphyroblast is defined using a vector layer that defines a network of boundary nodes connected by segments. The numerical simulation is achieved by iterative application of small time steps of each process in turn. After numerical convergence, the simulation is updated for all nodes (i.e. connected and spaced) assuming that the micromechanical fields

are constant in the incremental time step. However, this process destroys the regularity of the Fourier points after every update. Similar to Griera et al. (2011), a particle in-cell approach is used to remap all material and morphological information to a new regular computational mesh enabling high strains to be attained in the simulations

The initial square model (of size L=1) consisted of a single rigid circular inclusion of radius r=0.025 embedded in a homogenous anisotropic matrix. For all simulations the mechanical behaviour of the inclusion is defined as an isotropic non-linear viscoplastic aggregate, with critical resolved shear stress for all slip systems 50 times larger than that of matrix non-basal systems. A resolution of 128 × 128 Fourier points was used to define a unit cell composed by 16,384 discrete nodes. Dextral simple shear up to a shear strain of γ=8 parallel to the horizontal x-axis was applied using constant strain-rate velocity boundary conditions.
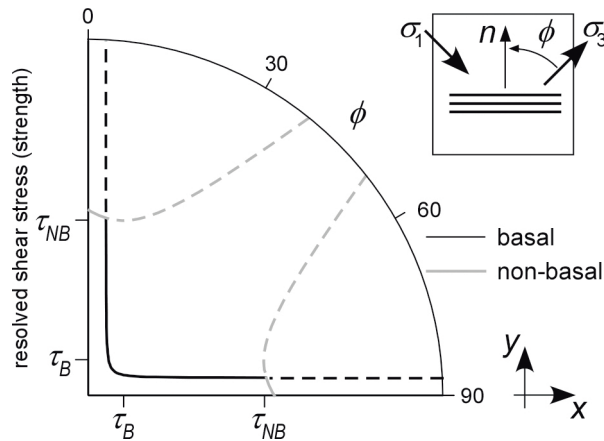
Figure 8.4: Dependence of the resolved shear stress in basal (black) and non-basal (grey) slip planes as function of the orientation with respect to the tensile axis (σ_3). The strength of the aggregate is defined by the slip system with minimum shear stress (thick line). A reference frame is defined parallel to the basal plane and φ is the angle between the normal and basal planes. The critical resolved shear stresses for basal and non-basal slip systems are indicated by τ_B and τ_{NB}, respectively.

8.3.2 Linear viscosity simulations of composite materials (FEM) (series B, C)

The numerical simulations of linear viscous composite materials were constructed and run with the non-linear viscous finite element code BASIL (Houseman et al., 2008 and references therein) within ELLE. For the models of the series B and C we use an initial 2D geometrical description of the microstructure based on polygons, which are defined by a network of boundary nodes connected by segments. An additional grid of regularly spaced unconnected nodes is used to create a passive grid initially parallel and perpendicular to layers to trace the deformation history of the deformation field as well as to trace the rigid object rotation history. In this study we assigned homogeneous rheological properties to

Experiment code	Anisotropy (a or δ)	Initial layer orientation (α)	Object growth rate (K)	Number of layers	Hosting layer
Series A (intrinsic anisotropy; $r \gg h$ and $h \to 0$; growing rigid object)					
A1	$a=1$	Isotropic	0	–	–
A2	$a=1$	Isotropic	1.8×10^{-2}	–	–
A3	$a=1$	Isotropic	9.0×10^{-3}	–	–
A4	$a=5$	180°	1.8×10^{-2}	–	–
A7	$a=20$	180°	1.8×10^{-2}	–	–
A8	$a=5$	135°	1.8×10^{-2}	–	–
A9	$a=5$	90°	1.8×10^{-2}	–	–
A10	$a=5$	45°	1.8×10^{-2}	–	–
Series B (composite material; $h \leq r$; growing rigid object)					
B1	$m=10, \delta=3$	180°	1.8×10^{-2}	20	Hard and soft
B2	$m=10, \delta=3$	180°	3.6×10^{-2}	20	Hard and soft
B3	$m=10, \delta=3$	180°	7.2×10^{-2}	20	Hard and soft
B4	$m=10, \delta=3$	180°	1.8×10^{-2}	10	Hard and soft
B5	$m=10, \delta=3$	180°	1.8×10^{-2}	40	Hard and soft
B6	$m=5, \delta=1.8$	180°	1.8×10^{-2}	20	Hard and soft
B7	$m=20, \delta=5.5$	180°	1.8×10^{-2}	20	Hard and soft
B8	$m=50, \delta=13$	180°	1.8×10^{-2}	20	Hard and soft
B9	$m=10, \delta=3$	135°	1.8×10^{-2}	20	Hard and soft
B10	$m=10, \delta=3$	90°	1.8×10^{-2}	20	Hard and soft
B11*	$m=50, \delta=13$	14°	1.8×10^{-2}	20	Hard and soft
Series C (composite material; $h > r$; non-growing rigid object)					
C1	$m=10, \delta=3$	180°	0	6	Hard
C2	$m=10, \delta=3$	180°	0	6	Soft
C3	$m=10, \delta=3$	135°	0	6	Hard
C4	$m=10, \delta=3$	135°	0	6	Soft
C5	$m=10, \delta=3$	90°	0	6	Hard
C6	$m=10, \delta=3$	90°	0	6	Soft

Table 8.2: Experimental setup. h: layer thickness; r: inclusion radius. * Note that the only model with non-perfect flat layers is B11 (see text for further descriptions).

the polygons (Fig. 8.5), which define layers and inclusions (i.e. porphyroclasts/blasts). Layering is assumed to be initially homogeneous and planar, and we impose a welded interface between matrix and inclusion. A triangular FEM mesh is created from boundary nodes every time step. Elle uses both horizontally and vertically wrapping boundaries so that, for example, a polygon that is cut by the right hand boundary continues on the left side. This fact makes the model to be periodic in all directions, reduces boundary effect problems and simplifies visualisation of the model even with very high strains.

BASIL is a general finite element deformation package that calculates the solution of viscous deformation of a 2D sheet in plane-strain. BASIL can be used within Elle to calculate the viscous strain rates and the associated stress field (including pressure) for different boundary conditions. A detailed description of the numerical algorithm used on

the coupling between ELLE and BASIL can be found in Jessell et al. (2005), Bons et al. (2008) and Jessell et al. (2009).

One experimental run consists of the iterative application of increments of dextral simple shear deformation to the initially square model (γ_{inc}=0.05 per step). BASIL supports periodic boundary conditions across two of the four sides of the model (vertical sides), so that it can be used within Elle to maintain a constant square boundary at the end of each increment of deformation (see Houseman et al., 2008 or Jessell et al., 2005 and Jessell et al., 2009 for further details). Although BASIL is capable of simulating power-law rheologies, calculation time significantly increases and numerical stability decreases when the stress exponent $n > 1$. Bons et al. (1997) showed that n actually has little effect on the rotation rate and we therefore ran all the experiments of series B and C assuming a linear viscosity. We applied a dextral simple shear up to a shear strain of γ=8 parallel to the x-axis using velocity boundary conditions with constant strain rate.

The degree of anisotropy δ is defined as the ratio between normal and shear viscosities of the material. For a layered medium defined by alternating isotropic layers, the effective anisotropy also depends on the relative proportion of both layer types. In this study we used equal thickness proportion between layers and the effective anisotropy is therefore (e.g. Biot, 1965 and Dabrowski and Schmid, 2011):

$$\delta = \frac{1}{4}\frac{(m+1)^2}{m} \tag{8.4}$$

where m is the viscosity contrast between strong and weak layers (η_s/η_w). As the degree of anisotropy and the viscosity contrast are not linearly proportional, both variables are used to indicate the anisotropic properties of the matrix. This definition of anisotropy is used for our composite models (series B and C).

The viscosity of the weak matrix layers was set to unity in all simulations, and that of the harder layers according to m. The simulations are aimed at investigating the behaviour of perfectly rigid objects. An infinite viscosity contrast between object and matrix is, however, numerically not possible. We therefore assigned the object a viscosity 100 times higher than that of the hard layers. This is a compromise between desired rigidity and numerical feasibility. As the objects are therefore semi-rigid, minimal deviations from a perfect circular shape may develop in the simulations.

To confirm the validity and stability of this numerical workflow, Jessell et al. (2009) presented a simulation with a single round rigid object embedded in a homogeneous matrix. The results showed that the object rotates according to the analytical model of Jeffery (1922).
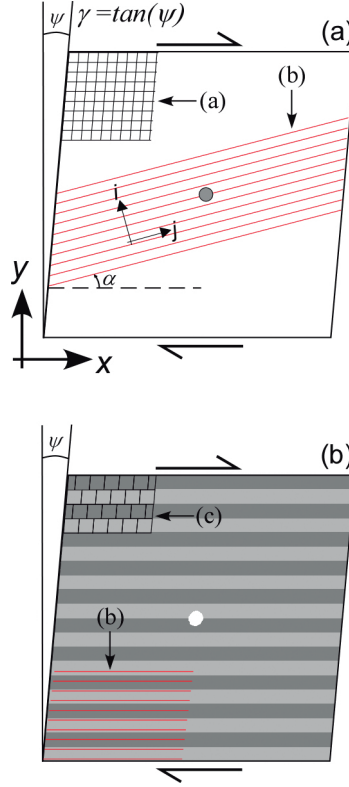
Figure 8.5: Examples of the initial configuration of the simulations with (a) intrinsic anisotropy and (b) composite anisotropy. Anisotropy initially makes an angle α with respect to the shear plane. Red lines show the Lagrangian marker lines parallel to anisotropy. Light and dark grey colours indicate soft and hard layers in composite materials, respectively. The circular inclusion is coloured in grey for the models with intrinsic anisotropy and in white for the composite simulations. All the models where deformed in dextral simple shear. Boundary conditions are periodic in x and y directions, with free vertical sides and imposed constant displacement on the horizontal sides of the model. (For interpretation of the references to colour in this figure legend, the reader is referred to the web version of this article).

8.3.3 Method for porphyroblast growth

The growth rate of the porphyroblast is simulated using a power-law relationship:

$$\left(\frac{r}{L}\right)^b = \frac{K'}{L^b} \cdot \gamma = K \cdot \gamma \tag{8.5}$$

where r is the radius of the porphyroblast, L is the length of the model, K' is the growth constant (with dimensions [length^b]), γ is the shear strain and b is the growth exponent. We use a normalised growth rate (K) for simplicity. The growth exponent has values of $b=1$ for linear increase of radius, $b=2$ for linear increase of area and $b=3$ for linear increase of volume with shear strain. In our case we assume a linear porphyroblast growth and we thus use an exponent of $b=1$ for all the simulations. This growth approach is similar to the one proposed by Gray and Busa (1994), and it was previously used in ELLE by Groome et al. (2006) and Bons et al., 2008 and Bons et al., 2009.

The numerical modelling scheme should in principal maintain a circular shape of the growing circular polygon that represents the porphyroblast. One should, however, bear in mind that the polygon is defined by straight boundary segments and that topological events (neighbour switches of polygons, see Bons et al., 2008) may cause small deviations from the perfect circular shape in the order of the distance between boundary nodes.

8.3.4 Experimental setup

In this study, we restrict ourselves to simple shear only and simulate the porphyroblast growth and matrix deformation during a single deformation phase. Under these conditions, the theoretical rotation rate of a circular inclusion in a viscous matrix is half the shear strain rate. We have systematically varied three input parameters (Table 8.2):

- The degree of anisotropy, that it is expressed by the parameter a for models with intrinsic anisotropy and δ (or m) for simulations of composite materials.

- The non-dimensional growth rate of the porphyroblast (K)

- The initial orientation of anisotropy with respect to the shear plane (α)

The layer in which the inclusion is embedded, either hard or soft is an additional variable for models of series C as the inclusion is smaller than the layer width. The influence of the number of layers and their thickness with respect to the length of the model was additionally investigated in series B. As stated above, the unit cell is not the entire model domain, as its boundaries are periodic and it repeats infinitely in both x and y directions. For all simulations, we use reference passive markers parallel to mechanical anisotropy or layering to visualise inclusion patterns, matrix deformation and rotation behaviour.

8.4 Results

The results of the numerical experiments of each series are presented in two different ways. First, the evolution of the microstructures and spiral geometry is shown at different deformation stages. For the simulation of series A, the phase distribution is indicated by a grey inclusion embedded in a white matrix. For simulations of series B and C, the rigid inclusion is white with dark and light greys representing the hard and soft layers, respectively. We also display the final microstructure overlain by the deformed set of passive marker lines initially parallel to the anisotropy orientation. Second, the rotation behaviour of each series is summarised in shear strain versus rigid inclusion rotation graphs.

8.4.1 Series A - growing rigid inclusions in materials with intrinsic anisotropy ($r \gg h$ and $h \to 0$)

This series of experiments simulates the behaviour of a porphyroblast embedded in a material with intrinsic anisotropy. We explored the role of the degree of anisotropy (Fig. 8.6 and Fig. 8.7) and its initial orientation (Fig. 8.8) on the final microstructures. The rotation behaviour is shown in Fig. 8.9.

Fig. 8.6 shows a comparison of the influence of anisotropy (a) on the final microstructure. All models were defined with the same initial anisotropy orientation (α=180°) and growth rate ($K = 1.8 \cdot 10^{-2}$), except case A1 with K=0. In case of a fixed-size inclusion in an isotropic matrix (case A1, Fig. 8.6a), asymmetric folds and shear bands develop close to the inclusion. A band with tight folds forms oblique to the shear plane and, with increasing strain, rotates towards it. Near the inclusion, folds are deflected and wrap around the rotating rigid inclusion. Foliation planes in the shortening bisector are more closely spaced and tightly wrapped around the inclusion. These results are very similar to the ones obtained by Bjørnerud (1989b) or Dabrowski and Schmid (2011). The final geometry resembles a δ-clast with stair stepping. As expected, the measured rotation matches Jeffery's theory (see Griera et al., 2011).

Increasing the degree of anisotropy a, expressed as the ratio between the critical stresses of the basal and non-basal slip systems, enhances deformation partitioning and preferential strain localisation at the upper and lower parts of the model (Fig. 8.6). Although the matrix has constant mechanical properties, the protection created by the porphyroblast produces strain refraction. In the case of an isotropic matrix (case A2 with a=1, Fig. 8.6b and e), a continuous and smoothly curving spiral of the foliation develops (Fig. 8.7). For a final shear strain of γ=16, the rotation measured from the inclusion patterns at the centre of the rigid object is approximately 440°, only slightly less than the theoretical prediction ($\sim$450°). A connection between both spiral arms is observed that is related to the incorporation of pressure shadows inside the spiral. From a qualitative point of view, the final geometry and intermediate cases resemble typical sigmoidal and spiral snowball patterns observed in field examples and thin sections (e.g. Johnson, 1993, Passchier and Trouw, 2005 and Passchier et al., 1992).

In case of moderate (case A4, a=5, Fig. 8.6c) and strong anisotropy (case A7, a=20, Fig. 8.6d) strain becomes highly heterogeneous and crenulation folds develop, especially above and below the inclusion. The development of crenulation folds is strongest at moderate anisotropy. A possible explanation is that when the degree of anisotropy is high it is more efficient to glide parallel to the anisotropy than by bending and propagation of a fold orthogonal to it. The object's rotation rate decreases and the size of the strain shadows increases with increasing anisotropy. This leads to a transition of snowball-type inclusion patterns to a simpler and straight internal foliation oblique to the external foliation.
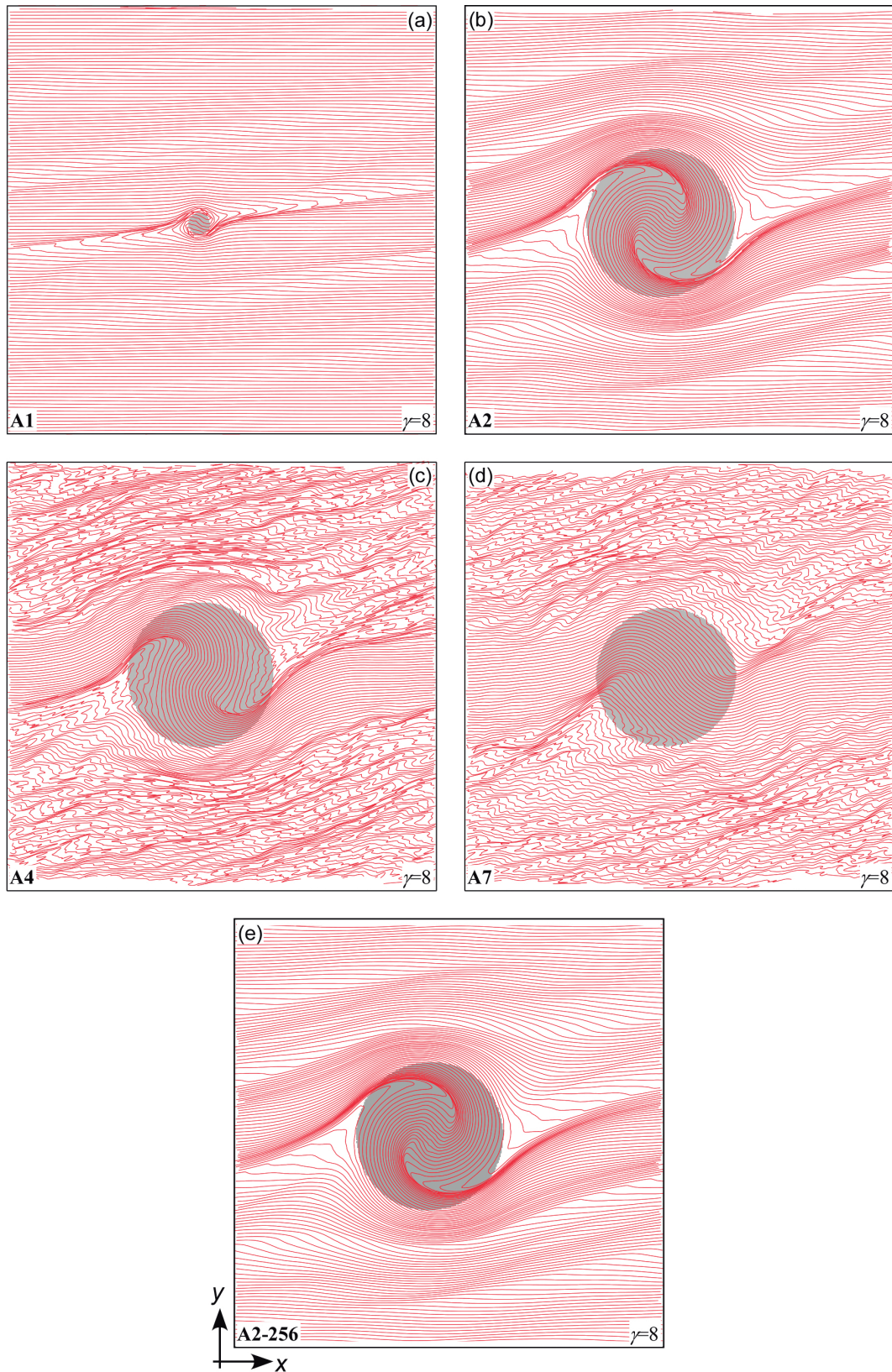
Figure 8.6: Examples of the initial configuration of the simulations with (a) intrinsic anisotropy and (b) composite anisotropy. Anisotropy initially makes an angle α with respect to the shear plane. Red lines show the Lagrangian marker lines parallel to anisotropy. Light and dark grey colours indicate soft and hard layers in composite materials, respectively. The circular inclusion is coloured in grey for the models with intrinsic anisotropy and in white for the composite simulations. All the models where deformed in dextral simple shear. Boundary conditions are periodic in x and y directions, with free vertical sides and imposed constant displacement on the horizontal sides of the model. (For interpretation of the references to colour in this figure legend, the reader is referred to the web version of this article).

Although a higher degree of anisotropy produces a decrease of the object's rotation rate, the rigid inclusion in all the investigated cases (with $\alpha=180°$): (1) rotates respect to the reference frame fixed parallel to the shear plane and (2) with the same sense as the imposed shear sense.

The initial angle (α) of anisotropy with respect to the shear plane is another important factor controlling porphyroblast rotation as well as developing inclusion patterns (Fig. 8.8 and Fig. 8.9b). The rotation in four investigated models (all with $a=5$) is shown in Fig. 8.9b. The first observation is that the rotation rate and the variation of rotation with increasing deformation are different depending on the initial orientation of anisotropy. While the $\alpha=180°$ case shows a quasi-linear rotation throughout the experiment, general orientation cases are characterised by an earlier stage of rotation that may even be faster than the theoretical solution, followed by a stage of slower rotation and almost stagnation. The stabilisation orientation depends on the initial orientation of the host anisotropy, but varies between 45° and 20°. This might be related to the stabilisation of the anisotropy orientation in the matrix at a low angle with respect to the shear plane.

A change of the inclusion pattern is observed with variation of initial anisotropy orientation. At $\alpha=180°$, a spiral shaped geometry is observed. However, when the anisotropy is initially oriented oblique to the shear plane, oppositely concave microfolds or millipede structures ($\alpha=135°$, Bell and Bruce, 2006 and references therein) or straight inclusion patterns develop, oblique to the external foliation ($\alpha=45°$ and 90°). This is not only a geometrical transition but it also a change in the asymmetry of the inclusion pattern. In the $\alpha=180°$ case, the internal foliation (S_i) is rotated synthetically relative to the external foliation (S_e), i.e. in the same sense as the bulk deformation with a clock-wise vorticity component. In the other cases Si is rotated antithetically with respect to Se. In all cases, the object rotated synthetically, and the difference in asymmetry arises from the fact that in the $a \neq 180°$ cases, Se rotates faster than the object (Ramsay and Lisle, 2000).

Simulations with a higher resolution (i.e. 256×256 Fourier points) were run in order to test the influence of the numerical resolution on the developing microstructures. The results indicate that the geometry of the inclusion patterns inside the porphyroblast (Fig. 8.6e) as well as the finite rotation of the object (Fig. 8.9a) are similar to the ones observed in the standard simulation.

Systematic variation of final structures developed in intrinsic anisotropy simulations ($r \gg h$, $h \to 0$) with initial orientation of $\alpha=180°$. (a) Non-growing and (b) growing objects in an isotropic medium ($a=1$). Growing objects in an (c) anisotropic ($a=5$) and (d) strongly anisotropic ($a=20$) medium. (e) Growing object in an isotropic medium ($a=1$) but with a higher resolution of 256×256 Fourier Points. Foliation traces (red lines) indicate that increasing anisotropy enhances deformation partitioning, with the development of crenulation folds and shear bands, and considerably reduces the finite rotation of the inclusion. The labels on the bottom left corner of each model indicate the simulation run

175

(see Table 8.2). Shear strain is $\gamma=8$ for all models. (For interpretation of the references to colour in this figure legend, the reader is referred to the web version of this article).
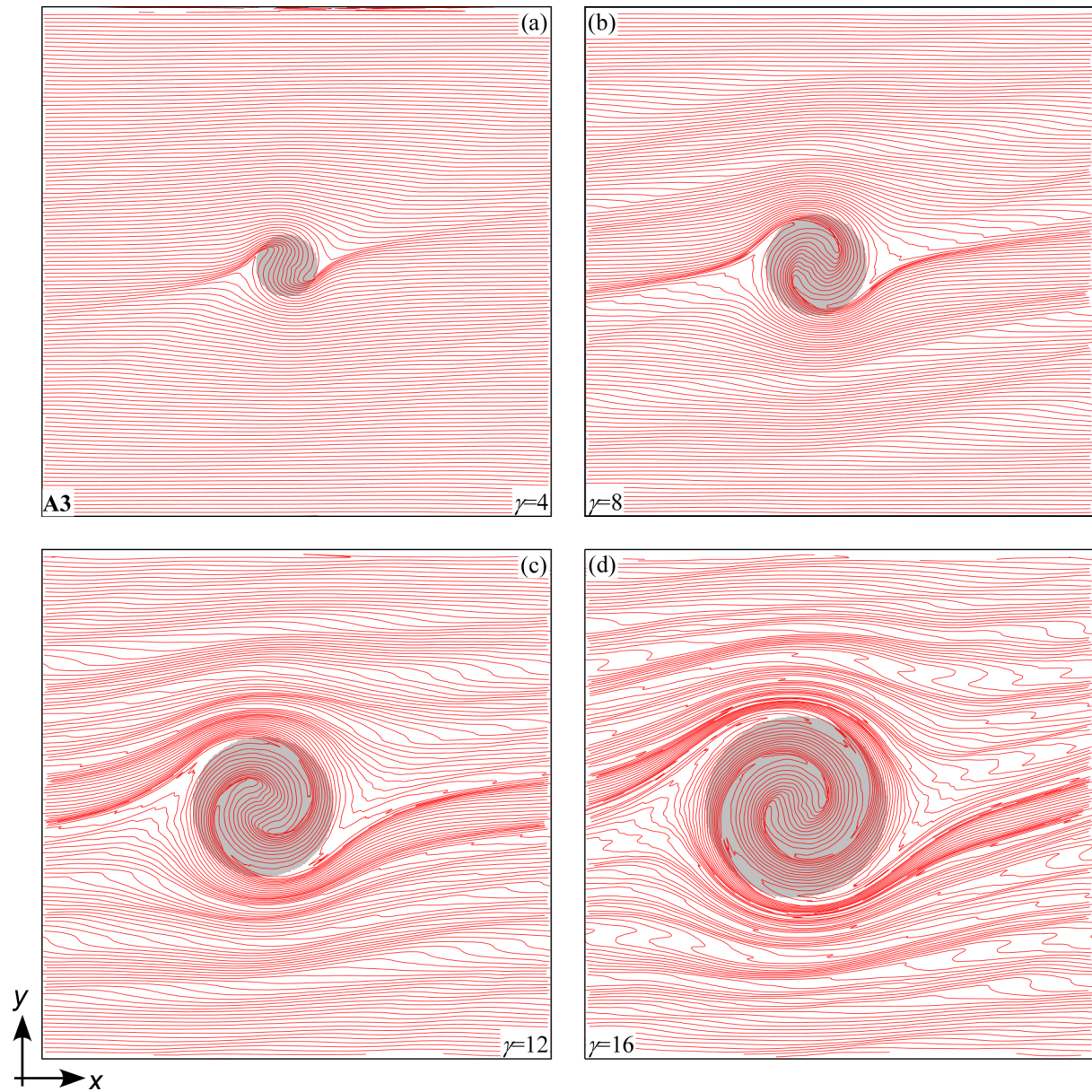
Figure 8.7: Sequential evolution of the simulation with intrinsic isotropic ($a=1$) at stages of shear strain (γ) of (a) 4, (b) 8, (c) 12 and (d) 16. A snowball pattern is developed with strain shadows gradually incorporated within the spiral during porphyroblast rotation and growth.
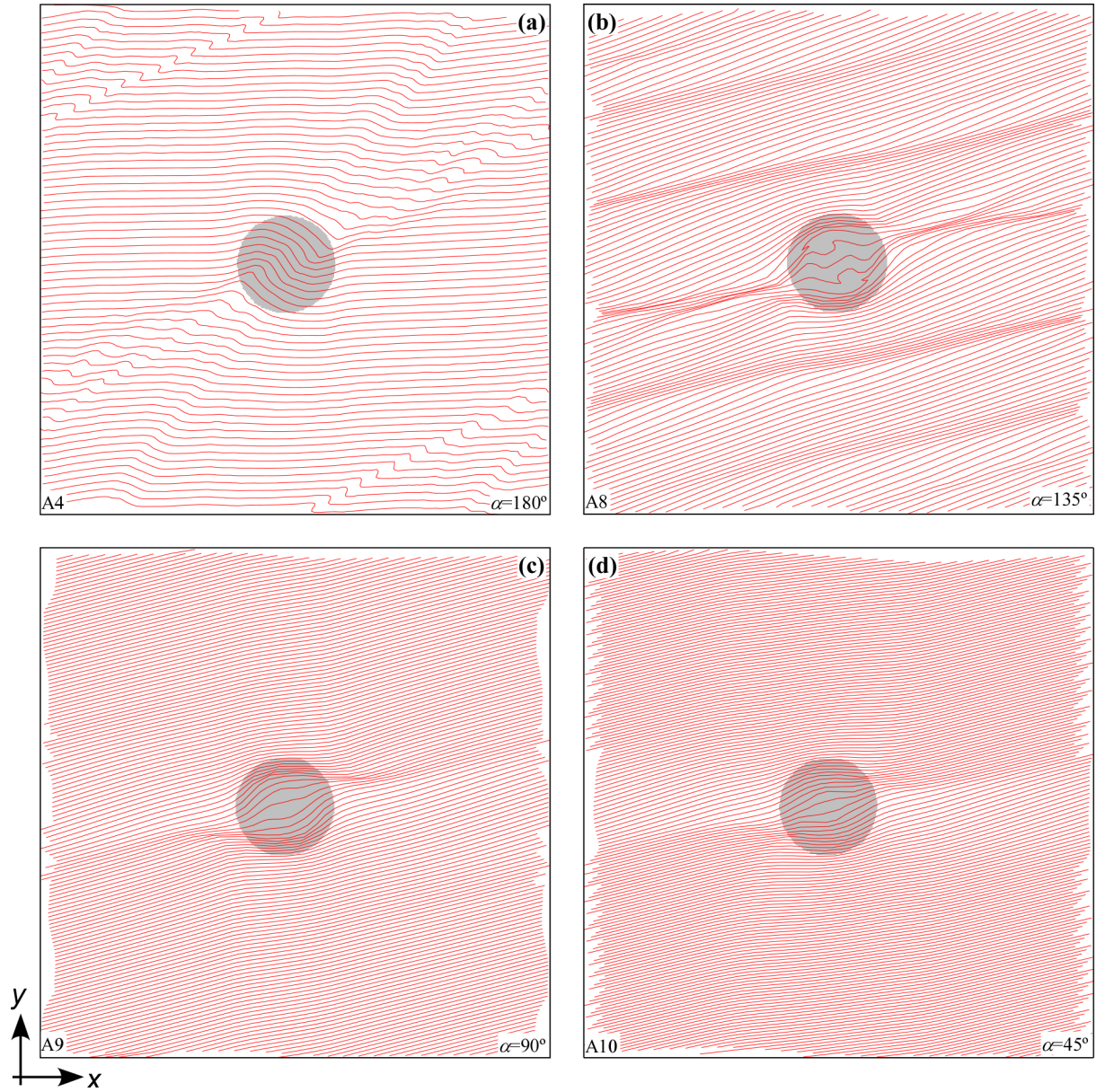
Figure 8.8: Comparison of rotation behaviour of growing circular inclusions ($r \gg h$ and $h \to 0$) embedded in a medium with intrinsic anisotropic (a=5) with the anisotropy planes initially oriented at (a) α=180°, (b) 135°, (c) 90°and (d) 45° with respect to the shear plane. All the figures show the stage of γ=4. The labels on the bottom left corner of each model indicate the simulation run (see Table 8.2).
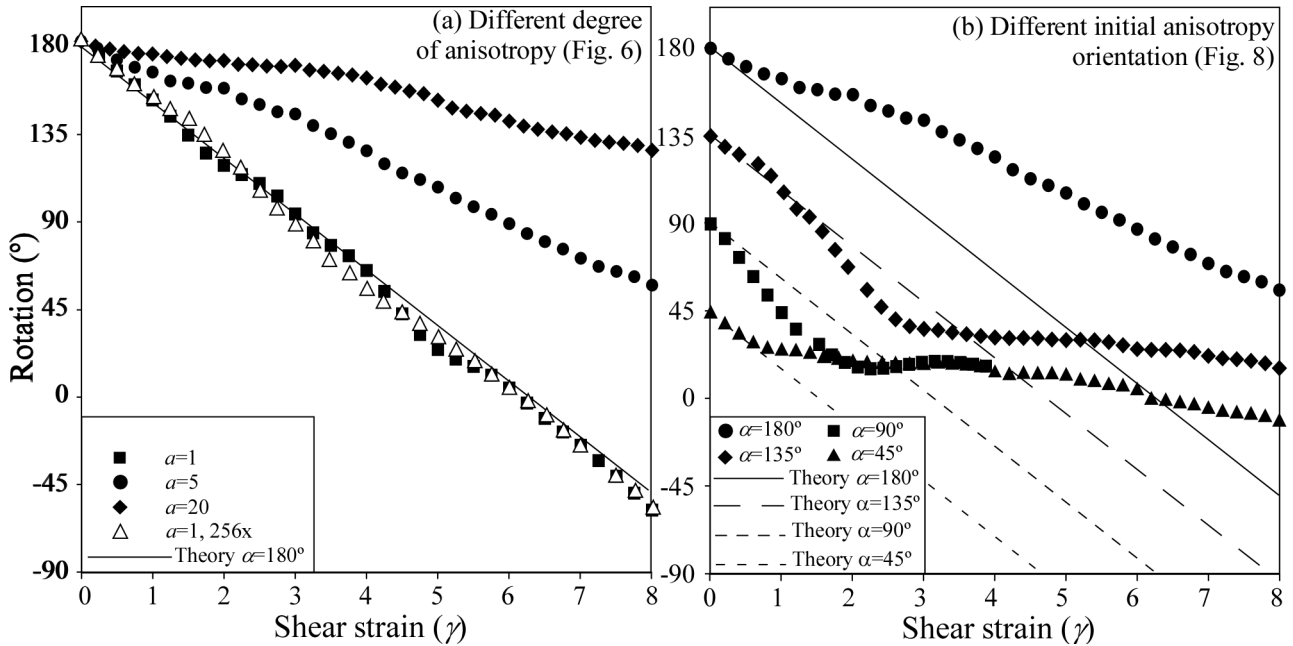
Figure 8.9: Rotation evolution of circular inclusions ($r \gg h$, $h \to 0$) presented in Figs. 8.6, 8.7 and 8.8. The graph (a) shows a comparison of simulations with different degree of anisotropy, while the graph (b) illustrates the rotational behaviour of rigid objects embedded in a medium with different initial anisotropy orientations. Solid and dashed straight lines indicate the theoretical rotation behaviour of inclusions embedded in an isotropic viscous media (Jeffery, 1922).

8.4.2 Series B - growing rigid inclusions in linear viscous composite materials (layer thickness < object)

We only show some stages of evolution of growing rigid porphyroblasts in a linear viscous composite material. The porphyroblast is indicated in white, while viscosity contrast between layers is indicated by different greys, with darker indicating more viscous material. In this series of experiments we have varied the growth rate of the inclusion (Fig. 8.10), the thickness of the host layers (Fig. 8.11), the viscosity contrast between the alternating host layers (Fig. 8.12) and their initial orientation (Fig. 8.13). The rotation behaviour of all experiments is compared in Fig. 8.14. All models, except the ones presented in Fig. 8.13 and Fig. 8.14d are for the special case of an anisotropy initially oriented parallel to the shear plane (α=180°).

The results presented in Fig. 8.10 and Fig. 8.14a indicate that the growth rate of a syntectonic porphyroblast does not influence its rotation rate, if we measure the evolution of the object's nucleus. The inclusion patterns obtained for simulations with different growth rates ($K = 1.8 \cdot 10^{-2}$, $3.6 \cdot 10^{-2}$ and $7.2 \cdot 10^2$) are very similar, although some differences can be observed at the outer part of the inclusion. Two consecutive microfolds (antiform and synform) are developed within the inclusion, leading to an S-shaped spiral geometry. Additional microfolds are also propagated within the matrix, as a consequence of the object's rotation, despite the lack of initial layer irregularities. Similar results were

178
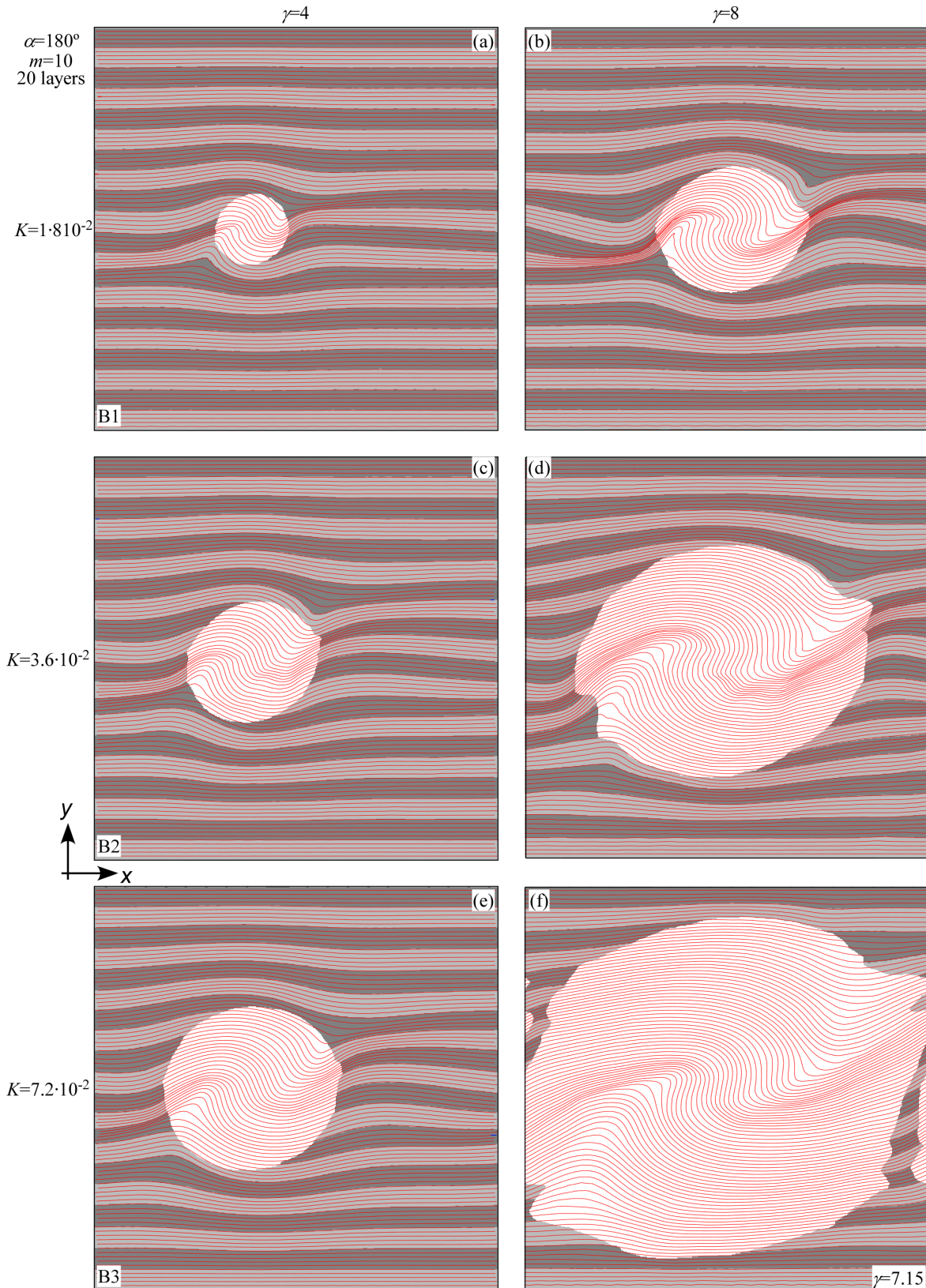
Figure 8.10: Comparison of circular inclusions ($r \geq h$) embedded in a composite medium (with viscosity contrast m=10) that grew at different rates: (a, b) $K = 1.8x10^{-2}$, (c, d) $K = 3.6x10^{-2}$ and (e, f) $K = 7.2x10^{-2}$. Panels (a), (c) and (e) show the inclusion patterns at a shear strain of γ=4, (b) and (d) at γ=8 stage and (f) at γ=7.15. All these models had an initial anisotropy orientation of α=180°. Although the porphyroblast in (f) is clearly far too large for a meaningful result, it is included for completeness sake. The labels on the bottom left corner of each model indicate the simulation run (see Table 8.2).
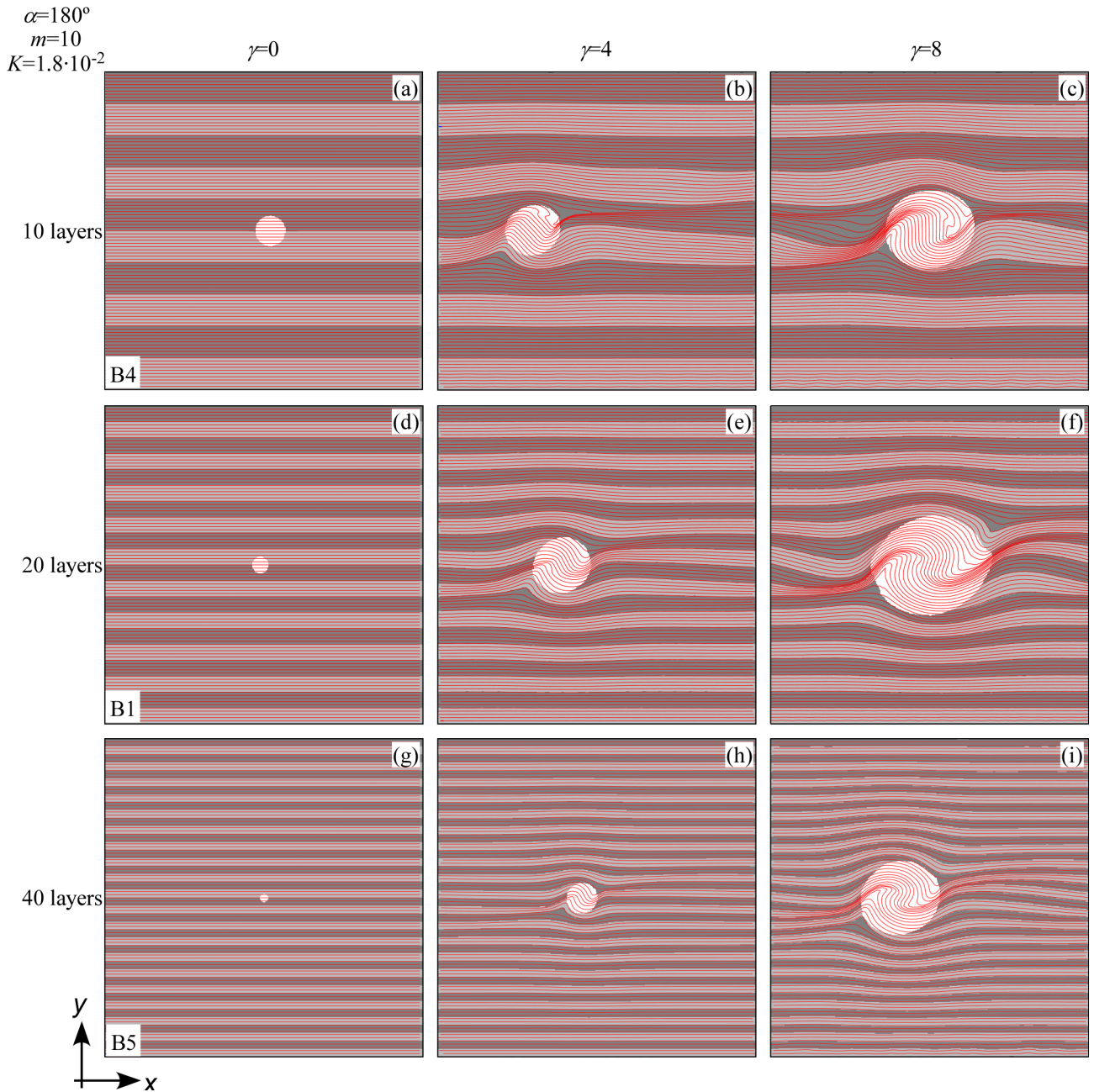
Figure 8.11: Comparison of rotation behaviour and inclusion patterns of growing circular inclusions ($r \geq h$) embedded in a composite medium with different layer thickness, expressed as total number of layers (a, b, c) 10, (d, e, f) 20 and (g, h, i) 40. All these models had an initial anisotropy orientation of α=180°. The labels in the bottom left corner of each model indicate the simulation run (see Table 8.2).

reported by Dabrowski and Schmid (2011). The spiral curvature is more distinct for the slowest growing porphyroblast ($K = 1.8 \cdot 10^{-2}$), while it becomes flatter with increasing growth rate. The tendency to develop similar spirals independently of the inclusion's growth rate was previously observed by Stallard et al. (2002).

The layer thickness (h) does not have a significant impact on the geometry of the inclusion pattern (Fig. 8.11), and slightly influences its rotation rate at relative high strains ($\gamma > 3$, Fig. 8.14b). For this particular case, the higher the number of layers, the
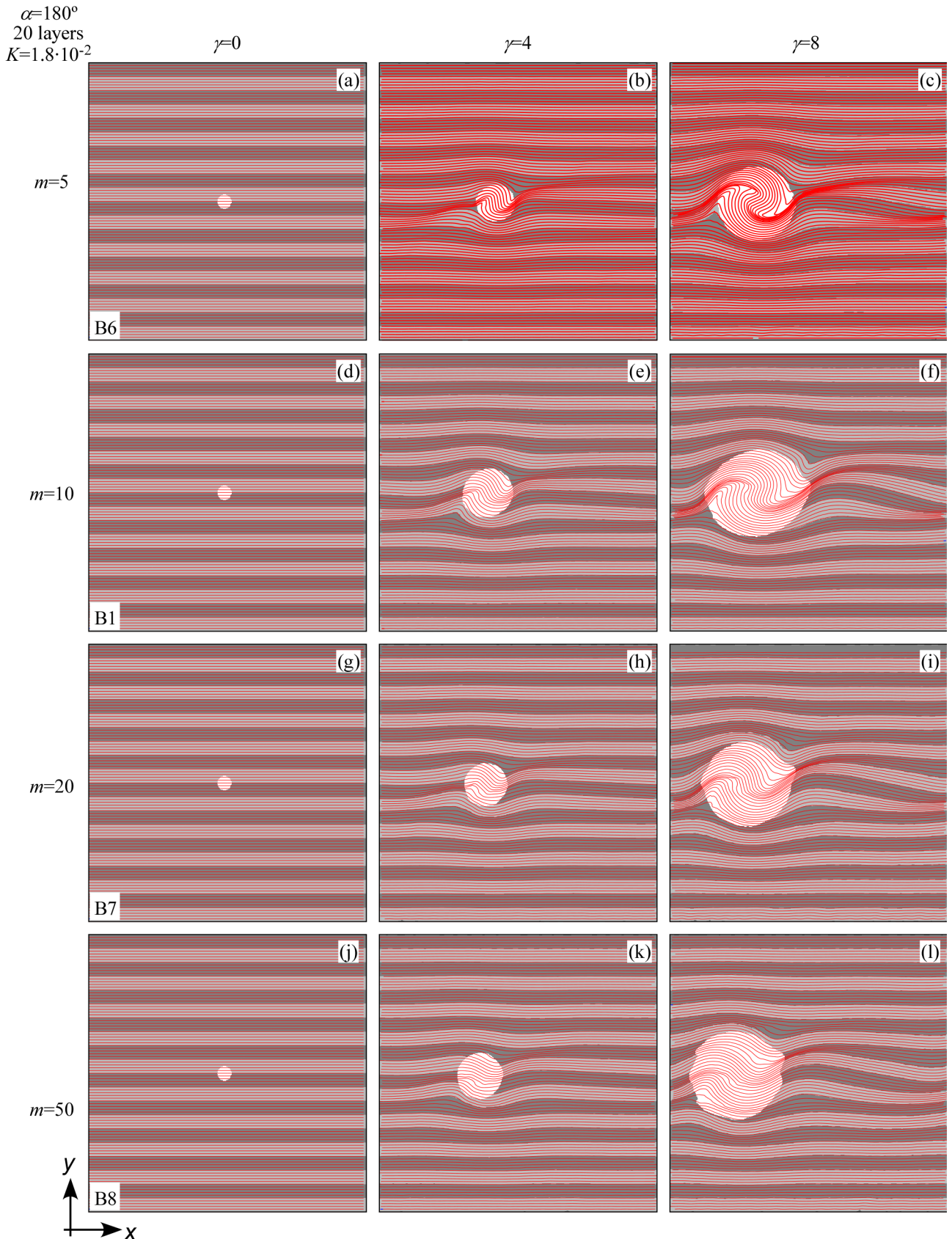
Figure 8.12: Comparison of rotation behaviour and inclusion patterns of growing circular inclusions ($r \geq h$) embedded in a composite medium with different degrees of anisotropy, expressed as viscosity contrasts of (a, b, c) m=5, (d, e, f) m=10, (g, h, i) m=20 and (j, k, l) m=50. The figures indicate that rotation rates significantly decrease when m is increased. All these models had an initial anisotropy orientation of α=180°. The labels in the bottom left corner of each model indicate the simulation run (see Table 8.2).
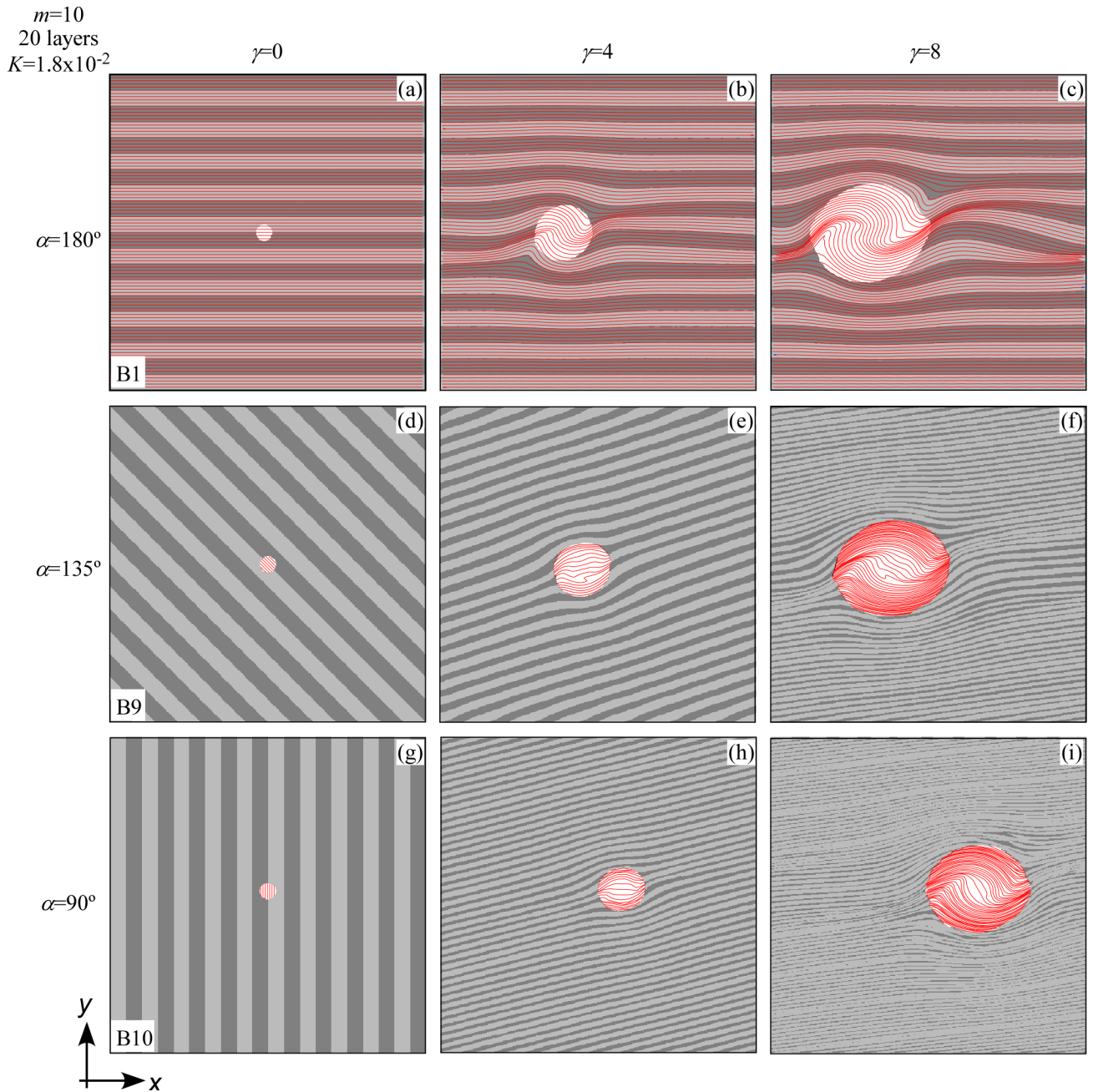
Figure 8.13: Comparison of rotation behaviour and inclusion patterns of growing circular inclusions ($r \geq h$) embedded in a composite medium with a viscosity contrast of $m=10$. Layers were initially oriented at (a, b, c) $\alpha=180°$, (d, e, f) $\alpha=135°$ and (g, h, i) $\alpha=90°$. The labels in the bottom left corner of each model indicate the simulation run (see Table 8.2). For clarity, Lagrangian marker lines are shown only within inclusions for panels (d) to (i).

slower the rotation rate and the more intense the spiral development. However, this tendency may be dependent on the initial location of the inclusion with respect to the multilayer. In this series of models, the inclusion is initially located at the interface between a hard and a soft layer, so that during initial growth two different types of layers bound the porphyroblast on its upper and lower parts. The inclusion geometry also displays an S-shape, and the associated fold developed within the matrix is more intense for the case with the smallest number of layers.

The viscosity ratio between alternating layers in a composite media (m) plays a strong role on the porphyroblast development (Fig. 8.12 and Fig. 8.14c). With increasing anisotropy the rotation rate decreases and the spiral pattern consequently becomes less pronounced. The grid lines make a marked inflexion on both left and right sides of the porphyroblast for all cases, although it is more intense in the simulations with lowest m, and grid lines get very close in this area indicating a more pronounced deformation localization. The rotation rate is strongly influenced by the degree of anisotropy: after a shear strain of $\gamma=8$, the inclusion embedded in a multilayer with $m=5$ has rotated 108° more than that of $m=50$. Inclusions embedded in an anisotropic composite material could be blocked and not rotate if the degree of anisotropy is very high. The models presented in Fig. 8.12 are a clear example that porphyroblasts show a very different rotation history depending on the degree of anisotropy of the hosting material, even if the starting configuration, inclusion growth and boundary conditions are identical (Dabrowski and Schmid, 2011 and Griera et al., 2011).

As in series A, the initial angle of anisotropy with respect to the shear plane is an important factor controlling porphyroblast rotation as well as inclusion pattern development (Fig. 8.13 and Fig. 8.14d). The spirals we have obtained have an S-shape, and are synthetic with the shear sense for the initial configuration of these models (Fig. 8.13). However, marked differences between the three cases can be observed. The central part of the inclusion shows a smooth antiform and synform microfold for the $\alpha=180°$ case, while a very slight microfold is developed for the $\alpha=90°$ simulation. In this case, a small inflexion with double-cusp or millipede geometry is developed. The $\alpha=135°$ model results in an inclusion pattern with kink-like folds determined by straight segments. The internal inclusion trail (S_i) at the inner zone of the inclusions tends to form a high angle with the external marker grid (S_e), developing a deflection plane. In contrast, Si becomes subparallel to Se at the outer zones of the rigid bodies. It is important to note that we have used initial marker lines parallel to layers.

The rotation history of the models with different initial anisotropy orientation shows marked differences (Fig. 8.13d). In the simulation with $\alpha=180°$, the inclusion rotates at all stages at a slower rate than the one predicted by the analytical solution for isotropic media (Jeffery, 1922). However, the porphyroblasts of the $\alpha=135°$ and 90° models first rotate faster than the predicted rate and then decelerate and rotate slower than the analytical

solution. The curves of the three experiments in Fig. 8.13d tend to become subparallel when a shear strain of γ=5 to 8 is achieved, although we could expect new divergences with increasing strain.
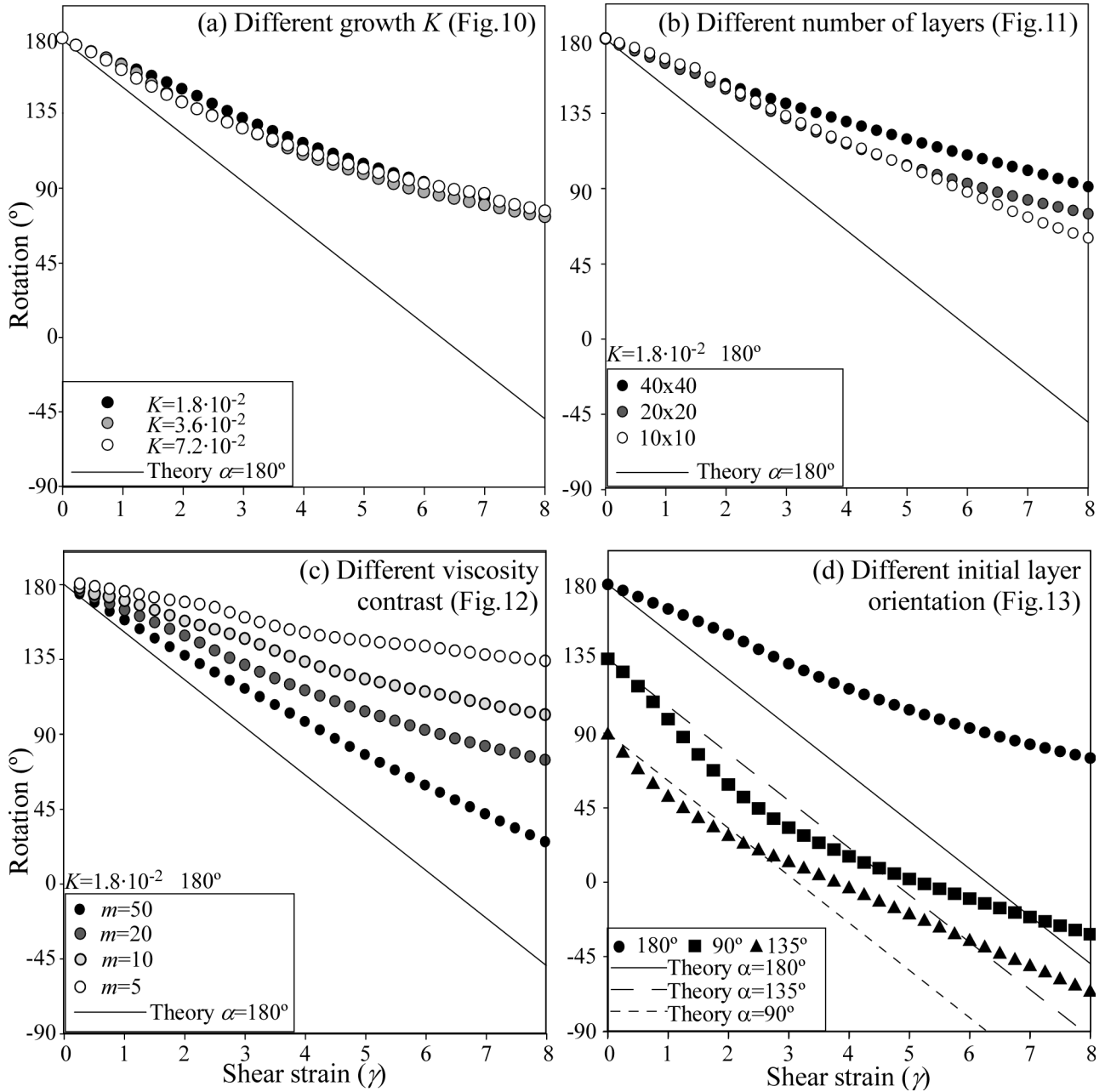
Figure 8.14: Rotation evolution of inclusions presented in Figs. 8.10, 8.11, 8.12 and 8.13 ($r \geq h$). Solid and dashed straight lines indicate the theoretical rotation behaviour of inclusions embedded in an isotropic viscous media (Jeffery, 1922).

8.4.3 Series C - fixed-size rigid inclusions in linear viscous composite materials (layer thickness > object)

This series of models simulate the behaviour of a non-growing rigid object embedded within a layer in a composite material. In this case the object diameter is smaller than

the layer thickness. For this study, we have inserted circular objects with a diameter of 1/3 of a layer within either competent (e.g. metapsammites) or incompetent layers (e.g. metapelites). We have run models with layers initially oriented at α=180°, 135° and 90° with respect to the shear plane. A viscosity contrast between alternating layers of m=10 was used for all models of this series.

The rotation tendency of the inclusions varies with α when they are inserted into competent layers (Fig. 8.15 and Fig. 8.17a). The model with layers parallel to the shear plane (α=180°) develops a strain perturbation in the matrix that leads to a millipede geometry. Two open microfolds are developed on both sides of the inclusion, and deformation may appear to look coaxial within the hard layer due to deformation partitioning (e.g. Ishii, 1992 and Jiang, 1994). The object rotates at a constant rate that is significantly slower than an inclusion embedded into an isotropic medium (Fig. 8.17a). In contrast, the simulations of rigid objects inserted into competent layers with initial α of 135° and 90° first rotate faster than the analytical model up to a shear strain of $\gamma \sim 5$, and then slower. The passive grid shows a highly symmetrical geometry with a ϕ-clast shape after γ=4 (e.g. Mandal et al., 2000 and Mandal et al., 2002). This geometry evolves towards a σ-clast with increasing deformation (i.e. γ=8), even if the objects are not elliptical. At this stage, a remarkable thinning of the soft layers, which develop a neck, can be observed adjacent to the inclusion. Fig. 8.15 shows that a 45° difference in the initial orientation of layers results in a very different inclusion pattern, rotation behaviour and vorticity indicators. In fact, the geometries displayed in Fig. 8.15h,k could be interpreted as the result of sinistral deformation around non-rotating objects. In contrast, these geometries have been developed as a consequence of a spherical object that has rotated dextrally about 180° after a bulk dextral simple shear strain of γ=8.

The behaviour of inclusions inside soft layers is significantly different (Fig. 8.16 and Fig. 8.17b). When layers are parallel to the shear plane (α=180°) the rigid object behaves as a stair-stepping δ-clast (Fig. 8.16b). This geometry is coherent with a bow tie pattern (Fig. 8.2b). This inclusion rotates synthetically and always faster than the analytical model for isotropic media (Fig. 8.17b). The object has rotated more than 360° after a shear strain of γ=8. In contrast, the inclusions embedded in soft layers initially oriented at α=135° and 90° rotate slower than the theoretical until the end of the simulations (γ=8). These objects also turn into δ-clasts with low-symmetry patterns (Fig. 8.16e,h). Wings are tighter for the α=90° model due to the higher deformation localization. These simulations illustrate the typical behaviour of rigid objects embedded into layers that tend to localise deformation at high strains.
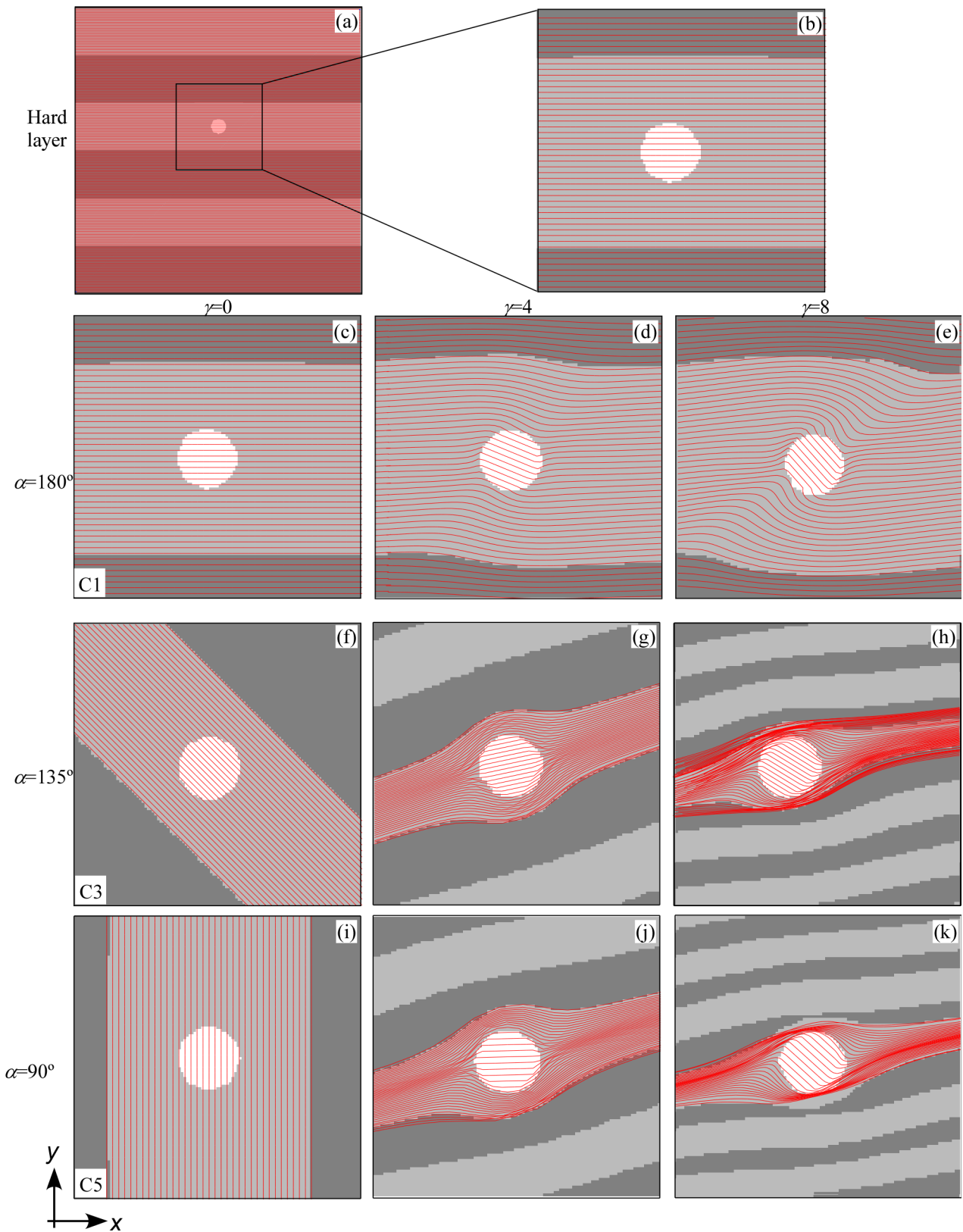
Figure 8.15: Behaviour of non-growing circular inclusions ($r \geq r$) embedded in hard layers in a multilayer with a viscosity contrast between alternating layers of $m=10$. Fig. (a) shows the whole model, while the rest of the panels (b–k) only show the inclusion and its immediate surroundings. Anisotropy is initially oriented at (c, d,e) $\alpha=180°$, (f, g, h) $\alpha=135°$ and (i,j, k) $\alpha=90°$. The labels in the bottom left corner of each model indicate the simulation run (see Table 8.2).
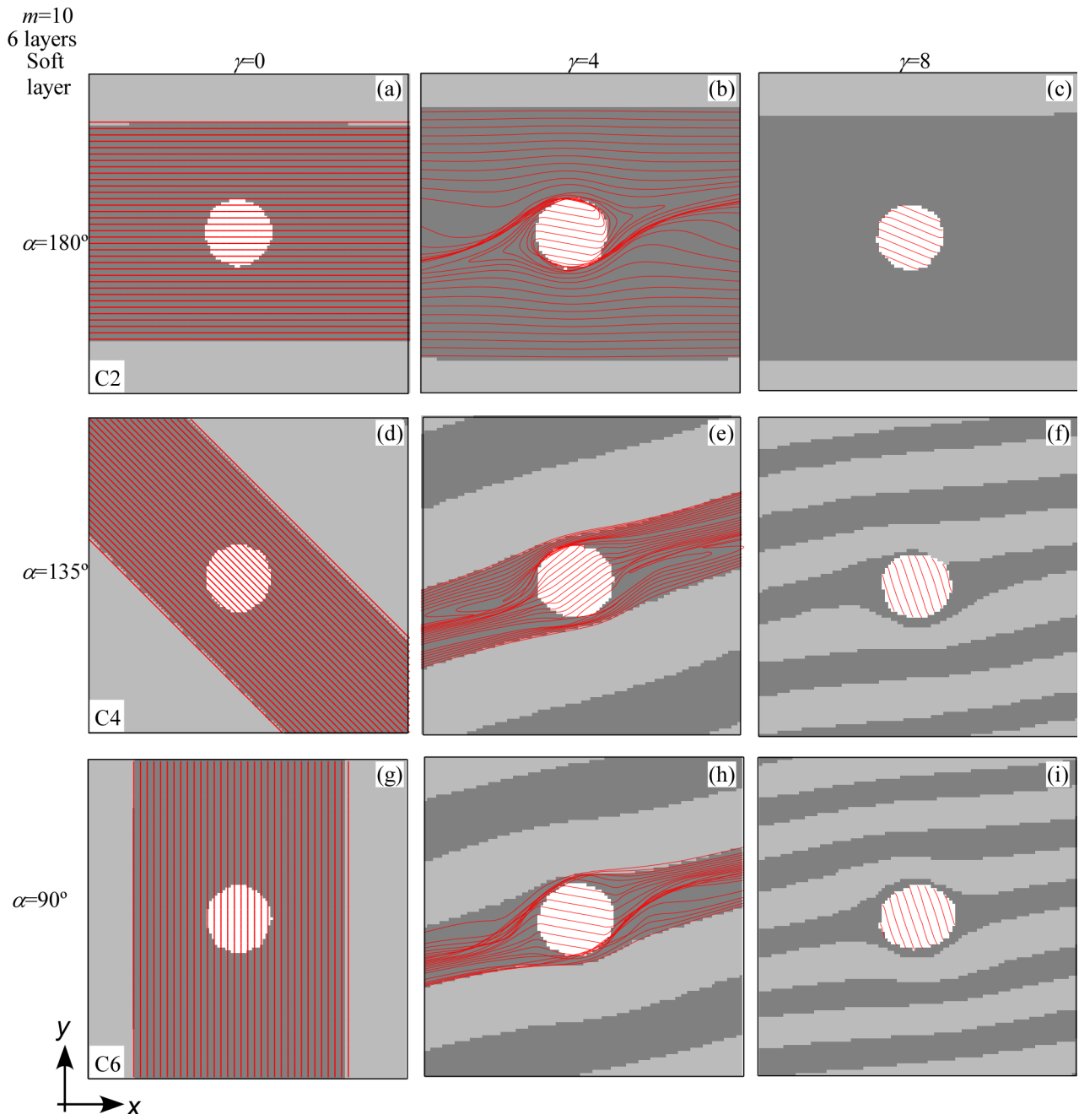
Figure 8.16: Behaviour of non-growing circular inclusions ($r \geq r$) embedded in hard layers in a multilayer with a viscosity contrast between alternating layers of $m=10$. As in Fig. 8.13, only the inclusion and its surroundings are displayed. Anisotropy is initially oriented at (a, b, c) $\alpha=180°$, (d, e, f) $\alpha=135°$ and (g, h, i) $\alpha=90°$. The labels on the bottom left corner of each model indicate the simulation run (see Table 8.2).
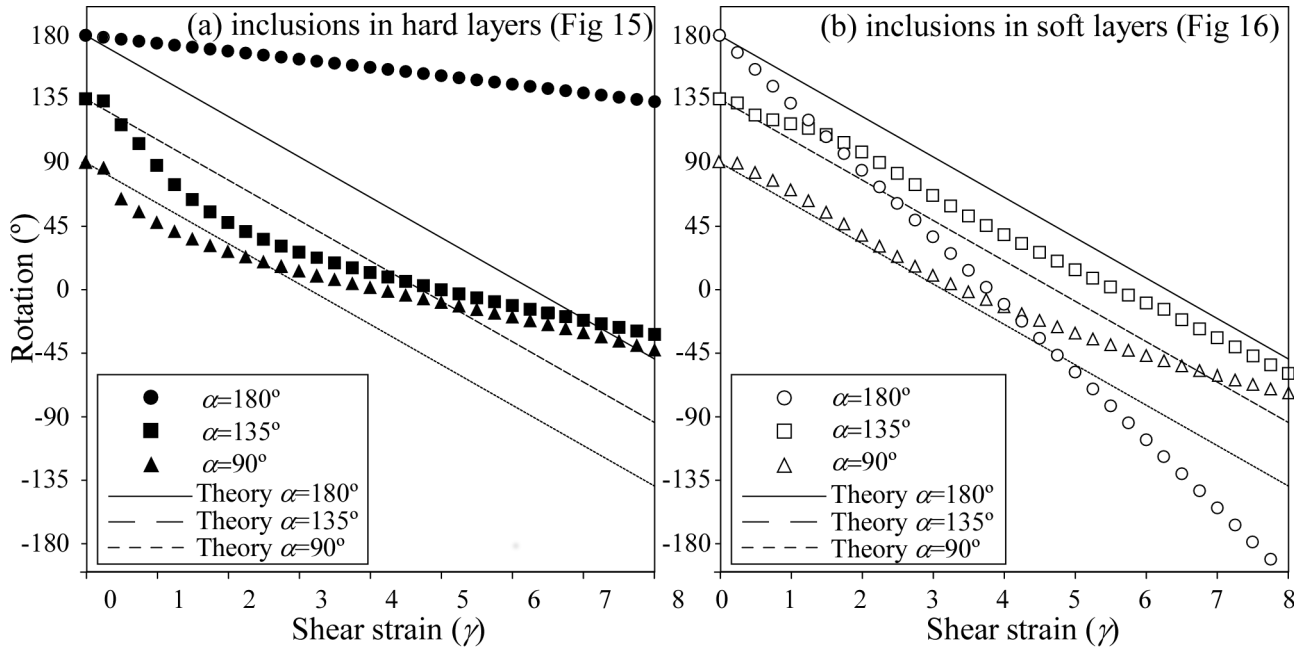
Figure 8.17: Rotation evolution of non-growing inclusions smaller than the layer width ($r \geq r$) embedded in a composite materials presented in Figs. 8.14 and 8.15. Solid and dashed straight lines indicate the theoretical rotation behaviour of inclusions embedded in an isotropic viscous media (Jeffery, 1922).

8.5 Discussion and future perspectives

The numerical results presented in this study illustrate the systematic variation in the behaviour of rigid objects (porphyroclasts and porphyroblasts) in anisotropic materials. The three series of experiments indicate that the presence of anisotropy produces a significant deviation in the rotation behaviour and development with respect to the theoretical solution based on isotropic viscous media, as well a strong variability of inclusion patterns. Deformation partitioning and the development of structures, such as folds, lead to a decrease of the vorticity and shear strain transferred to the rigid particle during matrix deformation, thus causing a significant decrease of its rotation rate (Fig. 8.6 and Fig. 8.9a, Fig. 8.12 and Fig. 8.14c, Fig. 8.15, Fig. 8.16 and Fig. 8.17). Although we have only explored some particular cases, our research results illustrate the general behaviour of rigid inclusions when anisotropy is present.

8.5.1 On the influence of the degree of anisotropy (a, m) and orientation (α)

For the range of studied parameters, all the rigid objects rotate with regard to the external coordinate system (i.e. x and y systems shown in Fig. 8.4), the external foliation reference system (i.e. i and j system of Fig. 8.4) and with a synthetic rotation sense with respect

to the imposed sense of shear. Examples of porphyroblasts/-clasts that remain fixed in their orientation, which would support the non-rotation hypothesis (e.g., Bell, 1985, Bell et al., 1992a, Bell et al., 1992b and Fay et al., 2008), have not been observed in this study. However, after a certain amount of deformation, stable orientations for circular rigid objects can be achieved (Griera et al., 2011). A general conclusion of this study for circular inclusions embedded in anisotropic media is that deformation partitioning may lead to stable rigid object orientations, but objects do always rotate before reaching a stagnant orientation. It is important to notice that this conclusion is made according to the setup and boundary conditions used in these simulations. Our observations apply to circular objects deformed in a single deformation phase in bulk simple shear conditions. For these conditions, a circular inclusion embedded in an isotropic matrix rotates at a rate that is half that of the shear strain rate (Jeffery, 1922) and the possible modifications by the matrix anisotropy are simple to be detected. In the end-member case of pure shear circular/spherical rigid inclusions do not rotate, thus limiting the possibility of exploring the influence of anisotropy on rigid object rotation behaviour and spiral geometry development.

Different authors have previously studied the effect of a pre-existing mechanical anisotropy on the development of tectonic structures. For example, the orientation of anisotropy has a strong influence on the orientation and geometry of developed shear fractures (Gomez-Rivas and Griera, 2011 and Gomez-Rivas and Griera, 2012). The degree of matrix anisotropy also plays a significant role on the geometry of deformed single layers (e.g. Kocher et al., 2008), on folding mechanisms and how strain is accommodated in folded layers (e.g. Toimil and Griera, 2007), on the reactivation of fault and shear zones (e.g. Tommasi et al., 2009) or on new fabric development over pre-existing fabrics (e.g. Michibayashi and Mainprice, 2004), among other examples. Our results also highlight the important role of anisotropy on the rotation of rigid objects and the associated spiral inclusion geometries.

Caution must be taken when interpreting cases where anisotropy is not parallel to the shear zone, a situation that is common in the field. Different authors have previously considered this situation using passive markers oriented at different angles with respect to the shear zone in isotropic materials (e.g. Bons et al., 2009, Ramsay and Lisle, 2000, Samanta et al., 2002a, Samanta et al., 2002b and Stallard et al., 2002). They observed that marker orientation plays an important role on the geometry of the developed inclusion patterns and may be used as a tool for inferring initial foliation orientations. A serious handicap of these broadly used analytical models for rigid object rotation is that porphyroblast/-clast kinematics are set and a certain rotation rate is used regardless of the marker orientation. Although this is a valid approach for isotropic materials, our experiments indicate that for situations where mechanical anisotropy is present, the general rule is that strong deviations of the object's rotation with respect to the analytical solutions occur. Consequently, inclusion patterns also differ from the expected ones. The question

then is whether it is possible to quantify and predict the deviation of the rigid object behaviour with respect to the theoretical one. This would depend on the orientation of anisotropy but also on its degree. Kinematic interpretations inferred from porphyroblasts/-clasts may significantly change depending on the relative orientation between the strain marker (e.g. foliation) and the inclusion. An opposite sense of rotation can even be obtained from the same object if two different markers are used. Therefore, care should be taken when using porphyroblasts/-clasts for shear sense determination. When possible, these interpretations should be compared and crosschecked with those made with other shear-sense indicators. Moreover, structural analysis should not be restricted to few sample observations. Most of our models were developed with an initial anisotropy orientation of α = 180°, which is a particular and special case. Simulations made with different anisotropy orientations (Fig. 8.8 and Fig. 8.9b, Fig. 8.13 and Fig. 8.14d) indicate its strong influence on the rigid object's inferred rotation.

8.5.2 On the influence of porphyroblast growth rate (K)

Our numerical results show that the relative porphyroblast growth rate relative to the shear strain rate has a significant influence on inclusion geometries. Spiral shaped inclusion patterns form in our isotropic simulations (a=1; Figs. 8.6b and 8.7) or in the layered models with a low viscosity contrast (e.g. m=5; Fig. 8.12). The increase of anisotropy and the general orientation of anisotropy planes tend to inhibit the development of snowball-type inclusions and favour oblique to sigmoidal inclusion patterns.

A fast porphyroblast growth rate with respect to the amplification of structural perturbations generates inclusion geometries within the porphyroblast that might resemble post-tectonic microstructures, even if they are syntectonic. Bell and Rubenach (1983) already showed that syntectonic porphyroblasts could potentially be misinterpreted as pre or post if they grow very early or late during deformation, respectively, highlighting that the relative growth rate is a key concept in understanding porphyroblast microstructures. Therefore, traditional interpretations of pre-, syn- and post-tectonic porphyroblasts (e.g. Passchier and Trouw, 2005, Zwart, 1960 and Zwart, 1962) may require independent lines of evidence to corroborate or refute them. Barker (1994) indicated that the relative timing between growth kinematics and strain rate may cause marked differences in the geometry of inclusion trails. For example, Fig. 8.10e, f shows that S_i and S_e are continuous, while S_e slightly wraps around the porphyroblast. Johnson and Vernon (1995a) and Johnson (1999) also pointed out that very similar inclusion trails could be formed as a consequence of porphyroblast growth at different rates. Fast growth rates produce straighter inclusion-trail patterns, which tend to preserve a nucleus with a straight geometry. It is thus essential to take into account multiple possible interpretations when trying to infer microstructure–timing relationships in the field, as they can be complex. Our numerical

modelling approach, which is based on combination of deformation and inclusion growth, is useful to visualise and explore the growth–timing relationships of porphyroblasts. However, we have seen that the growth rate does not indicate differences in rotation history if the nucleus of the object is used to trace it (Fig. 8.14a). Our results must be added to previously studied factors for porphyroclast/-blast rotation interpretation, such as mantle recrystallization, layer decoupling, layer slipping, interaction between multiple objects, etc.

8.5.3 Other factors that induce porphyroblast/-clast complex behaviour

The behaviour of porphyroblasts and porphyroclasts can be even more complex if we consider other factors that we have not fully explored in our simulations, like: (1) the presence of a strong degree of anisotropy and/or anisotropy orientations oblique to the shear plane ($\alpha \neq 180°$), (2) the use of irregular and heterogeneous layers or (3) the relative position of rigid objects with respect to layers and the relative relationship between object radius and layer thickness (r/h).

When a high degree of anisotropy is combined with an anisotropy orientation oblique to the shear plane ($\alpha \neq 180°$), the development of shear bands with different orientations produce a complex deformation and rotation history. For instance, Fig. 8.18a, b, c shows sequential snapshots of a simulation with intrinsic anisotropy of $a=20$ and initially oriented at $\alpha=135°$. Intense strain localisation and shear zone development induce a slow transfer of vorticity to the inclusion, thus causing a non-rotational behaviour between shear strains of $\gamma \sim 4$ to $\gamma \sim 8$ (Fig. 8.18b, c). A similar observation was obtained by Griera et al. (2011) in their numerical simulations of porphyroclast deformation in a polycrystalline matrix.

In all our simulations, most of the developed perturbations arise from strain partitioning around the inclusion. They are related to the inclusion's geometry and size but also to its relative position with respect to the matrix and degree of anisotropy. By predefining the initial anisotropy as homogenous and flat, we excluded perturbations that nucleated by folding of the multilayer. Therefore, at the beginning there is no competition between different structural perturbations (i.e. induced by the stiff inclusion or buckling folds induced by the viscosity contrast between layers) in our models. However, when layers are not regular and have some initial noise, much more complex geometries may develop, especially due to the interaction between rigid object rotation/growth and nucleation and amplification of folds in the matrix (Fig. 8.18d, e, f). This example may apply to cases of crenulation folds but it can also be applied to situations of epitaxial growth of garnets parallel to phyllosilicate layers. Complex relationships, with the possibility of fast inclusion rotation but also locking up, are expected to occur according to the ratio between fold wavelength and inclusion size.
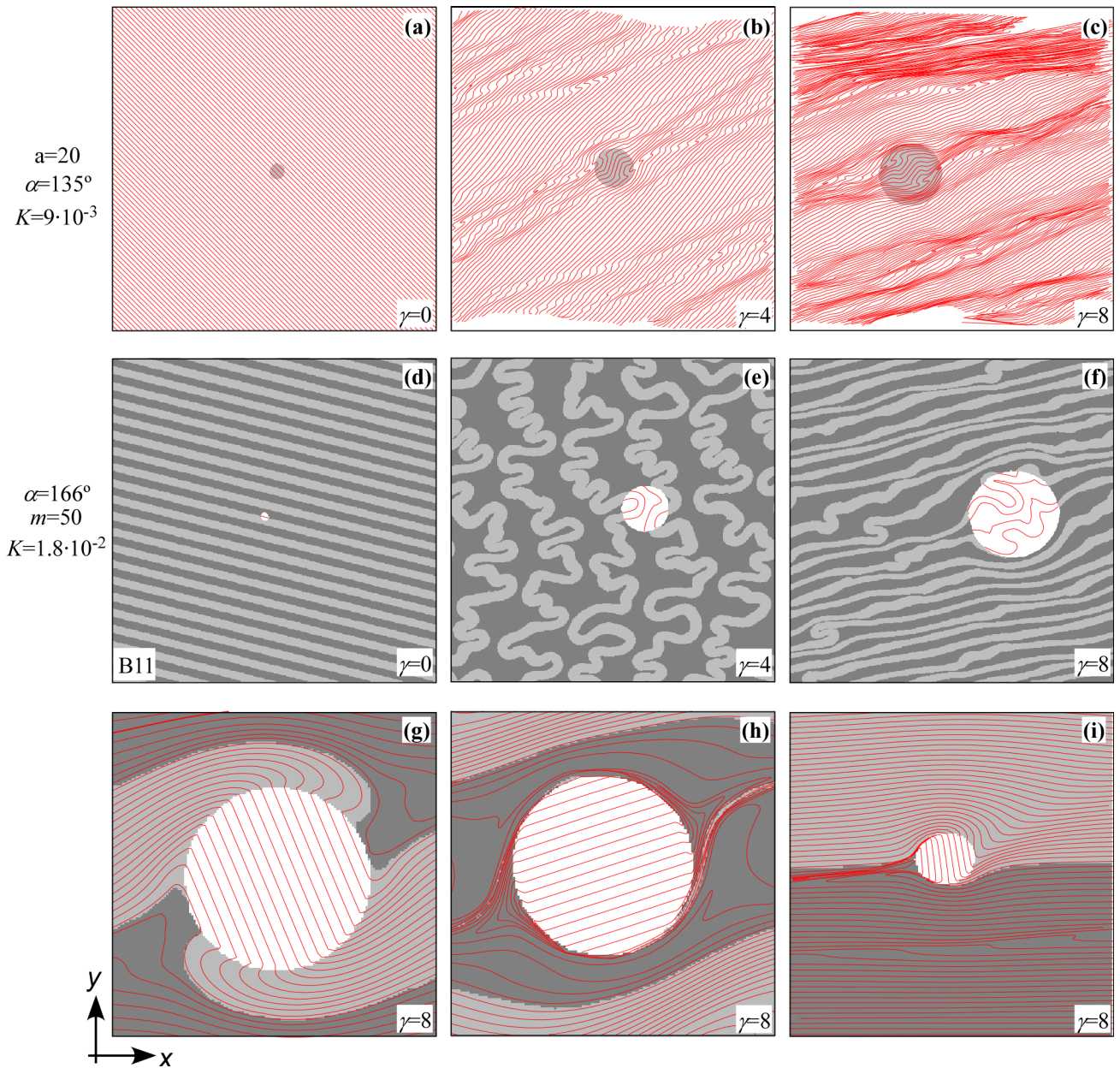
Figure 8.18: Examples of models with parameters not systematically covered in this study, but which may increase the complexity of porphyroblast/-clast behaviour: (a–c) simulation with intrinsic anisotropy of $a=20$ and initial anisotropy oriented at $\alpha=135°$ from the shear plane at stages of $\gamma=0$, 4 and 8; (d–f) simulation of a linear viscous multilayer ($m=10$) with initial random perturbations at layer interfaces (causing buckle folds) and a growing porphyroblast (stages of $\gamma=0$, 4 and 8); (g–h) non-growing rigid objects ($2r=h$) embedded in a hard and soft layer of a multilayer, respectively; (i) non-growing object that was initially placed at the interface between a hard and soft layer. Panels (g–i) show the $\gamma=8$ stage.

In addition to the scale factor between the inclusion radius and the layer or anisotropy thickness (r/h), the relative position of the object with respect to the anisotropy may also have a dramatic influence on the spiral geometry and rotation behaviour. Fig. 8.18g, h shows two models (at a shear strain of $\gamma \sim 8$) in which an inclusion with a diameter equal to the layer thickness (i.e. $2r = h$) was placed in a hard and soft layer, respectively. Quarter folds (i.e. microfolds in the quarters that lay in the extensional direction; Passchier and Trouw, 2005) are developed in the first case, while a stair-stepping δ-clast is formed in the second one. Strong differences in finite object rotation are also observed. For cases where $r<h$, there is no simple or predictable homogenisation scheme to infer bulk rotation or to predict the evolution of rigid objects, even if we only consider a medium with homogenous flat anisotropy. Additionally, the object behaviour does not only depend on whether it is located in a soft or a competent layer but also on its relative position with respect to the layer interface. An illustrative example is shown in Fig. 8.18i, where a non-growing object with the same radius as the ones shown in Fig. 8.13 and Fig. 8.16 was inserted at the interface between a hard and a soft layer. The result after a shear strain of $\gamma \sim 8$ shows a completely asymmetric geometry, both parallel and perpendicular to the shear plane. These examples indicate that there is no single predictable porphyroclast/-blast behaviour. Therefore, porphyroclast/-blast interpretations must be done in the field with care, as "everyone can be a special case".

8.5.4   Future perspectives

Future perspectives in this topic will mainly focus on the improvement of current observational techniques as well as on the development of more sophisticated and realistic 3D numerical modelling techniques.

Improvements on analytical methods have increased the available 2D (surface methods) and 3D (volumetric methods) information. Advances in complex 3D observational techniques such as HRXCT tomography (e.g. Huddlestone-Holmes and Ketcham, 2010 and Robyr et al., 2009), open up the possibility of 3D observation of volumes, reconstruction of cross sections and observation of 3D changes on the spiral geometry from the core to the rims of the porphyroblast. This technique will allow unravelling 3D porphyroblast inclusion patterns and will provide a better knowledge of foliation intersection axis distributions. The present-day advances in techniques such as SEM, EBSD and electron microprobe analyses indicate the complexity of porphyroblast growth (e.g., coalescence, epitaxial following phyllosilicate rich layers, etc.; see Fig. 8.1e; Spiess et al., 2001).

The current 3D numerical simulations are based on numerical integration of theoretical solutions and are limited to isotropic media and/or prefixed rigid object rotation rates. The extremely complex behaviour of porphyroblast development and rotation illustrated with our 2D simulations is much more complex if the third dimension is taken into account.

The behaviour of rigid objects in rocks is essentially a 3-dimensional problem, as recently indicated by Li and Jiang (2011). For example, the interpretation of the "Foliation Intersection Axis" (FIA) issue (e.g. Bell and Bruce, 2006 and Johnson, 1999 and references therein), which is one of the major problems of the rotation versus non-rotation debate, requires 3D approaches. Part of the large amount of available field data analysed in many contributions shows an apparent contradiction between the interpreted rotation behaviour of rigid objects in the field with respect to the theoretical rotation model. As pointed out by 2D simulations, a significant deviation with respect to classical analytical models is expected when anisotropy is taken into account, but 3D numerical simulations will be required to improve our knowledge and fully understand this topic. The advance of analytical spatial techniques, such as the possibility of combining compositional element maps with EBSD crystallographic orientation maps, point towards the direction that numerical simulations should tend to couple chemistry and deformation codes in order to fully incorporate the transport and precipitation of dissolved material (e.g. Hobbs et al., 2011). This is a challenging and major task for numerical research based on coupling between deformation and metamorphic processes. Recent advances in quantitative modelling of metamorphic processes (e.g. Carlson, 2011 and Gaidies et al., 2011) already include quantitative simulation of diffusion-controlled nucleation and growth of garnet porphyroblasts.

8.6 Conclusions

This contribution presents a review of numerical modelling of porphyroblast and porphyroclast rotation and it also provides new data and numerical experiments on the deformation and growth of a rigid porphyroblast embedded in an anisotropic matrix and subjected to simple shear deformation. The historical overview comprises the main advances that the scientific community has made on this topic, from the publication of first analytical solutions of rigid object rotation, to the development of complex numerical simulations. Numerical studies were first based on isotropic media and have become more sophisticated with the inclusion of anisotropy.

The results of the three series of numerical experiments, with either intrinsic or composite anisotropy, presented in this study lead to the following conclusions:

1. The prediction of the rotation behaviour and inclusion patterns of porphyroblasts/-clasts in anisotropic media is not a straightforward task. Complex inclusion patterns are developed when anisotropy is present.

2. The rotational behaviour and inclusion patterns of rigid inclusions are strongly controlled by strain localisation on the scale of the inclusion. Rigid objects do rotate during non-coaxial deformation. Their rotation evolution tends to follow the analytical solution of Jeffery (1922) when they are embedded in materials with low degree of anisotropy. Increasing anisotropy considerably reduces object rotation rates due to the onset of

stretching bands, shear bands and folds. Stalling of rotation can occur at relatively high strain.

3. The orientation of anisotropy with respect to the stress/strain axes is also a significant factor that strongly controls the rotational behaviour and spiral patterns of porphyroblasts/-clasts.

4. When rigid objects are smaller than the anisotropy/layer thickness, their rotation behaviour is strongly controlled by their relative position within the material (i.e. whether they are located in hard or soft layers), among other factors.

Finally, and in agreement with the last statement of Passchier et al. (1992), we do not claim that we understand the complete behaviour of porphyroblasts in anisotropic media. In fact, we believe that the effect of anisotropy on rigid object behaviour is far from being understood. However, we have provided a systematic study that explores a relevant part of the problem and displays the complexity of these systems. Although we have analysed the influence of some parameters (degree of anisotropy a or m, orientation of anisotropy $-\alpha$, scale and type of anisotropy $- r/h$, porphyroblast growth rate K, etc.) we think that more systematic studies are required to better constrain this issue. The following parameters need to be explored in the future: polyphase deformation, general shear deformation, interaction between multiple porphyroclasts/-blasts, variability of rigid-object geometries, deformable objects, 3D inclusion-pattern analyses, multiscale modelling to understand rigid object evolution in regions with strain gradients (i.e. shear zones), etc.

Acknowledgements

8.7 References

- Aerden, D., 2005. Comment on "Reference frame, angularmomentum, and porphyroblast rotation" by Dazhi Jiang and Paul F. Williams. Journal of Structural Geology 27, 1128–1133.

- Barker, A.J., 1994. Interpretation of porphyroblast inclusion trails: limitations imposed by growth kinetics and strain rates. Journal of Metamorphic Geology 12, 681–694.

- Beam, E.C., 1996. Modeling growth and rotation of porphyroblasts and inclusion trails. Computer Methods in the Geosciences 15, 247–258.

- Becker, J.K., Bons, P.D., Jessell, M.W., 2008. A new front-tracking method to model anisotropic grain and phase boundary motion in rocks. Computers and Geosciences 34, 201–212.

- Bell, T.H., 1985. Deformation partitioning and porphyroblast rotation in metamorphic rocks: a radical reinterpretation. Journal of Metamorphic Geology 3, 109–118.

- Bell, T.H., Bruce, M.D., 2006. The internal inclusion trail geometries preserved within a first phase of porphyroblast growth. Journal of Structural Geology 28, 236–252.

- Bell, T.H., Rubenach, M.J., 1983. Sequential porphyroblast growth and crenulation cleavage development during progressive deformation. Tectonophysics 92, 171–194.

- Bell, T.H., Duncan, A.C., Simmons, J.V., 1989. Deformation partitioning, shear zone development and the role of undeformable objects. Tectonophysics 158, 163–171.

- Bell, T.H., Forde, A., Hayward, N., 1992a. Do smoothly curving, spiral-shaped inclusions trails signify porphyroblast rotation? Geology 20, 59–62.

- Bell, T.H., Johnson, S.E., Davis, B., Forde, A., Hayward, N.,Wilkins, C., 1992b. Porphyroblast inclusion-trail orientation data: eppure non son girate! Journal of Metamorphic Geology 10, 295–307.

- Biermeier, C., Stuüwe, K., Barr, T.D., 2001. The rotation rate of cylindrical objects during simple shear. Journal of Structural Geology 23, 765–776.

- Bilby, B.A., Kolbuszewski, M.L., 1977. The finite deformation of an inhomogeneity in two-dimensional slow viscous incompressible flow. Proceedings of the Royal Society of London. Series A: Mathematical and Physical Sciences 355, 335–353.

- Bilby, B.A., Eshelby, J.D., Kundu, A.K., 1975. The change of shape of a viscous ellipsoidal region embedded in a slowly deforming matrix having a different viscosity. Tectonophysics 28, 265–274.

- Biot, M.A., 1965. Mechanics of Incremental Deformations: Theory of Elasticity and Viscoelasticity of Initially Stressed Solids and Fluids, Including Thermodynamic Foundations and Applications to Finite Strain. Wiley, New York.

- Bjørnerud, M., 1989a. Toward a unified conceptual framework for shear-sense indicators. Journal of Structural Geology 11, 1045–1049.

- Bjørnerud, M., 1989b. Mathematical model for folding of layering near rigid objects in shear deformation. Journal of Structural Geology 11, 245–254.

- Bjørnerud, M., Zhang, H., 1994. Rotation of porphyroblasts in non-coaxial deformation: insight from computer simulations. Journal of Metamorphic Geology 12, 135–139.

- Bons, P.D., Barr, T.D., ten Brink, C.E., 1997. The development of delta-clasts in non-linear viscous materials: a numerical approach. Tectonophysics 270, 29–41.

- Bons, P.D., Jessell, M.W., Evans, L., Barr, T.D., Stüwe, K., 2001. Modelling of anisotropic grain growth in minerals. In: Koyi, H.A., Mancktelow, N.S. (Eds.), Tectonic Modeling: A Volume in Honor of Hans RambergGeological Society of America Memoir 193, 39–49.

- Bons, P.D., Koehn, D., Jessell, M.W. (Eds.), 2008. Microdynamic Simulation. : Lecture Notes in Earth Sciences, 106. Springer, Berlin. 405 pp.

- Bons, P.D., Jessell, M.W., Griera, A., 2009. Porphyroblast rotation versus nonrotation: conflict resolution! COMMENT. Geology 37, e182.

- Carlson, W., 2011. Porphyroblast crystallization: linking processes, kinetics and microstructures. International Geology Review 53, 406–445.

- Ceriani, S., Mancktelow, N.S., Pennacchioni, G., 2003. Analogue modelling of the influence of shape and particle/matrix interface lubrication on the rotational behaviour of rigid particles in simple shear. Journal of Structural Geology 25, 2005–2021.

- Chwang, A.T., Wu, T.Y.-T., 1975. Hydromechanics of low-Reynolds-number flow. Part 2. Singularity method for Stokes flows. Journal of Fluid Mechanics 67, 787–815.

- Dabrowski, M., Schmid, D.W., 2011. A rigid circular inclusion in an anisotropic host subject to simple shear. Journal of Structural Geology 33, 1169–1177.

- Einstein, A., 1905. Eine neue Bestimmung der Moleküldimensionen. Annalen der Physik 19, 289–306.

- Einstein, A., 1956. Investigations on the Theory of Brownian Movement. Dover, New York . 119 pp.

- Eshelby, J.D., 1957. The determination of the elastic field of an ellipsoidal inclusion, and related problems. Proceedings of the Royal Society of London A241, 376–396.

- Eshelby, J.D., 1959. The elastic field outside an ellipsoidal inclusion. Proceedings of the Royal Society of London 252 (1271), 561–569.

- Fay, C., Bell, T.H., Hobbs, B.E., 2008. Porphyroblast rotation versus nonrotation: conflict resolution! Geology 36, 307–310.

- Fay, C., Bell, T.H., Hobbs, B.E., 2009. Porphyroblast rotation versus nonrotation: conflict resolution! REPLY. Geology 37, e188.

- Ferguson, C.C., 1979. Rotations of elongate rigid particles in slow non-Newtonian flows. Tectonophysics 60, 247–262.

- Fletcher, R.C., 2009. Deformable, rigid, and inviscid elliptical inclusions in a homogeneous incompressible anisotropic viscous fluid. Journal of Structural Geology 31, 382–387.

- Gaidies, F., Pattison, D.R.M., de Capitani, C., 2011. Toward a quantitative model of metamorphic nucleation and growth. Contributions to Mineralogy and Petrology 162, 975–993.

- Gay, N.C., 1968. Pure shear and simple shear deformation of inhomogeneous viscous fluids. 1. Theory. Tectonophysics 5, 211–234.

- Ghosh, S.K., Ramberg, H., 1976. Reorientation of inclusions by combination of pure shear and simple shear. Tectonophysics 34, 1–70.

- Gomez-Rivas, E., Griera, A., 2011. Strain rate influence on fracture development in experimental ductile multilayers. Tectonophysics 502, 345–357.

- Gomez-Rivas, E., Griera, A., 2012. Shear fractures in anisotropic ductile materials: an experimental approach. Journal of Structural Geology 34, 61–76.

- Gray, N.H., Busa, M.D., 1994. The 3-dimensional geometry of simulated porphyroblast inclusion trails — inert-marker, viscous-flow models. Journal of Metamorphic Geology 12, 575–587.

- Griera, A., Bons, P.D., Jessell, M.W., Lebensohn, R.A., Evans, L., Gomez-Rivas, E., 2011. Strain localization and porphyroclast rotation. Geology 39, 275–278.

- Groome,W.G., Johnson, S.E., 2008. Transient strain-rate partitioning during porphyroblast growth. In: Bons, P.D., Koehn, D., Jessell, M.W. (Eds.), Microdynamics Simulation, Lecture Notes in Earth Sciences, vol. 106. Springer, Berlin.

- Groome, W.G., Johnson, S.E., Koons, P.O., 2006. The effects of porphyroblast growth on the effective viscosity of metapelitic rocks: implications for the strength of the middle crust. Journal of Metamorphic Geology 24, 389–407.

- Hammer, S., Passchier, C.W., 1991. Shear-sense indicators: a review. Geological Survey of Canada Paper 90, 1–72.

- Hayward, N., 1990. Determination of early fold axis orientations within multiply deformed rocks using porphyroblasts. Tectonophysics 179, 353–369.

- Hobbs, B.E., Means, W.D., Williams, P.F., 1976. An Outline of Structural Geology. Wiley, New York . 571 pp.

- Hobbs, B.E., Ord, A., Regenauer, K., 2011. The thermodynamics of deformed metamorphic rocks: a review. Journal of Structural Geology 33, 758–818.

- Houseman, G., Barr, T., Evans, L., 2008. Basil: stress and deformation in a viscous material. In: Bons, P.D., Koehn, D., Jessell, M.W. (Eds.), Microdynamics Simulation.: Lecture Notes in Earth Sciences, 106. Springer, Berlin, p. 405.

- Huddlestone-Holmes, C.R., Ketcham, R.A., 2010. An X-ray computed tomography study of inclusion trail orientations in multiple porphyroblasts from a single sample. Tectonophysics 480, 305–320.

- Ildefonse, B., Mancktelow, N.S., 1993. Deformation around rigid particle: influence of slip at the particle/matrix interface. Tectonophysics 221, 345–359.

- Ildefonse, B., Launeau, P., Bouchez, J.L., Fernandez, A., 1992. Effect of mechanical interactions on the development of shape preferred orientations: a two dimensional experimental approach. Journal of Structural Geology 14, 73–83.

- Ishii, K., 1992. Partitioning of non-coaxiality in deforming layered rock masses. Tectonophysics 210, 33–43.

- Jeffery, G.B., 1922. The motion of ellipsoidal particles immersed in a viscous fluid. Proceedings of the Royal Society of London Series A 102, 161–179.

- Jessell, M., Bons, P.D., Evans, L., Barr, T., Stüwe, K., 2001. Elle: the numerical simulation of metamorphic and deformation microstructures. Computers and Geosciences 27, 17–30.

- Jessell, M.W., Kostenko, O., Jamtveit, B., 2003. The preservation potential of microstructures during static grain growth. Journal of Metamorphic Geology 21, 481–491.

- Jessell, M.W., Siebert, E., Bons, P.D., Evans, L., Piazolo, S., 2005. A new type of numerical experiment on the spatial and temporal patterns of localization of deformation in a material with a coupling of grain size and rheology. Earth and Planetary Science Letters 239, 309–326.

- Jessell, M.W., Bons, P.D., Griera, A., Evans, L.A., Wilson, C.J.L., 2009. A tale of two viscosities. Journal of Structural Geology 31, 719–736.

- Ježek, J., Saic, S., Segeth, K., Schulmann, K., 1999. Three-dimensional hydrodynamical modelling of viscous flow around a rotating ellipsoidal inclusion. Computers and Geosciences 25, 547–558.

- Jiang, D., 1994. Vorticity determination, distribution, partitioning and the heterogeneity and non-steadiness of natural deformations. Journal of Structural Geology 16, 121–130.

- Jiang, D., 2001. Reading history of folding from porphyroblasts. Journal of Structural Geology 23, 1327–1335.

- Jiang, D., 2007. Numerical modeling of the motion of deformable ellipsoidal objects in slow viscous flows. Journal of Structural Geology 29, 435–452.

- Jiang, D., Williams, P.F., 2004. Reference frame, angular momentum, and porphyroblast rotation. Journal of Structural Geology 26, 221–2224.

- Johnson, S.E., 1993. Testing models for the development of spiral-shaped inclusion trails in garnet porphyroblasts: to rotate or not to rotate, that is the question. Journal of Metamorphic Geology 11, 635–659.

- Johnson, S.E., 1999. Porphyroblast microstructures: a review of current and future trends. American Mineralogist 84, 1711–1726.

- Johnson, S.E., 2008. Strain localisation and rigid-object kinematics. In: Bons, P.D., Koehn, D., Jessell, M.W. (Eds.), Microdynamics Simulation, Lecture Notes in Earth Sciences, vol. 106. Springer, Berlin.

- Johnson, S.E., 2009. Porphyroblast rotation and strain localization: debate settled! Geology 37, 663–666.

- Johnson, S.E., 2010. Porphyroblast rotation and strain localization: debate settled!. REPLY. Geology 38, e205.

- Johnson, S.E., Vernon, R.H., 1995. Stepping stones and pitfalls in the determination of an anticlockwise P–T–t-deformation path: the low-P, high-T Cooma Complex, Australia. Journal of Metamorphic Geology 13, 165–183.

- Johnson, S.E., Lenferink, H.J., Marsh, J.H., Price, N.A., Koons, P.O., West, D.P., 2009. Kinematic vorticity analysis and evolving strength of mylonitic shear zones: new data and numerical results. Geology 37, 1075–1078.

- Kenkmann, T., Dresen, G., 1998. Stress gradients around porphyroclasts: palaeopiezometric estimates and numerical modelling. Journal of Structural Geology 20, 163–173.

- Kocher, T., Mancktelow, N.S., Schmalholz, S.M., 2008. Numerical modelling of the effect of matrix anisotropy orientation on single layer fold development. Journal of Structural Geology 30, 1013–1023.

- Lebensohn, R.A., 2001. N-site modeling of a 3D viscoplastic polycrystal using fast Fourier transform. Acta Materialia 49, 2723–2737.

- Lebensohn, R.A., Brenner, R., Castelnau, O., Rollett, A.D., 2008. Orientation image-based micromechanical modelling of subgrain texture evolution in polycrystalline copper. Acta Materialia 56, 3914–3926.

- Lebensohn, R.A., Ponte Castañeda, P., Brenner, R., Castelnau, O., 2011. Full-field vs. Homogenization methods to predict microstructure-property relations for polycrystalline materials. In: Ghosh, S., Dimiduk, D. (Eds.), Computational Methods for Microstructure-Property Relationships, Chapter 11. Springer, pp. 393–442.

- Li, C., Jiang, D., 2011. A critique of vorticity analysis using rigid clasts. Journal of Structural Geology 33, 203–219.

- Llorens, M-.G., Bons, P.D., Griera, A., Gomez-Rivas, E. and Evans, L.A., 2013. Single layer folding in simple shear. Journal of Structural Geology 50, 209-220.

- Mancktelow, N.S., 2011. Deformation of an elliptical inclusion in two-dimensional incompressible power-lawviscous flow. Journal of Structural Geology 33, 1378–1393.

- Mancktelow, N.S., Arbaret, L., Pennacchioni, G., 2002. Experimental observations on the effect of interface slip on rotation and stabilisation of rigid particles in simple shear and a comparison with naturalmylonites. Journal of Structural Geology 24, 567–585.

- Mandal, N., Samanta, S.K., Chakraborty, C., 2000. Progressive development of mantle structures around elongate porphyroclasts: insights from numerical models. Journal of Structural Geology 22, 993–1008.

- Mandal, N., Samanta, S.K., Chakraborty, C., 2002. Numerical modeling of heterogeneous flow fields around rigid objects with special reference to particle paths, strain shadows and foliation drag. Tectonophysics 330, 177–194.

- Mandal, N., Misra, S., Samanta, S.K., 2005a. Rotation of single rigid inclusions embedded in an anisotropic matrix: a theoretical study. Journal of Structural Geology 27, 731–743.

- Mandal, N., Samanta, S.K., Chakraborty, C., 2005b. Numerical models of flow patterns around a rigid inclusion in a viscous matrix undergoing simple shear: implications of model parameters and boundary conditions. Journal of Structural Geology 27, 1599–1609.

- Marques, F.O., Coelho, S., 2001. Rotation of rigid elliptical cylinders in viscous simple shear flow: analogue experiments. Journal of Structural Geology 23, 609–617.

- Marques, F.O., Taborda, R., Bose, S., Antunes, J., 2005a. Effects of confinement on matrix flow around a rigid inclusion in viscous simple shear: insights from analogue and numerical modelling. Journal of Structural Geology 27, 379–396.

- Marques, F.O., Taborda, R., Antunes, J., 2005b. Influence of a low-viscosity layer between rigid inclusion and viscous matrix on inclusion rotation and matrix flow: a numerical study. Tectonophysics 407, 101–115.

- Marques, F.O., Taborda, R., Antunes, J., 2005c. 2D rotation of rigid inclusions in confined bulk simple shear flow: a numerical study. Journal of Structural Geology 27, 2171–2180.

- Masuda, T., Ando, S., 1988. Viscous flow around rigid spherical body a hydrodynamical approach. Tectonophysics 148, 337–346.

- Masuda, T., Mizuno, N., 1995. Deflection of pure shear viscous flow around a rigid spherical body. Journal of Structural Geology 17, 1615–1620.

- Masuda, T., Mizuno, N., 1996a. Deflection of non-Newtonian simple shear flow around a rigid cylindrical body by the Finite Element Method. Journal of Structural Geology 18, 1089–1100.

- Masuda, T., Mizuno, N., 1996b. Computer modelling of mantled porphyroclasts in Newtonian and non-Newtonian simple shear viscous flows. Journal of Structural Geology 18, 1487–1491.

- Masuda, T., Mochizuki, S., 1989. Development of snowball structure: numerical simulation of inclusion trails during synkinematic porphyroblast growth in metamorphic rocks. Tectonophysics 170, 141–150.

- Masuda, T., Michibayashi, K., Ohta, H., 1995. Shape preferred orientation of rigid particles in a viscous matrix: re-evaluation to determine kinematic parameters of ductile deformation. Journal of Structural Geology 17, 115–129.

- Michibayashi, K., Mainprice, D., 2004. The role of pre-existing mechanical anisotropy on shear zone development within oceanic mantle lithosphere: an example from the Oman ophiolite. Journal of Petrology 45, 405–414.

- Mulchrone, K.F., 2007. An analytical solution in 2D for the motion of rigid elliptical particles with a slipping interface under a general deformation. Journal of Structural Geology 29, 950–960.

- Muskhelishvili, N.I., 1953. Some Basic Problems of the Mathematical Theory of Elasticity. Noordhoff, Groningen . 704 pp.

- Passchier, C.W., 1987. Stable positions of rigid objects in non-coaxial flow — a study in vorticity analysis. Journal of Structural Geology 9, 679–690.

- Passchier, C.W., 1994. Mixing in flow perturbations: a model for development of mantle porphyroclasts in mylonites. Journal of Structural Geology 16, 733–736.

- Passchier, C.W., Simpson, C., 1986. Porphyroclast systems as kinematic indicators. Journal of Structural Geology 8, 831–843.

- Passchier, C.W., Trouw, R.A.J., 2005. Microtectonics, 2nd enlarged edition. Springer Verlag, Berlin.

- Passchier, C.W., Trouw, R.A.J., Zwart, H.J., Vissers, R.L.M., 1992. Porphyroblast rotation: eppur si muove? Journal of Metamorphic Geology 10, 283–294.

- Passchier, C.W., ten Brink, C.E., Bons, P.D., Sokoutis, D., 1993. δ -objects as a gauge for stress sensitivity of strain rate inmylonites. Earth and Planetary Science Letters 120, 239–245.

- Pennacchioni, G., Fasolo, L., Cecchi, M.M., Salasnich, L., 2000. Finite-element modelling of simple shear flow in Newtonian and non-Newtonian fluids around a circular rigid particle. Journal of Structural Geology 22, 683–692.

- Pennacchioni, G., Di Toro, G., Mancktelow, N.S., 2001. Strain insensitive preferred orientation of porphyroblasts in Mont Mary mylonites. Journal of Structural Geology 23, 1281–1298.

- Piazolo, S., Bons, P.D., Jessell, M.W., Evans, L., Passchier, C.W., 2002. Dominance of microstructural processes and their effect on microstructural development; insights from numerical modelling of dynamic recrystallization. Geological Society of London Special Publication 200, 149–170.

- Piazolo, S., Jessell, M.W., Bons, P.D., Evans, L., Becker, J.K., 2010. Numerical simulations of microstructures using the Elle platform: a modern research and teaching tool. Journal of the Geological Society of India 75, 110–127.

- Ramsay, J.G., Huber, M.I., 1983. The Techniques of Modern Structural Geology, vol. 1: Strain Analysis. Academic Press, London.

- Ramsay, J.G., Huber, M.I., 1987. The Techniques of Modern Structural Geology, vol. 2: Folds and Fractures. Academic Press, London.

- Ramsay, J.G., Lisle, R.J., 2000. The Techniques of Modern Structural Geology, vol 3: Applications of Continuum Mechanics in Structural Geology. Academic Press, London.

- Reche Estrada, J., Martinez, F.J., 2002. Evolution of bulk composition, mineralogy, strain style and fluid flow during an HT–LP metamorphic event: sillimanite zone of the Catalan Coastal Ranges Variscan basement, NE Iberia. Tectonophysics 348, 111–134.

- Reed, L.J., Tryggvason, E., 1974. Preferred orientations of rigid particles in a viscous matrix deformed by pure shear and simple shear. Tectonophysics 24, 85–98.

- Robyr, M., Carlson, W.D., Passchier, C., Vonlanthen, P., 2009. Microstructural, chemical and textural records during growth of snowball garnet. Journal of Metamorphic Geology 27, 423–437.

- Rosenfeld, J.L., 1970. Rotated garnets in metamorphic rocks. Special Paper of the Geological Society of America 129.

- Samanta, S.K., Mandal, N., Chakraborty, C., Majumder, K., 2002a. Simulation of inclusion trail patterns within rotating synkinematic porphyroblasts. Computers and Geosciences 28, 297–308.

- Samanta, S.K., Mandal, N., Chakraborty, C., 2002b. Development of structures under the influence of heterogeneous flow field around rigid inclusions: insights from theoretical and numerical models. Earth-Science Reviews 58, 85–119.

- Samanta, S.K., Mandal, N., Chakraborty, C., 2003. Flow patterns around rigid inclusions in a multiple inclusion system undergoing bulk simple shear deformation. Journal of Structural Geology 25, 209–221.

- Sanislav, I.V., 2010. Porphyroblast rotation and strain localization: debate settled!: COMMENT. Geology 38, e204.

- Schmid, D.W., 2005. Rigid polygons in shear. Geological Society of London Special Publications 245, 421–431.

- Schmid, D.W., Podladchikov, Y.Y., 2004. Are isolated stable rigid clasts in shear zones equivalent to voids? Tectonophysics 384, 233–242.

- Schmid, D.W., Podladchikov, Y.Y., 2005. Manteld porphyroclast gauges. Journal of Structural Geology 27, 571–585.

- Schoneveld, C., 1977. A study of some typical inclusion patterns in strongly paracrystalline rotated garnets. Tectonophysics 39, 453–471.

- Spiess, R., Peruzzo, L., Prior, D.J., Wheeler, J., 2001. Development of garnet porphyroblasts by multiple nucleation, coalescence and boundary misorientation-driven rotations. Journal of Metamorphic Geology 19, 269–290.

- Stallard, A., Hickey, K., 2001. Fold mechanisms in the Canton Schist: constraints on the contribution of flexural flow. Journal of Structural Geology 23, 1865–1881.

- Stallard, A., Ikei, H., Masuda, T., 2002. Numerical simulations of spiral-shaped inclusion trails: can 3D distinguish between end-member models of spiral formation? Journal of Metamorphic Geology 20, 801–812.

- Taborda, R., Antunes, J., Marques, F.O., 2004. 2-D rotation behavior of a rigid ellipse in confined viscous simple shear: numerical experiments using FEM. Tectonophysics 379, 127–137.

- Takeda, Y.-T., Griera, A., 2006. Rheological and kinematical responses to flow of two phase rocks. Tectonophysics 427, 95–114.

- ten Brink, C.E., Passchier, C.W., 1995. Modelling of mantled porphyroclasts using non-Newtonian rock analogue materials. Journal of Structural Geology 17, 131–146.

- ten Grotenhius, S., 2001. Mica fish in mylonites: deformation mechanisms and implications for rheology. PhD thesis, University of Mainz.

- ten Grotenhuis, S.M., Passchier, C.W., Bons, P.D., 2002. The influence of strain localisation on the rotation behaviour of rigid objects in experimental shear zones. Journal of Structural Geology 24, 485–499.

- ten Grotenhuis, S.M., Trouw, R.A.J., Passchier, C.W., 2003. Evolution of mica fish in mylonitic rocks. Tectonophysics 372, 1–21.

- Tenczer, V., Stüwe, K., Barr, T., 2001. Pressure anomalies around cylindrical objects in simple shear. Journal of Structural Geology 23, 777–788.

- Toimil, N.C., Griera, A., 2007. Influence of viscosity contrast and anisotropy on strain accommodation in competent layers. Journal of Structural Geology 29, 787–801.

- Tommasi, A., Knoll, M., Vauchez, A., Signorelli, J., Thoraval, C., Loge, R., 2009. Structural reactivation in plate tectonics controlled by olivine crystals anisotropy. Nature Geoscience 2, 423–427.

- Treagus, S.H., 1997. Deformation partitioning in folds: implications for fold geometry and cleavage patterns. In: Sengupta, S. (Ed.), Evolution of Geological Structures in Micro- to Macro-Scales. Chapman & Hall, London, pp. 341–372.

- Treagus, S.H., Lan, L., 2000. Pure shear deformation of square objects, and applications to geological strain analysis. Journal of Structural Geology 22, 105–122.

- Treagus, S.H., Lan, L., 2003. Simple shear of deformable square objects. Journal of Structural Geology 25, 1993–2003.

- Treagus, S.H., Lan, L., 2004. Deformation of square objects and boudins. Journal of Structural Geology 26, 1361–1376.

- Vernon, R.H., 1978. Porphyroblast–matrix microstructural relationships in deformed metamorphic rocks. Geologische Rundschau 67, 288–305.

- Vernon, R.H., 2004. A Practical Guide to Rock Microstructures. Cambridge University Press, Cambridge.

- Williams, P.F., Jiang, D., 1999. Rotating garnets. Journal of Metamorphic Geology 17, 367–378.

- Wilson, M.R., 1971. On syntectonic porphyroblast growth. Tectonophysics 11, 239–260.

- Wilson, C.J.L., Evans, L., Delle Piane, C., 2009. Modelling of porphyroclasts in simple shear and the role of stress variations at grain boundaries. Journal of Structural Geology 31, 1350–1364.

- Zwart, H.J., 1960. The chronological succession of folding and metamorphism in the central Pyrenees. Geologische Rundschau 50, 203–218.

- Zwart, H.J., 1962. On the determination of polymetamorphic mineral associations and its application to the Bosost area (Central Pyrenees). Geologische Rundschau 52, 38–65.

Chapter 9

The effect of dynamic recrystallisation on the rheology and microstructures of partially molten rocks

Anne-Céline Ganzhorn[a,b,c,d,e], **Maria-Gema Llorens[f,g]**, Enrique Gomez-Rivas[h], Jens Roessiger[f], Loic Labrousse[a,b], Nico P. Walte[i] and Paul D. Bons[f]

[a]UPMC Université Paris 06, UMR 7193, ISTeP, F-75005 Paris, France

[b]CNRS, UMR 7193, ISTeP, F-75005 Paris, France

[c]Université d'Orléans, UMR 7327, ISTO, F-45071 Orleans, France

[d]CNRS/INSU, UMR 7327, ISTO, F-45071 Orleans, France

[e]BRGM, ISTO, UMR 7327, F-45071 Orleans, France

[f]Departament of Geosciences, Eberhard Karls University Tübingen, Wilhemstr. 56, 72074 Tübingen, Germany

[g]Alfred Wegener Institute for Polar and Marine Research, Bremerhaven, Germany

[h]School of Geosciences, King's College, University of Aberdeen, AB24 3UE Aberdeen, United Kingdom

[i]Bayerisches Geoinstitut, Universität Bayreuth, Bayreuth, Germany

Abstract

21 simple shear numerical experiments on two-phase linear viscous material are used to investigate the mechanical behaviour of geological two-phase aggregates. The first phase has a high viscosity (representing a solid material) while the second phase is weak, with a lower viscosity (representing melt). These simulations couple, for first time, linear viscous deformation with dynamic recrystallisation induced by grain boundary migration. The aim is to investigate the competition between both processes, and how they affect the mechanical behaviour and resulting microstructures of the deforming material. We systematically vary the relative abundance of melt, the viscosity contrast between the two phases, the wetting angle of melt and the ratio of dynamic recrystallisation vs deformation. The amount of dynamic recrystallisation and the wetting angle of the melt phase have a first order impact on the deformational behaviour of the. Additionally, the relative abundance of melt and its viscosity contrast with respect to the solid phase have a more limited influence on the resulting microstructures and mechanical behaviour. At low wetting angles (30° or 60°) a connected network of elongated melt pockets develops. This network tends to form perpendicular to the shear plane in models with a high degree of dynamic recrystallisation, and oblique to it in cases where viscous deformation dominates over dynamic recrystallisation. On the contrary, melt connectivity is significantly lower in models with melt pockets with a high wetting angle (173°) and a high degree of dynamic recrystallisation. In these situations, the initial round melt pockets merge into fewer ones but preserve their original round shape. Pockets in models with high wetting angles tend to become ellipsoidal when the degree of dynamic recrystallisation is low. The numerical results allow defining two regimes, depending on the relative balance between viscous deformation and grain boundary migration: (1) a deformation-dominated regime at high strain rates (i.e. low ratio of recrystallisation vs viscous deformation) and (2) a recrystallisation-dominated regime at low strain rates (i.e. high ratio of recrystallisation vs viscous deformation). The first case results in systems bearing large and connected melt pockets where their viscous deformation controls the deformation of the aggregate, while disconnected and smaller melt pockets develop in models where dynamic recrystallisation dominates.

Keywords

9.1 Introduction

Partial melting and subsequent melt transport are processes of primary importance for differentiation in the Earth, from core-mantle separation (Stevenson, 1990, Rubie et al., 2007, Wood et al., 2006) to differentiation within the mantle and crust (Vielzeuf et al., 1990; Rudnick, 1995). Partial melting in the crust also has a strong effect on the strength of the lithosphere, since it reduces it. Such a weakening effect has been considered a key process in the exhumation of ultra-high pressure (UHP) rocks during continental subduction (Whitney et al., 2009; Labrousse et al., 2011) and in syn- to late-orogenic ductile flow of the lower crust in mature collision zones (Hollister and Crawford, 1986; Teyssier and Whitney, 2002).

The weakening effect of partial melting (ω) is mostly due to the addition of melt, because it has a very low strength compared to that of the solid, and the bulk strength is an integral of the strengths of the different material phases. Takeda and Obata (2003) argue that the viscosity (η) of a partially molten rock decreases steadily with increasing melt fraction (ϕ). This can be described with an exponential law:

$$\frac{\eta_{(\phi)}}{\eta_{(\phi=0)}} = exp(-\lambda\phi)$$

(9.1)

The parameter λ depends on the wetting angle and was found to range between $\sim$21 and $\sim$32 for olivine with MORB ($\omega\sim$30°; Mei et al., 2002; Scott and Kohlstedt, 2006) and to be $\sim$4 for olivine bearing a metallic melt phase (ω>60°; Hustoft et al., 2007). In the latter case the low value of λ is partly associated with the compact shape of high-wetting angle melt pockets that reduces their effect on the rock's bulk strength. The weakening effect is not only restricted to rocks containing melt, but also applies to materials bearing a second phase with a relatively lower viscosity, such as air bubbles within polar or glacial ice.

The spatial distribution and, in particular, the connectivity of melt, is one of the main parameters controlling the effective weakening of partially molten rocks, especially when the melt fraction in the rock is relatively low (Cooper and Kohlstedt, 1984; Rosenberg and Handy, 2005; Kohlstedt and Holtzman, 2009). Indeed, for a given amount of melt a rock containing connected melt pockets (e.g. in sheet-like lenses) is significantly weaker than a rock in which pockets are isolated (Bons and Cox, 1994). The equilibrium distribution of melt in a non-deforming aggregate is controlled by the dihedral angle, which is also called the wetting angle (Bulau et al., 1979; Walte et al., 2003). The wetting angle (ω) is the equilibrium angle between two solid-melt (SM) boundaries and a solid-solid (SS) boundary (see Table 9.1 for the list of symbols used). This angle is determined by the relative magnitudes of the SM and SS surface energies (J) through:

$$\omega = 2\cos^{-1}(J_{SS}/2J_{SM})$$

(9.2)

Partially molten silicate rocks typically have low wetting angles, which are assumed to be around 30° (see review in Laporte et al., 1997), whereas Fe-Ni-rich melt in olivine or perovskite aggregates have higher values (between 60° and 130°; see Terasaki et al., 2009). Air bubbles in glacial or polar ice are close to spherical, and therefore have $\omega \sim 180°$ (Roessiger et al., 2011; Azuma et al., 2012; Faria et al., 2014).

Deformation perturbs the distribution of melt by changing the shape of a volume of rock, and hence the shape of melt pockets. Moreover, a composite anisotropy can develop and or be enhanced when two phases are present. Viscous deformation tends to deform melt pockets more than solid grains in the absence of other processes, since melt is the weakest of the two phases (e.g. Jessell et al. 2009). This would result in characteristic microstructures with a certain melt pocket distribution and connectivity, which in turn would translate into a specific bulk rheology. However, the shape of solid grains and melt pockets can be constantly modified by recrystallisation processes. One of the main ones is grain boundary migration (GBM), which is driven by surface energy and variations in strain energy (Urai et al., 1986; Walte et al., 2003). The resulting shape of melt pockets and their distribution within a deforming partially molten rock thus depend on the competition between deformation and grain boundary migration (Groebner and Kohlstedt, 2006; Walte et al., 2011). In the absence of viscous deformation, melt distribution will achieve a dynamic equilibrium that is controlled by surface energies of the interfaces between the various phases in the rock (Bulau et al., 1979; Alley and Fitzpatrick, 1999; Walte et al., 2003). This state of equilibrium can be disturbed if the rock is being deformed as a consequence of external loading. Experiments demonstrate that viscous deformation changes the shape of melt pockets, altering their distribution and potentially creating new structures such as melt-rich shear bands or fractures (Rushmer, 1995; Holtzman et al., 2003; Katz et al., 2006). Recovery from such disturbances of the equilibrium state is a time-dependent process. There are two regimes depending on the competition between viscous deformation and recrystallisation: (1) melt distribution is controlled by deformation at high strain rates and in systems with large grain sizes (resulting in a deformation-dominated regime) and (2) it is determined by surface tension and recrystallisation at low strain rates and in rocks with small grain sizes, causing a high solid-melt boundary curvature (leading towards a recrystallisation-dominated regime; Groebner and Kohlstedt, 2006; Walte et al., 2011). Therefore, caution must be taken when extrapolating experimental results to natural deformation conditions, since strain rates in experiments usually exceed natural ones by several orders of magnitude. This means that both natural and dynamically-scaled experimental strain rates and the amount of dynamic recrystallisation must be in balance in order to have comparable results, in a way that both fall in the same regime (see discussion in Walte et al., 2011). This limitation of laboratory experiments can be overcome by performing numerical simulations, which allow investigating the rheological and microstructural behaviour of partially molten rocks in all

the spectra covering both regimes, because both length and time scales can be varied at will.

In this study we use numerical modelling to investigate the microstructural and mechanical evolution of aggregates of solid grains with small (≤20%) percentages of low-viscosity melt, distributed in pockets between grains. Our two-phase simple shear simulations are based on the methods and models presented in Jessell et al. (2009), but incorporate dynamic recrystallisation by grain boundary migration as a key process. These two processes are numerically coupled for first time, allowing the systematic study of the mechanical behaviour of partially molten rocks in both recrystallisation- and deformation-dominated systems. We explore and compare systems with different melt fractions, dynamic recrystallisation vs. deformation ratios and wetting angles. Although this work is primarily focused on partially molten rocks with low to moderate wetting angles (30° and 60°), we also include simulations of rocks with wetting angles of ∼173°. The latter would apply to air bubbles in ice, in which case one should read "air" for melt or to sulfure-poor Fe-Ni metal alloys in olivine or perovskite, in which case one should read "sulfure-poor Fe-Ni metal alloy" for melt.

9.2 Methods and experimental setup

Table 9.1: Symbols used in this study.

Symbol	Explanation
Parameters used in the experiments:	
m	viscosity contrast (η_{solid}/η_{melt}) [-]
N_{GBM}	number of *GBM* steps per deformation step [-]
ϕ	melt fraction [%]
ω	wetting angle [°]
α_M	angle between long axis of melt pocket and horizontal shear plane [°]
R_M	ratio between long and short axis of best-fit ellipse to melt pocket [-]
N	melt pocket number [-]
Parameters linked to rheological laws:	
γ, $\dot{\gamma}$, $\Delta\gamma$	shear strain [-], shear strain rate [s^{-1}], incremental shear strain [-]
η	viscosity [Pa·s]
τ	deviatoric stress tensor [Pa]
$\Delta\tau$	bulk differential stress of aggregate (difference between maximum and minimum deviatoric stress) [Pa]
λ	wetting-angle dependent constant in exponential strength law [-]
B	constant of the power law (Eq. (9.6)) [-]
n	stress exponent (Eq. (9.6)) [-]

Table 9.1 – continued from previous page

Symbol	Explanation
Parameters used for grain boundary migration:	
a	"compressibility" parameter in Eq. (9.4) [-]
A	area of melt region [m^2]
A_0	equilibrium area of melt region [m^2]
E	energy [J]
J	surface energy [J/m^2]
M	boundary mobility [m/Pa·s]
t	time [s]
X	position vector [m]
σ	driving stress for grain boundary migration [Pa/m2]
Parameters used for scaling:	
P_{th}, P_{kin}	dimensionless thermodynamic and kinematic scaling parameter, respectively (eqs. 9.6, 9.7)
r	melt pocket radius [m]
D	melt pocket diameter [m]
k	"growth" parameter (Eq. (9.9)) [-]
Subscripts:	
M	melt
S	solid

9.2.1 The numerical model

The numerical simulation platform ELLE (Jessell et al., 2001; Bons et al., 2008), including the non-linear viscous deformation 2D finite-element code BASIL (Barr and Houseman, 1996), is used to study the microstructural and mechanical evolution of aggregates of solid grains (referred to as "solid") with a low-viscosity second phase, referred to as "melt". ELLE is an open-source software platform that provides a generalised framework for the numerical simulation of microstructure evolution during geological processes such as deformation and metamorphism. It allows coupling different processes acting on the microstructure in a sequential order for small time steps (Jessell et al., 2001). ELLE has been applied to a range of problems in geology (Bons et al., 2008), of which the ones most relevant to this study are simulations of static and dynamic grain boundary migration in single and two-phase materials (Bons et al., 2001; Becker et al., 2004; 2008; Roessiger et al., 2011; 2014) and viscous or viscoplastic deformation (Bons et al., 1997; Jessell et al., 2005; 2009; Griera et al., 2011; 2013; Llorens et al., 2013a; 2013b). Jessell et al. (2009) carried out a series of deformation simulations of two-phase aggregates up to relatively high shear strains. They showed that interactions between regions with different viscosities lead

to a variety of deformation patterns, including shear bands or elongated soft inclusions, depending on composition, viscosity contrast and the non-linearity of the viscosities. These authors did not include the effect of grain boundary migration on the microstructure evolution, although it is expected that this is a fundamental control especially at low strain rates. The effect of grain boundary migration is therefore incorporated in this study, together with a mechanical analysis of the deforming media, not yet included in Jessell et al. (2009).

9.2.2 Definition of the aggregate

The microstructure is defined in ELLE by a set of polygons in a two-dimensional section of the modelled material. Polygons are defined by a network of boundary nodes (bnodes) that are connected by straight segments (Fig. 9.1a). The solid grains and melt pocket regions are defined by polygons with a constant viscosity, which is high for solid and low for melt polygons. Therefore, there three types of boundaries are in the model, each with different properties: (1) solid-solid, (2) solid-melt and (3) melt-melt. The latter has no physical meaning and has no effect on the microstructural evolution, but has to be used in the models in order to maintain the polygon topology.

ELLE uses both horizontally and vertically wrapping boundaries, so that the upper and lower parts of the model are connected, as well as the left and right ones (Fig. 9.1a; Jessell et al., 2001). This makes the model periodic in all directions, and has the advantage that the unit cell remains square through deformation in simple shear. Regions that fall out of the square bounding box can be repositioned within the box after each calculation step. This approach considerably reduces boundary effects and facilitates visualisation of the deformation structures, even at very high shear strains.

The initial microstructure for all simulations is an isotropic aggregate consisting of solid grains and melt pockets created from a foam texture of solid grains. Melt polygons are inserted at all triple junctions between the grain of the foam texture. Their initial size is determined by the imposed melt fraction (ϕ), which is set at 5, 10, 12 and 20% (see Table 9.2 for experimental settings). The aggregate is then equilibrated by static grain boundary migration (described in section 9.2.4) until all melt pockets reach the desired wetting angle (i.e. ω=30°, 60° or 173°; Fig. 9.1 and Table 9.2).

9.2.3 Finite element viscous deformation

The finite-element software BASIL calculates non-linear viscous deformation in plane strain, computing viscous strain rates and the associated stress fields for different boundary conditions. The numerical algorithm used by BASIL within ELLE is extensively described in Bons et al., (2008) and Jessell et al., (2009). At each deformation step, all polygons are divided into triangles using a Delaunay triangulation. BASIL then calculates the stress
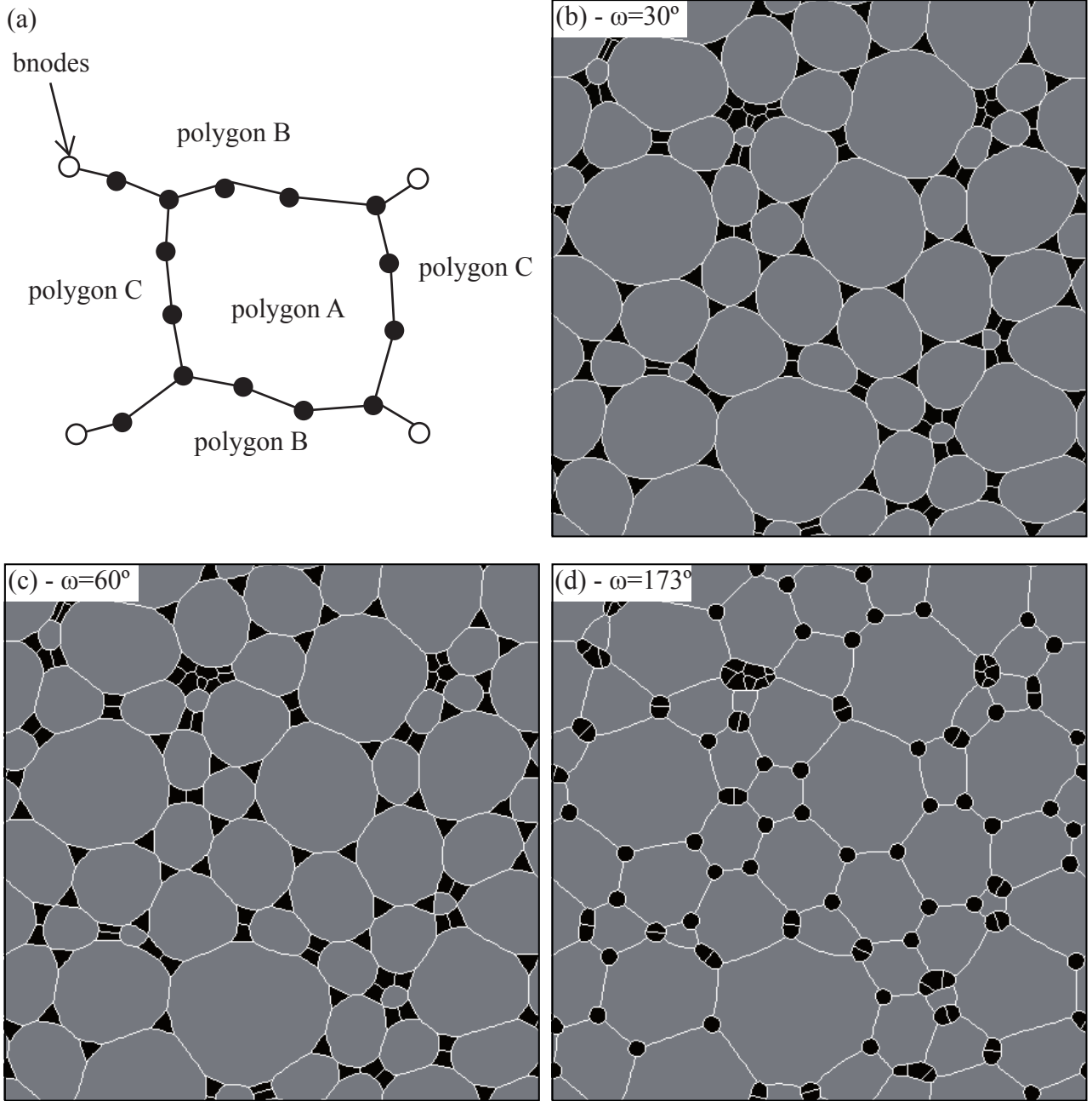
Figure 9.1: Initial microstructures: (a) polygons are defined by boundary nodes (*bnodes*) that are connected by straight boundary segments. (b-d) different starting microstructures for the three wetting angles (ϕ=10%). Solid grains are shown in grey, melt is displayed in black and polygon boundaries in white.

and strain rate fields that maintain compatibility between the mesh triangles according to the applied stress and velocity boundary conditions. In our simulations we use the following linear constitutive law for the relationship between deviatoric stress (τ) and strain rate (*gamma*), with a viscosity (η):

$$\tau = \eta\dot{\gamma} \tag{9.3}$$

All simulations are carried out in simple shear. Horizontal dextral simple shear is

Simulation	Viscosity ratio (m)	Wetting angle (ω)	Melt fraction (ϕ)	N_{GBM}
1	12.5	30°	10%	0
2	25	30°	10%	0
3	50	30°	10%	0
4	100	30°	10%	0
5	50	30°	5%	0
6	50	30°	12%	0
7	50	30°	20%	0
8	100	30°	5%	0
9	100	30°	12%	0
10	100	30°	20%	0
11	50	60°	12%	0
12	50	173°	12%	0
13	50	30°	12%	1
14	50	60°	12%	1
15	50	173°	12%	1
16	50	30°	12%	10
17	50	60°	12%	10
18	50	173°	12%	10
19	50	30°	12%	100
20	50	60°	12%	100
21	5	173°	12%	100

Table 9.2: Experiment name related to used parameters

applied to the top and bottom of the square model in incremental steps of γ=0.025 of shear strain. Normal stress conditions are applied to the lateral boundaries, ensuring that velocities on the left and right boundary are identical, to maintain lateral wrapping. The velocity conditions at the top and bottom boundaries cause a systematic error by suppressing vertical velocities at these boundaries. Taking advantage of the vertical wrapping of the model geometry, we use an algorithm to apply these boundary conditions at a different random level each step. This routine significantly reduces the inevitable influence of boundary conditions and spreads it equally throughout the model (Jessell et al., 2009; Llorens et al., 2013a,b). Where possible, experiments are run up to a shear strain of γ=4. However, this strain cannot always be achieved, because extremely stretched melt polygons form in some models thus not allowing numerical convergence.

The viscosity contrasts between melt (η_M) and solid grains (η_S), or air and ice grains, vary over ten orders of magnitude in nature. Such extreme viscosity contrasts are numerically extremely difficult to achieve. Simulations are run with viscosity ratios ($m=\eta_S/\eta_M$) of m=12.5, 25, 50 and 100. From m>25, microstructures do not vary significantly with increasing viscosity contrast (see Section 9.3.1). As high viscosity contrasts are numerically expensive and produce convergence errors, we use m=50 for all the experiments.

Stress and strain rate tensors are calculated for six points in each triangle of the mesh.

From this, the average or bulk stress and strain rates can be calculated and recorded for each deformation increment. The bulk viscosity is derived from the bulk strain rate and stress using Eq. (9.3).

9.2.4   Grain boundary migration (*GBM)*

The grain boundary migration (*GBM*) module used in this study is the one used by Roessiger et al. (2014) to simulate air bubble growth in polar ice and it is based on the free-energy minimisation scheme of Becker et al. (2008), which was designed for the simulation of static *GBM* of partially molten rocks. *GBM* is implemented by moving nodes that define the boundaries of polygons. Every time step (Δt) each single boundary node is moved over a small distance (ΔX) in the direction that minimises the total free energy of the local system. The change in total free energy (ΔE) is set equal to the work of the driving stress (σ) over the distance ΔX.

The total free energy for nodes within solid-solid (*SS*) boundaries is determined by: (1) the length of the two or three segments that connect the node under consideration with its neighbours and (2) the surface energy (J_{SS}) of the segment, which is assumed to be constant for all SS-boundaries. A boundary node will thus move in the direction that reduces the length of the considered segments. Nodes with two neighbour nodes will move to reduce the local curvature of the two segments together, while and those sitting on triple junctions (i.e. with three neighbours) will move towards achieving 120° angles between the segments, which corresponds to the state of minimum energy.

The movement of solid-melt boundaries (*SM*) is slightly more complex, since mass conservation needs to be considered. In this case, a second energy term is included, besides the aforementioned surface energy (J_{SM}) of the segment. This additional term takes into account the changes in solid and melt polygon area caused by a node movement. If a *SM*-node moves into a melt region, the area of this region is reduced by the amount ΔA, while the solid region is expanded by -ΔA. This implies a compression of the melt and a decompression of the solid phase, because the mass of regions are kept constant. This process requires work and a change in the local energy state. The total local energy (E_{tot}) as a function of node position (X) is therefore the sum of the surface energy (E_{surf}, see above) and the area of the melt region ($A_{(X)}$) in relation to the original or equilibrium area (A_0):

$$E_{tot}(X) = E_{surf}(X) + a \left(\frac{A_X - A_0}{A_0} \right)^2 \tag{9.4}$$

where a is a constant, set by the user, which can be regarded as effectively a proxy for the compressibility of the melt. For further details, the reader is referred to Becker et al. (2008) and Roessiger et al. (2014).

Once the driving stress is determined, a node is then moved using:

$$\Delta X = M_{ij}\sigma\Delta t \tag{9.5}$$

where (M_{ij} represents the mobility of the boundary for the (i phases (M_{SS} for solid-solid and M_{SM} for solid-melt boundaries). Surface energies (J_{SS}) and mobilities (M_{SS}) of solid-solid boundaries of minerals are reasonably well constrained, as these can be derived from static grain growth experiments (e.g. Evans et al., 2001). Once the magnitude of J_{SS} is known, J_{SM} can be determined with Eq. (9.2) for a given wetting angle of the solid-melt system. The magnitude of M_{SM} is much less constrained, for which reason we consider here that $M_{SM} = M_{SS}$. To achieve different wetting angles in our simulations, a constant unit J_{SS} is used, and J_{SM} is set at: J_{SM}/J_{SS}=0.52 for ω=30°, J_{SM}/J_{SS}=0.58 for ω =60°, and J_{SM}/J_{SS}=8.00 for ω=173° (cf. Eq. (9.1)). Scaling of the numerical parameters to natural systems is discussed later (Section 9.4).

As migrating boundaries may become longer or shorter during *GBM*, the routine automatically inserts a boundary node when the distance between two neighbour nodes becomes greater than $11 \cdot 10^{-3}$ (with a model size of 1x1) and removes one when its neighbours are closer than $5 \cdot 10^{-3}$ apart. Additionally, the *GBM* code also carries out topological checks in order to keep a consistent model topology. One of these checks consists of removing a polygon when it becomes too small, in order to avoid meshing problems. Another check is a neighbour switch, which takes place when two neighbouring triple junctions approach each other and are less than $5 \cdot 10^{-3}$ apart. In such case, two polygons that were originally neighbours are forced to separate, while the other two associated polygons become neighbours. These changes are crucial for keeping a coherent microstructure, because they allow reorganisation and merging of melt pockets (Roessiger et al., 2014) and remeshing every time step, thus allowing attaining high strains.

9.2.5 Coupling deformation and grain boundary migration

The coupling of deformation and *GBM* is achieved by applying each process in isolation in alternating steps. Strain has a constant incremental value, in a way that strain rate is unscaled if grain size is not prescribed. The *GBM* routine (Section 9.2.4), however, requires to be applied with a proper and small time step size. Thus, we can vary the relative amount of dynamic recrystallisation in the form of *GBM* by keeping the strain increment constant, and vary the number of time steps per deformation step. Therefore, the number of *GBM* steps (N_{GBM}) per strain increment (with constant time $\Delta t(GBM)$) is set to 1, 10 and 100, covering two orders of magnitude in scaled strain rates. A test confirmed that using $\Delta\gamma$=0.00025 and N_{GBM}=1 gives the same results as the combination of $\Delta\gamma$=0.025 and N_{GBM}=100. For comparison, simulations are also run with only deformation, i.e. without *GBM* (N_{GBM}=0), which effectively simulates unscaled strain rate.

9.2.6 Microstructural analysis

The size and shape of melt pockets are determined with the image-analysis software ImageJ (Collins, 2007), at shear strains of γ=1, 2, 3 and 4. To reduce artefacts due to melt pockets truncated by model boundaries, each image is repeated three times both horizontally and vertically to obtain a mosaic of 9 identical images. A best-fit ellipse is determined for each melt pocket, from which the average shape ratio (R_M) is defined as the average of the long and short axis ratios. The average orientation of the main axis (α_M) is defined as the average angle between the horizontal axis (i.e. shear plane) and the long axis of the pockets, measured anticlockwise. Using 3x3 mosaics is sufficient, as control measurements on 4x4 and 5x5 mosaics provide identical results.

9.3 Results

9.3.1 Simulations without grain boundary migration (N_{GBM}=0)

The effect of the viscosity contrast is investigated with different experiments at different viscosity contrasts (m=12.5, 25, 50, 100) for a constant wetting angle of ω=30° and for a constant melt fraction of ϕ=10% without GBM (N_{GBM}=0; experiments 1 to 4, Table 9.2). After a shear strain of γ=2 the number of melt pockets (N=65-66) is almost identical to the initial number (N=68). The mean elongation orientation (α_M) varies between 22.5° and 24° in the four experiments (Fig. 9.2), while their axial ratios (R_M) range between 5.4 (m=50) and 7.4 (m=12.5 and 25, Fig. 9.2). Strength of the aggregate changes with increasing strain, but it is almost identical for the m=50 and m=100 cases (experiments 3, 4, 5 to 7 and 8 to 10; Fig. 9.2e). Up to ϕ=12% it is close to the upper (Voigt) bound, which is the strength of the system if strain rates in both phases are assumed to be identical. Only bulk strengths at ϕ=20% deviate significantly from this bound. As results for the model with m=100 are close to those for m=50, we use m=50 for all other experiments, in order to save computing time and to ensure that high strains are achieved.

The effect of varying the melt fraction is explored by means of four experiments (with melt fractions of ϕ=5%, 10%, 12%, 20%) at a viscosity contrast of m=50, a wetting angle of ω=30° and without GBM (N_{GBM}=0; experiments 3 to 7 in Table 9.2; Fig. 9.3). Melt pockets get stretched, and their elongation varies between R_M=3.8 (ϕ=20) and 6.5 (ϕ=12) at a shear strain of γ=2. In the absence of GBM melt pockets rarely merge and their number slightly decreases with progressive deformation.

The effect of varying the wetting angle is tested with three experiments (ω=30°, 60° and 173°) at m=50 and ϕ=12% and without GBM (N_{GBM}=0; experiments 6, 11 and 12; Table 9.2; Fig. 9.4). The axial ratio (R_M) of melt pockets counter increases from R_M=6.5 at ω=30° to R_M=10.1 at ω=173°. The mean orientation of the long axis, however, only varies slightly around 23°. The number of melt pockets decreases more for
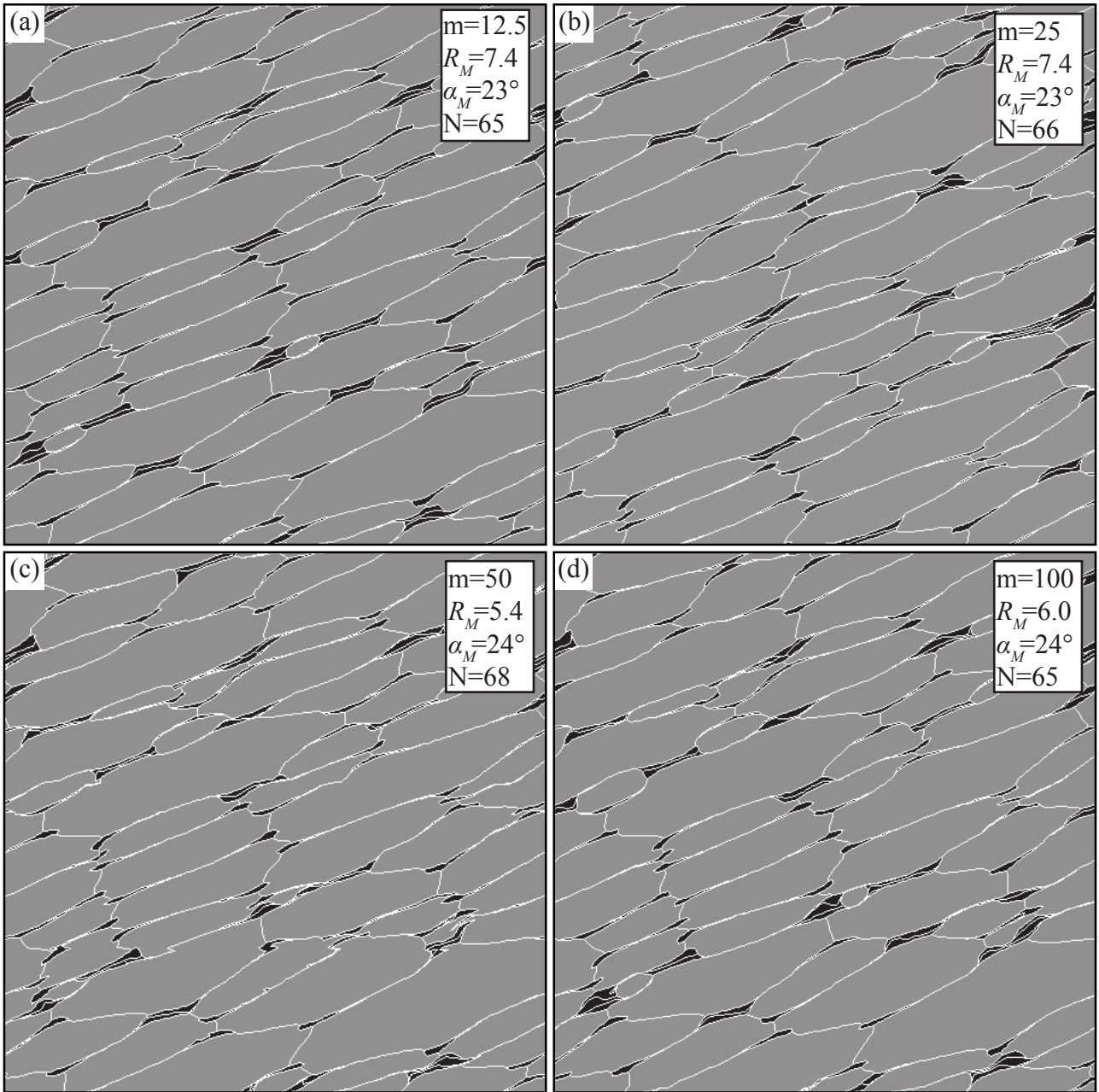
Figure 9.2: Effects of viscosity contrast (m) on the resulting microstructures (a, b, c, d) and on bulk strength (e), for models with viscosity contrast of (a) $m=12.5$, (b) $m=25$, (c) $m=50$, and (d) $m=100$. All images correspond to a dextral shear strain of $\gamma=2$, a wetting angle of $\omega=30°$, a melt fraction $\phi=10$ and for models without GBM ($N_{GBM}=0$). Solid grains are displayed in grey, the melt appears in black and polygon boundaries are shown in white. The bulk strength in (e) is normalised to the strength of the solid. Please check Table 9.1 for the meaning of R_M, α_M and N.
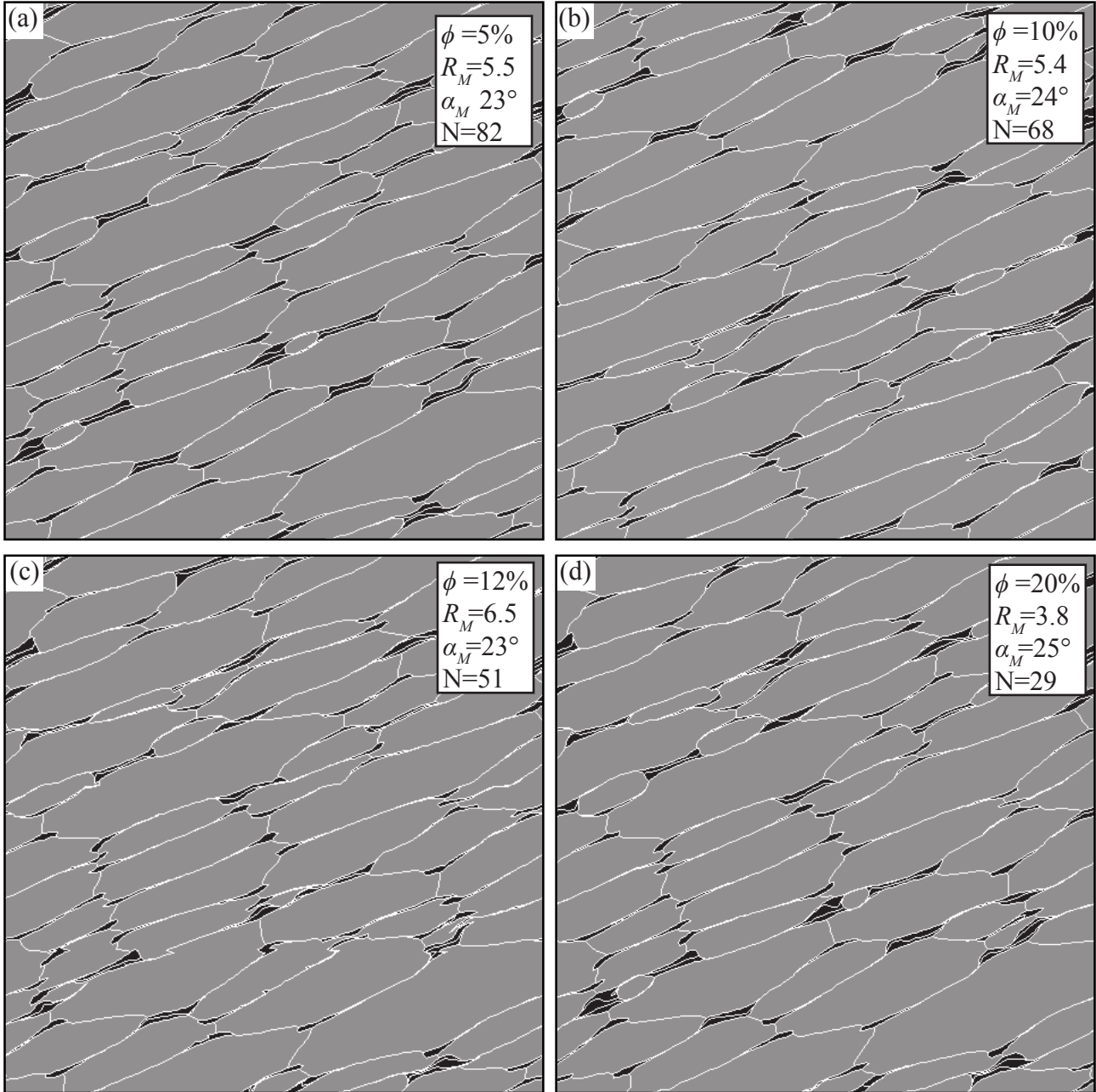
Figure 9.3: Melt distribution at a shear strain of $\gamma=2$, for melt fractions of (a) $\phi=5\%$, (b) 10%, (c) 12% and (d) 20%. All these models do not include *GBM* ($N_{GBM}=0$). The wetting angle and viscosity contrast were kept constant ($\omega=30°$ and $m=50$). Solid grains are shown in grey, melt appears in black and polygon boundaries in white. Please check Table 9.1 for the meaning of R_M, α_M and *N*.
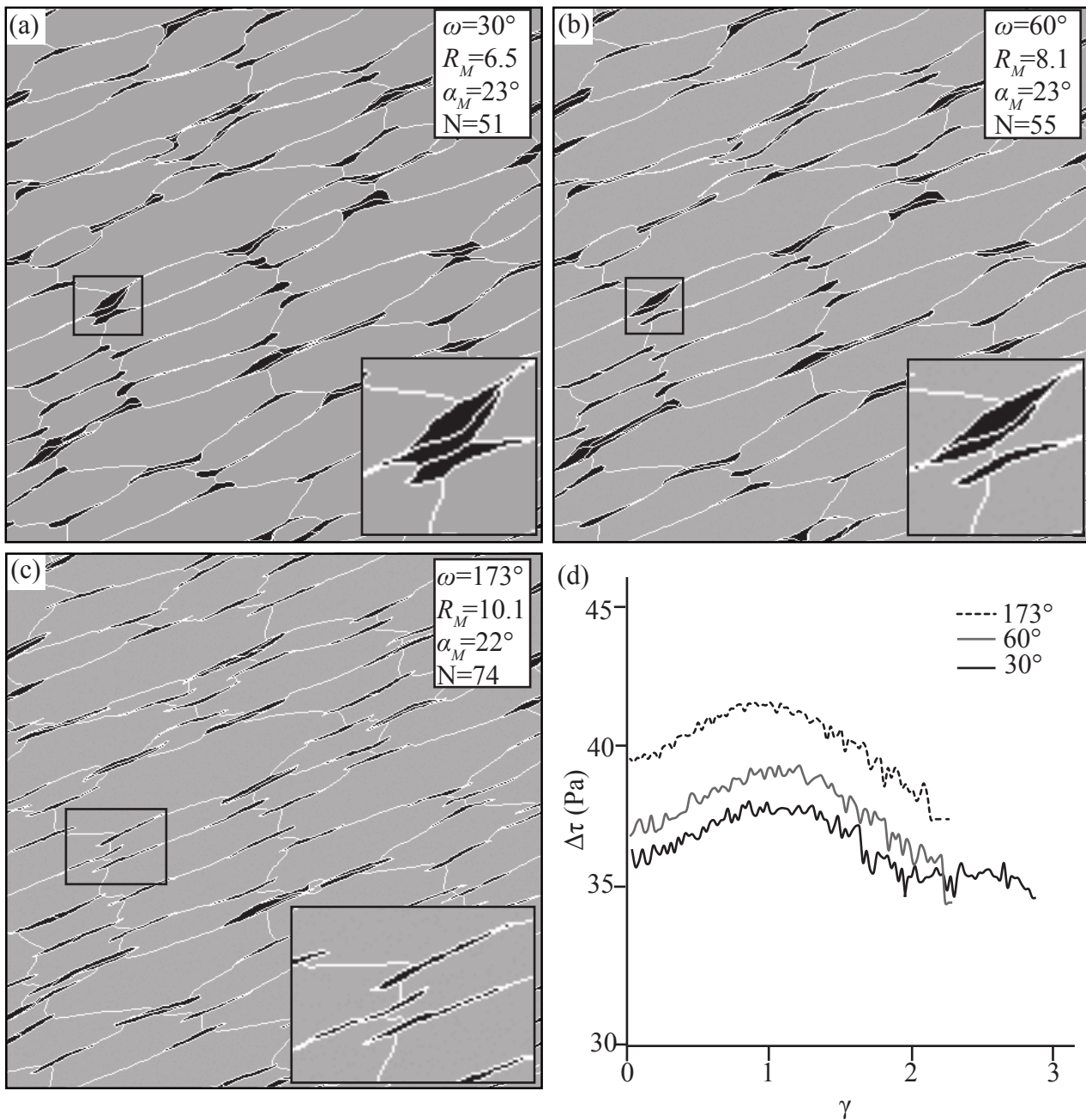
Figure 9.4: Effect of varying the wetting angle on the resulting microstructures (a, b, c) and on the bulk strength (d) for experiments without GBM ($N_{GBM}=0$), at a shear strain of $\gamma=2$. The wetting angles were set to (a) $\omega=30°$, (b) $60°$ and (c) $173°$. The melt fraction ($\phi=12\%$) and the viscosity ratio ($m=50$) were the same for the three experiments. Black squares indicate the position of the close up below the image, showing differences in coalescence behaviour. Solid grains are shown in grey, melt appears in black and polygon boundaries in white. Please check Table 9.1 for the meaning of R_M, α_M and N.

the model with ω=30° (N=51 left at γ=2) than for that with ω=173° (N=74 pockets left). Merging in the direction normal to the shear plane is more common when the wetting angle is low. This explains both the decreasing number of melt pockets with progressive deformation and the lower R_M for models with a low wetting angle (ω=30°) compared to those with ω=173° (Fig. 9.2).

All three experiments show a similar trend of stress-strain curves, with an initial increase in stress (hardening) followed by a decrease (softening) after $\gamma\sim1$ (Fig. 9.2d). The bulk strength rises with increasing wetting angle.

9.3.2   Simulations coupling viscous deformation with grain boundary migration

In the next series of experiments (experiments 13 to 21 of Table 9.2), the viscosity contrast (m) and the melt fraction (ϕ) are fixed (m=50, ϕ=12%), while the wetting angle (ω) and the relative balance of grain boundary migration with respect to viscous deformation are systematically varied (ω= 30, 60 or 173°; N_{GBM}=1, 10 or 100). As explained above, varying the number of GBM steps (N_{GBM}) per deformation step is equivalent to changing the strain rate at which the material is deformed.

9.3.2.1. Experiments with low wetting angles (30 and 60°)

The resulting microstructure for the ω=30° model with N_{GBM}=1 is very similar to that of the experiment without GBM (Figs. 9.4a and 9.5a). Melt pockets are stretched and get connected in the stretching direction, thus forming weak zones oriented at a small angle to the shear plane. Increasing N_{GBM} to 10 causes a dramatic change of the resulting microstructure (Fig. 9.5), since it allows the melt pockets to retain their concave shape, which in turn results in melt pocket merging and associated formation of pockets oriented at high angles with respect to the shear direction (see marked zones in Figs. 9.5d, e, and f). These large melt pools form weak zones that result in antithetic shearing while they rotate clockwise with progressive deformation. This effect is significantly enhanced if GBM is increased to N_{GBM}=100 (Figs. 9.5g and h). GBM causes an increase both in grain and melt pocket size, with the latter being more pronounced as a consequence of pocket merging. The behaviour for ω=60° is very similar to that for ω=30°.

9.3.2.2. Experiment with high wetting angle (ω=173°)

Grain boundary migration has a very strong influence on the resulting microstructures when the wetting angle is high (ω=173°), even for the cases of N_{GBM}=1. This is not surprising as the driving force for GBM, determined by the solid-melt surface energy (J_{SM}), is eight times higher for the ω=173° case than for ω=60°. GBM controls the contraction
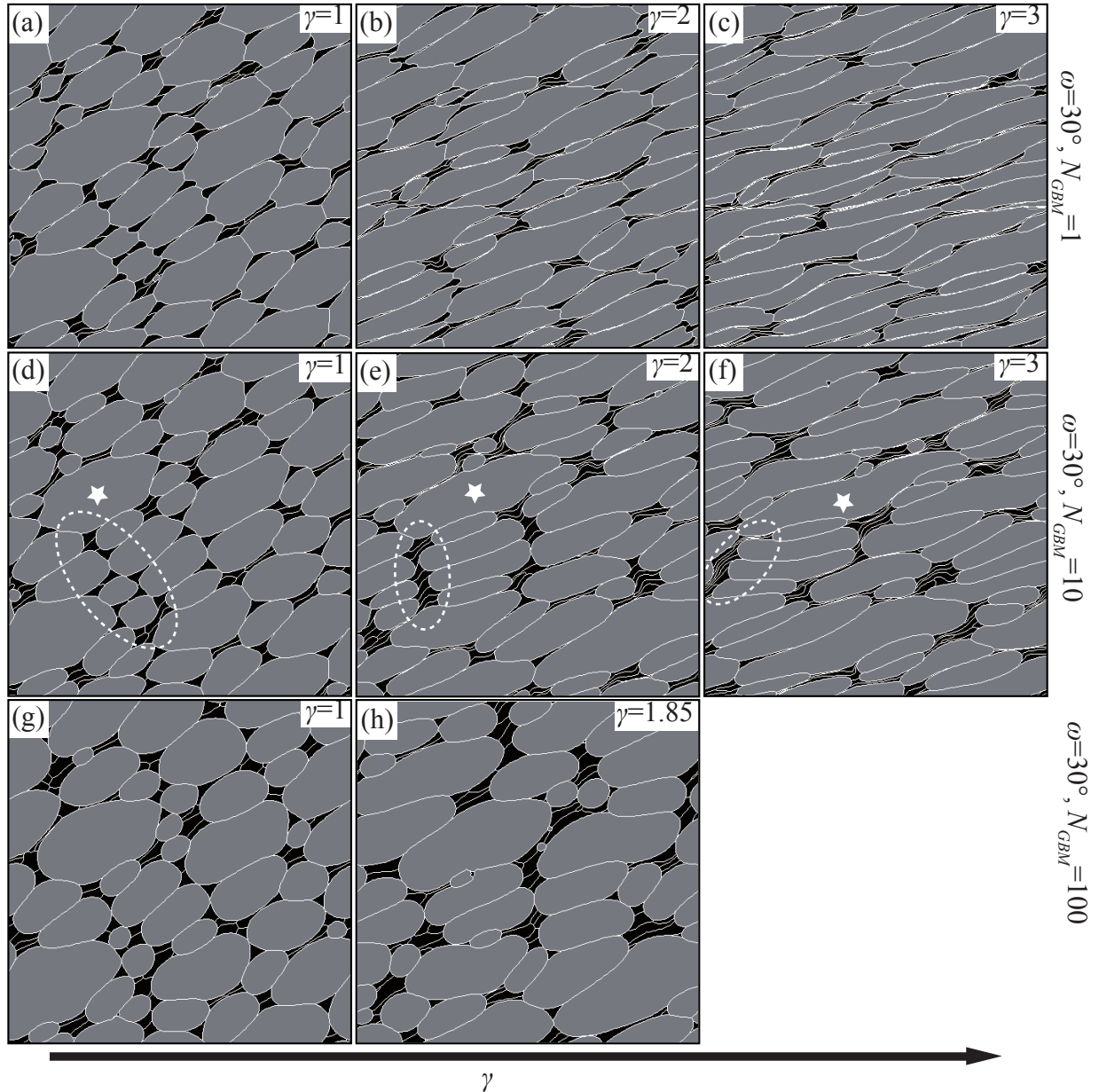
Figure 9.5: Microstructure evolution with increasing shear strain for models with different amounts of grain boundary migration (N_{GBM}). The solid grain marked with a star in figures (d), (e) and (f) is used as a marker to identify the encircled area (dashed white ellipse). These models were run with a viscosity contrast of m=50, A melt fraction ϕ=12 and a wetting angle of ω=30°. Solid grains are shown in grey, melt appears in black and polygon boundaries in white.
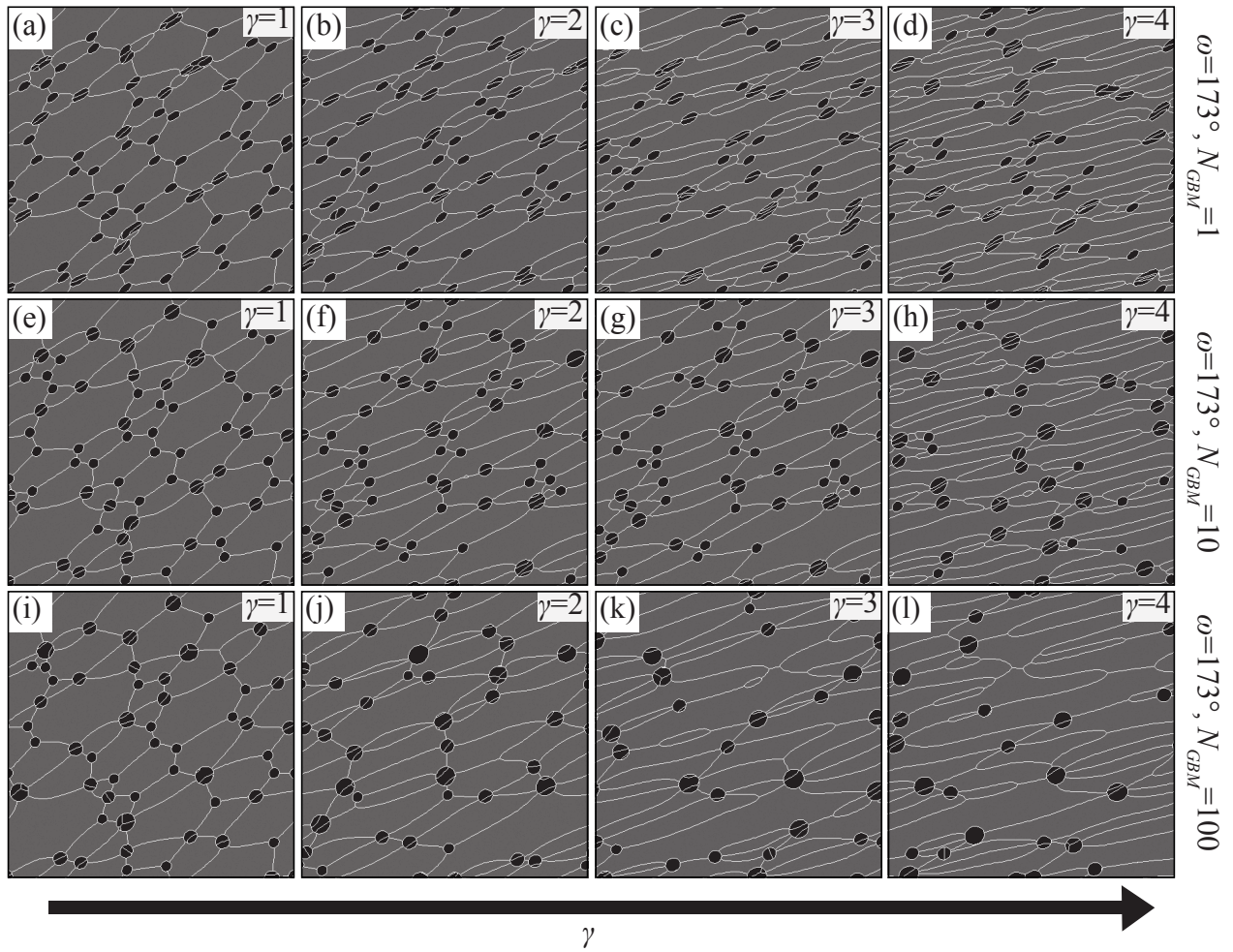
Figure 9.6: Microstructure evolution with increasing deformation for models with different amount of dynamic recrystallisation (N_{GBM}). These models are run with a viscosity contrast of m=50, a melt fraction of ϕ=12 and a wetting angle of ω=173°. Solid grains are shown in grey, melt appears in black and polygon boundaries in white.

of melt pockets and competes with their stretching as a consequence of dextral simple shear. The melt pockets are still elongate in the direction of the XY plane ($R_M \approx 2$) for the experiment with N_{GBM}=1 (experiment 15 in Table 9.2; Figs. 9.6a, b, c and d). When N_{GBM} increases, melt pockets retain an approximately circular shape (Fig. 9.6). Increasing N_{GBM} also leads to melt pocket merging, which results in an increase of both their average size and size distribution (cf. Roessiger et al., 2014).

9.3.2.3. Rheological effects

Bulk shear stress (τ) versus strain (γ) curves evidence an initial increase in γ and a subsequent decrease after a shear strain of γ~1, for models without *GBM* (Fig. 9.4d). When the melt fraction is ϕ=12% this trend becomes independent of the wetting angle. However, the bulk shear stress is ~10% higher for the model with ω=173° compared to that for the experiment with ω =30°. This is probably due to differences in the geometry of melt pockets. The stress-strain evolution can be explained by the increasing stretching of the melt pockets, which is not counteracted by *GBM*. The developing anisotropy weakens the material for shearing parallel to the stretching direction, which is initially oriented at 45° to the shear plane. However, as this direction is approximately perpendicular to the maximum compressive stress, the shear stress needed for horizontal shearing of the anisotropic medium is at first higher than that for the starting material. The shear stress decreases again steadily (after γ~1) once anisotropy has developed enough and has rotated towards the horizontal shear plane (Takeda and Griera, 2006; Dabrowski, 2008).
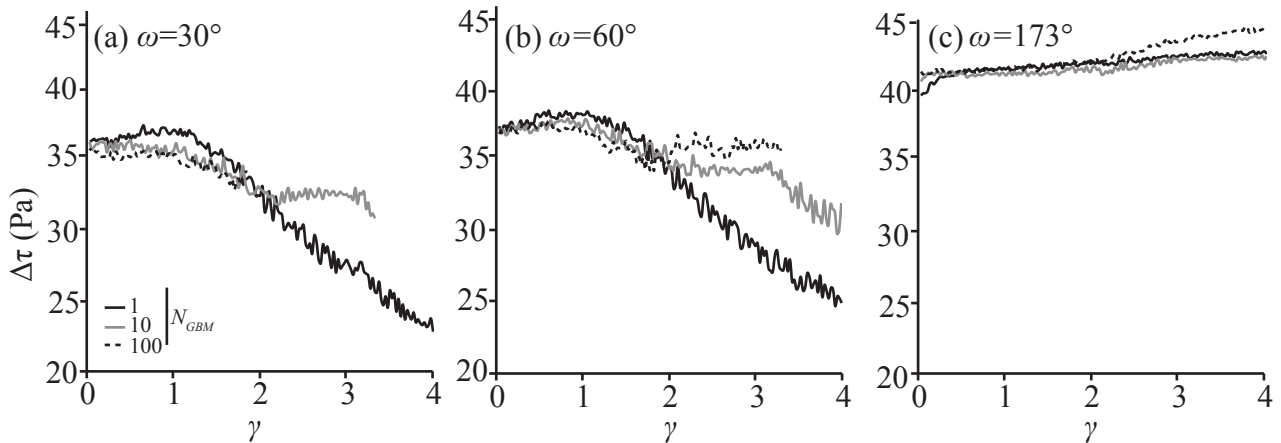
Figure 9.7: Effect of N_{GBM} on the strength of the aggregate for models with the three different wetting angles.

GBM reduces both the initial strain hardening and the subsequent strain softening, as it counteracts the stretching of melt pockets (Fig. 9.7). This is best seen in models with a wetting angle of ω=173°, where the melt pockets remain spherical when $N_{GBM} \geq 10$. The only difference in the microstructures with increasing strain is a change in size and spacing of the melt pockets, which result in a minor strain hardening. At low wetting

angles, the strain-induced change of the microstructure is primarily the merging of melt pockets in elongate pools parallel to the maximum compressive stress, and their subsequent rotation towards the shear direction (Figs. 9.5d, e, and f). This process suppresses the development of weak zones parallel to the finite stretching direction and thus reduces the initial hardening and subsequent softening that is observed when *GBM* is absent.

9.4   Discussion

9.4.1   Model limitations

The experiments described in this paper intentionally ignore a number of factors that in natural systems will complicate matters. Their utility is precisely that they provide a baseline to understand more complex systems and particularly to investigate the effect of coupling two fundamental processes: viscous deformation and dynamic recrystallisation driven by grain boundary migration.

Both solid and melt phases are set up to have a linear viscosity (i.e., the stress exponent (n) is set to 1 in all experiments). This is reasonable for the melt phase, since it can be considered as a Newtonian phase. However, this assumption is more questionable for the solid phase, since using $n>1$ would increase the effective viscosity ratio (a function of strain rate ratio in both phases and spatial distribution) and would probably induce a stronger strain localisation than in the linear case. Jessell et al. (2009) and Llorens et al. (2013a) demonstrated that increasing the stress exponent in experiments without *GBM* has the same effect as increasing the viscosity ratio. In this study, we demonstrated that increasing the viscosity ratio above a value of 50 has a very small influence on the resulting microstructures. Accordingly, we conclude that using stress exponents higher than 1 is not necessary in our simulations. This would not alter the results but will significantly alter calculation time and cause numerical convergence problems.

The effect of the dihedral angle and surface tension on rheology and melt distribution is twofold (Kohlstedt and Holtzman 2009). First, there is a direct effect of surface tension and capillary forces of melt pockets on the melt network ($\omega<60°$) that opposes the change of shape associated with deformation. The differential stress $\Delta\sigma$ must exceed capillary forces of a given melt pocket in order to cause a shape change in the first place. This can be expressed with equation (9.6), which follows the philosophy of a force balance between the differential stress and the surface tension (J_{SM}):

$$P_{th} = \frac{2J_{SM}}{r_M\Delta\sigma} = \frac{2J_{SM}}{r_M B(\dot{\gamma})^{(1/n)}} \tag{9.6}$$

where r is the radius of the melt pocket, B and n are parameters of the power-law equation that relates the differential stress to the strain rate ($\Delta\sigma = B(\dot{\gamma})^{1/n}$) and P_{th} is a non-dimensional parameter. This relation has previously been considered as dominant

for the interplay of deformation with surface tension, and has accordingly been used to interpret and scale experimental results (Groebner and Kohlstedt 2006; Walte et al. 2011). However, a second factor that has previously been largely ignored is the mobility of solid-melt grain boundaries (M_{SM}). Even if D_s is sufficiently high and Eq. (9.6) is fulfilled, the melt distribution (e.g. the melt pocket shape) can only be altered if the mobility of the solid-melt interface is sufficiently high. This mechanism depends on the product of surface tension and mobility and can be expressed by (Eq. (9.7)), which is modified from (Kohlstedt and Holtzman 2009):

$$P_{kin} = \frac{J_{SM} M_{SM}}{r^2 \dot{\gamma}} \tag{9.7}$$

where J_{SM} is the surface energy of a solid-liquid boundary, M_{SM} the mobility of such boundary and r is the radius of the melt pocket. While Eq. (9.6) could be summarised to divide a surface tension–dominated regime from a (differential) stress–dominated regime (cf. Walte et al. 2011), Eq. (9.7) divides a GBM – dominated regime from a strain–dominated regime. However, in order to evaluate whether the melt distribution is altered by deformation, both equations must be fulfilled (Kohlstedt and Holtzman, 2009).

9.4.2 Model scaling

In order to compare our numerical simulations to laboratory experiments or nature, length and time have to be scaled. The presented numerical simulations show that the microstructural and rheological behaviour of the aggregate is determined by the balance between a change of shape of melt pockets induced by deformation and their recovery towards an equilibrium shape produced by grain boundary migration. The first is related to the imposed strain rate, related to the stress associated with the aggregate viscosity, while the latter is controlled by the size of melt pockets and the ability of the solid-melt boundaries to move as a function of surface energy and mobility. Most authors propose a dimensionless thermodynamic scaling parameter (P_{th}) that compares the imposed differential stress (Δs) to the surface energy and the mean melt-pocket radius (r) (Eq. (9.6); Kohlstedt and Holzman, 2009; Walte et al., 2011). The above thermodynamic dimensionless number does not take into account the mobility of solid-liquid boundaries. It is clear from the numerical simulations that these boundaries would only move passively according to the imposed deformation if their mobility is set to zero (cf. Eq. (9.4)). On the contrary, the kinematic dimensionless number (P_{kin}) takes into account this boundary mobility (Eq. (9.7)).

The choice of the two scaling parameters is far from trivial, since they predict very different scaling: P_{th} scales with strain rate to the power $1/n$ and r, while P_{kin} scales with strain rate and r squared. As our numerical model includes grain-boundary mobility, a proper scaling of these experiments can only be achieved by using the kinematic scaling

parameter P_{kin}.
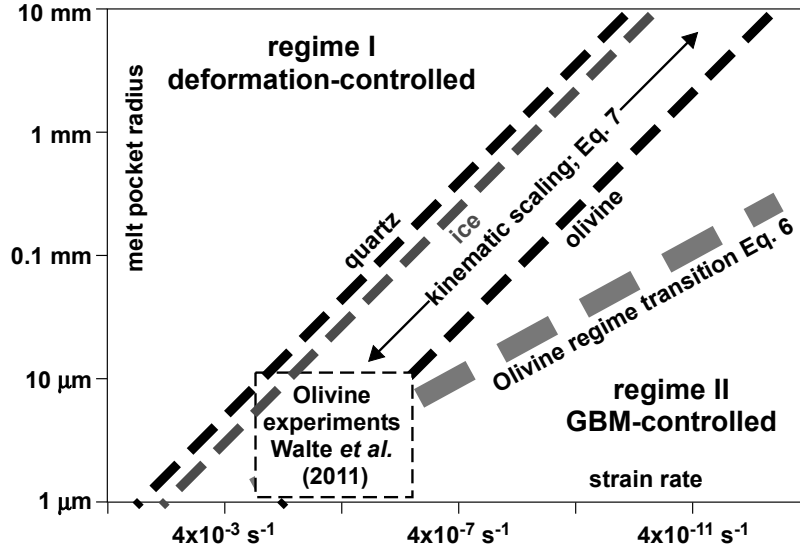
Figure 9.8: Transition between the deformation- and *GBM*-controlled regimes, predicted from the simulations using a kinematic scaling law (Eq. 9.7). Experiments at this transition for olivine + FeS-melt of Walte et al. (2011) are shown, together with the associated transition according to the thermodynamic scaling law (Eq. 9.7).

In order to scale our numerical experiments using P_{kin}, we need to determine the surface energies J_{SM} and J_{SS}. J_{SM} can be determined with relative accuracy using Eq. (9.1) if J_{SS} and the wetting angle are known for the system under consideration (e.g. quartz with granitic melt - Laporte and Watson, 1995). M_{SM} is relatively poorly constrained and will depend on the actual mechanism of migration of solid-melt boundaries, which involved dissolution-precipitation reactions, as well as diffusion (Azuma et al., 2012; Kohlstedt and Holzman, 2009). Here we assume, as in the numerical simulations, that $M_{SM}=M_{SS}$ (M_{SS} being the mobility of solid-solid boundary). The advantage is that the product $J_{SM} \cdot M_{SM}$ can be determined if $J_{SS} \cdot M_{SS}$ and ω are known, through:

$$J_{SM} M_{SM} = 2 \cos(0.5\omega) J_{SS} M_{SS} \qquad (9.8)$$

Natural values of $J_{SS} \cdot M_{SS}$ can be estimated from static grain growth experiments (e.g. Tullis and Yund, 1982). In case of grain growth controlled by the curvature of grain boundaries, the relationship between grain size ($D=2r$) and time (t) is given by (Evans et al., 2001):

$$D^2_{(f)} - D^2_0 = kM\gamma t \qquad (9.9)$$

Here D_0 is the initial grain size (which should be $\ll D(t)$) and k is a dimensionless parameter that depends on the microstructure (Roessiger et al., 2014) and on the number of dimensions of the system. For an equilibrated foam texture $k_{(2D)}=4.48$ and $k_{(3D)}=2$ (Mullins, 1989). The product $J_{SS} \cdot M_{SS}$ for various minerals can thus be calculated

from experimental data, using Eq. (9.8). We used data of Masuda (1997) for quartz at 800-1000°C, Evans et al., (2001) for olivine at 1300°C and Azuma et al. (2012) for ice at -20°C. Note that $J_{SS} \cdot M_{SS}$ is strongly temperature-dependent, in particular because of the temperature dependence of M (Tullis and Yund, 1982; Masuda, 1997; Evans et al., 2011). $(J_{SS} \cdot M_{SS})$(ELLE) can be determined in essentially in the same way by performing a numerical grain growth experiment with a pure, single-phase solid. It has been shown before that the ELLE routine results in a linear growth of the grain area, as expected from Eq. (9.8) (Bons et al., 2001). Using the effective $(J_{SS} \cdot M_{SS})$(ELLE), P_{kin} can be determined for the various simulations.

9.4.3   Dynamic recrystallisation − dominated system vs deformation − dominated system

Using P_{kin} calculated for the different numerical experiments, it is possible to propose a "deformation like" map; showing the position of the transition between a deformation-dominated system (regime I) and a dynamic recrystallisation-dominated system (regimes IIa and IIb; Fig. 9.8).

The numerical simulations roughly span the transition from the deformation-dominated regime I to the *GBM*-dominated regime II. The transition, using kinematic scaling of the simulations, is plotted as a function of melt-pocket radius versus strain rate in Fig. 9.8. The transition from one regime to the other is not sharp, but roughly spans one to two orders of magnitude in strain rate. At a given strain rate, the transition is at larger grain sizes for quartz and ice than for olivine.

I: deformation-controlled

In the deformation-controlled regime, dynamic recrystallisation is too slow to counteract the shearing of melt pockets. The initial shape of melt pockets, and therefore the resulting wetting angles, are not important. This is because pockets get continuously stretched without shape recovery by grain boundary migration. The aggregate develops a strong anisotropy in such cases. As this anisotropy starts at a high angle to the maximum compressive stress, the aggregate initially hardens before weakening sets in. Although not reached in the simulations, it is expected that stretched melt pockets will eventually merge into melt films parallel to the shear plane, causing a dramatic weakening of the aggregate.

Regime I is favoured by high strain rates and/or large grain sizes (Fig. 9.8). A typical example is experiment 11 (m=50, ϕ=12%, ω=30° and N_{GBM}=1, Table 9.2).

9.4.3.1. Regime IIa: *GBM*-controlled for low wetting angle

Regime IIa prevails when the strain rate is so slow that *GBM* can counteract the stretching of melt pockets and these can retain their concave shape with $\omega<60°$. Typical examples are experiments 12 and 13 (m=50, ϕ=12%, ω=30° and N_{GBM}=10 or 100; Table 9.2). As solid grains get flattened in the shortening direction and melt pockets reside at triple junctions, melt pockets tend to connect in the shortening direction forming elongate melt pools at a high angle to shear plane (Fig. 9.5e). As these melt pools are unfavourably oriented to accommodate shearing, they do not cause much weakening of the aggregate. Rotation in the shear sense causes the melt pools to fall apart into smaller melt pockets (Fig. 9.5f). A dynamic equilibrium is expected to set in with ongoing formation, rotation and destruction of melt pools. Mechanically, the effect of strain is a minor transient weakening before steady state is reached.

In this regime, *GBM* is expected to have a significant effect on permeability, which becomes anisotropic. The maximum permeability develops at a high angle to the stretching direction, which may play a role in focusing melt flow (Katz et al., 2006). Since melt is not fully connected in our 2D models, the formation of melt pools is here an effect of connecting melt pockets solely, and not of proper porous flow through melt pockets (Spiegelman, 2003). The small-scale melt pools may, however, play a role in the formation of larger scale melt-enriched shear bands (compared to the grain size) (Kohlstedt and Holtzman, 2009).

9.4.3.2. Regime IIb: *GBM*-controlled for high wetting angle

At high wetting angles, *GBM* enables melt pockets to fully retain their convex shape (Fig. 9.6). The compact shape reduces melt pocket connectivity. Melt pockets are not inert, but are dragged by solid-solid boundaries. This process leads to their occasional merging, but without forming elongate melt pools. The bulk strength hardly changes with strain, since only the size distribution of melt pockets changes, but not their shape.

A similar behaviour has been described in aggregates containing melt with a high dihedral angle (Walte et al. 2011). At natural strain rates, sulphur-poor Fe alloys that have a very high dihedral angle (ω>130°) are inferred to behave essentially like convex inclusions dragged passively within the matrix (Walte et al. 2011). Air bubbles-bearing ice constituting the upper 600-1200m of polar ice sheets (Faria et al., 2014) are another natural case evolving into the IIb regime. Grain sizes here are in the order of mm's and strain rates $< 10^{-11}$ s^{-1}, where regime-II behaviour is expected according to Fig. 9.8. Bubbles are almost spherical in this layer, indicating that they do not cause a major change in the ice rheology.

9.4.3.2. Comparison with laboratory experiments

Walte et al. (2011) carried out experiments on olivine-melt systems that spanned the transition between deformation- and *GBM*-dominated behaviour (regimes I and II). The transition at strain rates of 10^{-5} to 10^{-6} s^{-1} at melt pocket sizes in the order of microns is as predicted from our simulations. Using the thermodynamic scaling parameter (P_{th}), Walte et al. (2011) predict mantle convection (grain sizes in the order of mm, and strain rates $\leq 10^{-12}$ s^{-5}) to be close to the transition between regimes II and I. However, scaling our numerical simulations with the kinematic scaling parameter (P_{kin}) would place mantle convection well into regime II (Fig. 9.8). This shows that care should be taken when extrapolating physical or numerical experiments to natural conditions, especially since most natural cases appear to lie between the two scaling lines.

9.5   Conclusions

Our numerical simulations that take into account viscous deformation and simultaneous dynamic recrystallisation driven by grain boundary migration (*GBM*) demonstrate that *GBM* significantly influences the microstructural and rheological behaviour of partially molten rocks, provided that *GBM* can compete with deformation (regime II). *GBM* reduces the ability of deforming partially molten aggregates to form through-going shear bands. Instead, melt pools continually form and get destroyed when wetting angles are low (concave melt pockets with $\omega \leq 60°$). This causes some strain softening, but less than that of shear bands that form in the absence of *GBM* in regime I. The compact shape of high-wetting angle melt pockets inhibits the formation of melt pools. As a consequence, there is almost no microstructure change at high relative *GBM* rates and only a very minor change in bulk strength is observed as not the shape, but the size distribution of the melt pockets changes with strain.

Acknowledgements

9.6   References

- Alley, R.B. & Fitzpatrick, J.J., 1999. Conditions for bubble elongation in cold ice-sheet ice. Journal of Glaciology, 45, 147-153.
- Azuma, N., Miyakoshi, T., Yokoyama, S. & Takata, M., 2012, Impeding effect of air bubbles on normal grain growth of ice. Journal of Structural Geology, 42, 184-193.

- Barr, T. D. & Houseman, G. A. 1996, Deformation Fields Around A Fault Embedded In A Non Linear Ductile Medium. Geophysical Journal International, 125, 473-490.

- Becker, J.K., Koehn, D., Walte, N., Jessell, M., Bons, P.D., Passchier, C.W. & Evans, L., 2004. Numerical simulation of disequilibrium structures in solid-melt systems during grain growth. (on-line) Journal of the Virtual Explorer, 11, paper 2.

- Becker, J.K., Bons, P.D. & Jessell, M.W., 2008. A new front-tracking method to model anisotropic grain and phase boundary motion in rocks. Computers & Geosciences, 34, 201-212

- Bons, P.D. & Cox, S.J.D. 1994. Analogue experiments and numerical modelling on the relation between microgeometry and flow properties of polyphase materials. Materials Science and Engineering A175, 237-245.

- Bons, P.D., Barr, T.D. & ten Brink, C.E. 1997. The development of delta-clasts in non-linear viscous materials: a numerical approach.Tectonophysics 270, 29-41.

- Bons, P.D., Jessell, M.W., Evans, L., Barr, T.D. & Stäwe, K. 2001. Modelling of anisotropic grain growth in minerals. Geological Society of America Memoir 193, 39-49

- Bons, P.D., Koehn, D. & Jessell, M.W., 2008. Microdynamic Simulation. Lecture Notes in Earth Sciences 106, Springer, Berlin. 405 pp.

- Bulau, J.R., Waff, H.S. & Tyburczy, J.A., 1979. Mechanical and thermodynamic constraints on fluid distribution in partial melts. Journal of Geophysical Research, 84, 6102–6108.

- Collins, T.J., 2007. ImageJ for microscopy. BioTechniques, 43, S25–S30.

- Cooper, R.F. & Kohlstedt, D.L., 1984. Solution-precipitation enhanced diffusional creep of partially molten olivine-basalt aggregates during hot-pressing. Tectonophysics, 107, 207-233.

- Dabrowski, M., 2008. Anisotropy and heterogeneity in finite deformation: resolving versus upscaling. Unpubl. PhD-thesis, Univ. of Olso, Norway, 156 pp.

- Evans, B., Renner, J. & Hirth, G., 2001. A few remarks on the kinetics of static grain growth in rocks. International Journal of Earth Sciences, 90, 88-103.

- Faria, S.H., Weikusat, I. & Azuma, N., 2014. The microstructure of polar ice. Journal of Structural Geology, 61, 2-20.

- Griera, A., Bons, P.D., Jessell, M.W., Lebensohn, R.A., Evans, L. & Gomez-Rivas, E., 2011. Strain localization and porphyroclast rotation. Geology, 39, 275-278.

- Griera, A., Llorens, M.-G., Gomez-Rivas, E., Bons, P.D., Jessell, M.W., Evans, L.A. & Lebensohn, R., 2013. Numerical modelling of porphyroclast and porphyroblast rotation in anisotropic rocks. Tectonpophysics, 587, 4-29

- Groebner, N. & Kohlstedt, D.L., 2006. Deformation-induced metal melt networks in silicates: implications for core–mantle interactions in planetary bodies. Earth and Planetary Science Letters, 245, 571–580.

- Hollister, L. & M. L. Crawford, 1986. Melt-enhanced deformation: A major tectonic process. Geology, 14, 55–59.

- Holtzman, B.K., Kohlstedt, D.L., Zimmerman, M.E., Heidelbach, F., Hiraga,T. & Hustoft, J., 2003. Melt Segregation and Strain Partitioning: Implications for Seismic Anisotropy and Mantle Flow. Science, 301, 1227-1230.

230

- Hustoft, J., Scott, T. & Kohlstedt, D.L., 2007. Effect of metallic melt on the viscosity of peridotite. Earth and Planetary Science Letters 260, 355-360.

- Jessell, M.W., Bons, P., Evans, L., Barr, T. & Stäwe, K., 2001, Elle: the numerical simulation of metamorphic and deformation microstructures. Computers & Geosciences, 27, 17-30.

- Jessell, M.W., Siebert, E., Bons, P.D., Evans, L. & Piazolo, S. 2005. A new type of numerical experiment on the spatial and temporal patterns of localization of deformation in a material with a coupling of grain size and rheology. Earth and Planetary Science Letters, 239, 309-326.

- Jessell, M.W., Bons, P.D., Griera, A., Evans, L.A. & Wilson, C.J.L, 2009. A tale of two viscosities. Journal of Structural Geology, 31, 719-736.

- Katz, R.F., Spiegelman, M. & Holtzman, B., 2006. The dynamics of melt and shear localization in partially molten aggregates. Nature, 442, 676-679.

- Kohlstedt, D.L. & Holtzman, B.K., 2009. Shearing melt out of the Earth: An experimentalist's perspective on the influence of deformation on melt extraction. Annual Review of Earth Planetary Sciences, 37, 561–93.

- Labrousse, L., Prouteau, G. & Ganzhorn, A.C., 2011. Continental exhumation triggered by partial melting at ultrahigh pressure. Geology, 39, 12, 1171-1174.

- Laporte, D. & Watson, E. B., 1995, Experimental and theoretical constraints on melt distribution in crustal sources: the effect of crystalline anisotropy on melt interconnectivity. Chemical Geology, 124, 161-184.

- Laporte, D., Rapaille, C. & Provost A., 1997. Wetting angles, equilibrium melt geometry and the permeability threshold of partially molten crustal protoliths. In: Bouchez, J.L., Hutton, D.H.W. & Stephens, D.E., (Eds.). Granite: from segregation of melt to emplacement fabric, Kluwert, Dordrecht, 31-54.

- Llorens, M.-G., Bons, P.D., Griera, A., Gomez-Rivas, E. 2013a. When do folds unfold during progressive shearing? Geology, 41, 563-566.

- Llorens, M.-G., Bons, P.D., Griera, A. & Gomez-Rivas, E. 2013b. Single layer folding in simple shear. Journal of Structural Geology. 50, 209-220.

- Masuda, T., 1997, Grain-boundary migration of quartz during annealing experiments at high temperatures and pressures, with implications for metamorphic geology. Journal of Metamorphic Geology, 15, 311-322.

- Mei, S., Bai, W., Hiraga, T., and Kohlstedt, D. L. (2002). Influence of melt on the creep behavior of olivine–basalt aggregates under hydrous conditions. Earth and Planetary Science Letters, 201(3), 491-507.

- Mullins, W.W., (1989). Estimation of the geometrical rate-constant in idealized 3 dimensional grain-growth. Acta Metallurgica, 37, 2979-2984.

- Rubie, D. C., Nimmo, F., & Melosh, H. J. (2007). Formation of Earth's core. Treatise on geophysics, 9, 51-90.

- Roessiger, J., Bons, P.D., Griera, A., Jessell, M.W., Evans, L. Montagnat, M., Kipfstuhl, S., Faria, S.H. & Weikusat, I. 2011. Competition between grain growth and grain size reduction in polar ice. Journal of Glaciology 57, 942-948.

- Roessiger, J., Bons, P.D. & Faria, S.H. 2014. Influence of bubbles on grain growth in ice. Journal of Structural Geology. Journal of Structural Geology 61, 123-132.

- Rosenberg, C.L. & Handy, M.R., 2005. Experimental deformation of partially melted granite revisited: implications for the continental crust. Journal of Metamorphic Geology, 23, 19-28

- Rudnik, R.L., 1995. Making continental crust. Nature, 378, 571-578.

- Rushmer, T., 1995. An experimental deformation study of partially molten amphibolite: application to low-melt fraction segregation. Journal of Geophysical Research, 100, 15681–15695.

- Scott, T. & Kohlstedt, D.L., 2006. The effect of large melt fraction on the deformation behavior of peridotite. Earth and Planetary Science Letters, 246, 177-187.

- Stevenson, D. J. (1990). Fluid dynamics of core formation. Origin of the Earth, 1, 231-249.

- Spiegelman, M. 2003. Linear analysis of melt band formation by simple shear. Geochemistry, Geophysics, Geosystems 4, 8615, doi:10.1029/2002GC000499.

- Takeda, Y.-.T. & Griera, A., 2006. Rheological and kinematical responses to flow of two-phase rocks. Tectonophysics, 427, 95–114.

- Takeda, Y.-T. & Obata, M., 2003. Some comments on the rheologically critical melt percentage. Journal of Structural Geolology, 25, 813-818.

- Terasaki, H., Urakawa, S., Funakoshi, K., Nishiyama, N., Wang, Y., Nishida, K., Sakamaki, T., Suzuki, A. & Ohtani, E., 2009. In situ measurement of interfacial tension of Fe-S and Fe-P liquids under high pressure using X-ray radiography and tomography techniques. Physics of the Earth and Planetary Interior, 174, 220-226.

- Teyssier, C. & Whitney, D., 2002. Gneiss domes and orogeny. Geology, 30, 1139-1142.

- Tullis, J. & Yund, R. A., 1982, Grain growth kinetics of quartz and calcite aggregates. The Journal of Geology, 301-318.

- Urai, J.L., Means, W.D. & Lister, G.S. 1986. Dynamic recrystallization of minerals. Am. Geophys. Un. Geophys. Monogr. 36, 161-199.

- Vielzeuf, D., Clemens, J.D., Pin, C. & Moinet, E., 1990. Granites, granulites and crustal differentiation. In: Vielzeuf, D., Vidal, Ph. (Eds.). Granulites and crustal evolution. Kluwer. Dordrecht, 59-85.

- Walte, N.P., Bons, P.D., Passchier, C.W. & Koehn, D., 2003. Disequilibrium melt distribution during static recrystallization. Geology 31, 1009–1012.

- Walte, N.P., Rubie, D.C., Bons, P.D. & Frost, D.J. 2011. Deformation of a crystalline aggregate with a small percentage of high dihedral-angle liquid: Implications for core-mantle differentiation during planetary formation. Earth and Planetary Science Letters, 305, 124-134.

- Whitney, D., Teyssier, C. & Rey, P.F., 2009. The consequences of crustal melting in continental subduction. Lithosphere, 1, 323-327.

- Wood, B. J., Walter, M. J., & Wade, J. (2006). Accretion of the Earth and segregation of its core. Nature, 441(7095), 825-833.

Appendix A

Setup of numerical simulations

A.1 Setup of ELLE + FFT simulations

The main loop, which includes all processes that operate in an ELLE + FFT simulation (used in chapters 2, 3, 4 and 8) are included in a bash script file (Fig. A.1). This file calls sequentially different main processes: (1) viscoplastic deformation (FFT), (2) grain boundary migration (full_gbmunodes) and (3) recovery (serialSGG) (Fig. A.1). Simulations always start with a deformation step (FFT) and then continue with grain boundary migration and finally recovery processes. There are other processes in between them, to perform operations such as conversion from different formats (e.g. fft2elle or ellefft), reposition the model back to the bounding box after a simple shear deformation step (reposition), and other additional utilities to make sure the data is properly shared between the different processes.

The following files are required to run a FFT calculation:

- 1) make.out is the texture file. It stores the local information of the Fourier points, as euler angles, equivalent stress and strain, rotation work, dislocation density, relative activity of slip systems, number of Fourier point, xy location and grain to which it belongs.

- 2) ice3d.sx is a file containing information of the energy required to activate the different slip systems (critical resolved shear stresses, stress exponents, etc.)

- 3) ppc.in is the FFT settings file, where the texture and the crystal files are specified. It sets the number of phases, relative volume fraction of each phases, the resolution (number of *unodes*), boundary conditions, step size (in seconds), cell dimension, number of iterations of the FFT calculation and the scale and burgers vector for basal slip system (in m).

Different processes are required to run a simulation that combines deformation and

dynamic recrystallisation. Most of them can be downloaded from the ELLE Sourceforge website.

- FFT. This code was created by Ricardo Lebensohn and was adapted to ELLE by Albert Griera. The code can be downloaded, together with the crystal and texture files at http://elle.ws/development/elle-at-sourceforge-net (elle/processes/fft/FFT_256).

- fft2elle and elle2fft, created by Albert Griera and Lynn Evans. They are the transformation files from FFT to ELLE and vice-versa. These modules can be downloaded from http://elle.ws/development/elle-at-sourceforge-net (folder elle/utilities/convert/fft).

- importFFT-data_user_DDsum, created by Albert Griera. This module import sthe FFT results and converts the variables to the ELLE format. It can be downloaded from http://elle.ws/development/elle-at-sourceforge-net (folder elle/processes/fft/fft2elle_data).

- ful_gbmunodes, created by Albert Griera. Front-tracking code that simulates grain boundary migration. It can be downloaded from http://elle.ws/development/elle-at-sourceforge-net (folder elle/processes/fft/full_gbmunodes).

- serialSGG, created by Albert Griera, Verity Borthwick and Sandra Piazolo. This code simulates recovery. It can be found at the attached cd.

```
gbmsteps=1                                    Number of gbm steps
gbmfile="gbmunodes001.elle"                   Grain boundary migration file
sggsteps=1                                     Number of recovery steps
sggfile="pSGG.001.elle"                       Recovery file

for ((i=0 ; i<=45 ; i++ ))                    Steps (i)
do

 mkdir step$i
                                              Create the step folder
## FFT

 ./fft256/fft_256                             Run FFT

  cp temp-FFT.out temp.out                    Copy an output file

  fft2elle -i elle2fft001.elle -n             Transformation from FFT to ELLE

  reposition -i movenodes.elle -n             Reposition

  importFFTdata_user_DDsum -i repos.elle -u 4 5 -n   Import the FFT results to variables in ELLE

## FFT finished

shiftphase -i fft_out.elle -s 1 -f 1 -n -u -1       Necessary if processes are using different phase numbers

cp shiftphase001.elle tmp.elle                Copy output file in a temporary file

## Step of GBM

full_gbmunode -i tmp.elle -s $gbmsteps -f 1 -n -u 0 0 0 Run gbm

cp $gbmfile gbm_1ok.elle                      Copy the output file

mv $gbmfile SGG.elle                          Rename the output file

## GBM finished

# STEP of SGG

serialSGG -i SGG.elle -n -u 2                 Run recovery

cp $sggfile tmp.elle                          copy in a temporary file

# SGG finished

checkangle -i tmp.elle -s 1 -f 1 -n -u 0.4 1    check angle between segments, checkarea of new flynns and checkratio
shiftphase -i checkangle001.elle -s 1 -f 1 -n -u 1         Shift phases to FFT
 elle2fft -i shiftfase001.elle -u 256 0 -n     Export to a new FFT mesh
 rar a -df step$i.rar *.elle *.out             Store and compress data
rar e step$i.rar make.out elle2fft001.elle temp.out
mv step$i.rar step$i/
done                                          End
```

Figure A.1: Example of a launch file including all the modules involved in a simulation of viscoplastic deformation coupled with dynamic recrystallisation (GBM and recovery)

A.2 Setup of ELLE + BASIL simulations

Simulations presented in chapters 5,6,7 and 8 are performed with ELLE + BASIL. Several processes have to be executed in order to run these simulations (see batch file in Fig. A.2). BASIL is a finite element code for the simulation of non-linear viscous deformation. BASIL uses a .in file to define the deformation conditions (type of mesh, error for the calculations, stress exponent, time step size, boundary conditions, etc.). Examples of these files can be found in the attached CD. The loop starts with shifty, which is a process that shifts the model depending on a horizontal random plane. The model is subsequently repositioned with the module reposition. After that, the ELLE microstructure is transformed to a mesh for BASIL, using the code triangle (process elle2poly). A Delaunay triangulation mesh is created. BASIL deforms this mesh, and produces some output files, which are converted again to the ELLE format (basil2elle). Then a subsequent reposition step is required. The loop finishes by calling shifty and reposition, to bring back the model geometry to the visualisation state (i.e. without shifting the model according to a random plane).

```
STARTFILE=m4_g2.elle
ROOTNAME=model
BASINFILE=ssh-fault.in
istep=1
fstep=160

GGSTAGES=1

mkdir FD.sols FD.out 98
cp $STARTFILE tmp.elle

for ((i=$istep ; i<=$fstep ; i++ ))
do

#1 shifty
    shifty -i tmp.elle -s 1 -f 1 -n
    /bin/cp shifty001.elle tmp.elle
    /bin/cp shifty001.elle $ROOTNAME.$i.99.elle
    /bin/mv shifty001.elle $ROOTNAME

 #2 reposition
    reposition -i tmp.elle -s 1 -f 1 -n
    /bin/cp repos.elle tmp.elle
    /bin/cp repos.elle $ROOTNAME.$i.13.elle
    /bin/mv repos.elle $ROOTNAME

#3 elle2poly
    elle2poly tmp.elle tmp.poly pb

#4 basil
    basil $BASINFILE
    /bin/cp FD.sols/basil FD.sols/$ROOTNAME.$i
    /bin/cp FD.out/basil.out FD.out/$ROOTNAME.out.$i

#5 basil2elle
    basil2elle -i FD.sols/basil -r 2 -o tmp2.elle
    /bin/cp tmp2.elle tmp.elle
    /bin/mv tmp2.elle $ROOTNAME

 #6 reposition
    reposition -i tmp.elle -s 1 -f 1 -n
    /bin/cp repos.elle tmp.elle
    /bin/cp repos.elle $ROOTNAME.$i.13.elle
    /bin/mv repos.elle $ROOTNAME

#7 shifty
    shifty -i tmp.elle -s 1 -f 1  -n
    /bin/cp shifty001.elle tmp.elle
    /bin/mv shifty001.elle $ROOTNAME

 #8 reposition
    reposition -i tmp.elle -s 1 -f 1 -n
    /bin/cp repos.elle tmp.elle
    /bin/cp repos.elle $ROOTNAME.$i.98.elle
    /bin/cp $ROOTNAME.$i.98.elle 98/
    /bin/mv repos.elle $ROOTNAME

 #9 grain growth
    elle_gg -i tmp.elle -u $i -s $GGSTAGES -f $GGSTAGES -n
    /bin/cp growth00$GGSTAGES.elle tmp.elle
    /bin/cp growth00$GGSTAGES.elle $ROOTNAME.$i.18.elle
    /bin/mv growth00$GGSTAGES.elle $ROOTNAME

 #10 compress files
    rar a -df FD.sols/model.$i.rar FD.sols/model.$i
    rar a -df step.$i.rar $ROOTNAME.$i.*.elle

done
```

Figure A.2: Example of a bash file for launching a folding simulation.

A.3 Setup of ELLE + BASIL simulations, including grain boundary migration

Simulation of partially molten rocks, including linear viscous deformation and dynamic recrystallisation by grain boundary migration, is presented in chapter 9. These simulations couple the finite element viscous deformation code BASIL with a front-tracking approach that simulates grain boundary migration (*GBM*). The *GBM* code was written by Jens Röessiger. These simulations also make use of the BASIL .in file (described in Appendix B). A file containing information for the *GBM* process (phase_db.txt) is also required (see in attached CD). This file contains the data of surface energies and mobilities for the *GBM* calculation. The loop (Fig. A.3) starts with the *GBM* process, followed by an utility to check that the process has successfully done all the *GBM* steps (GBMSTAGES). If the *GBM* process cannot do all the steps, then the simulation run stops. This process is followed by the same loop as described in the previous section (shifty, reposition, elle2poly, BASIL basil2elle, reposition, shifty and reposition again).

```
STARTFILE=m_50-mf_10-wa_60.elle
ROOTNAME=model
BASINFILE=ssh-fault.in
istep=1
fstep=160
GBMSTAGES=200
mkdir FD.sols FD.out 98
cp $STARTFILE tmp.elle
for ((i=$istep ; i<=$fstep ; i++ ))
do
   #1 grain boundary migration Jens Rössiger code
     elle_gbm_pp_unodes-old -i tmp.elle -s $GBMSTAGES -f $GBMSTAGES -n
    /bin/cp gbm_pp$GBMSTAGES.elle tmp.elle
    /bin/cp gbm_pp$GBMSTAGES.elle $ROOTNAME.$i.80.elle
    /bin/mv gbm_pp$GBMSTAGES.elle $ROOTNAME
    rm PhaseAreaHistory.txt avg_areas.txt
   #2 check whether gbm_pp_unodes did all the steps or not
     for GBMCHECK in `cat GBM-check.txt`
     do
      echo $GBMCHECK
     done
     if [ "$GBMCHECK" = "1" ]
      then
       echo ------------------------------------------------------------
       echo SHELLE STOPS BECAUSE gbm_pp_unodes COULD NOT DO ALL THE STEPS
       echo PLEASE CHECK YOUR FILES AND RELAUNCH THE SIMULATION
       echo ------------------------------------------------------------
       break
      else
       echo ------------------------------------------------------------
       echo EVERYTHING WENT WELL WITH GBM FOR TIME STEP $i
       echo ------------------------------------------------------------
      fi
  #3 shifty
    shifty -i tmp.elle -s 1 -f 1 -n
    /bin/cp shifty001.elle tmp.elle
    /bin/cp shifty001.elle $ROOTNAME.$i.99.elle
    /bin/mv shifty001.elle $ROOTNAME
  #4 reposition
    reposition -i tmp.elle -s 1 -f 1 -n
    /bin/cp repos.elle tmp.elle
    /bin/cp repos.elle $ROOTNAME.$i.13.elle
    /bin/mv repos.elle $ROOTNAME
  #5 elle2poly
    elle2poly tmp.elle tmp.poly pb
  #6 basil
    basil $BASINFILE
    /bin/cp FD.sols/basil FD.sols/$ROOTNAME.$i
    /bin/cp FD.out/basil.out FD.out/$ROOTNAME.out.$i
  #7 basil2elle
    basil2elle -i FD.sols/basil -r 2 -o tmp2.elle
    /bin/cp tmp2.elle tmp.elle
    /bin/mv tmp2.elle $ROOTNAME
  #8 reposition
    reposition -i tmp.elle -s 1 -f 1 -n
    /bin/cp repos.elle tmp.elle
    /bin/cp repos.elle $ROOTNAME.$i.13.elle
    /bin/mv repos.elle $ROOTNAME
  #9 shifty
    shifty -i tmp.elle -s 1 -f 1  -n
    /bin/cp shifty001.elle tmp.elle
    /bin/mv shifty001.elle $ROOTNAME
  #10 reposition
    reposition -i tmp.elle -s 1 -f 1 -n
    /bin/cp repos.elle tmp.elle
    /bin/cp repos.elle $ROOTNAME.$i.98.elle
    /bin/cp $ROOTNAME.$i.98.elle 98/
    /bin/mv repos.elle $ROOTNAME
  #11 compress files
    rar a -df FD.sols/model.$i.rar FD.sols/model.$i
    rar a -df step.$i.rar $ROOTNAME.$i.*.elle
done
```

Figure A.3: Example of a bash file for the simulation of partially molten rocks, including linear viscous deformation and grain boundary migration.